

NATIONAL AERONAUTICS AND SPACE ADMINISTRATION

Space Programs Summary 37-49, Vol. II

The Deep Space Network

For the Period November 1 to December 31, 1967

GPO PRICE \$ _____

CSFTI PRICE(S) \$ _____

Hard copy (HC) _____

Microfiche (MF) _____

ff 653 July 65

FACILITY FORM 602

N68-20335
(ACCESSION NUMBER) (THRU)
155
(PAGES) (CODE)
CR 93821
(NASA CR OR TMX OR AD NUMBER) (CATEGORY) **07**



JET PROPULSION LABORATORY
CALIFORNIA INSTITUTE OF TECHNOLOGY
PASADENA, CALIFORNIA

January 31, 1968

NATIONAL AERONAUTICS AND SPACE ADMINISTRATION

Space Programs Summary 37-49, Vol. II

The Deep Space Network

For the Period November 1 to December 31, 1967

JET PROPULSION LABORATORY
CALIFORNIA INSTITUTE OF TECHNOLOGY
PASADENA, CALIFORNIA

January 31, 1968

SPACE PROGRAMS SUMMARY 37-49, VOL. II

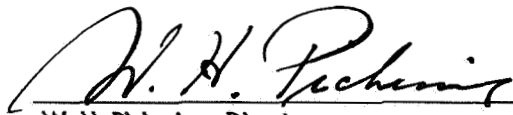
Copyright © 1968
Jet Propulsion Laboratory
California Institute of Technology
Prepared Under Contract No. NAS 7-100
National Aeronautics & Space Administration

Preface

The Space Programs Summary is a bimonthly publication that presents a review of engineering and scientific work performed, or managed, by the Jet Propulsion Laboratory for the National Aeronautics and Space Administration during a two-month period. Beginning with the 37-47 series, the Space Programs Summary is composed of four volumes:

- Vol. I. *Flight Projects* (Unclassified)
- Vol. II. *The Deep Space Network* (Unclassified)
- Vol. III. *Supporting Research and Advanced Development* (Unclassified)
- Vol. IV. *Flight Projects and Supporting Research and Advanced Development* (Confidential)

Approved by:



W. H. Pickering, Director
Jet Propulsion Laboratory

Contents

I. Introduction	1
II. Tracking and Navigational Accuracy Analysis	3
A. DSN Inherent Accuracy Project	
<i>T. W. Hamilton and D. W. Trask</i>	3
B. A Possible Explanation of Landed Surveyor Residuals	
<i>J. D. Mulholland</i>	4
C. Analysis of the Mariner V Midcourse Maneuver From Radio Tracking Data	
<i>G. E. Pease</i>	6
D. Status of DSS Location Solutions for Deep Space Probe Missions: II. Mariner V Real-Time Solutions	
<i>N. A. Mottinger</i>	10
E. A Method of Constrained Least-Squares Polynomial Fitting With Application to Analysis of A.1 — WWV From 1955 to 1968	
<i>P. M. Muller</i>	23
F. Navigation Technology Project	
<i>D. W. Curkendall</i>	32
G. Navigation Technology: Dynamic Programming Approach to Optimal Stochastic Orbit-Transfer Strategy	
<i>T. Nishimura</i>	34
H. Navigation Technology: Continuous Estimation of the State of a Distant Spacecraft During a Single Pass of Data	
<i>J. F. Jordan</i>	43
I. Double-Precision Trajectory Program: DPTRAJ	
<i>A. R. Khatib</i>	52
III. Communications Engineering and Development	57
A. Rotating Linear Polarization Modification of the DSS 14 Receiver	
<i>G. S. Levy and B. L. Seidel</i>	57
B. Ultracone Rotatable Linear Polarization Modifications	
<i>F. E. McCrea</i>	58
C. Low-Noise Receivers: Microwave Maser Development, Second Generation TWM	
<i>R. C. Clauss</i>	60
D. Improved RF Calibration Techniques: Ultracone-on-Ground Noise Temperature Calibrations	
<i>T. Y. Otoshi</i>	62
E. Efficient Antenna Systems: X-Band Gain Measurements	
<i>D. A. Bathker</i>	65

Contents (contd)

F. Prototype Frequency Agile Receiver (Wide-Band Receiver System)	
<i>K. D. Schreder</i>	67
G. Solution to Phase Jitter Problem in MSFN Range Receiver	
<i>R. W. Tappan and J. H. Wilcher</i>	82
H. 450-kW 2.388-GHz Transmitter	
<i>C. P. Wiggins and R. L. Leu</i>	84
I. DSN 20-kW Transmitter	
<i>B. W. Harness</i>	88
J. 500-kW (CW) WR-430 Waveguide Switch Tests	
<i>B. W. Harness</i>	92
K. DSS 13 Mariner Venus 67 Occultation and CW Signal Power Calibration Receiver	
<i>C. F. Foster</i>	95
L. Multiple-Mission Telemetry System	
<i>W. S. Baumgartner, W. Frey, J. K. Woo, R. G. Petrie, J. E. Stelzried, and M. H. Brockman</i>	98
IV. High-Rate Telemetry Project	115
A. Introduction	
<i>R. C. Tausworthe</i>	115
B. Test Equipment	
<i>R. I. Greenberg</i>	115
C. Digital Equipment	
<i>R. A. Winkelstein</i>	120
D. Verification Tests	
<i>R. W. Burt</i>	123
E. Subcarrier Demodulator	
<i>M. H. Brockman</i>	127
V. Facility Engineering and Operations	128
A. Goldstone DSCC Flight Project Support	
<i>W. E. Larkin and R. M. Cuberly</i>	128
B. Multiple-Mission Telemetry Implementation	
<i>R. L. Weber</i>	130
C. DSIF Station Control and Data Equipment	
<i>E. Bann, R. N. Flanders, A. T. Burke, P. C. Harrison, and E. Garcia</i>	130
D. Venus DSS Operations	
<i>J. D. Campbell, M. A. Gregg, E. B. Jackson, and A. L. Price</i>	132
E. CTA 21 Implementation	
<i>R. C. Rydgig</i>	133

Contents (contd)

F. High Performance Microwave Link Between DSS 61 and DSS 62	
<i>B. Bridges</i>	137
G. Ground Instrumentation Configuration for the <i>Mariner Venus 67</i> (<i>Mariner V</i>) Occultation Experiment	
<i>P. L. Parsons and G. S. Levy</i>	137
H. Advanced Data Systems Project: Proposed Configuration of a Third-Generation SFOF Computing System	
<i>A. T. Arcand</i>	140
I. Advanced Data Systems Project: A Demonstration of Computer-Assisted Entry	
<i>K. R. Carter</i>	142
J. Antenna Engineering	
<i>V. B. Lobb, M. Kron, W. J. Kissane, H. D. McGinness, D. L. Lambdin, C. Lundy, A. Nicula,</i> <i>R. McKee, J. Carlucci, Jr., M. S. Katow, W. W. Van Keuren, and M. G. Newsted</i>	145
Abbreviations	155

I. Introduction

The DSN is a facility established by the NASA Office of Tracking and Data Acquisition under the system management and technical direction of JPL, and is responsible for two-way communications with unmanned spacecraft traveling approximately 10,000 miles from earth to interplanetary distances. The DSN is distinct from other NASA networks such as the STADAN, which tracks earth-orbiting scientific and communication satellites, and the MSFN, which tracks the manned spacecraft of the *Gemini* and *Apollo* Projects.

The DSN performs four basic functions in support of each space flight project: tracking, data acquisition, command, and control. Tracking is the function of locating the spacecraft, calculating its distance, velocity, and position, and following its course. Data acquisition consists of the recovery of information from the spacecraft in the form of telemetry—the recorded measurements of the condition of, and the scientific data obtained by, the spacecraft. The command function involves the sending of signals to the spacecraft to guide it in its flight and to operate scientific and engineering equipment on board the spacecraft. Control refers to the making of command decisions from a central facility and to the overall direction of flight operations, including the network of ground stations, during a mission. Present facilities permit simultaneous control of a newly launched spacecraft and a

second one already in flight. In preparation for the increased number of U.S. activities in space, a capability is being developed for simultaneous control of either two newly launched spacecraft plus two in flight, or four spacecraft in flight. With the advanced communications techniques now being implemented, it may soon be possible to obtain data from, and track spacecraft to, planets as far out in space as Jupiter.

The DSN supports, or has supported, the following NASA space exploration projects: *Ranger*, *Surveyor*, and *Mariner* (JPL); *Lunar Orbiter* (Langley Research Center); *Pioneer* (Ames Research Center); and *Apollo* (Manned Spacecraft Center), as backup to the MSFN.

The main elements of the network are the DSIF, with space communications and tracking stations located around the world; the GCF, which provides communications between all elements of the DSN; and the JPL SFOF, the command and control center.

The DSIF is a worldwide chain of DSSs that provide radio contact with the spacecraft (Table 1). JPL operates the U.S. and the Ascension Island stations. The overseas stations are normally staffed and operated by government agencies of the respective countries, with the assistance

Table 1. DSIF station nomenclature

DSCC	DSS	DSS serial designation	Geodetic longitude, deg
Goldstone	Pioneer	11	243.1 E
	Echo	12	243.2 E
	Venus	13	243.2 E
	Mars	14	243.1 E
Canberra	Woomera	41	136.9 E
	Tidbinbilla	42	149.0 E
	Booroomba ^a	43	—
	Johannesburg	51	27.7 E
Madrid	Robledo	61	355.7 E
	Cebreros	62	355.6 E
	Rio Cofio ^a	63	—
	Cape Kennedy (Spacecraft Monitoring)	71	279.4 E
	Ascension Island (Spacecraft Guidance and Command)	72	345.7 E
^a Not yet authorized.			

of U.S. support personnel. To maintain continuous mission coverage, the stations are placed approximately 120 deg apart in longitude around the earth, so that the spacecraft is always within the field of view of at least one of the ground stations.

Radio contact with the spacecraft begins when it is poised on the launch pad at Cape Kennedy, and is maintained throughout the mission as the spacecraft passes from the field of view of one station to that of another. The Cape Kennedy tracking facility monitors the spacecraft during and immediately after launch. Later in the launch trajectory, while the spacecraft is relatively low in altitude, the signal is picked up by the 30-ft-diam antenna at Ascension Island. Once the spacecraft is in orbit, the DSSs with the large antennas, low-noise phase-lock receiving systems, and high-power transmitters take over radio communications and follow the vehicle to its destination. These stations obtain angular position, velocity (doppler), and distance (range) data for the spacecraft, and provide command control (up-link) and data reception (down-link) for the spacecraft. The standard 85-ft-diam antennas in use at the DSSs have gains of 53 dB at 2295 MHz, permitting the receipt of significant data at distances as far as Mars. To improve the data-rate and distance capability, a 210-ft-diam antenna having a gain of 61.81 ± 0.32 dB at 2295 MHz has been built at DSS 14; two additional

antennas of this size are planned for installation at overseas stations. In the present configuration, with the exception of DSS 51 which has an S-band receiver-exciter subsystem, all stations are full S-band.

The DSN continuously conducts research and development of new components and systems to maintain a state-of-the-art capability. Therefore, the Goldstone DSCC is also used for extensive investigation of space tracking and telecommunications techniques, establishment of DSIF-spacecraft compatibility, and development of new DSIF hardware and software. New DSIF system equipment is installed and tested at the Goldstone DSCC before being accepted for systemwide integration into the DSIF. After acceptance for general use, it is classed as GSDS equipment, thus standardizing the design and operation of identical items throughout the system.

The GCF, using facilities of the worldwide NASCOM, provides voice and teletype communications among the overseas DSIF stations, the Goldstone DSCC, Cape Kennedy, and the SFOF. A special microwave link, which includes a video channel, is used between the SFOF and the Goldstone DSCC to transmit critical data during a mission. Overseas communications are transmitted by land lines, submarine cables, microwave relays, high-frequency radio circuits, and even communication satellites.

Teletype is the primary means of transmitting tracking and telemetry data from the DSSs to the SFOF and sending predictions and other data to the stations. Voice circuits are used for transmission of high-priority communications other than data.

The SFOF at JPL is equipped with operations control consoles, status and operations displays, computers, and data-processing systems, and is the focal point of the DSN. From launch through mission completion, it is the control center for DSIF tracking and data-acquisition activities, as well as for spacecraft trajectory determinations, generation of the commands transmitted to the spacecraft, and analysis and interpretation of the data received.

Internal communications at the SFOF are maintained by means of telephones, voice intercom units, a public address system, closed-circuit TV, and other types of visual displays. Incoming spacecraft telemetry and tracking data from the DSSs are automatically routed to the SFOF data-processing system, where special telemetry-processing equipment and high-speed digital computers convert the data into information for use by scientific experimenters and spacecraft engineers.

II. Tracking and Navigational Accuracy Analysis

A. DSN Inherent Accuracy Project,

T. W. Hamilton and D. W. Trask

The DSN Inherent Accuracy Project was formally established by the DSN Executive Committee in July 1965. The objectives of the project are:

- (1) Determination (and verification) of the inherent accuracy of the DSN as a radio navigation instrument for lunar and planetary missions.
- (2) Formulation of designs and plans for refining this accuracy to its practical limits.

Achievement of these goals is the joint responsibility of the Telecommunications Division (33) and the Systems Division (31) of JPL. To this end, regular monthly meetings are held to coordinate and initiate relevant activities. The project leader and his assistant (from Divisions 31 and 33, respectively) report to the DSN Executive Committee, and are authorized to task project members to (1) conduct analyses of proposed experiments, (2) prepare reports on current work, and (3) write descriptions of proposed experiments. The project is further authorized to deal directly with those flight projects using the DSN regarding data-gathering procedures that bear on inherent accuracy.

The various data types and tracking modes provided by the DSIF in support of lunar and planetary missions are discussed in SPS 37-39, Vol. III, pp. 6-8. Technical work directly related to the Inherent Accuracy Project is presented in SPS 37-38, Vol. III, and in subsequent *Deep Space Network* SPS volumes, and is continued in the following sections of this volume.

Processing range-rate data from *Surveyor* spacecraft resting on the lunar surface has resulted in unusual residuals. Initially these residuals exhibited both a 10-day and a daily periodic variation. The use of an improved lunar ephemeris obtained by fitting an integrated lunar trajectory to the positions available from the Improved Brown Lunar Theory was discussed in SPS 37-48, Vol. II, pp. 4-7. Although the 10-day periodic signature of 1.5-mm/s amplitude is no longer visible using this latest lunar ephemeris, daily anomalies with amplitudes exceeding 0.5 mm/s remain. However, as stated in Section B, the lunar ephemeris is still the prime suspected cause of these residuals. An explanation may be found in the work currently being carried out at the U.S. Naval Observatory by Van Flandern, who, through processing grazing occultation optical data, has arrived at corrective terms to the Brown Lunar Theory. Inadequacies may exist in the original theory because of the then-unknown effects,

such as variations of the earth's rotation rate and of the center of figure of the moon.

Section C illustrates the effect of radio tracking data in the analysis of spacecraft maneuvers. In this case, the *Mariner V* midcourse maneuver magnitude and turns are analyzed. Errors in the execution of the maneuver, which resulted in the spacecraft passing 2000 km further from Venus than the nominal aim point, were due primarily to the midcourse maneuver not delivering its designed thrust, while errors in the execution of the maneuver turns accounted for less than 400 km.

Sections D and E pertain to the task of determining DSS locations to the order of 1 m. This accuracy is necessary to fulfill the navigational accuracy goals being considered for future planetary projects. The DSS location solutions from *Mariner V* tracking data are described in Section D, where particular emphasis is placed on the behavior of the solutions during the mission. Data on polar motion is routinely available from the International Polar Motion Service 90 days after the fact and, therefore, must be extrapolated to support the mission in real time. It is interesting to note that the *Mariner V* mission occurred during a region of "poor predictability" and that the extrapolated information used during the flight contributed up to 3 m in DSS location errors.

Section E describes a method for constrained polynomial fitting to long data spans. The program is applied to the A.1-WWV time differences in this article, but it is intended primarily for applications which will be discussed in later articles on A.1-UT1 and polar motion. These quantities affect navigational accuracy in two ways: (1) The navigational accuracy realizable in support of planetary encounter operations is directly limited by errors in DSS locations, as well as errors in the above timing relationships and polar motion which exist during the encounter phase of the mission; and (2) the DSS locations resulting from post-flight analysis of tracking data from past deep space probe missions are themselves limited by errors in the timing relationships and polar motion which existed during these past missions.

A description of the Navigational Technology Project is contained in Section F along with an introduction to the two following articles, each of which relates to this project. Section G describes an optimal stochastic orbit trim strategy for a planetary satellite, and the article comprising Section H is the second of a series giving results from the continuous estimation program.

Section I describes the Double-Precision Trajectory Program which has been developed at JPL and is now operational. This program is an integral part of the Double-Precision Orbit Determination Program described in a series of 10 articles in the *Deep Space Network* SPS volumes starting with SPS 37-38.

B. A Possible Explanation of Landed Surveyor Residuals, J. D. Mulholland

Recent progress in the lunar ephemeris improvement effort [Devine, SPS 37-48, Vol. III, pp. 33-39, and (to be published) Mulholland, SPS 37-49, Vol. III] has provided the tool for confirmation of the belief that gravitational defects in the operational ephemeris LE 4 (Ref. 1) have significantly degraded the analysis of tracking data from lunar spacecraft. Sjogren and Cary (SPS 37-48, Vol. II, pp. 4-7) have found the use of a numerically integrated ephemeris to yield notable reductions in the residuals for range-rate data from *Lunar Orbiter* spacecraft and doppler data from the landed *Surveyor I*. Nonetheless, as they noted, the *Surveyor I* doppler residuals are still rather large and quite systematic. On the basis of discussions with this author, Sjogren and Cary suggested that a major cause of the remaining residuals was the archaic value of the dynamical form factor J_2 for earth that was used in the ephemeris (Mulholland, SPS 37-47, Vol. III, pp. 6, 7). Although plausible, the basic idea conveyed by the author in these discussions was erroneous; i.e., the incorrect J_2 is incapable of being the primary cause of the residuals shown in Fig. 3(b) in SPS 37-48, Vol. II, p. 6.

The effect on topocentric range rate $\dot{\rho}$ of errors in the longitude and latitude of the moon can be simulated in the following way: Cary (SPS 37-47, Vol. II, pp. 4-11) has given partial derivatives of $\dot{\rho}$ with respect to the selenographic coordinates x_1, x_2, x_3 . Since the moon's equatorial plane is not greatly different from the ecliptic plane, one can say that, to a reasonable approximation, errors in the lunar longitude λ and latitude β will resemble errors in x_2 and x_3 . Thus, the relationship

$$\Delta \dot{\rho} = \frac{\partial \dot{\rho}}{\partial x_2} \Delta \lambda + \frac{\partial \dot{\rho}}{\partial x_3} \Delta \beta \quad (1)$$

will give a reasonable simulation of the effect of changes $\Delta \lambda$ and $\Delta \beta$ to the ephemeris. In performing this computation, it is necessary that any constant or long-period parts of $\Delta \lambda$ and $\Delta \beta$ be ignored, for these will be artificially absorbed into the least-squares solution for spacecraft location and will not be apparent in the residuals.

When Cary's derivatives are evaluated in units of (mm/s)/second of arc, one obtains

$$\begin{aligned}\frac{\partial \dot{\rho}}{\partial x_2} &= +0.543 \cos \ell - 2.16 \cos (\alpha_\tau - L) \\ \frac{\partial \dot{\rho}}{\partial x_3} &= -0.575 \cos (L - \Omega) - 0.837 \cos \alpha_\tau\end{aligned}\quad (2)$$

where ℓ is the mean anomaly, L is the mean longitude, and Ω is the longitude of the ascending node of the lunar orbit. The rotation of the earth appears through α_τ , the geocentric right ascension of the tracking station.

The primary part of interest in the J_2 correction required by the ephemeris is (Ref. 2)

$$\begin{aligned}\Delta \lambda_1 &= 0 \\ \Delta \beta_1 &= +0''.215 \sin L\end{aligned}\quad (3)$$

(The major term in $\Delta \lambda$ has a 19-yr period and is thus omitted here.) The angles in Eqs. (2) and (3) were evaluated, using only their constant and linear terms, for the interval of *Surveyor 1*'s first lunar day. Figure 1(a) shows the simulated corrections to the residuals for this case. Comparison with the residuals reveals that the phase does not match that of the residuals very well, the maximum amplitude is too small by a factor of 3, and the amplitude modulation is unsatisfactory. It seems reasonable to infer that something else is wrong with the ephemeris.

The present work is totally vulnerable to errors in the Lunar Theory upon which the ephemeris is based. There exists relative certainty that no significant errors exist in the derivation of the solar part of the theory, and the numerical integration is presumed to have overcome the effects of series truncation. It seems very possible, however, that, because of then-unknown effects such as variations of the earth's rotation rate and of the center of figure of the moon, Brown was not able to properly fit the observations (Ref. 3). Preliminary results¹ of research currently under way at the U.S. Naval Observatory indicate that the following corrections should be applied to the Lunar Theory:

$$\begin{aligned}\Delta \lambda_2 &= +0''.15 \cos \ell + 0.05 \sin \ell \\ &\quad - 0.11 \cos L - 0.10 \sin L \\ \Delta \beta_2 &= -0''.28 \cos F - 0.33 \sin F \\ &\quad - 0.14 \cos L - 0.18 \sin L\end{aligned}\quad (4)$$

where F is the argument of latitude. Combining these expressions with Eqs. (2) and (3), the simulated corrections to the residuals shown in Fig. 1(b) are obtained. Figure 2 presents this curve inverted and superimposed on the residual plot. The correlation is not perfect, or

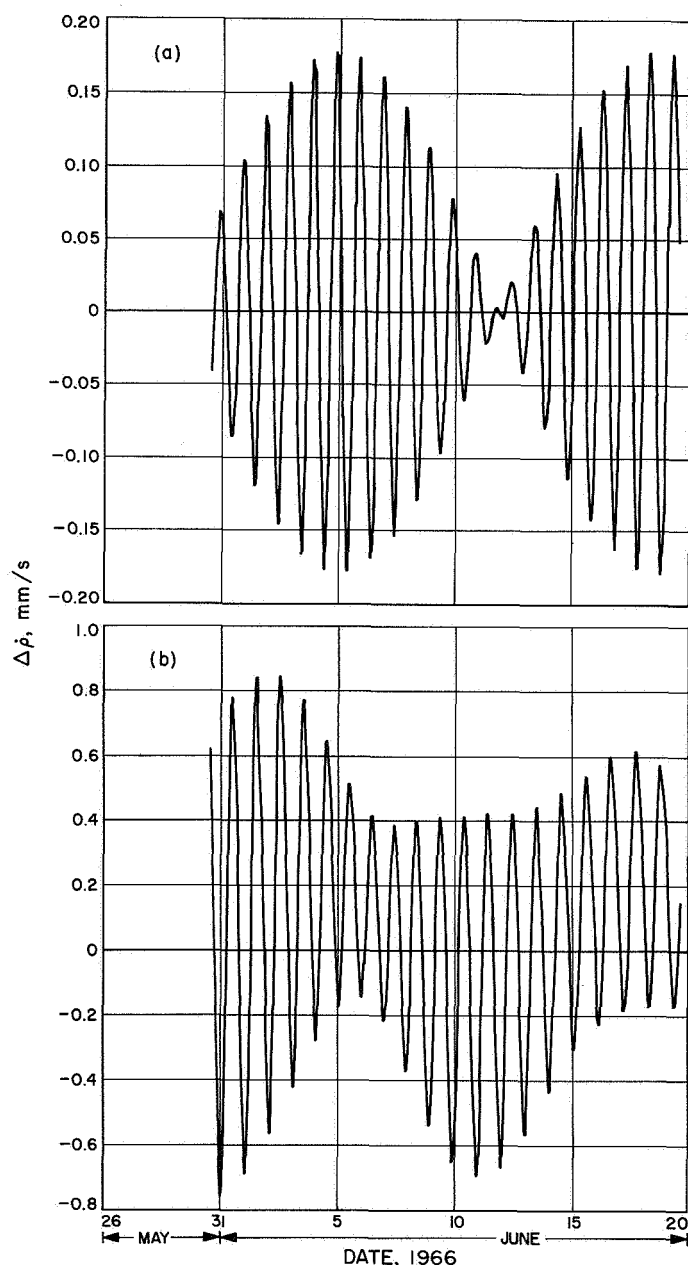


Fig. 1. Simulated effect on range-rate observations at DSS 42 of: (a) J_2 correction, and (b) combined Van Flandern corrections and J_2 correction

¹Private communication with T. C. Van Flandern.

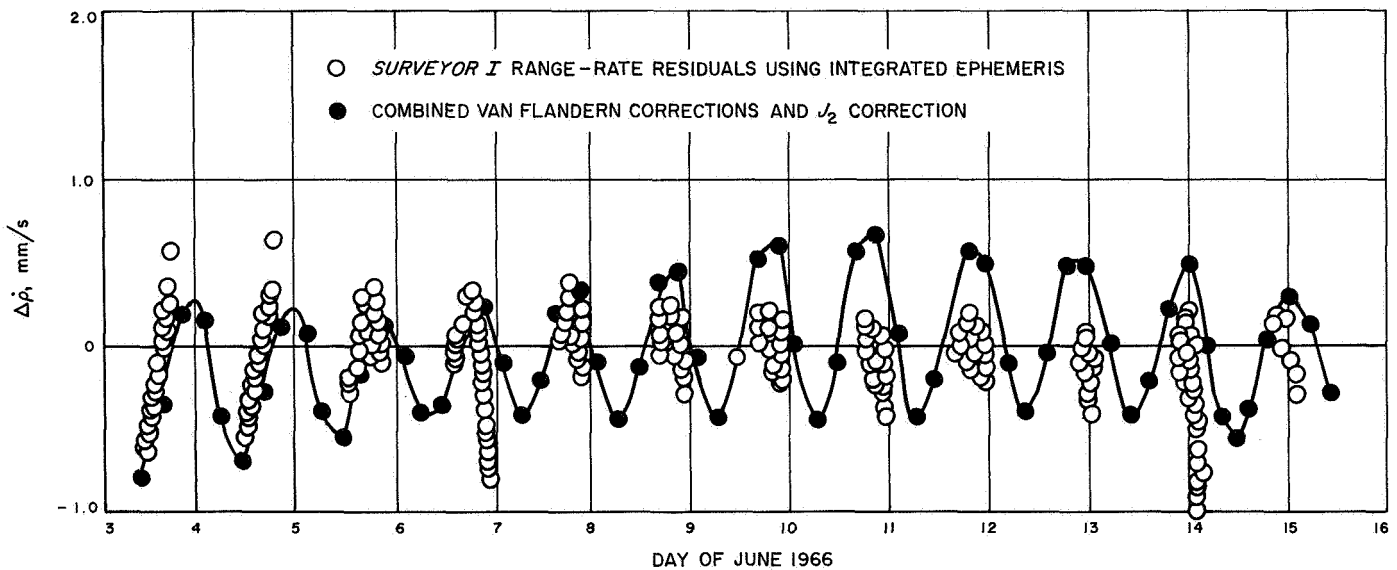


Fig. 2. Comparison of Surveyor I range-rate residuals with data from Fig. 1b

even conclusive, but it is certainly suggestive. The phase, amplitude, and modulation are not unreasonable. The mean lines of the two curves are skewed, but this might possibly be an effect of the least-squares processing of the data. It is planned to construct a short, experimental integrated ephemeris which will include the J_2 corrections and provisional corrections (Eq. 4), so that the Surveyor I data can be reprocessed.

If this investigation does, in fact, yield greatly reduced residuals, this would constitute a partial confirmation of Van Flandern's work. At present, however, it must be stressed that the corrections (Eq. 4) are provisional and incomplete. Furthermore, Van Flandern's general conclusions may yet be disproven, although this now seems very unlikely to the author. On the other hand, the suggestion that this is the source of the Surveyor I residuals must be regarded as only a promising speculation.

One interesting sidelight is worthy of mention. Van Flandern's discovery of the error described above required the development and application of an entirely new optical data type: the grazing occultation. The Surveyor I data, which may provide the first independent test of his work, also represents an entirely new data type: a radio transponder fixed on the lunar surface.

References

1. Mulholland, J. D., and Block, N., *JPL Lunar Ephemeris Number 4*, Technical Memorandum 33-346. Jet Propulsion Laboratory, Pasadena, Calif., Aug. 1, 1967.

2. "Supplement to the A. E. 1968," in *The American Ephemeris and Nautical Almanac for 1968*. U.S. Government Printing Office, Washington, 1966.
3. Van Flandern, T. C., "A Preliminary Report on a Lunar Latitude Fluctuation," in *Proceedings of the JPL Seminar on Uncertainties in the Lunar Ephemeris*. Edited by J. D. Mulholland. Technical Report 32-1247. Jet Propulsion Laboratory, Pasadena, Calif. (in press).

C. Analysis of the Mariner V Midcourse Maneuver From Radio Tracking Data,²

G. E. Pease

1. Introduction

The Mariner V spacecraft was injected into its earth-Venus trajectory at 6^h24^m19^s.2 UT on June 14, 1967. The nominal closest approach point was 8165 km from the center of Venus, to be reached on October 19, 1967; however, at injection, this was deliberately biased out to 75,000 km from the center of Venus to avoid any chance of impacting the planet. Hence, a midcourse maneuver was planned at the outset to achieve the nominal aiming point. The spacecraft actually had the capability for two maneuvers, but the second maneuver capability was considered to be in the category of a backup procedure, to be used only if the primary mission objectives were not

²Information contained herein concerning midcourse maneuver parameters was supplied by H. J. Gordon and R. T. Mitchell of JPL Technical Section 312; H. J. Gordon also provided the program to compute roll and pitch uncertainties.

achieved by the first maneuver. The second maneuver capability was not, in fact, exercised during the *Mariner V* mission.

Subsequent orbit determination after injection showed that the spacecraft would fly just within 76,000 km of the center of Venus if a midcourse maneuver were not performed. Accordingly, a midcourse maneuver was planned and executed at 23^h08^m06^s UT on June 19, 1967. The motor burn was planned to last 17.66 s and to impart an additional velocity of 16.1272 m/s to the spacecraft. This was to have put the spacecraft within 8200 km of the planet's center at closest approach on October 19. Telemetry and tracking data proved the duration of the motor burn to have been approximately nominal (Fig. 3) and the direction of the impulse to have been within ½ deg of the nominal pointing angle. Yet, orbit determination soon indicated that the probe would fly by Venus at a closest approach distance not less than 10,000 km from the planet's center, and that the velocity imparted to the spacecraft by the motor burn was 15.4123 ± 0.0163 m/s rather than

the planned 16.1272 ± 0.13 m/s. Because the primary mission objectives were not jeopardized by the new arrival point, a decision was made not to attempt a second maneuver. The following analysis shows the orbit-determination procedures used to analyze the magnitude and direction of the midcourse maneuver.

2. Comparison of Premidcourse and Postmidcourse Velocities at Midcourse Epoch

The orbit-determination procedure used involves a weighted least-squares fit of approximately 1200 points of 600-s count-interval, two-way, coherent, doppler tracking data in the 5 days from injection to the midcourse maneuver. In the 28-day period from the midcourse maneuver to July 17, approximately 2000 points of 600-s doppler data and 900 points of ranging data were included in the least-squares fit. Table 1 gives the premidcourse least-squares solution for the spacecraft velocity at 23^h08^m20^s650 UT on June 19 if no maneuver had been performed. Actually, this time occurs during the motor-burn interval, but only premidcourse tracking data were used in the solution. This solution is labeled "estimated premidcourse" in Table 1. The next column gives the "nominal postmidcourse" solution, i.e., the velocity which would have been achieved at this time had a nominal maneuver been executed before the time. Lastly the column labeled "estimated postmidcourse" tabulates the least-squares solution for the velocity based on postmidcourse-maneuver tracking data to July 17. This is felt to be an adequate data arc for the solution; a longer arc allows the corrupting effect of small forces in the orbit fit.

By comparing the nominal maneuver with that actually achieved (Table 2), it can be seen that an error of 0.715 ± 0.016 m/s was made in the magnitude of the maneuver velocity increment. If no pointing error were made, this error accounts closely for the achieved closest approach distance of 10,151 km, compared to the nominal value of 8165 km from the center of Venus. Furthermore, the pointing error of the maneuver thrust axis is easily

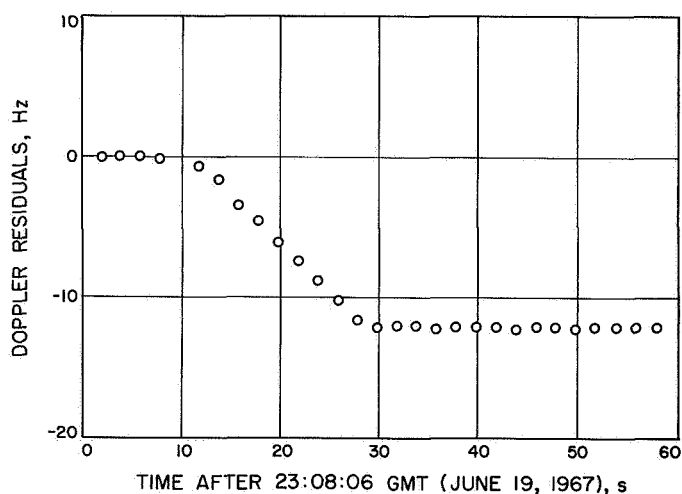


Fig. 3. Two-way doppler residuals during the *Mariner V* midcourse maneuver (DSS 11)

Table 1. *Mariner V* nominal and estimated velocities at 23^h08^m20^s650 UT on June 19, 1967

Velocity component (geocentric equatorial of-date)	Velocity ± σ, m/s		
	Estimated premidcourse	Nominal postmidcourse	Estimated postmidcourse
\dot{x}	-2280.1899 ± 0.0065	-2280.931 ± 0.13	-2280.8194 ± 0.0067
\dot{y}	1849.3605 ± 0.0067	1842.512 ± 0.13	1842.7422 ± 0.0071
\dot{z}	-574.33642 ± 0.01668	-588.9205 ± 0.13	-588.24114 ± 0.00567

Table 2. Nominal and achieved maneuver velocity increments for Mariner V at 23^h08^m20^s.650 UT on June 19, 1967

Velocity component	Postmidcourse-minus-premidcourse velocity increment $\pm\sigma$, m/s		Achieved-minus-nominal value, m/s
	Nominal ^a	Achieved	
$\Delta\dot{x}$	-0.73797 ± 0.13	-0.6295 ± 0.0093	0.1085
$\Delta\dot{y}$	-6.84993 ± 0.13	-6.6183 ± 0.0098	0.2316
$\Delta\dot{z}$	-14.5815 ± 0.13	-13.90472 ± 0.0176	0.6768
$\Delta\dot{v}$	16.1272 ± 0.13	15.4123 ± 0.0163	-0.7149

^aBased on an earlier premidcourse orbit than that tabulated in Table 1. This was of necessity a "real-time" orbit, whereas the tabulated premidcourse orbit was the best estimate after the maneuver.

calculated. The pitch and roll turns are obtained in the following manner:

$$\begin{aligned}
 \text{pitch turn} &= \arctan \left(\frac{\mathbf{V} \cdot \mathbf{j}}{\mathbf{V} \cdot \mathbf{k}} \right) \\
 &+ \arccos \left[\frac{-\cos \xi}{\left(1 - \frac{\mathbf{V} \cdot \mathbf{i}^2}{V^2} \right)^{1/2}} \right] \\
 &= 55.453 \pm 0.062 \text{ deg} \\
 \text{roll turn} &= -\gamma - \arccos \left(\frac{-\mathbf{V} \cdot \mathbf{i}}{V \sin \xi} \right) \\
 &= 70.660 \pm 0.004 \text{ deg}
 \end{aligned}$$

where

\mathbf{V} = maneuver velocity

$\mathbf{i}, \mathbf{j}, \mathbf{k}$ = unit vectors of the premaneuver pitch, yaw, and roll axes at mid-position of the attitude-control deadband

ξ = orientation of the maneuver thrust axis to the roll axis
 $= 88.5 \text{ deg}$

γ = orientation of the projection of the maneuver thrust axis on the pitch-yaw plane from the pitch axis
 $= 45 \text{ deg}$ (Fig. 4)

The pitch and roll uncertainties were obtained from a computer program written by H. J. Gordon which makes use of the 3×3 velocity covariance matrix of $\Delta\dot{x}$, $\Delta\dot{y}$, $\Delta\dot{z}$. The unit vectors used in the above calculations assume

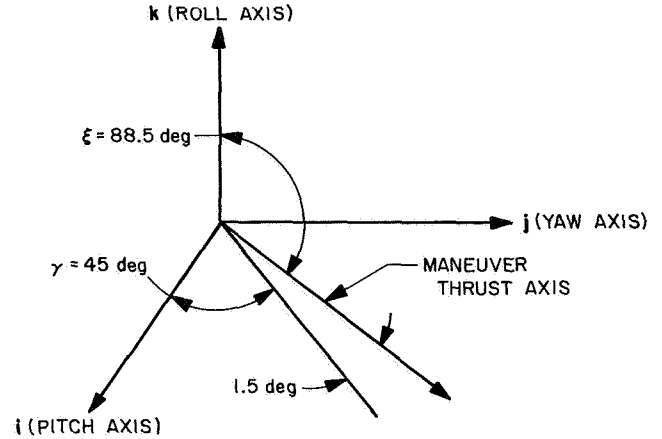


Fig. 4. Mariner V attitude reference system

the attitude control error to be zero. Table 3 shows the corrections indicated by limit-cycle telemetry and the commanded values of the turns.

Thus, errors of about 0.3 deg were made in the execution of the turns. However, the actual errors must include the effects of attitude-control displacement. It is readily seen that the execution and displacement errors partially cancel. An additional limitation on the system is imposed by the command pulse system used to fire the gas jets. This system limits the duration of gas-jet firing to an even number of seconds. Thus, the commanded turns differ from the nominal turns. Table 4 shows the nominal turns

Table 3. Execution errors

Turn	Premaneuver telemetry correction (attitude-control limit-cycle information), deg	Corrected turn (achieved), deg	Commanded turn, deg	Achieved-minus-commanded value, deg
Pitch	0.333 ± 0.020	55.120 ± 0.065	55.267	-0.147 ± 0.065
Roll	0.028 ± 0.014	70.632 ± 0.015	70.946	-0.314 ± 0.015

Table 4. Summary of measured pointing error

Turn	Nominal turn		Achieved turn, deg	Commanded turn duration, s	Total achieved-minus-nominal pointing error, deg
	deg	s			
Pitch	55.350	304.46	55.453 ± 0.062	304.0	0.103 ± 0.062
Roll	71.025	380.43	70.660 ± 0.004	380.0	-0.365 ± 0.004

and the total achieved-minus-nominal pointing error, including the attitude-control contribution. This result is directly measured to a high degree of accuracy by orbit determination.

If subscripts denote achieved and nominal velocities and ψ is the total angle of the achieved thrust axis from the nominal thrust axis, then

$$\begin{aligned}\sin \psi &= \frac{\mathbf{V}_A \times \mathbf{V}_N}{V_A V_N \hat{\psi}} \\ &= 0.00706 \\ \hat{\psi} &= 0.405 \text{ deg}\end{aligned}$$

This pointing error contributes to the closest approach distance 57 km from pitch error and 250 km from roll. Since the actual motor-burn time was very close to the nominal value, the unavoidable conclusion is that the midcourse motor did not deliver its designed thrust.

3. Other Parameter Solutions and Uncertainties Contributing to Orbit-Determination Errors

The standard deviations quoted above were obtained by assuming σ values of 1.65 mm/s per 600-s doppler point and 1 km per ranging point. The actual high-frequency noise on the tracking data is much less than this, but these numbers reflect modeling limitations and lack of precision in the computations. In addition to the effects of these assumed data uncertainties, the effects of uncertainties in the probe position solutions, astronomical unit, solar radiation pressure, and tracking station locations are considered. The effects of these uncertainties are represented in the "achieved-minus-nominal" statistics.

a. Probe position solutions. The solutions for position should agree, of course, since, at the epoch chosen, the velocity increment imparted by the maneuver changes the probe position by a negligible amount. Table 5 compares the premidcourse and postmidcourse position determinations, which may be seen to agree roughly with the computed uncertainties. Positional uncertainties of this size map to negligible target errors and do not materially affect the preceding discussion of velocity errors.

b. Astronomical unit. The uncertainty in the astronomical unit was input at 500 km and was not improved upon in the solutions.

Table 5. Mariner V premidcourse and postmidcourse probe position determinations

Position component	Position $\pm \sigma$, km		Postmidcourse-minus-premidcourse value, km
	Premidcourse	Postmidcourse	
x	-1194557.7 ± 3.2	-1194553.1 ± 3.3	4.6
y	986069.08 ± 3.3	986080.15 ± 3.9	11.07
z	-319692.25 ± 8.5	-319678.20 ± 6.2	13.96

c. Solar radiation pressure. The perturbative spacecraft acceleration resulting from solar radiation pressure is modeled by:

$$\ddot{\mathbf{R}} = \frac{kA}{mR^2} \gamma$$

where

R = probe-sun vector, km

$k = 1.031 \times 10^8$, a solar radiation constant

A = spacecraft effective area normal to r , nominally 6.60519 m²

m = spacecraft mass, nominally 245.71 kg

γ = reflectivity coefficient of the spacecraft, nominally 0.40123054

Table 6 compares the premidcourse and postmidcourse solutions for γ . It is apparent that the span of tracking data available in the premidcourse solution is not adequate for a strong solution, since the standard deviation was not significantly improved over the *a priori* standard deviation assigned to the nominal value. By contrast, the postmidcourse solution contains nearly one month's worth of tracking data, including ranging data. Moreover, the ranging data is particularly effective in this type of solution.

d. Tracking station locations. The orbit-determination program is capable of estimating tracking station locations to a high degree of precision when sufficient doppler tracking data has been obtained. In the premidcourse phase of the mission, solutions were obtained for the locations of DSSs 11, 42, and 61. These solutions are tabulated and compared with nominal values and postmidcourse solutions in Table 6, where r is the geocentric radius vector to the station, ϕ the geocentric latitude, and λ the longitude. The systematic differences in longitude

Table 6. Mariner V premidcourse and postmidcourse γ and tracking station solutions

Parameter	Solution $\pm \sigma$			Postmidcourse-minus-premidcourse value
	Nominal	Observed premidcourse	Observed postmidcourse	
γ	0.40123054 \pm 0.0400	0.40864007 \pm 0.0288	0.37740661 \pm 0.0112	-0.03123346
$r_{31} \cos \phi_{31}$, m	5206353.3 \pm 20.0	5206331.4 \pm 6.3	5206327.1 \pm 3.5	-4.3
λ_{31} , deg	243.15091 \pm 0.00050	243.15101 \pm 0.00015	243.15070 \pm 0.00018	-0.00031
$r_{42} \cos \phi_{42}$, m	5205341.6 \pm 20.0	5205353.5 \pm 6.0	5205347.3 \pm 2.7	-6.2
λ_{42} , deg	148.98148 \pm 0.00050	148.98174 \pm 0.00015	148.98141 \pm 0.00018	-0.00033
$r_{61} \cos \phi_{61}$, m	4862604.5 \pm 18.7	4862606.4 \pm 6.0	4862597.6 \pm 4.3	-8.8
λ_{61} , deg	355.75113 \pm 0.00050	355.75146 \pm 0.00015	355.75114 \pm 0.00018	-0.00032

of about 0.0003 deg between the premidcourse and postmidcourse solutions are probably partially caused by variations in the way time differences between WWV and UT are represented in the orbit's error at target. The cause of the systematic differences in $r \cos \phi$, the distance from the earth's spin axis, is unknown; however, these differences are also very small (4.3–8.8 m).

4. Conclusions

Orbit determination indicates that an error of 0.715 ± 0.016 m/s was made in the magnitude of the *Mariner V* midcourse correction, resulting in an additional 2000 km of closest approach distance to Venus. The total calculated pointing error of the maneuver thrust axis is only 0.4 deg. In addition, telemetry and tracking data residuals indicate a motor-burn interval close to the planned interval of 17.66 s. The conclusion is that the motor failed to achieve the expected thrust.

D. Status of DSS Location Solutions for Deep Space Probe Missions: II. *Mariner V* Real-Time Solutions, N. A. Mottinger

1. Introduction

As discussed in Part I of this series by Mottinger and Trask (SPS 37-48, Vol. II, pp. 12–22), the uncertainties in DSS locations can become limiting factors to the navigational accuracy obtainable with earth-based radio tracking data. To meet the navigational goals under consideration for some planetary projects, the uncertainties in the DSS longitude, σ_λ , and the distance off the earth's spin axis,³ σ_{r_s} , must be known on the order of 1 m. In an earlier SPS article by Hamilton, Grimes, and Trask

(SPS 37-44, Vol. III, pp. 4–11), an approximate method for determining the navigational accuracy obtainable during the encounter phase of a mission was presented, and the parameters that limit this accuracy were discussed.

In reporting the work being performed to meet these future goals, this series on DSS location solutions as obtained from post-flight analyses was initiated with a general discussion of their present status in SPS 37-48. This article in the series is concerned with the real-time solutions for DSS locations obtained from *Mariner V* and discusses several error sources which may be affecting them. In particular, attention is devoted to the polar motion which occurred during the flight, with the discussion centering around the accuracy of its prediction and how it may affect the solutions.

Some of these error sources which do limit the analysis are: (1) the limited numerical computational accuracy of the SPODP (Ref. 1), and (2) discrepancies between the real universe and its model in the SPODP. These include timing errors and polar motion effects.⁴ Error or limiting-accuracy source 1 is essentially invariant with time and will not be eliminated until the next-generation program, the double-precision OD program (DPODP),⁵ is in operation.

Timing errors between ET (used to look up the position of celestial bodies) and UT.1 (determined by the

⁴These error sources were discussed in more detail by Mottinger and Trask in SPS 37-48. Further insight into timing in the OD process is given by P. M. Muller and D. W. Trask in SPS 37-39, Vol. III, pp. 7–16. Polar motion and DSN locations are discussed in SPS 37-45, Vol. III, p. 10.

⁵Reported by M. R. Warner, *DPODP, Volume I*, Nov. 1, 1966 (JPL internal document) and by T. D. Moyer in SPS 37-38, Vol. III, pp. 24–27, and subsequent issues of the *Deep Space Network* SPS volume.

³Distance off the spin axis equals the geocentric radius times the cosine of the geocentric latitude.

rotation of the earth and used to fix the location of a DSS in space) may affect the OD process by misrepresenting the trajectory of a probe with respect to the earth and other celestial bodies. Additional effects on the OD effort arise with UT.1 and UTC (UT coordinated, the time broadcast by the NBS) differences, since the DSN synchronizes with UTC and uses this time as a tag on the data received. The polar motion which affects the earth's axis of figure with respect to its axis of rotation, hence inducing changes in the DSS locations, presently lacks a model which will enable adequate predictions to be made or which will permit correcting for it during the processing of radio data with the SPODP commensurate with the future navigational accuracy goals. These goals will, however, become attainable with the DPODP, which will contain models to correct for both the timing and polar motion phenomena.

2. Estimation of Polar Motion and Reduction of Initial Station Location Solutions

The initial values for station locations to be used by the *Mariner V* OD group were supplied in early-June 1967. Two steps were involved in deriving these values. First, a set of values was obtained from existing probe results which could be considered a hypothetical average of the solutions available. In this manner, locations for DSSs 12, 41, and 51 were determined. From there, relative locations were used to associate DSSs 11, 42, and 61 with the first set of DSSs. The location for DSS 14 was taken from a JPL land survey source. These values, which came from probe results, had been reduced to the reference pole of 1903.0.⁶ The practice for reduction of extended flights is to average the polar motion for such times, and, assuming that the SPODP has effectively done the same, use this value to correct the final solutions back to the 1903.0 pole.

Included in the figures of solutions for station locations are the launch estimates with an estimated uncertainty of 20 m, except for DSS 14 which was obtained from a land survey with much larger uncertainties listed. A graphic display of past polar motion by P. Muller⁷ was

⁶The year 1903.0 is used to describe the International Polar Motion Service (IPMS) "epoch" or reference point. Actually, the polar motion for the years 1900.0 through 1906.0 was averaged by the IPMS to define this reference pole. The terms x and y are cartesian coordinates describing instantaneous pole position with respect to the averaged pole.

⁷P. Muller, *Polar Motion and DSN Station Locations*, Apr. 20, 1967 (JPL internal technical memorandum). Muller's article in SPS 37-45, Vol. III, p. 10, parallels that internal technical memorandum in describing the effects of polar motion on DSS locations. Also, Mottinger and Trask discuss it briefly in SPS 37-48.

used to estimate the x and y values of the instantaneous pole position to convert the above DSS locations to the launch epoch.

In relating the procedures involved in tracing the polar motion during the flight of *Mariner V*, a table and a figure have been included which list the polar motion estimates and the data received from the IPMS, which publishes monthly notices of the pole position. The relative success attained in estimating launch, cruise, and encounter pole positions is shown in Table 7 and Fig. 5. The points at launch and encounter in Fig. 5b are the specific points estimated. The prediction for launch was not too difficult to make, even though it was necessary to estimate 3 mo ahead due to the usual delay involved in receiving IPMS reports. To make the prediction, the previous polar motion minima passage was overlayed upon the existing points and adjusted to obtain as good an agreement as possible with the existing pre-minima points and thus make the estimate shown by the broken line in Fig. 5b. Figure 5a shows these past minima occurring in 1961 which were used as a guide.

Predicting just when the minima would occur is very difficult and to estimate positions accurately following such a passage is even more difficult. Another IPMS bulletin received in September was really the one used to obtain the cruise and encounter estimates shown in Fig. 5b. This bulletin contained the July data and gave a slight indication of when the minima might occur. Since the launch estimate was made before these data were available, it does not lie on the estimate line of Fig. 5b, illustrating the difficulty of predicting in the time of minimum motion.

Without a full awareness of the true complexity of the situation, it was felt that a good estimate had been made. This estimate is shown in Table 7 in the column "estimated uncertainty of extrapolated pole position." The IPMS bulletin used to evaluate these estimates was not available until November.

Having made the estimate for the pole position at launch, the previously mentioned locations were updated from the 1903.0 reference position to the assumed pole position for the launch week in June 1967. Soon after the launch of *Mariner V*, the operating procedures involving the SPODP were changed to include estimates of station locations as part of the OD process. In September, the DSS location solutions from two particular ODP runs using cruise data, labeled Post 17 and Post 19 (Table 8), which were destined to be used by the OD group for

Table 7. Estimated pole position in a real-time situation for Mariner V

Event	Estimation interval, ^a yr	Estimated uncertainty of extrapolated pole position, m		Error of estimate (estimated-minus-final value), m		rms of x, y error, m	Estimated pole position, m		Final pole position, m ^e			
		x	y	x	y		x	y	x	Range in x	y	Range in y
Launch	0.3	1 ^c	1 ^c	-1.4	-0.8	1.6	-1.5	4.0	0.37	—	4.8	—
Cruise	0.5 to 0.4 ^b	1 ^c	1 ^c	-1.2 ^e	-0.7 ^e	1.4	-0.9 ^e	4.7 ^e	1.1	0.5 to 1.7 to -0.8	5.4	4.8 to 5.7
Encounter	0.5	1 ^{c, d}	1 ^{c, d}	-0.3 ^f	-2.2 ^f	2.2	-1.0	5.0	-0.7	—	7.2	—

^aTime from last IPMS data to time desired.

^bAdditional data received during cruise.

^cEven though the polar motion was known to be approaching a time of minimum motion, it was felt that a simple extrapolation ahead would give an accurate estimation.

^dA very optimistic estimation; see Footnote c.

^eThis estimate is difficult to make since the polar motion effects on the SPDP are unknown. These represent an average error or value across the cruise portion of the flight. Error could be 2 to 2.5 m in each component.

^fDespite the motion through the minima, it is coincidence rather than a mathematical modeling capability that accounts for such a small error.

^gAlthough the IPMS does not quote an uncertainty for its pole position, private discussion with P. Muller at JPL indicates that such a statistic could realistically be 0.5 m.

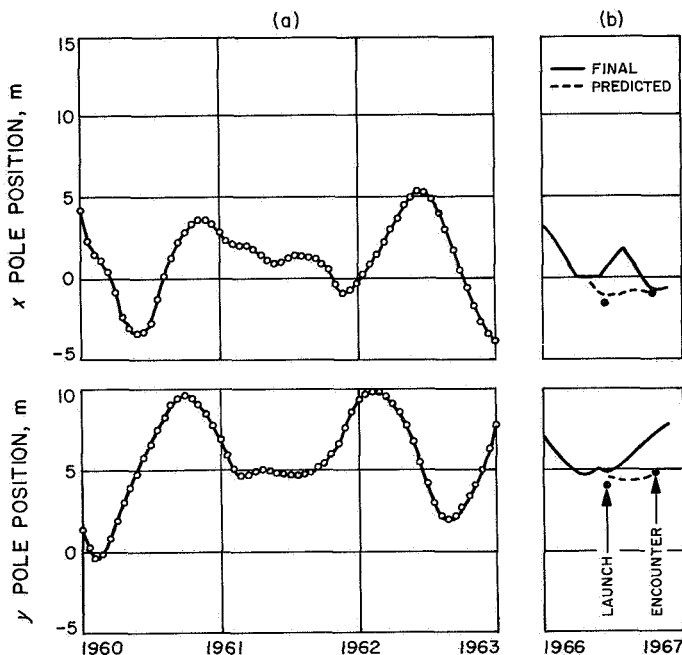


Fig. 5. x, y pole positions: (a) previous minima used as model, and (b) prediction and final results for Mariner V

nominal locations for encounter OD work, were reduced to the 1903.0 pole to see how they compared with other probe results. The September IPMS bulletin mentioned earlier was used to provide the estimates for pole position. Table 7 shows that the same optimism still existed for the accuracy of these estimates. Although Post 17 and Post 19 differ slightly in their data spans (Table 8),

Table 8. Guide to OD runs

OD run identification	Data span (epoch: 23:08 GMT, June 19, 1967)	Description
Post 17	June 20 to Aug 2	Cruise run
Post 19	June 20 to Aug 28	Cruise run; used in conjunction with Post 17 for encounter nominal values for station locations
Cruise	June 19 to Sept 16	Auxiliary cruise run without earth ephemeris estimation; uses Post 17 and Post 19 as a priori for station locations; contains about 0.5 mo more data than Post 19
Cruise E	June 19 to Sept 16	Auxiliary cruise run with earth ephemeris estimation; uses Post 17 and Post 19 as a priori for station locations; contains about 0.5 mo more data than Post 19

essentially the same values were used to reduce their station solution sets. The value listed in Table 7 is that used for the longer cruise analysis run, Post 19. The attempt at this time to average the assumed pole positions for the data span covered by Post 17 and Post 19 yielded the following x, y values: -1, 4.6 and -9, 4.7 m, respectively, as opposed to the final averaged values of 1.3, 5.2 and 1.1, 5.4 m. These final values were used to give the locations at the 1903.0 pole which are included in Table 9 and Figs. 6-12.

**Table 9. Mariner V station location solutions
referenced to 1903.0 pole**

Solution	DSS	r_s , km	σ_{r_s} , m	λ , deg	σ_λ^a	z^b
Post 17	11	5206 .3334	2.7	243.15077	4.6	3673.7580
Post 19 ^c		.3313	2.3	.15072	2.2	.7561
Cruise		.3314 ^d		.15061 ^d	3.6	.7559
Cruise E		.3314 ^d		.15069 ^d	15.4	.7559
Post 19 ^c	12	5212 .0408	2.9	243.19467	2.5	3665.4412
Cruise		.0409 ^d		.19455	3.8	.4410 ^d
Cruise E		.0409 ^d		.19464	15.2	.4410 ^d
Post 17	14	5203 .9897	3.4	243.11068	3.	3677.3548
Post 19 ^c		.9871	3.0	.11064	2.9	.3525
Cruise		.9872 ^d		.11053	4.6	.3523 ^d
Cruise E		.9872 ^d		.11059	15.6	.3523 ^d
Post 17 ^c	41	5450 .2047	3.2	136.88767	2.9	-3302.3561
Cruise		.1996 ^d		.88752	3.7	.3530 ^d
Cruise E		.1996 ^d		.88759	15.3	.3530 ^d
Post 17	42	5205 .3513	1.9	148.98144	2.1	-3674.6124
Post 19 ^c		.3480	1.4	.98137	1.9	.6102
Cruise		.3481 ^d		.98126	3.4	.6103 ^d
Cruise E		.3481 ^d		.98134	15.4	.6103 ^d
Post 17	61	4862 .6033	2.1	355.75117	2.2	4114.8534
Post 19 ^c		.6018	1.4	.75110	2.1	.8523
Cruise		.6021 ^d		.75100	3.5	.8528 ^d
Cruise E		.6021 ^d		.75107	15.3	.8528 ^d
Post 17 ^c	62	4860 .8121	5.3	355.63238	4.6	4116.9704
Cruise		.8132 ^d		.63222	4.1	.9718 ^d
Cruise E		.8132 ^d		.63231	15.6	.9718 ^d

^aUncertainty expressed in angular units $\times 10^{-5}$, 1 m $\sim 10^{-5}$ deg.

^b $z = R \sin \phi$, included only for completeness.

^cUsed as *a priori* for cruise ephemeris comparison runs.

^dNot estimated; a fixed value.

The values indicated as nominals in Table 9 were used for encounter OD work, except, of course, the values in this table have been reduced to the 1903.0 pole. The non-reduced values were given *a priori* standard deviations of 50 m and were continuously estimated throughout encounter. Of particular interest are three encounter SPODP runs which all start at encounter (E) - 5 days 17 h and continue to E - 5 h, E + 1 h, and E + 1 day. They are identified as ODP 1030, 1031, and 1032, respectively. (Following the discussion of the polar motion predictions versus the final IPMS data for encounter, these encounter runs will be discussed briefly.) At the time of encounter, October 19, 1967, the estimated pole position was $x = -1$ m and $y = 5$ m, again optimistically assumed to be accurate to 1 m despite the 0.5-yr lapse from the last data point.

So far, the discussion has centered around the ODP results which were specifically destined for other operational uses during the mission. However, accompanying these solution results are others for the cruise phase of the flight which were obtained by two slightly different methods. One method included an estimate of earth ephemeris elements, while the other did not (Table 8). These particular solutions used the station locations given as encounter nominal values as *a priori* and then proceeded to solve for DSS longitudes. All these results reduced to the 1903.0 pole as given in Table 9 and Figs. 6-12 are labeled Cruise E (with earth ephemeris) and Cruise (without earth ephemeris). They will be discussed in slightly more detail below.

The first indication of the correctness of the pole position estimates came in mid-November with the receipt of the August IPMS bulletin. These data were the first to identify when the minima had occurred and, therefore, permit a better estimate of the encounter pole by the comparison method outlined earlier in this article. The receipt of the September IPMS bulletin in mid-December essentially allows the final-value reports of the pole positions to be made. Although this bulletin only reports to October 1, an estimate to within 0.5 m could readily be made to arrive at the encounter pole position on October 19. These final pole-position values, which appear in Table 7 and Fig. 5, were used for the reduction of the real-time station solutions which are discussed in the next section.

The receipt of this final IPMS data made it possible to complete Table 7 and Fig. 5 and compare the estimates with the final values. Of particular interest is the "error of estimate" column, which shows the errors in the components of pole position; the errors in radial pole position are shown in the column labeled "*rms of x, y error*." The rms error for cruise may be more representative of a lower bound on the error for this phase of the flight. With over a 2-m variation in the components and no precise knowledge of how the SPODP, which assumes a constant pole location, is affected by the motion, a more realistic error might be closer to 2.5 or 3 m. The launch error should be the smallest, since the least amount of extrapolation was necessary to obtain this point; however, as Fig. 5 shows, passage through the minima occurred just about at launch time, thereby inducing a larger error than anticipated.

Perhaps it is only a coincidence that the estimate for encounter is as good as it is. A partial cause of this is the sinusoidal nature of the polar motion. Were the motion not such, a poorer estimate would have resulted.

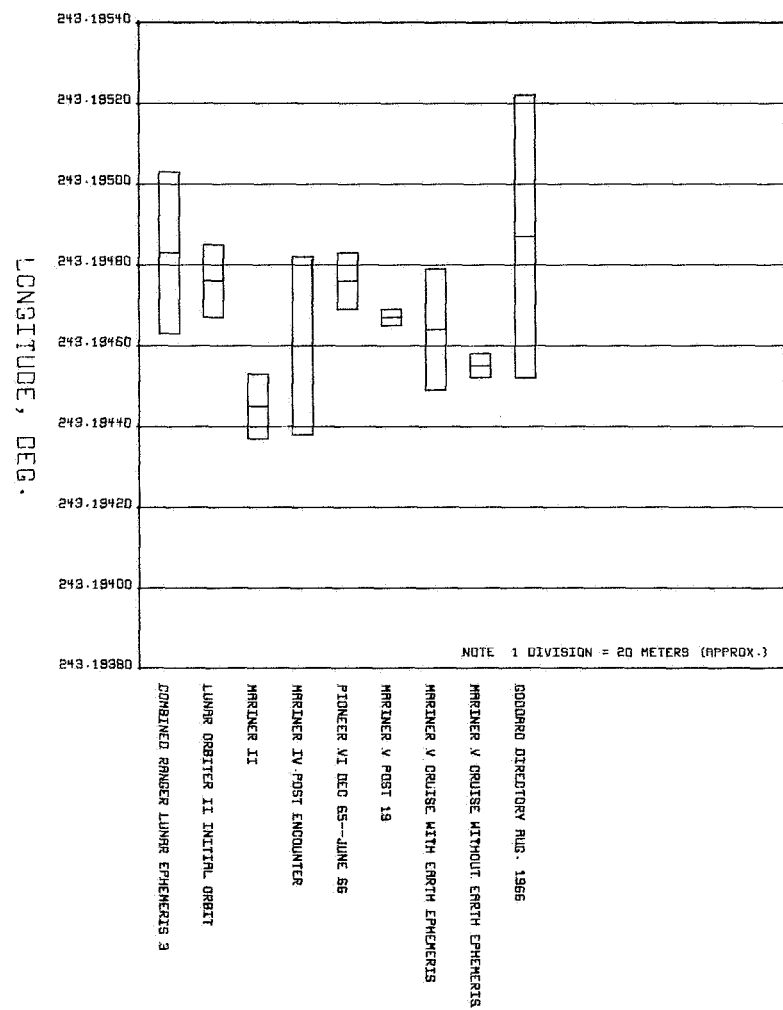


Fig. 6. Geocentric longitude referenced to 1903.0 pole: DSS 12

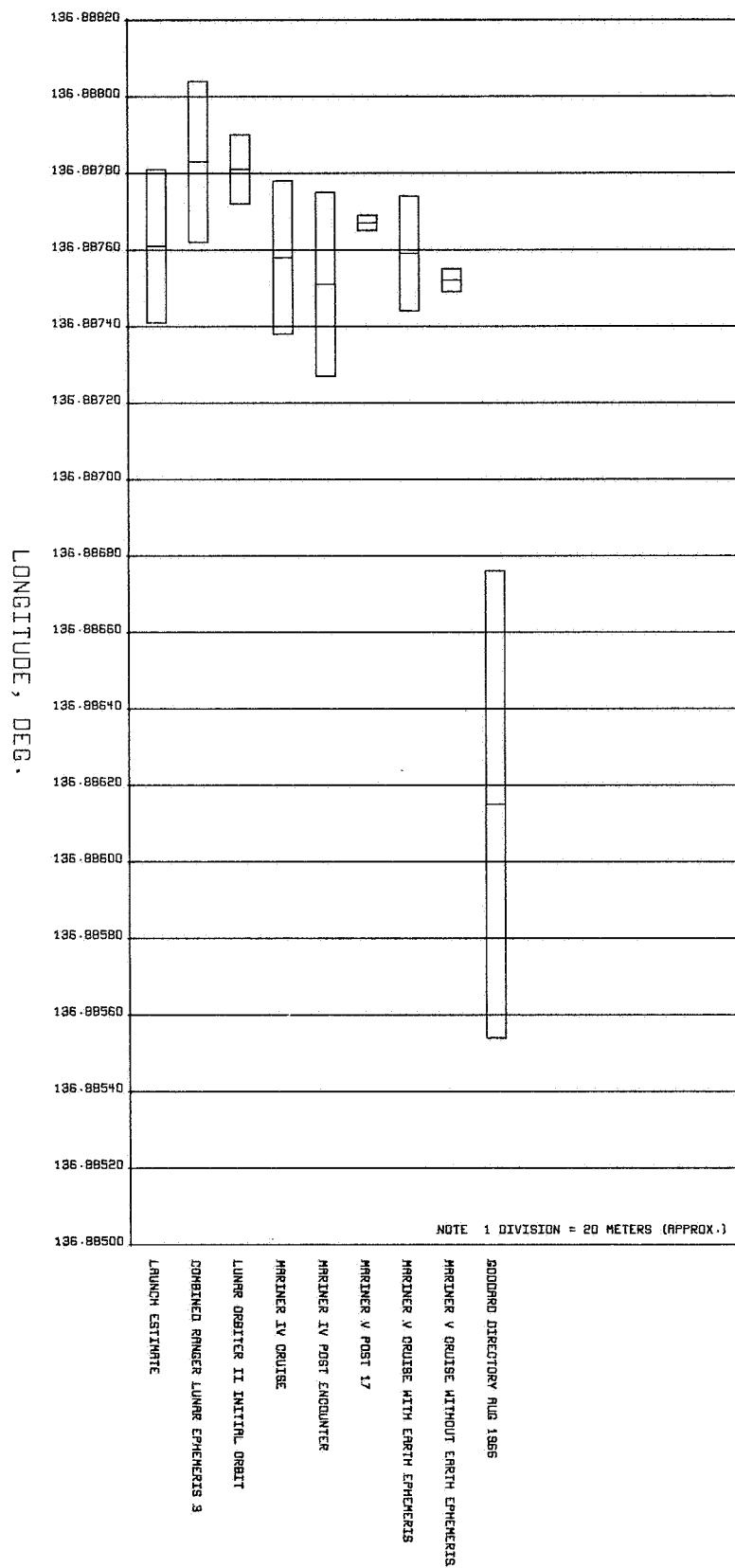


Fig. 7. Geocentric longitude referenced to 1903.0 pole: DSS 41

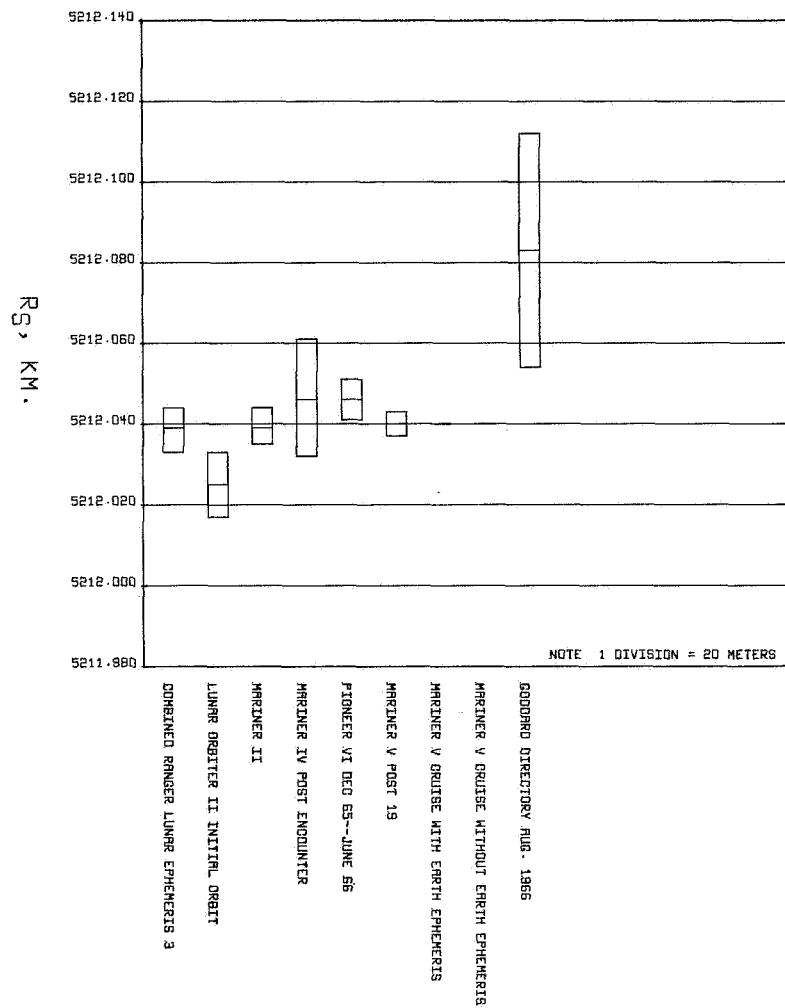


Fig. 8. Distance off spin axis referenced to 1903.0 pole: DSS 12

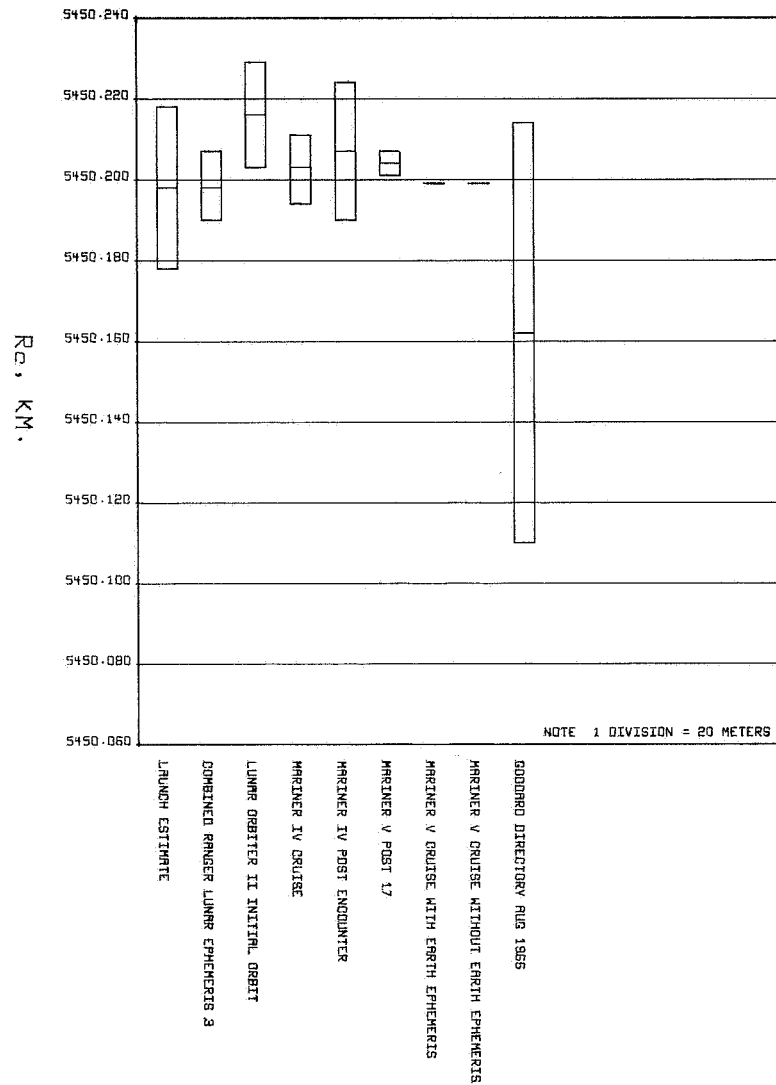


Fig. 9. Distance off spin axis referenced to 1903.0 pole: DSS 41

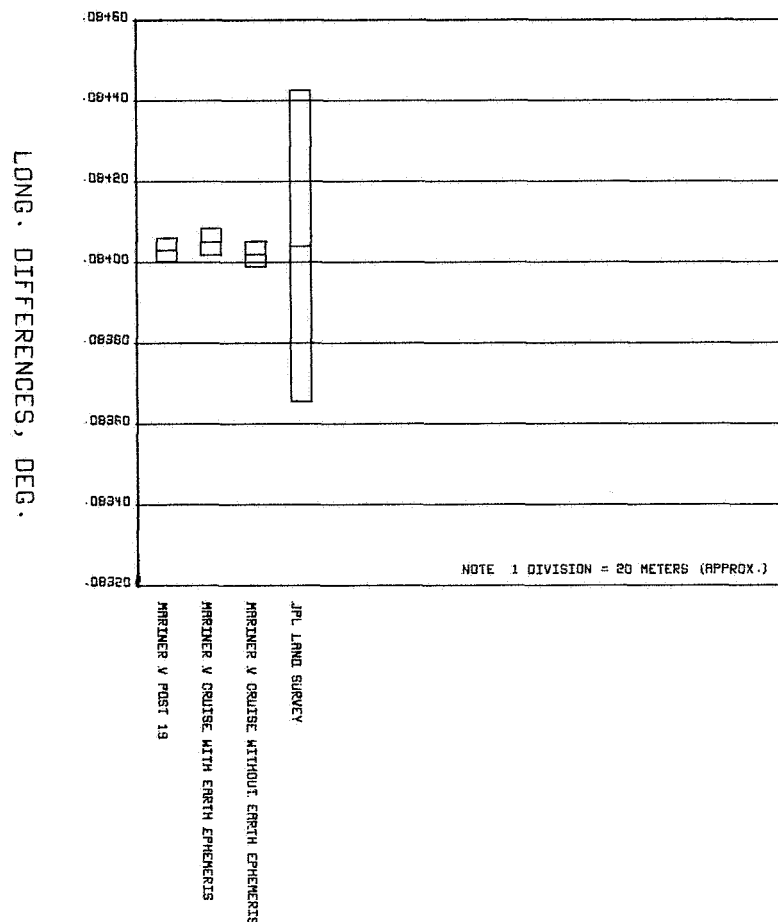


Fig. 10. Geocentric longitude differences referenced to 1903.0 pole: DSS 12 minus DSS 14

For the general approximation that the error at the pole is equivalent to the error in station location, Table 7 shows that it remains essentially to halve these errors to meet the navigational accuracy goals through 1969. To this end, the prospects of constructing a model to accomplish the task are encouraging.

3. Real-Time Station Location Solutions

This section is concerned with the interpretation of two sets of solutions obtained for station locations throughout the flight and attempts to inject, where possible, the effects of the polar motion during this time in conjunction with the ability of the SPODP to solve for DSS locations. The remaining item is a brief discussion of the problems which arose when estimating station locations during encounter. The particular solutions to be discussed are taken from the four OD runs discussed previously (Post 17, Post 19, Cruise, and Cruise E, described in Table 8).

As discussed in SPS 37-48, polar motion affects the SPODP⁸ reductions involving long data spans; i.e., factors such as the time during which a station tracked a probe (i.e., continuously or intermittently during a flight), combined with the degree of polar motion over that period, affect the final solution.

The effect of polar motion on the SPODP results is also important in determining a true uncertainty to associate with the location estimates. The formal statistics produced by the SPODP need further interpretation with regard to polar motion and other items. Lacking a model for the motion of the pole in the SPODP means that the induced uncertainty in the final estimate of station locations should vary directly with the time of flight and the associated motion of the pole. In the case of *Mariner V* (when polar motion was passing through a minima), the effect could be about 3 to 4 m for the cruise solutions.

⁸The SPODP does not have a model for polar motion.

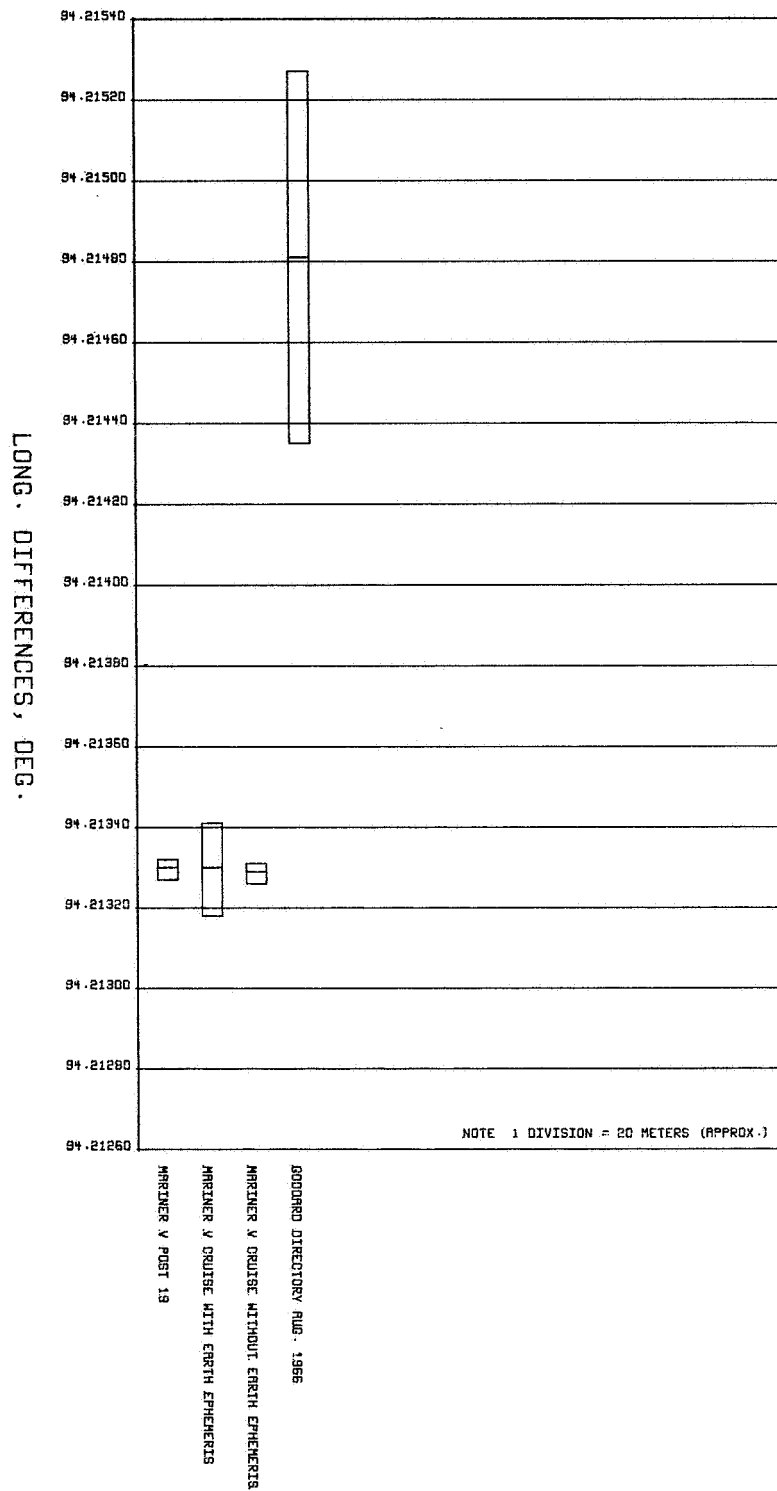


Fig. 11. Geocentric longitude differences referenced to 1903 pole: DSS 12 minus DSS 42

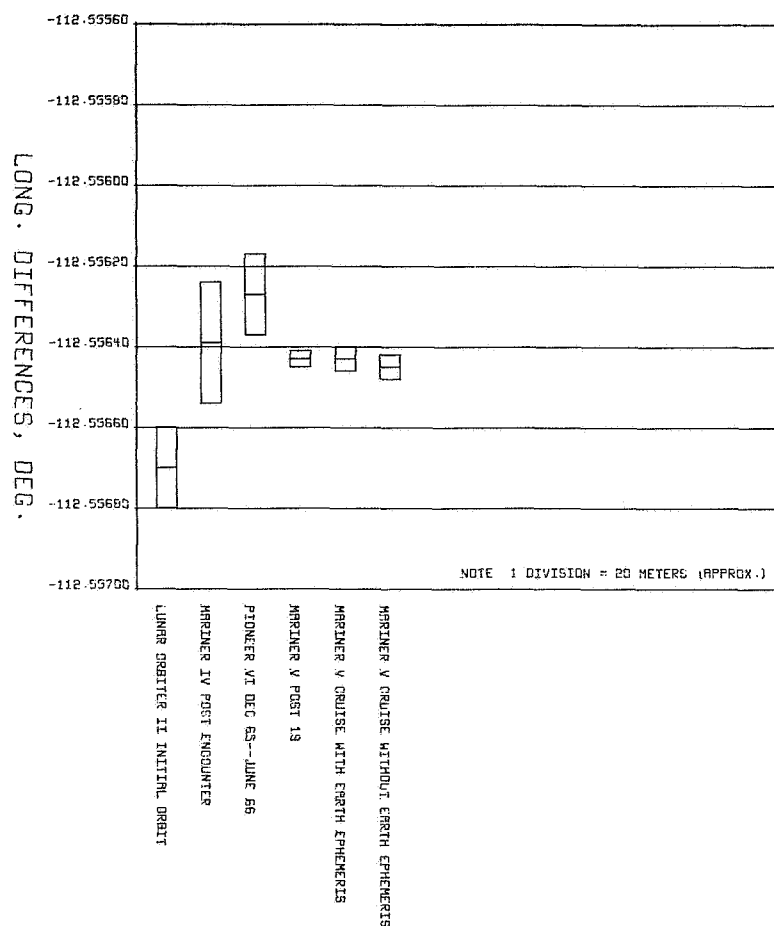


Fig. 12. Geocentric longitude differences referenced to 1903.0 pole: DSS 12 minus DSS 61

This is about twice the size of the formal statistics given for some of the Post 17 and 19 results and approximately the same for the others (Table 9 and Fig. 6). However, the two auxiliary-cruise-solution station locations give varying formal statistics. Those obtained without estimating ephemeris elements quote uncertainties nearly the same as some of the Post 17 and 19 results. On the other hand, when estimating the elements, a larger uncertainty exists for the same data and may be much more representative of the true uncertainty for the cruise solutions. Allowing for changes in the space position of the earth has induced an additional weakness in the capability to estimate station locations. More study is in order to completely understand the situation and possibly correct any modeling discrepancies which may also be responsible for this.

For the cases quoting uncertainties equal to or less than what the effects of polar motion might be, a more realistic statistic is obtained by root-mean-squaring the

variation of polar motion during that time interval with the quoted statistic.

The figures chosen for this report are representative of all sets of solutions for DSSs 12, 14, 41, 42, 61, and 62, and present the various solutions for both r_s and λ . In addition to absolute values for r_s and λ , three figures show the relative longitude solutions for three sets of stations.

The most noticeable characteristic of the *Mariner V* longitude solutions is that the cruise values are generally quite different from the results obtained tracking lunar probes. These disagreements run from 15 to 20 m for the worst cases. Some of the lunar probe data, e.g., *Lunar Orbiter II* initial orbit solutions and some *Surveyor* results, are essentially real-time and not final solutions, but have been included in the instances when other solutions are not available. The combined *Ranger* Block III (*Ranger VI-IX*) solutions are taken as most representative of locations obtained from tracking a lunar probe

because they have been analyzed the most, but, of course, these solutions are only directly available for DSSs 12, 41, and 51.

On the other hand, much finer agreement exists between the *Mariner IV* cruise and post-encounter results and the *Mariner V* values. Presently, it is not fully understood why the cruise solutions depart from the values derived from lunar-probe studies. Partial explanation lies with the inherent weakness associated with trying to determine the probe's right ascension and, hence, infer station longitudes during the interplanetary cruise portion of the mission. For the lunar probes, once the spacecraft is under the gravitational influence of the moon, its right ascension can be inferred from that of the body and hence longitudes can be determined; but, in interplanetary space, this cannot be done since the only attracting body is the distant sun. However, at encounter the same thing occurs as with the lunar probes nearing the moon, allowing longitudes to be definitely determined.

That the *Mariner V* longitude solutions do not agree with the *Ranger* values is not meant to imply that the *Ranger* Block III combined estimate of DSS locations is without error, because existing errors may be shared equally by both. Similarities among all *Ranger* Block III missions, i.e., earth-moon geometry, lunar ephemeris error, or possibly dissimilar effects caused by the ionosphere, may be forcing false solutions. The longitude solutions obtained from the two cruise sets involving ephemeris considerations do not agree too well with their Post 17 and 19 *a priori* counterparts. Of particular interest are the estimates without earth ephemeris estimation. These are less than those with earth ephemeris estimation, the latter also disagreeing with the Post 17 and 19 results.

Unlike the various agreements noted for the longitude solutions with the other lunar and planetary missions, the cruise solutions for r_s do not vary by more than perhaps 5 m from the combined *Ranger* Block III value and about 10 m from some of the other initial *Lunar Orbiter II* results. At the same time, however, there is much closer agreement with the *Mariner IV* solutions for r_s .

Of course, solutions for r_s are not affected by all the items which may cause longitude solutions to vary. The biggest factors affecting them are polar motion and the ionosphere. In the course of the cruise phase, the polar motion produces 2- to 3-m changes, while the daily ionospheric effects might account for 2 m; however, these

latter effects could cancel from day to day, whereas the polar motion should have a noticeable effect upon the SPODP reduction. Trask and Vegos in SPS 37-43, Vol. III, p. 16, point out that, for the *Ranger* Block III flights, the ionosphere alone could have caused 5- to 10-m errors in r_s solutions; so, the small disagreement noted here may be within the uncertainty surrounding the *Ranger* Block III value.

Figures 10-12 are concerned with relative longitudes. Relative longitude solutions, even though they are the best solved for parameters from radio tracking, are affected by the ionosphere, errors in time synchronization among the DSSs, and polar motion; ephemeris errors and time errors (UT.1 - UTC and UT.1 - A.1)⁹ common to the DSSs cancel. In SPS 37-45, Vol. III, p. 10, P. Muller dramatically illustrated the effects of polar motion on relative longitudes.

These three figures, showing longitude differences for DSS 12 minus DSS 14, DSS 12 minus DSS 42, and DSS 12 minus DSS 61, reflect varying degrees of agreement. The worst case for all *Mariner V* results is a scatter of about 3 m. The figure for DSS 12 minus DSS 61 (Fig. 12) shows better agreement among the planetary missions than the lunar missions. It should be noted that, even though the solutions for absolute longitudes may have changed quite significantly, the relative solutions have not. This is shown in Fig. 7, the figure for DSS 12 minus DSS 42. The solutions for DSS 42 behaved very nearly the same as did those for DSS 41, but it should be noted that these relative solutions remained nearly constant.

As may be observed, land survey results do not always agree very well, in either the relative or the absolute sense, with probe results. Efforts are also being devoted to eliminating these serious discrepancies. Early analysis indicates that land survey results may not have been uniformly reduced to the station location point defined from radio tracking.

As mentioned previously, the solutions for DSS locations obtained in Post 17 and Post 19 were used as nominals for encounter OD work; in this work, locations for DSSs 12, 14, 41, 42, and 62 were obtained for each encounter orbit of increasing time span (1030, 1031, and 1032), as described earlier. The present amount of analysis is not sufficient to explain the difficulties encountered in estimating station locations during this time. To explain the difficulties encountered, Table 10

⁹References enumerated in Footnote 4 contain descriptions of atomic time A.1.

Table 10. Iteration-to-iteration changes in station location estimates

ODP case	Iteration	QSOS ^a	DSS	Station location changes, m	
				Δr_s	$\Delta \lambda$
Post 17	1	406.20	14	3.2	3.3
	2	185.98		1.6	2.1
	3	159.76		0.2	0.2
	1	406.20	62	2.0	3.9
	2	185.98		0.9	1.5
	3	159.76		0.1	-0.13
Post 19	1	667.79	14	-0.08	0.9
	2	214.78		-0.9	-0.4
	3	129.69		0.6	1.1
	1	667.79	62	—	—
	2	214.78		—	—
	3	129.69		—	—
1030	1	45,541.00	14	1.1	2.8
	2	778.80		-2.7	-3.5
	3	591.59		5.3	-5.0
	1	45,541.00	62	-1.7	14.1
	2	778.80		2.1	-4.1
	3	591.59		-6.7	-2.8
1031	1	1,276.5	14	4.6	-0.8
	2	1,864.6		4.6	26.9
	3	3,987.7		-5.2	-31.4
	4	8,641.7		-1.0	7.6
	1	1,276.5	62	2.2	2.2
	2	1,864.6		-6.1	28.7
	3	3,987.7		-5.2	-31.4
	4	8,641.7		-1.5	7.5
1032	1	21,837.00	14	-3.4	8.3
	2	25,192.00		1.0	18.4
	3	12,467.00		-1.9	-21.5
	1	21,837.00	62	-4.3	16.1
	2	25,192.00		-4.1	14.6
	3	12,467.00		4.3	-19.8

^a Essentially the sum of the squares of the residuals plus the sum of the squares of the changes in the parameters being estimated.

has been included to show the changes in location estimates which occurred from iteration to iteration in five different ODP cases. Selected as typical examples are the changes for DSSs 14 and 62, starting with the iteration-to-iteration changes in Post 17, Post 19, and the encounter orbits 1030, 1031, and 1032 (the latter spanning to E + 1 day). In the cruise runs, the changes are seen to be very small and may indeed lie within computational

noise limitations. An indication of the accuracy of a particular fit is given by a QSOS value (defined in Footnote a, Table 10). A large QSOS may indicate a poor fit to the data and a large change in the estimated parameters in attempting to fit to the data, while a small QSOS would be indicative of small residuals and a converging set of parameters.

Post 17 and Post 19 show decreasing QSOS for each iteration and small changes in station locations. Orbit 1030, which includes data up to E - 5h, is nearly as stable as the cruise, but large fluctuations are beginning to appear in the QSOS and location changes. Finally, in the 1031 and 1032 orbits containing post-encounter data, large QSOS values and changes between iterations in station locations are present, indicating an unstable situation which is not converging. The formal statistics, however, were on the order of 5 m and are unrealistic in view of the situation.

To date, only a temporary solution to this problem has been obtained. This solution, which involved deleting the estimate of r_s and solving only for longitudes for a data span from E - 5 days to E + 5 days, has yielded more stable solutions. This should not be the final method for solving this problem, because, at the time of encounter, station solutions should be a well-solved-for parameter due to the gravitational attraction of the body on the probe. This situation, which involved using cruise solutions for DSS locations for encounter work, holds something very important, but yet undiscovered, in the problem of tracking during encounter.

4. Conclusion

To meet certain future navigational accuracy goals, it will be necessary to predict the pole position to 1 m, possibly as much as 5 mo in advance. This article has discussed how this was attempted for the *Mariner V* flight and shows that, in the time of maximum difficulty for predicting, the best accuracy that can be obtained with a non-rigorous approach is about 2 m. Were the times those of least difficulty, the 1-m goal might be feasible, and, at best, this would only satisfy the requirements of the current decade. To this end, it is essential to develop a model for this motion which will permit highly accurate estimates.

The variations between the various probe results for DSS location solutions and the real-time *Mariner V* cruise values, when coupled with the stability problems at encounter, cast doubts concerning the advisability of

using the solved-for cruise values for the more important phases of the mission. This present inability to solve for DSS locations at the time when opportunities are the best is an item in need of still further analysis, since initial results are unsatisfactory.

Reference

1. Warner, M. R., and Nead, M. W., *SPODP — Single Precision Orbit Determination Program*, Technical Memorandum 33-204, Jet Propulsion Laboratory, Pasadena, Calif., Feb. 15, 1965.

E. A Method of Constrained Least-Squares Polynomial Fitting With Application to Analysis of A.1 — WWV From 1955 to 1968,

P. M. Muller

1. Introduction

This article reports on the second of several dependent studies required for implementation of the DPODP.¹⁰ The DPODP operates with respect to uniform time, arbitrarily chosen to be A.1. Since the DSSs put WWV time tags on the observed doppler and range data, it is necessary to know the relationship of A.1 to WWV in order to process the tracking data. [The DPODP also has the capability to correct any local station clock errors between station time and WWV time (SPS 37-39, Vol. III, pp. 36-38), but the problems related to this capability are not discussed here.]

In addition, the author requires A.1 — WWV, and A.1 — Mo as well, in order to attempt the reduction of UT0 PZT observations (the next step in the updating of these timing matters). A.1 — Mo, or any other time scales required for these future tasks, are not discussed here. It is sufficient to point out that, with suitable data from the agency in question, the same computer program used for this study will produce appropriate polynomials for the additional time scales. These requirements in no way affect the DPODP, which requires only A.1 — WWV, as noted above.

Three related subjects are discussed herein. First, a method for constrained polynomial fitting to long data

spans is derived. It is usefully applied to the A.1 — WWV problem, but is primarily intended for application in subsequent articles on timing and polar motion.¹⁰ These future articles will reference this SPS article in matters relating to the polynomial fitting method.

Second, a discussion of timing and polar motion is begun which will eventually delineate the steps necessary to fulfillment of present navigational accuracy goals. These goals, which are currently being considered for future planetary projects, will require the knowledge of DSS locations to the order of 1 m. For this reason, the DPODP has made provision for inclusion of timing and polar motion corrections in its model, as discussed in SPS 37-39, Vol. III, pp. 36-38. SPS 37-39, Vol. III, pp. 18-24, and SPS 37-44, Vol. III, pp. 4-11, discuss the more general aspects of the importance of station locations in navigational accuracy.

Third, the function A.1 — WWV, which is required for the DPODP as well as for the future studies, is obtained. Initially, definitions of terms used are presented, and some problems in interpreting UTC as represented by WWV are discussed. This article thereby continues and expands the contents of SPS 37-41, Vol. III, pp. 18-24.

As will be seen in the results, there is no problem in determining A.1 — WWV to 0.1 ms, or about 0.04 m in station longitude. JPL is currently considering an error goal in station location solutions of 1 m (2.5 ms in DSS longitude) for future missions. Since A.1 versus UT1 may require a large portion of this error budget, it was desired to eliminate any contribution from the clock times A.1 — WWV (which are accurately known). The sensitive fitting methods described here, though not essential, make the detection of errors and omissions fail-safe. For these reasons, it was considered essential to lay this groundwork for the future studies¹⁰ with care and precision, even though it is otherwise straightforward.

2. Definitions of Terms¹¹

A.1. Time indicated by the atomic time scale kept by the USNO. It differs from NBS(A) as noted below.

DSS longitude determinations. DSS longitude, as determined from probe tracking data, is the DSS angular position with respect to the reference meridian (nominally Greenwich) used as the origin for UT1. The parameter actually determined from probe tracking data is the time of meridian passage of the spacecraft over the DSS.

¹⁰The Polar Motion Survey was completed (SPS 37-45, Vol. III, pp. 10-13). Future studies will include:

- (1) Analysis of A.1 — UT1 from PZT Observations of UT0.
- (2) Prediction System for A.1 — UT1 and Its Applicability.
- (3) Polar Implementation for DPODP.
- (4) Prediction System for A.1 — UT1 and Its Applicability.
- (5) Program TPOLY for DPODP Support: Computer Program Document.

¹¹Addition to definitions listing given in SPS 37-39, Vol. III, pp. 3-12.

Therefore, all other things being equal, an error of 2.5 ms in $A.1 - UT1$ (or the necessary intermediate, $A.1 - WWV$) will result in a 1-m DSS longitude error. A more complete discussion of this matter will appear in a future SPS article.

Epoch. All timing data and observations must be referred to an epoch; i.e., if one states that $A.1 - WWV = +5.1784$, it must be known at what time the observation was made. "Time" used in this second sense is sometimes confusing. It should be noted that, for defining an epoch, it does not matter what scale is used ($A.1$ or GMT, etc.), since any error introduced is extremely small (second-order). All epochs in this article are 00 h GMT, unless specified otherwise (see "Time" below).

Mo or USNO master clock. This refers to the UTC as kept by the USNO. It is not broadcast on any radio channel used in this work. It is important because some of the USNO PZT observations are based on this scale.

NBS(A). Atomic time as kept by the NBS. Since December 1, 1966 (the epoch of importance), $A.1 - NBS(A) = -10.9$ ms. It is likely that this relationship will hold within 0.1 ms for several years. The name was changed to NBS-A in November 1967, and appears that way currently.

NBS(UA). The UTC as kept by the NBS. It differs from Mo above (see also WWV). This quantity was renamed NBS(UTC) in November 1967, and so appears in current NBS bulletins.

Offset. UTC is related to atomic time (from which it is derived) by a fixed-frequency offset. The historical values over past years are given in Fig. 14 (subsection 6). A positive sign indicates that the UTC seconds are longer than the atomic seconds by the indicated frequency difference. Changes are made when required at 00 h on January 1.

PZT. Photographic zenith tube, used in determinations of UT0.

Step adjustment. If, with the adopted offset, UTC drifts more than about 100 ms from UT2, a step adjustment of 100 ms is introduced into the UTC scale at 00 h on the first day of the month. Figure 14 (subsection 6) contains the recent values. A positive sign indicates that $A.1 - UTC$ changed by the amount indicated; a positive sign indicates *retardation* of the UTC clock.

Time. All times indicated in this article are clock readings at the epoch. All time differences ($A.1 - WWV$, for example) are given in clock differences; i.e., if $A.1 - WWV$ is positive, the time read on the $A.1$ clock was ahead of the time read on the WWV clock. It is as though a flash-camera picture was taken of both clocks at the epoch, and the readings were differenced. Since there are other equally good conventions such as event differences, it should be pointed out that the author is using the USNO convention. Ambiguity can easily introduce sign errors.

UTC. A time scale offset by a fixed-frequency difference from atomic time. The atomic time scale from which it is taken by offset determines the "version" of UTC and its name, as noted under "WWV" below, and the various "UTC" scales do differ from each other.

WWV. A set of radio transmitters which disseminate UTC. Since December 1, 1967, $WWV = NBS(UA)$ to within 100 μ s. Prior to that time, it determined its own time scale. That is, WWV or any other radio station determines its own time, which stands in some reasonable relationship to UTC, the theoretical standard. All broadcast "UTC" scales differ, and have differed historically, because the clocks controlling them cannot be perfectly synchronized. Since the DSSs synchronize to WWV, $A.1 - WWV$ is the subject of this article, and WWV time is, for the purposes of this discussion, "UTC."

3. History of $A.1 - WWV$ Determinations

The first cesium clock went into operation in 1955 at the National Physical Laboratories in Teddington, England. Transmissions from radio station GBR (England) reflected this change, and reception of these high-frequency transatlantic time signals allowed the USNO to compare WWV with GBR and thereby, indirectly, with atomic time as determined in Britain.

Since, by 1960, the USNO had its own $A.1$ scale well-determined, it was able to back-analyze the WWV versus GBR observations and extend knowledge of $A.1 - WWV$ back to June 1955. The data appear excellent, judging from the results of this paper, after September 1956. (The earlier data is unofficial.) Therefore, an extremely precise determination of $A.1 - WWV$ is available from at least September 1956.

On December 1, 1966, WWV was moved from Greenbelt, Maryland to Fort Collins, Colorado. The $A.1 - WWV$ data prior to this date is available in Refs. 1 and 2. After the move, $A.1 - WWV$ must be inferred

from $WWV = NBS(UA)$. The difference, $NBS(UA) - NBS(A)$, is given in Ref. 3 (monthly), and knowledge of $A.1 - NBS(A)$ allows $A.1 - WWV$ to be computed.

There is, therefore, a discontinuity in the input data to the program on December 1, 1966. Before that date, $A.1 - WWV$ is input from USNO bulletins; after that date, $NBS(A) - NBS(UA)$ is used. The program corrects for this, and the change does not constitute a step adjustment in WWV . Figure 14 (subsection 6) shows a step in WWV on this date, but it represents only the inevitable small timing error made when the transmitter was relocated. Its cause, under investigation by the NBS, probably was delay time changes in the transmitter and antenna.

The method of polynomial fitting to the entire data span was an extremely sensitive method for determining errors or missing data (such as step adjustments). These determinations¹² may now seem trivial, and, if we had known in 1955 what we know today, they would have been. The progress in timing over the last 12 yr brought changes, and it was a considerable task to rectify all of these matters and present the results in a unified form. This also points up the problems which may arise if we process PZT observations from several observatories (to reduce systematic errors), as now appears likely. Each will be giving its data with respect to different time sources, and the relationship of each to $A.1$ must be determined prior to any other work.

Prediction of $A.1 - WWV$ into the future is limited only by knowledge of when the International Bureau of Time (B.I.H.) in Paris, France will require step adjust-

ments or offset changes in UTC. If these are known, the predictability of $A.1 - WWV$ will be limited only by clock drifts which may amount to 0.1 ms in 1 yr. In general, the Bureau does not make these decisions much more than 60 days in advance, so prediction is limited to this interval.

4. Discussion of Polynomial Fitting Method

As an example of the method, consider the desire to fit the polynomial:

$$A_0 + A_1 \cdot t_i + A_2 \cdot t_i^2 + A_3 \cdot t_i^3 + A_4 \cdot t_i^4 = D_i \quad (1)$$

where t_i is the argument corresponding to data point D_i for some set of observations D . Consider further the desire to include known values of the derivatives for certain arguments, i.e.,

$$\left. \begin{aligned} A_1 + 2A_2 \cdot t_j + 3A_3 \cdot t_j^2 + 4A_4 \cdot t_j^3 &= D_j \\ 2A_2 + 6A_3 \cdot t_k + 12A_4 \cdot t_k^2 &= D_k \\ 6A_3 + 24A_4 \cdot t_m &= D_m \\ 24A_4 &= D_n \end{aligned} \right\} \quad (2)$$

The generalization to higher- and lower-order cases is obvious.

Such a least-squares polynomial fit with constraints can be solved by minimizing the Euclidean length of the vector \mathbf{R} , where

$$\mathbf{R} = \mathbf{A} \cdot \mathbf{X} - \mathbf{D}$$

\mathbf{X} = vector of coefficients (A_0, A_1, A_2, A_3, A_4) to be solved for

\mathbf{D} = vector of data points (D_i, D_j, D_k, D_m, D_n) corresponding to the rows of \mathbf{A}

$$\mathbf{A} = \begin{bmatrix} 1, & t_i, & t_i^2, & t_i^3, & t_i^4 \\ 0, & 1, & 2t_j, & 3t_j^2, & 4t_j^3 \\ 0, & 0, & 2, & 6t_k, & 12t_k^2 \\ 0, & 0, & 0, & 6, & 24t_m \\ 0, & 0, & 0, & 0, & 24 \end{bmatrix} \begin{array}{l} \leftarrow \text{data points} \\ \leftarrow \text{first-derivative points} \\ \leftarrow \text{second-derivative points} \\ \leftarrow \text{third-derivative points} \\ \leftarrow \text{fourth-derivative point} \end{array}$$

¹²Obtained through the cooperation of Mr. Keating of the USNO Time Service.

The inclusion of derivative constraints, as they might be called, should be noted in the above. This means that one may force the polynomial to fit, subject to any of these constraints; they may be weighted heavily or not as the application requires. Construction of the **A** matrix in this fashion will achieve the desired result, noting the weighting method below, using any suitable scheme for minimizing the residual vector **R**.

The various derivatives may be thought of as distinct data types in the more conventional and well-known sense of least-squares fitting to a data set. Each row of the **A** matrix, when multiplied by the **X** vector of coefficients, clearly produces the simultaneous Eqs. (1) and (2) above. It may be noted that trigonometric or other functions may be included just as well, and each data point need not involve all the terms in the coefficient set.

If it is desired to separately weight the data, whether the usual kind or the constraints themselves, it is necessary only to multiply each row of the **A** matrix and **D** vector by the square-root of the weight, and proceed with the minimization. The result is an increase in the Euclidean length contribution of the weighted terms in the amount of the "weight" itself. This is the desired result, and will have the same effect as a weight used in standard least-squares work. It should be noted that, if the user desires an exact constraint, he need only increase the weight sufficiently to guarantee the desired precision of the answer. Some schemes for minimization of the **R** vector include exact constraints as a special option, and such can be used. Less-sophisticated systems, without the constraints provision, can still be used to advantage, as noted above.

The subroutine MOPOLY, written under the MOP system (SPS 37-42, Vol. III, pp. 12-15) is used to minimize the **R** vector. It is capable of doing so with the so-called normal equation method or the subroutine LSQSOL (SPS 37-48, Vol. III, p. 26), which uses orthogonal transformations (a superior scheme).

The method described is used to fit each interval of the timing data, as further explained below.

5. Data-Reduction Methods

The derived method is not an iterative process, and the solution coefficients are obtained directly by constructing **A**, the entire data matrix, which can include data points based on higher derivatives. This interpretation of these well-known expressions is distinct from the so-called

"normal equations" scheme used in the JPL OD programs. The latter never constructs the entire data matrix because it is too large, and, since the **A** matrix changes with each fit, iterative techniques are employed.

The program MOPATS (Fig. 13) calls the subroutine MOPOLY. Since the separate fitting of each interval will result in "open" polynomials at the end points, an iterative method is used for the simultaneous fitting of a string of polynomials to a continuous data span. For the A.1 - WWV data, linear polynomials are used. Iteration "0" fits each interval separately, in sequence, with the A.1 - WWV data points plus the average slope for the month in the fit. The slope average over the month is a strong data type and markedly improves the fit, because the A.1 - WWV data over such short intervals does not determine accurate slope. The USNO measures the monthly slope averages for WWV, and these were used with appropriate weights, as explained below.

The result after iteration "0" is a set of polynomials which do not meet at their end points. A continuous least-squares fit to the entire interval is desired. There are two reasons why the polynomials may not meet. First, there may have been a step adjustment at that point. Indeed, it is necessary to create an end-of-interval condition at all such points because of the discontinuity. Second, the polynomials are not yet a least-squares continuous fit to the entire data span.

The first condition is handled internally to program MOPATS, and the comments below are based upon the inclusion of such step adjustments as are required. The subsequent iterations, nominally four, force the end points to meet. This is accomplished by inserting two additional A.1 - WWV points, one at each end of the interval. They are set half-way between the points given by the polynomial pair in question, as determined by the previous iteration (corrected for a step adjustment if present). The weight on these two points for iteration "1" is set to the square-root of the number of regular data points in the interval. For subsequent iterations, the weight is increased by factors equal to the original weight, being equal to points-squared for the fourth iteration. This gradual tightening of the end-point weights causes the entire sequence of polynomials to move until the desired least-squares fit is obtained over the entire data span. The process is an extremely sensitive detector of input errors and bad data, and this is its best application in this context. In fact, it should be pointed out that, while the old (pre-1960) data need the constrained

fitting supplied by this method, all recent data are essentially perfect, and the fitting process is merely a convenient way of handling the data.

As mentioned above, use of such sophisticated techniques on the fairly tractable A.1 — WWV problem may seem unnecessary. It should be noted, however, that this same system will be employed for fitting the PZT data, excepting only that the polynomial order will be increased to "2," and the end points will be required to meet in point and slope through a similar iterative scheme.

The weights used on the data, as well as the data sources, are given in subsection 6 along with explanations for the tables.

6. Results and Explanation of Tables

Figure 14 is a partial listing of the computer input governing the polynomial intervals, step adjustments, and measured offset with its standard deviation. It includes all WWV events, offset, and step changes from 1955 to the present. Column 1 is the date in YYMMDDHH format, Y = year, M = month, D = day, and H = hour if not 0. Column 2 is the step adjustment, if any, for the date and time of column 1. Column 3 is the measured offset. Prior to September 1956, offsets were not measured, and the program was given 0.0 as the value with the standard deviation equal to zero, which it interpreted as "do not include a point for the slope." From that time until January 1, 1960, there was no adopted offset, but it was measured. After 1960, the offsets were adopted by the B.I.H., as noted above, and the WWV transmissions were held as close to the value as possible. The measured amounts sometimes differed from the intended values, as indicated in column 3. Column 4, "sigma offset," is the standard deviation of the measured offset, or, for recent years, an adopted standard deviation which gives the desired weight for the fit. Column 5, "events," indicates the dates on which either the offset was changed or a step adjustment was made.

The A.1 — WWV data was supplied to the program from the following sources: (1) 1955 to September 1956 from unofficial USNO files (unpublished). (2) 1956 through 1958 from Ref. 1. (3) 1958 through July 1961 from Ref. 2. (4) 1961 through November 1966 from Ref. 3. (5) 1966 to the present, and into the foreseeable future, from Ref. 4. A sample data input interval is given in Fig. 14.

The standard deviation assumed for weighting purposes on all A.1 — WWV data points was 1 ms. The

units for the offset observations are seconds per second. The offset weights were computed from the above units, scaled to be in milliseconds per second, the internal scale of the program. This can be seen in Fig. 15, which lists the complete MOPOLY output from the last iteration on a representative polynomial interval. There follows a list of the computer output labels and their equivalent meaning in terms of the nomenclature used in this article. This comparison and Fig. 15 yield a numerical example of the process derived in subsection 4.

LABEL	Interval number
ARGUMENT MATRIX	A transposed (unweighted for normal equations option)
COEFFICIENT MATRIX	J (normal equations option)
COEFFICIENT MATRIX INVERSE	J inverse (normal equations option)
POLYNOMIAL COEFFICIENT SOLUTION VECTOR	X
DATA MATRIX INPUT ^a	Data and weights used in the fit
SOS	Sum of squares of the residuals, slope points not included
SIGMA	Standard deviation of the fit
SOR	Sum of residuals, should be very small
NFIT	Number of points in the fit

^aArgument is seconds past the interval start; residuals are given in the sense "data-fit"; the first and last points are the "weighted end points."

Figure 16 gives a sample of the plots produced for each interval. The parabolic residual profile, typical of the crystal oscillators used at that time to control WWV, is clearly evident. After about January 1958, the residuals are all less than 0.1 ms, which is the very fortunate result of using high-quality atomic oscillators to control the transmissions. The illustrated plot is, therefore, not typical of modern data, for which the residual plots serve only to detect errors in the data input. The diagnostic output and plots eliminate any reasonable possibility of undetected input errors. This is the most important function of the program for current data.

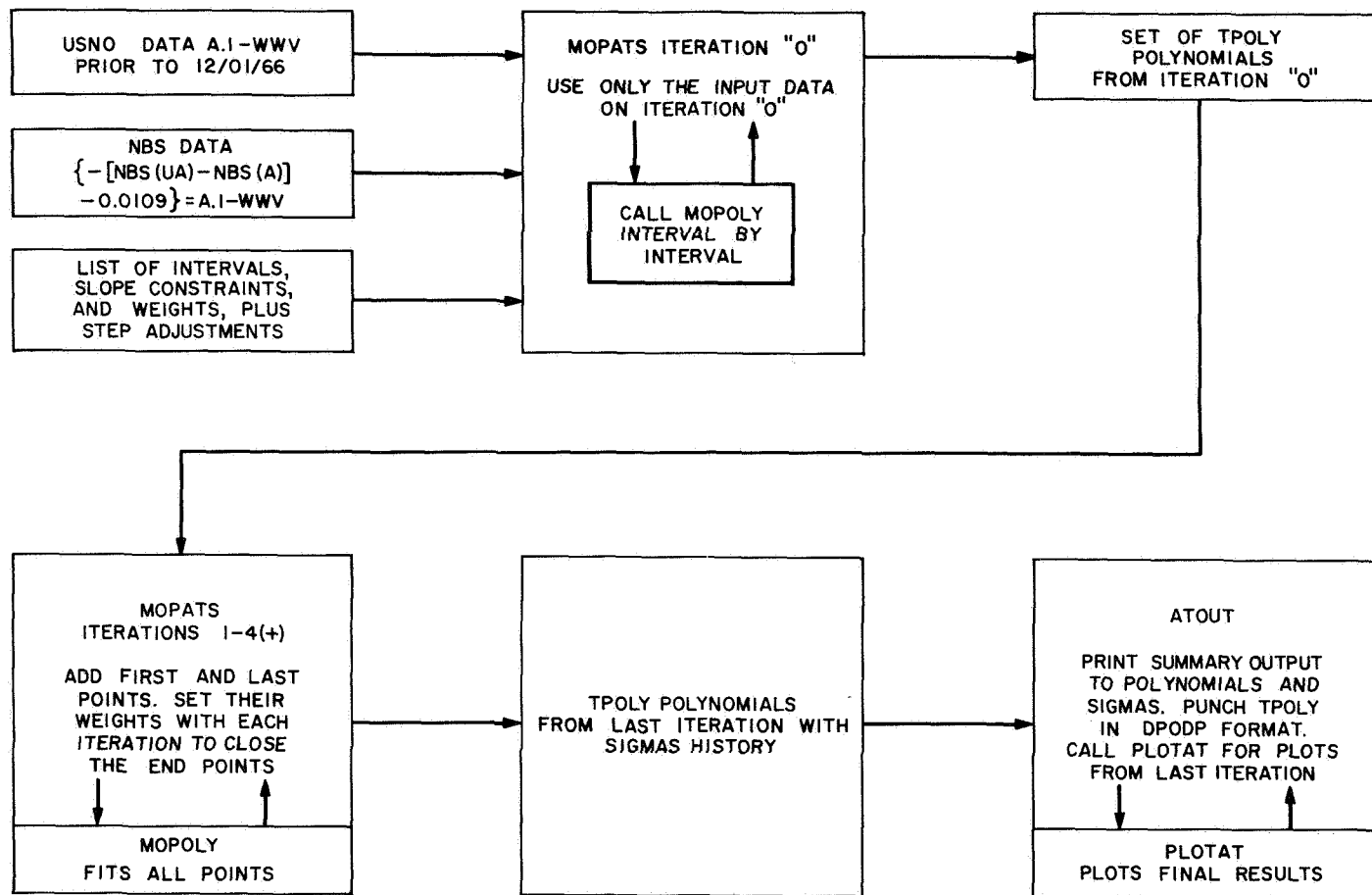


Fig. 13. Flow chart for computations

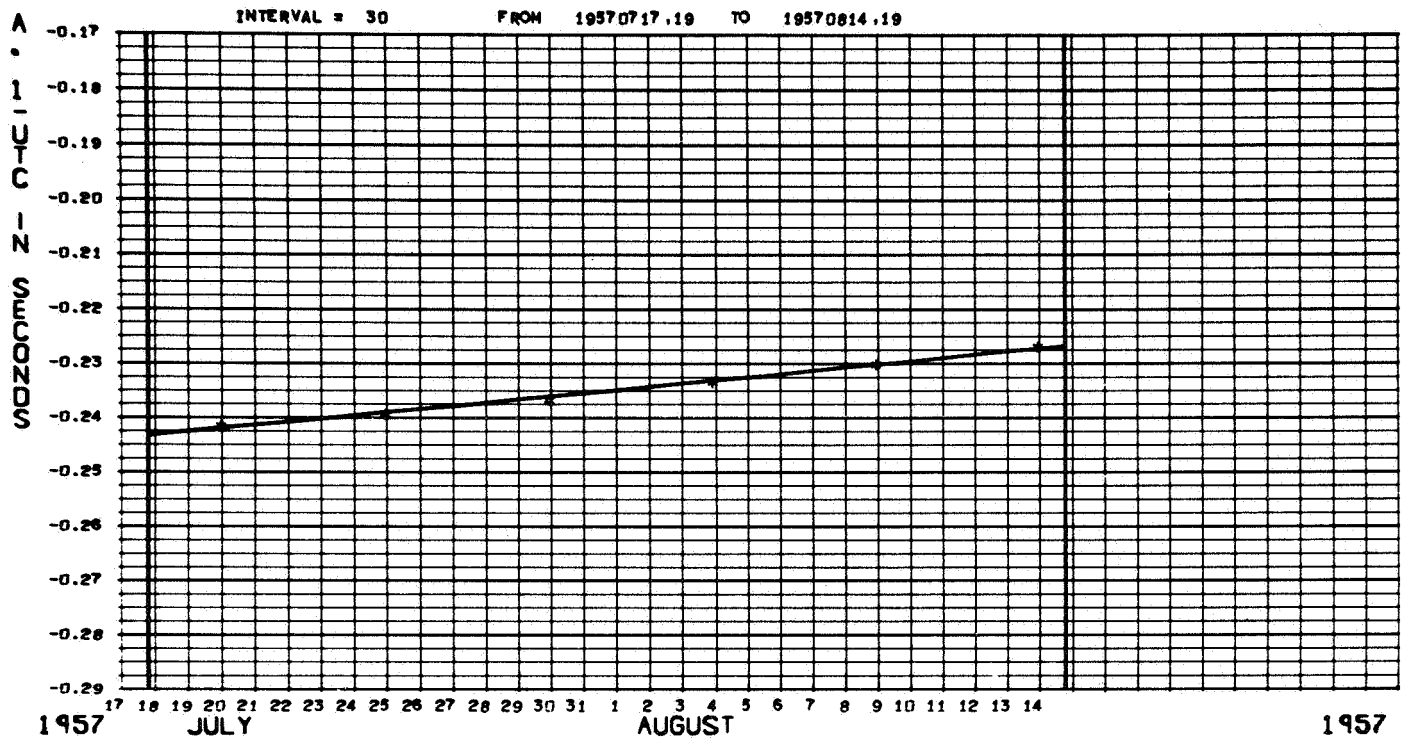
56010419	60.	0.	10.0	STEP +60 MILLISECONDS
56030719	-20.	0.	10.0	STEP -20 MILLISECONDS
56032819	-20.	0.	10.0	STEP -20 MILLISECONDS
56072519	20.	0.	10.0	STEP +20 MILLISECONDS
56082219	20.	0.	10.0	STEP +20 MILLISECONDS
56091919	20.	55.	10.0	STEP +20 MILLISECONDS, BEGIN SLOPE MEASUREMENTS
56103119	20.	40.	10.0	STEP +20 MILLISECONDS
56111419	20.	66.	10.0	STEP +20 MILLISECONDS
57012319	20.	90.	10.0	STEP +20 MILLISECONDS
57031319	20.	73.	10.0	STEP +20 MILLISECONDS
57050119	20.	70.	10.0	STEP +20 MILLISECONDS
57060519	20.	63.	10.0	STEP +20 MILLISECONDS
57061919	20.	64.	10.0	STEP +20 MILLISECONDS
57070319	20.	63.	10.0	STEP +20 MILLISECONDS
57071719	20.	70.	10.0	STEP +20 MILLISECONDS
57081419	20.	103.	10.0	STEP +20 MILLISECONDS
57101619	20.	108.	10.0	STEP +20 MILLISECONDS
57110619	20.	108.	10.0	STEP +20 MILLISECONDS
57121119	20.	110.	10.0	STEP +20 MILLISECONDS
58011519	20.	102.	5.0	STEP +20 MILLISECONDS
58020519	20.	95.	5.0	STEP +20 MILLISECONDS
58021919	20.	98.	5.0	STEP +20 MILLISECONDS
58040919	20.	100.	5.0	STEP +20 MILLISECONDS
58061119	20.	106.	5.0	STEP +20 MILLISECONDS
58070219	20.	105.	5.0	STEP +20 MILLISECONDS
58071619	20.	103.	5.0	STEP +20 MILLISECONDS
58102219	20.	96.	5.0	STEP +20 MILLISECONDS
58112619	20.	97.	5.0	STEP +20 MILLISECONDS
58122419	20.	106.7	5.0	STEP +20 MILLISECONDS
59012819	20.	107.0	5.0	STEP +20 MILLISECONDS
59022519	20.	109.5	5.0	STEP +20 MILLISECONDS
59080519	20.	100.0	5.0	STEP +20 MILLISECONDS
59082619	20.	100.0	5.0	STEP +20 MILLISECONDS
59093019	20.	102.0	5.0	STEP +20 MILLISECONDS
59110419	20.	101.6	5.0	STEP +20 MILLISECONDS
59111819	20.	101.0	5.0	STEP +20 MILLISECONDS
59121619	20.	100.0	5.0	STEP +20 MILLISECONDS
600101	0.	147.9	5.0	B.I.H. ADOPTED OFFSET = 150.E-10 SEC/SEC
610101	5.0	149.5	2.0	STEP +5 MILLISECONDS IN WWV, NOT B.I.H. REQUIRED
610801	-50.0	149.7	2.0	STEP -50 MILLISECONDS IN UTC/WWV
620101	0.	129.6	1.0	OFFSET CHANGED TO 130. E-10
631101	100.0	129.6	1.0	STEP +100 MILLISECONDS IN UTC/WWV
640101	0.	150.2	1.0	OFFSET CHANGED TO 150. E-10
640401	100.	150.2	1.0	STEP +100 MILLISECONDS IN UTC/WWV
640901	100.0	150.0	1.0	STEP +100 MILLISECONDS IN UTC/WWV
641001	1.	150.0	1.0	STEP +1 MILLISECOND IN WWV ONLY
650101	100.0	149.8	.5	STEP +100 MILLISECONDS IN UTC/WWV
650301	100.0	150.1	.5	STEP +100 MILLISECONDS IN UTC/WWV
650701	100.0+150.1	.5	.5	STEP +100 MILLISECONDS IN UTC/WWV
650901	100.0+150.0	.5	.5	STEP +100 MILLISECONDS IN UTC/WWV
660101	000.0+300.0	.5	.5	CHANGE OFFSET TO 300. E-10
661201	-.7+300.0	.5	.5	STEP -.7 MILLISECONDS IN WWV DUE TO RELOCATION
671001	-000.2+300.0	.5	.5	STEP OF -.2 MS. (FORWARDED FROM 670920)
680201	-100.0+300.0	.5	.5	STEP OF -100 MILLISECONDS IN UTC/WWV
YYMMDD A.I-UTC INPUT DATA FOR INTERVAL 570717 TO 570814				
570720	-.2419			
570725	-.2395			
570730	-.2368			
570804	-.2337			
570809	-.2304			
570814	-.2270			

Fig. 14. WWV events, 1955 to the present, and interval listing

RUN OF MOPOLY SUBROUTINE FOR CONSTRAINED WEIGHTED LEAST SQ.										PAGE 237	
MOPOLY FIT TO A1-UTC ITERATION (08) INTERVAL=LABEL NO.										LABEL = 30	
PRINT OF ARGUMENT MATRIX BY DATA POINT (XX) AND COEFFICIENT										LABEL = 30	
	(01) COLUMN 1	(02) COLUMN 2	(03) COLUMN 3	(04) COLUMN 4	(05) COLUMN 5	(06) COLUMN 6					
A0	1.000000000000 00	0.000000000000 39	1.000000000000 00	1.000000000000 00	1.000000000000 00	1.000000000000 00					
A1	0.000000000000 39	1.000000000000 00	1.908000000000 05	6.223000000000 05	1.054800000000 06	1.486800000000 06					
	(07) COLUMN 7	(08) COLUMN 8	(09) COLUMN 9								
A0	1.000000000000 00	1.000000000000 00	1.000000000000 00								
A1	1.918800000000 06	2.350800000000 06	2.419200000000 06								
COEFFICIENT MATRIX										LABEL = 30	
	A0 COLUMN 1	A1 COLUMN 2									
A0	4.807999572750 03	5.816123483200 09									
A1	5.816123483200 09	1.406587553020 16									
COEFFICIENT MATRIX INVERSE										LABEL = 30	
	A0 COLUMN 1	A1 COLUMN 2									
A0	4.161325436300 04	-1.720673735470 10									
A1	-1.720673735470 10	1.422424652030 16									
POLYNOMIAL COEFFICIENTS SOLUTION VECTOR										LABEL = 30	
A0	= -2.433239606600 01		A1	= 6.830569538590 09							
MOPOLY FIT TO A1-UTC ITERATION (08) INTERVAL=LABEL NO.										LABEL = 30	
LIST OF DATA MATRIX INPUT AND MOPOLY FIT										LABEL = 30	
POINT ARGUMENT	DATA POINT	WEIGHT	FIT VALUE	RESIDUAL	TYPE-NOTE						
1	0.00000000 39	-2.4332359E-01	2.4009998E 03	-2.4332396E-01	3.7377869E-07	0	POLYNOMIAL				
2	0.00000000 39	7.0000000E-09	1.0000000E 12	6.8305695E-09	1.6943043E-10	1	DERIVATIVE				
3	1.9080000E 05	-2.4190000E-01	1.0000000E 00	-2.4202069E-01	1.2068727E-04	0	POLYNOMIAL				
4	6.2230000E 05	-2.3950000E-01	1.0000000E 00	-2.3906988E-01	-4.3011726E-04	0	POLYNOMIAL				
5	1.0548000E 06	-2.3680000E-01	1.0000000E 00	-2.3611907E-01	-6.8092416E-04	0	POLYNOMIAL				
6	1.4868000E 06	-2.3370000E-01	1.0000000E 00	-2.3316827E-01	-5.3172988E-04	0	POLYNOMIAL				
7	1.9188000E 06	-2.3040000E-01	1.0000000E 00	-2.3021746E-01	-1.8253594E-04	0	POLYNOMIAL				
8	2.3508000E 06	-2.2700000E-01	1.0000000E 00	-2.2726666E-01	2.6665783E-04	0	POLYNOMIAL				
9	2.4192000E 06	-2.2679922E-01	2.4009998E 03	-2.2679945E-01	2.2512271E-07	0	POLYNOMIAL				
SQS= 1.050386611090 06 SIGMA= 3.623511092660 04 SOR= 2.40477223710 13 NFIT= 9											

Fig. 15. Example of a computer-generated fit to an interval

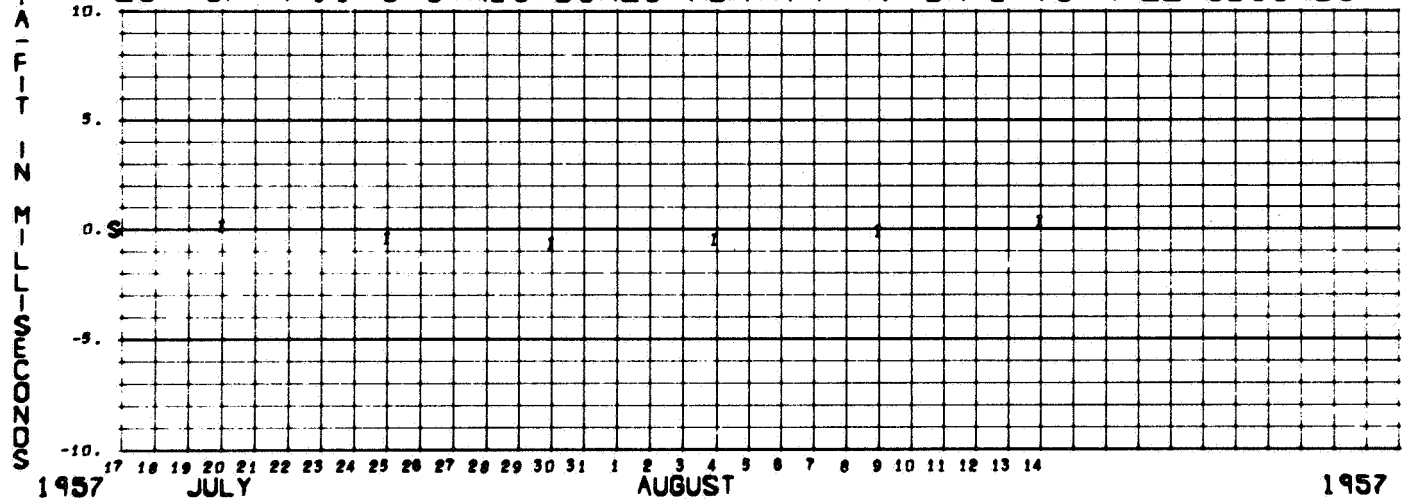
PLOT OF FIT TO A .1-UTC CALENDAR DATE VS SECONDS



SCALE ABOVE = 2.5 MS (1-METER LONGITUDE) PER SMALL DIVISION

POLY A0= -2.4332398D-01 A1= 8.8309895D-09 A2= 0.0000000D-39 SIGMA= 3.6235111D-04 STEP= 20.0 OFFSET= 70.0

PLOT OF A .1-UTC RESIDUALS (DATA-FIT) DATE VS MILLISECONDS



I=RESIDUAL(I=SIGMA),()=OFF SCALE, X=DELETED, S=STEP, +=DEL POLY
RUN OF TPOLY SYSTEM UPDATE 01 DECEMBER 1967

Fig. 16. Sample plot for interval

FIT 1955-1967 A.1-WWV DECEMBER 1967											
POLYNOMIAL AND SIGMA HISTORY SUMMARY - MOPATS FIT TO A1-UTC						LABEL = 156					
NO.	YYMMDD,HH	STEP(MS)	OFFSET	A0	A1	SIGMA 0	SIGMA 1	SIGMA 2	SIGMA 3	SIGMA 4	DPOLY
29	570703,19	20.0	63.0	-2.7064755D-01	6.0565358D-09	2.90D-05	1.53D-04	1.54D-04	1.54D-04	1.55D-04	-3.43D-08
30	570717,19	20.0	70.0	-2.4332396D-01	6.8305695D-09	3.34D-04	3.58D-04	3.60D-04	3.62D-04	3.62D-04	-2.39D-06
31	570814,19	20.0	103.0	-2.0679912D-01	1.0211931D-08	2.05D-04	2.20D-04	2.21D-04	2.21D-04	2.21D-04	3.22D-07
32	570918,00	0.0	120.0	-1.7661654D-01	1.2171250D-08	9.51D-05	1.10D-04	1.11D-04	1.11D-04	1.11D-04	2.01D-07

Fig. 17. Polynomial and sigma's history

Figure 17 lists the final output of polynomials for the period from June 1955 through June 1968, where the data for January to June 1968 are predictions. For an argument in seconds past the start of a given interval, the series of linear polynomials will generate A.1 - WWV for this period of time. Each polynomial applies over the period, commencing on the date given with it and ending on the date given for the next polynomial. A0 refers to the constant term, and is also the value of A.1 - WWV for the epoch. A1 refers to the coefficient of the linear term. SIGMA0 through SIGMA4 (sample intervals shown in Fig. 17a) give the history of the standard deviations of the fits for the five iterations. STEP and OFFSET for each interval are given, and DPOLY is the difference between the two adjacent polynomials at the end points (should be small). These data are useful in detecting input errors and in proving that the convergence is complete. Changes in the polynomial coefficients themselves are much smaller than the changes in sigmas indicated by the table. Convergence may be considered complete when the sigmas remain fixed to within 0.1 ms for the older data and 0.01 ms for the modern data.

References

1. *Time Service Notice 6*, USNO, Washington, Jan. 1, 1959.
2. *Bulletins B-152-B-194*, USNO, Washington, Jan. 22, 1959 to Aug. 3, 1961.
3. *Bulletins 195-213, Final Times of Emission*, USNO, Washington, Mar. 15, 1962 to Oct. 1, 1967.
4. *Time and Frequency Service Bulletins and Supplement 1*, NBS, Washington, Mar. 1966 to Dec. 1967.

F. Navigation Technology Project, D. W. Curkendall

The Navigation Technology Project was formally established within the JPL Systems Analysis and Systems Analysis Research Sections in June 1966 to organize and coordinate the technological development of estimation and maneuver-strategy techniques necessary to realize flight-project guidance-accuracy goals. It forms a companion to the Inherent Accuracy and the Ephemeris

Development Projects. The Navigation Technology Project has six principal objectives:

- (1) To understand and develop adequate statistical models describing the nongravitational forces affecting the spacecraft trajectory.
- (2) To develop computationally tractable techniques for trajectory estimation in the presence of these nongravitational forces and to describe the navigation accuracy achieved, with the use of these techniques, from the navigational data available.
- (3) To perform approach-navigation studies and explore the potentialities of the combination of earth-based tracking data and spacecraft onboard observables.
- (4) To construct simple geometrical approaches to compute navigation accuracies and develop data-compression techniques to facilitate the tasks of orbit selection and processing of long spans of tracking data.
- (5) To develop the navigation technology required for orbital-capsule operations, including trajectory integration and observable computational techniques, bus-capsule relay-link navigation data, and landed-capsule observation.
- (6) To develop appropriate guidance-maneuver strategies for such advanced interplanetary missions as *Voyager*.

Work relating to the Navigation Technology Project is supported by the various flight projects, by the Supporting Research and Advanced Development Office, and by the Deep Space Network. However, to simplify presentation, it is planned to report all such work progress in the *Deep Space Network* SPS volume.

In this issue, an optimal stochastic orbit-trim strategy for a planetary satellite is presented. The formulation considers three in-plane state variables and seeks to minimize a quadratic performance index in terms of the

FIT 1955-1967 A.1-WHV DECEMBER 1967				FIT 1955-1967 A.1-WHV DECEMBER 1967			
NO.	YYMMDD,HH	A0	A1	NO.	YYMMDD,HH	A0	A1
1	550601,00	-9.7675529D-01	1.4981943D-08	83	611001,00	1.7631852D 00	1.4943596D-08
2	550701,00	-9.3791926D-01	1.2256391D-08	84	611101,00	1.8032104D 00	1.4986139D-08
3	550801,00	-9.0509652D-01	-4.6914116D-10	85	611201,00	1.8420548D 00	1.5070432D-08
4	550901,00	-9.0635210D-01	-3.5537736D-09	86	620101,00	1.8824192D 00	1.2957736D-08
5	551001,00	-9.1556674D-01	5.3429852D-10	87	620201,00	1.9171243D 00	1.2976471D-08
6	551101,00	-9.1413343D-01	1.2981119D-09	88	620301,00	1.9485161D 00	1.3038913D-08
7	551201,00	-9.1077327D-01	8.6728846D-09	89	620401,00	1.9834394D 00	1.3000555D-08
8	560104,19	-8.2469658D-01	1.6805367D-08	90	620501,00	2.0171369D 00	1.2950803D-08
9	560201,00	-7.8519218D-01	1.4235998D-08	91	620601,00	2.0518245D 00	1.2939419D-08
10	560307,19	-7.6116947D-01	1.2361713D-08	92	620701,00	2.0853634D 00	1.2950186D-08
11	560328,19	-7.5873939D-01	9.3038367D-09	93	620801,00	2.1200492D 00	1.2969963D-08
12	560501,00	-7.3204547D-01	7.8048083D-09	94	620901,00	2.1547878D 00	1.2938582D-08
13	560601,00	-7.1114067D-01	7.8814333D-09	95	621001,00	2.1883241D 00	1.2980522D-08
14	560701,00	-6.9071274D-01	4.3632858D-09	96	621101,00	2.2230914D 00	1.2960914D-08
15	560725,19	-6.6136553D-01	3.4427458D-09	97	621201,00	2.2566860D 00	1.2956381D-08
16	560822,19	-6.3303856D-01	3.1407380D-09	98	630101,00	2.2913874D 00	1.2944652D-08
17	560919,19	-6.0543815D-01	6.0198842D-09	99	630201,00	2.3260571D 00	1.2969423D-08
18	561010,00	-5.9492712D-01	3.8451744D-09	100	630301,00	2.3574330D 00	1.3015521D-08
19	561031,19	-5.6768750D-01	3.8106238D-09	101	630401,00	2.3922948D 00	1.2984737D-08
20	561114,19	-5.4307968D-01	6.5275257D-09	102	630501,00	2.4259528D 00	1.3014597D-08
21	561219,00	-5.2378665D-01	9.4600798D-09	103	630601,00	2.4608119D 00	1.3002201D-08
22	570123,19	-4.7453210D-01	9.2052308D-09	104	630701,00	2.4945140D 00	1.3001108D-08
23	570221,00	-4.5209742D-01	6.8918859D-09	105	630801,00	2.5293362D 00	1.2948167D-08
24	570313,19	-4.1971653D-01	7.1624038D-09	106	630901,00	2.5640159D 00	1.2957903D-08
25	570403,00	-4.0721250D-01	7.9027496D-09	107	631001,00	2.5976020D 00	1.2958784D-08
26	570501,19	-3.6755201D-01	7.2008567D-09	108	631101,00	2.7323110D 00	1.2962491D-08
27	570605,19	-3.2578239D-01	6.0727046D-09	109	631201,00	2.7659108D 00	1.2953938D-08
28	570619,19	-2.9843581D-01	6.4387334D-09	110	640101,00	2.8006074D 00	1.5020818D-08
29	570703,19	-2.7064755D-01	6.0565358D-09	111	640201,00	2.8408385D 00	1.5016801D-08
30	570717,19	-2.4332396D-01	6.8305695D-09	112	640301,00	2.8784628D 00	1.4989800D-08
31	570814,19	-2.0679912D-01	1.0211931D-08	113	640401,00	3.0186074D 00	1.5003567D-08
32	570918,00	-1.7661654D-01	1.2171250D-08	114	640501,00	3.0574919D 00	1.4966715D-08
33	571016,19	-1.2633858D-01	1.0160782D-08	115	640601,00	3.0975757D 00	1.4981105D-08
34	571106,19	-8.7906408D-02	1.0689004D-08	116	640701,00	3.1364057D 00	1.4974194D-08
35	571211,19	-3.5581515D-02	1.1341894D-08	117	640801,00	3.1765101D 00	1.4957291D-08
36	580115,19	1.8715588D-02	1.0029541D-08	118	640901,00	3.3165716D 00	1.5000347D-08
37	580205,19	5.6909296D-02	9.4233705D-09	119	641001,00	3.3564526D 00	1.4998911D-08
38	580219,19	8.8304306D-02	9.7450435D-09	120	641101,00	3.3966253D 00	1.4987949D-08
39	580312,00	1.0531924D-01	1.0162483D-08	121	641201,00	3.4354733D 00	1.4976688D-08
40	580409,19	1.5059981D-01	9.9511900D-09	122	650101,00	3.5755857D 00	1.4979186D-08
41	580514,00	1.8001066D-01	9.5702507D-09	123	650201,00	3.6157057D 00	1.5000277D-08
42	580611,19	2.2381914D-01	1.0728637D-08	124	650301,00	3.7519953D 00	1.5011106D-08
43	580702,19	2.6328539D-01	1.0506174D-08	125	650401,00	3.7922025D 00	1.5001105D-08
44	580716,19	2.9599366D-01	1.0333310D-08	126	650501,00	3.8310862D 00	1.5000098D-08
45	580820,00	3.2653504D-01	1.0220146D-08	127	650601,00	3.8712620D 00	1.4989369D-08
46	580917,00	3.5125963D-01	1.0077387D-08	128	650701,00	4.0101137D 00	1.5009098D-08
47	581022,19	4.0242904D-01	9.5549443D-09	129	650801,00	4.0503128D 00	1.4988758D-08
48	581126,19	4.5132298D-01	9.5972722D-09	130	650901,00	4.1904571D 00	1.4998704D-08
49	581224,19	4.9454066D-01	1.0584437D-08	131	651001,00	4.2293321D 00	1.4998618D-08
50	590128,19	5.4654801D-01	1.0770480D-08	132	651101,00	4.2695031D 00	1.4999234D-08
51	590225,19	5.9260415D-01	1.0913743D-08	133	651201,00	4.3083803D 00	1.4989015D-08
52	590401,00	6.2486071D-01	1.0746730D-08	134	660101,00	4.3485253D 00	2.9998639D-08
53	590501,00	6.5271622D-01	1.0514122D-08	135	660201,00	4.4288722D 00	2.9998415D-08
54	590601,00	6.8087745D-01	1.0562273D-08	136	660301,00	4.5014424D 00	2.9998792D-08
55	590701,00	7.0825494D-01	1.0105413D-08	137	660401,00	4.5817907D 00	2.9999821D-08
56	590805,19	7.5950461D-01	9.9831996D-09	138	660501,00	4.6595506D 00	3.0001179D-08
57	590826,19	7.9761818D-01	1.0016303D-08	139	660601,00	4.7399079D 00	3.0002469D-08
58	590930,19	8.4790728D-01	1.0328289D-08	140	660701,00	4.8176777D 00	3.0002644D-08
59	591104,19	8.9914197D-01	1.0273643D-08	141	660801,00	4.8980394D 00	3.0001950D-08
60	591118,19	9.3157019D-01	1.0274445D-08	142	660901,00	4.9783988D 00	3.0001980D-08
61	591216,19	9.7642861D-01	1.0199630D-08	143	661001,00	5.0561663D 00	3.0004458D-08
62	600101,00	9.8983349D-01	1.5013770D-08	144	661101,00	5.1365328D 00	3.0002066D-08
63	600201,00	1.0300465D 00	1.4818363D-08	145	661201,00	5.2135997D 00	3.0001214D-08
64	600301,00	1.0671756D 00	1.4585855D-08	146	670101,00	5.2939551D 00	2.9999718D-08
65	600401,00	1.1062424D 00	1.4807192D-08	147	670201,00	5.3743060D 00	2.9998823D-08
66	600501,00	1.1446228D 00	1.4698355D-08	148	670301,00	5.4468787D 00	2.9998844D-08
67	600601,00	1.1839908D 00	1.4617742D-08	149	670401,00	5.5272274D 00	2.9998160D-08
68	600701,00	1.2218801D 00	1.4822369D-08	150	670501,00	5.6049868D 00	2.9998823D-08
69	600801,00	1.2615803D 00	1.4548097D-08	151	670601,00	5.6853350D 00	2.9998213D-08
70	600901,00	1.3005460D 00	1.4615126D-08	152	670701,00	5.7630898D 00	2.9999540D-08
71	601001,00	1.3384283D 00	1.4645004D-08	153	670801,00	5.8434410D 00	3.0002836D-08
72	601101,00	1.3776535D 00	1.4797359D-08	154	670901,00	5.9238013D 00	3.0001322D-08
73	601201,00	1.4160083D 00	1.5011097D-08	155	671001,00	6.0013651D 00	3.0000514D-08
74	610101,00	1.4612144D 00	1.4961222D-08	156	671101,00	6.0817186D 00	3.0000036D-08
75	610201,00	1.5012877D 00	1.4903971D-08	157	671201,00	6.1594787D 00	3.0000000D-08
76	610301,00	1.5373436D 00	1.4908504D-08	158	680101,00	6.2398307D 00	3.0000000D-08
77	610401,00	1.5772750D 00	1.4909443D-08	159	680201,00	6.2201827D 00	3.0000000D-08
78	610501,00	1.6159213D 00	1.4880112D-08	160	680301,00	6.2953507D 00	3.0000000D-08
79	610601,00	1.6557764D 00	1.4841001D-08	161	680401,00	6.3757027D 00	3.0000000D-08
80	610701,00	1.6942431D 00	1.4869542D-08	162	680501,00	6.4534627D 00	3.0000000D-08
81	610801,00	1.6840698D 00	1.4982198D-08	163	680601,00	6.5338147D 00	3.0000000D-08
82	610901,00	1.7241994D 00	1.5041109D-08				

Fig. 17 (contd)

deviations of these variables from the desired values. A stochastic element is introduced in that the maneuvers are subject to random execution errors. This formulation has been carefully modeled after the requirements of an orbiter mission such as *Voyager* and should represent a realistic description of future operational situations.

Also, in the second of a series of articles giving results from the continuous estimation program, results from the analysis of the information content of a single pass of doppler data are presented. The effects of data noise are plotted, and results with and without ranging data are compared.

G. Navigation Technology: Dynamic Programming Approach to Optimal Stochastic Orbit-Transfer Strategy, T. Nishimura

1. Introduction

An important objective of space missions is frequently to achieve a specified elliptical orbit around the target planet. After an insertion maneuver, however, the spacecraft may reach a dispersed orbit apart from the target orbit due to orbit-determination and execution errors. Then, a sequence of corrections (possibly two) becomes mandatory in order to accomplish the mission objective. Even when only two corrections are performed, for example, there is almost an infinite number of candidate modes to be considered concerning how and when these two maneuvers shall be executed. Especially when execution errors are inevitable which are stochastic in nature, the classical deterministic approach to orbit-transfer problems is not too promising in solving this formidable problem.

Hence, a dynamic programming approach^{13,14} is taken in this article in order to formulate an optimal stochastic orbit-transfer strategy. The performance index employed here is the weighted mean-squared distance in the parameter space between the final orbit and the target orbit, and the final objective of the maneuvers is to minimize this performance index. The goal here is different than that of the classical deterministic approach, which is mostly concerned with minimizing the fuel consumption. In this formulation, the fuel will enter into the problem

only through a constraint imposed on the maximum correction capability. Finally, this article will describe the analytical aspect of the program which has been developed for use of the IBM 7094.

2. State Variables

This article is confined to the problem of orbit transfer between two coplanar elliptical orbits. Coordinates of a spacecraft along an elliptical orbit around the planet are described by the following four parameters:

θ = true anomaly

T = orbital period

h_p = periapsis altitude

ω = angular rotation of line of apsides

The last three parameters form a state vector \bar{x} to be controlled by this program, namely,

$$\bar{x} = \begin{bmatrix} T \\ h_p \\ \omega \end{bmatrix} \quad (1)$$

Let the target orbit be described by a vector \bar{x}_d :

$$\bar{x}_d = \begin{bmatrix} T_d \\ h_{pd} \\ \omega_d \end{bmatrix} \quad (2)$$

The velocity vector \bar{u} of the spacecraft is defined by a speed component v and a path angle γ (measured counter-clockwise, as shown in Fig. 18):

$$\bar{u} = \begin{bmatrix} v \\ \gamma \end{bmatrix}, \quad -\pi \leq \gamma \leq \pi \quad (3)$$

Suppose the initial velocity \bar{u}_0 is modified to \bar{u}_1 as a result of an impulsive correction \bar{u}_c , where

$$\bar{u}_1 = \begin{bmatrix} v_1 \\ \gamma_1 \end{bmatrix} = \begin{bmatrix} v_0 + \Delta v \\ \gamma_0 + \Delta \gamma \end{bmatrix} \quad (4)$$

Then the components of \bar{u}_c are obtained as a vector difference between \bar{u}_1 and \bar{u}_0 (Fig. 19):

$$\bar{u}_c = \begin{bmatrix} v_c \\ \gamma \end{bmatrix} = \bar{u}_1 - \bar{u}_0 \quad (5)$$

¹³Pfeiffer, C. G., *A Computational Technique for Determining the Optimal Stochastic Orbit Transfer Strategy*, Nov. 22, 1966 (JPL Section 312 internal technical memorandum).

¹⁴Nishimura, T., *Dynamic Programming Approach to Optimal Stochastic Orbit Transfer Strategy—Single-Stage Problem*, Sept. 25, 1967 (JPL Section 311 internal technical memorandum).

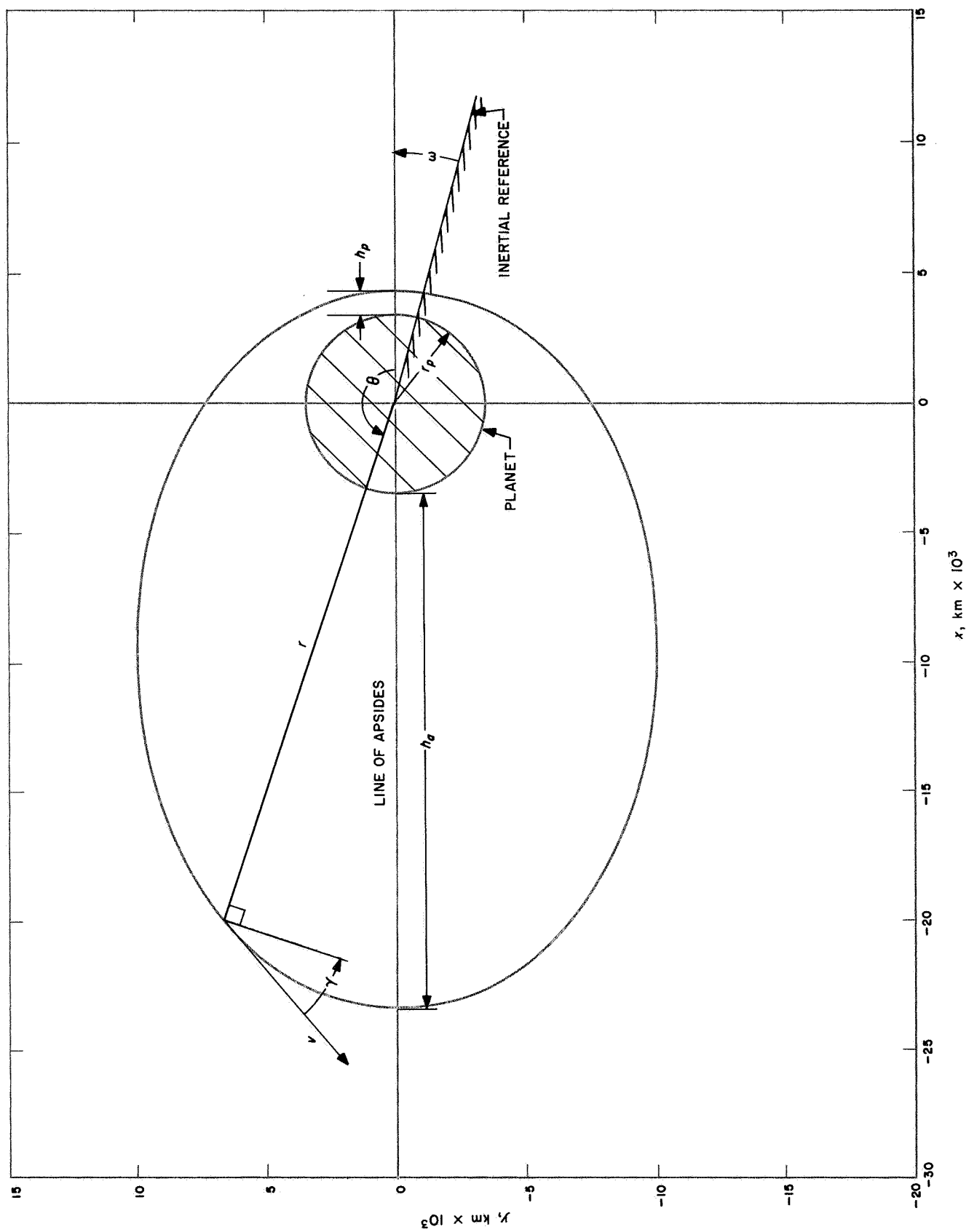


Fig. 18. Definition of orbital parameters

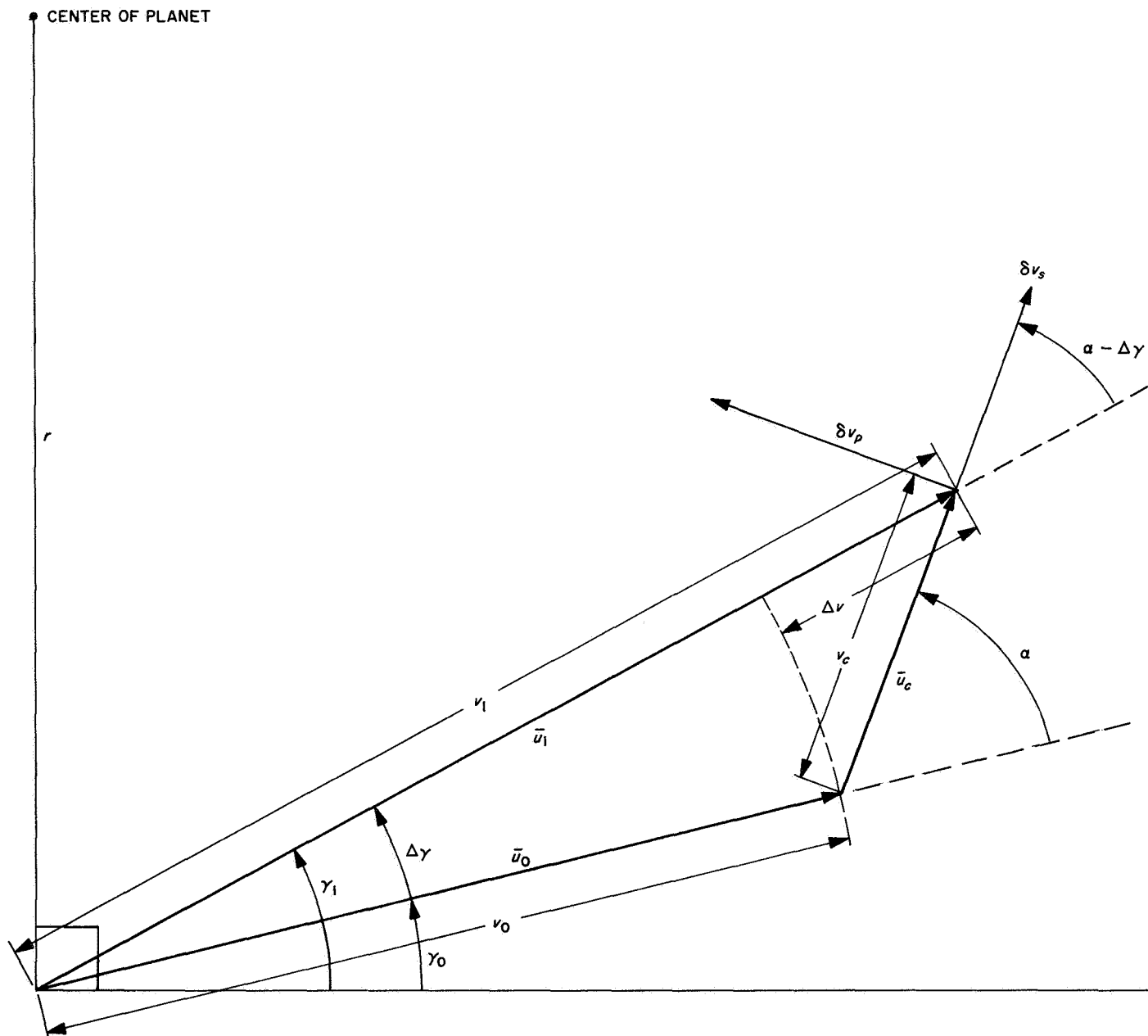


Fig. 19. Initial and final velocity vectors and impulsive correction vector

where

$$v_c = (v_1^2 + v_0^2 - 2v_0v_1\cos\Delta\gamma)^{1/2} \quad (6)$$

$$\alpha = \sin^{-1}\left(\frac{v_1\sin\Delta\gamma}{v_c}\right), \quad -\pi \leq \alpha \leq \pi \quad (7)$$

Also, the state vector \bar{x}_0 is transferred to \bar{x}_1 as a result of this correction \bar{u}_c :

$$\bar{x}_1 = \begin{bmatrix} T_1 \\ h_{p1} \\ \omega_1 \end{bmatrix} \quad (8)$$

The components of \bar{x}_1 are computed from \bar{x}_0 and \bar{u}_1 through the use of the following relationships:

$$T_1 = 2\pi\left(\frac{a_1^3}{\mu}\right)^{1/2} \quad (9)$$

$$h_{p1} = a_1(1 - e_1) - r_p \quad (10)$$

$$\omega_1 = \omega_0 + \theta_0 - \theta_1 \quad (11)$$

where

$$a_1 = \frac{r\mu}{2\mu - rv_1^2} \quad (12)$$

$$e_1 = \left(1 - \frac{r^2v_1^2}{a_1\mu}\cos^2\gamma_1\right)^{1/2} \quad (13)$$

$$\theta_1 = \cos^{-1}\left[\frac{a_1(1 - e_1^2) - r}{re_1}\right] \quad (14)$$

with

r = radial distance from the center of the planet

μ = gravitational constant of the planet

r_p = average radius of the planet

a_1 = magnitude of the semimajor axis after correction

e_1 = eccentricity of the orbit after correction

θ_1 = true anomaly of the vehicle after correction

3. Performance Index

The performance index is chosen in the following quadratic form:

$$J(\bar{x}_0, \Delta\bar{u}_0, \theta_0) = E[(\bar{x}_1 - \bar{x}_d)'W(\bar{x}_1 - \bar{x}_d)] \quad (15)$$

where \bar{x}_1 is the final state (orbit) resulting from the correction and W is a (3×3) , symmetric, weighting (semi-positive definite) matrix (Fig. 20).

Concerning the single-stage optimization problem, the objective of the program is to find such a control \bar{u}_c minimizing the performance index $J(\bar{x}_0, \Delta\bar{u}, \theta_0)$, as well as the associated true anomaly θ_0^* and the final orbit $\bar{x}_f = \bar{x}_1^*$ (the final state resulting from the optimal correction \bar{u}_c^*), under the constraint on the fuel. Namely, the maximum correction capability is limited by

$$v_c \leq c$$

No limitation is imposed on the direction of correction α ; i.e., the correction may be pointed in any direction. The performance index thus minimized is denoted as p , which is a function of θ_0 as well as \bar{x}_0 :

$$\begin{aligned} p_1(\bar{x}_0, \theta_0) &= \min_{\Delta\bar{u}_0} J(\bar{x}_0, \theta_0, \Delta\bar{u}_0) \\ &= \min_{\Delta\bar{u}_0} E[(\bar{x}_1 - \bar{x}_d)'W(\bar{x}_1 - \bar{x}_d)] \end{aligned} \quad (16)$$

4. Stochastic Error Models

Two kinds of stochastic errors may be considered: namely, an estimation error of orbital parameters and an execution error of correction. The estimation error is neglected in this program under the assumption that it may be reduced to a sufficiently small value if the spacecraft is permitted to go around the planet for an adequate period before the correction. Also, it is not too difficult to modify the program later when this assumption is to be removed.

As for the execution error, only a scale-factor error and a pointing error are taken into account. The scale-factor error is in the direction of \bar{u}_c and is proportional to $|\bar{u}_c| = v_c$. The pointing error is in the direction perpendicular to \bar{u}_c and is proportional to v_c . Let s and p be dimensionless random variables associated with these two execution errors having zero mean and variances σ_s^2 and

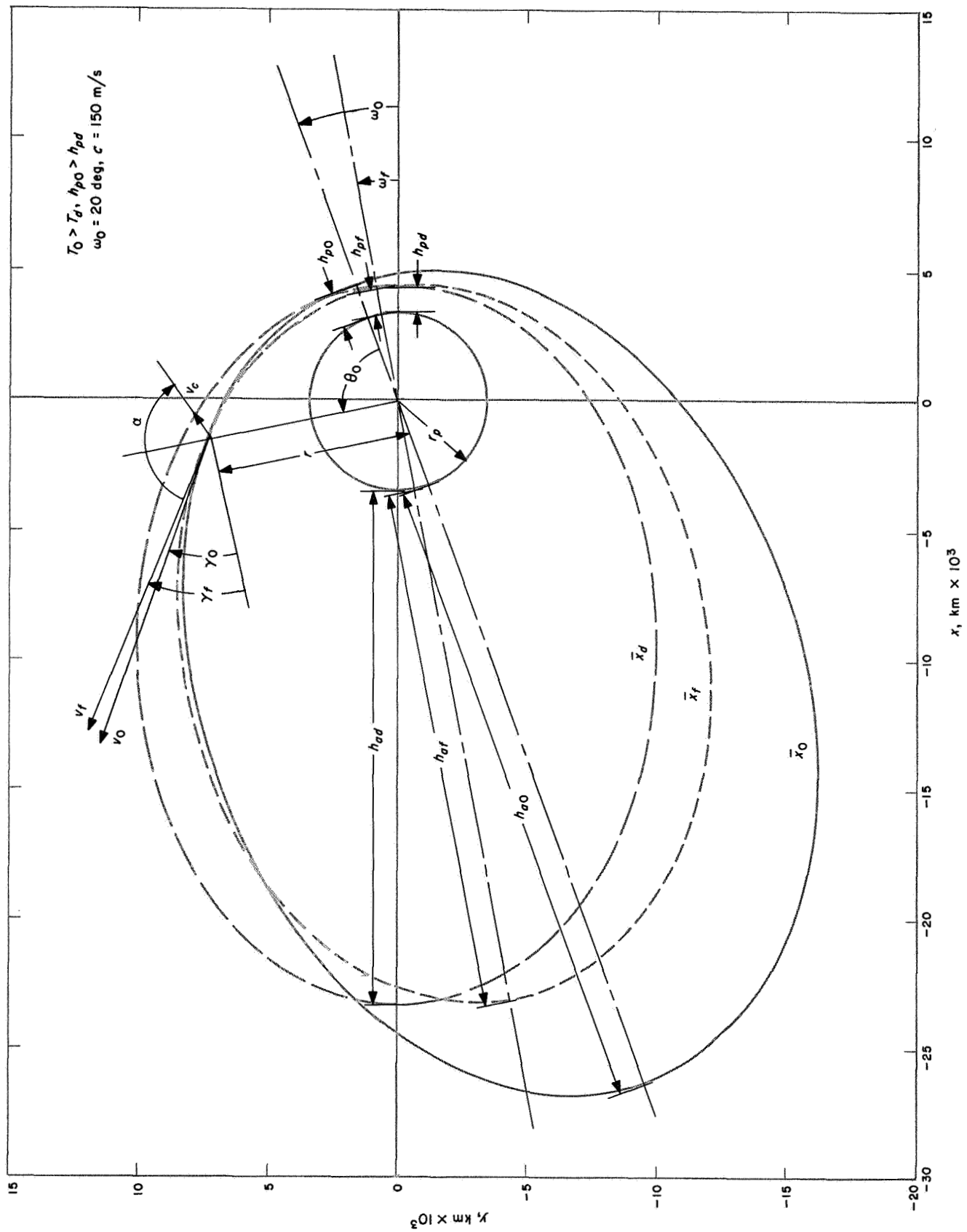


Fig. 20. Optimal orbit transfer

σ_p^2 , respectively. Let \bar{e} be an execution-error vector consisting of e_v and e_γ , which are, respectively, the errors in the final values of v and γ .

$$\bar{e} = \begin{bmatrix} e_v \\ e_\gamma \end{bmatrix} \quad (17)$$

These two components are then described by the following equations:

$$e_v = sv_c \cos(\alpha - \Delta\gamma) - pv_c \sin(\alpha - \Delta\gamma) \quad (18)$$

$$e_\gamma = s \frac{v_c}{v_1} \sin(\alpha - \Delta\gamma) + p \frac{v_c}{v_1} \cos(\alpha - \Delta\gamma) \quad (19)$$

Using the expressions for v_c and α of Eqs. (6) and (7), the equations for \bar{e} can be simplified and expressed in the following vector form:

$$\bar{e} = B \bar{s} \quad (20)$$

where B is a (2×2) matrix with

$$B_{11} = (1 - \cos \Delta\gamma)v + \Delta v \quad (21)$$

$$B_{12} = -v \sin \Delta\gamma \quad (22)$$

$$B_{21} = \left(1 - \frac{\Delta v}{v}\right) \sin \Delta\gamma \quad (23)$$

$$B_{22} = \left(1 - \cos \Delta\gamma + \frac{\Delta v}{v}\right) \left(1 - \frac{\Delta v}{v}\right) \quad (24)$$

and \bar{s} is a stochastic variable vector composed of

$$\bar{s} = \begin{bmatrix} s \\ p \end{bmatrix} \quad (25)$$

5. Iterative Method of Finding Optimal Control

An iterative technique (Newton's method) is used to find an optimal control $\Delta \bar{u}$ composed of

$$\Delta \bar{u} = \begin{bmatrix} \Delta v \\ \Delta \gamma \end{bmatrix} \quad (26)$$

The final state \bar{x}_1 is expanded into a Taylor series with respect to $\Delta \bar{u}$, and the higher-order terms are dropped.

Then,

$$\bar{x}_1 \approx \bar{x}_0 + \Delta \bar{x} + \bar{\eta} \quad (27)$$

where

$$\Delta \bar{x} \cong \frac{\partial \bar{x}}{\partial \bar{u}} \Delta \bar{u} = X_u \Delta \bar{u} \quad (28)$$

$$\bar{\eta} = \frac{\partial \bar{x}}{\partial \bar{u}} \bar{e} = X_u \bar{e} \quad (29)$$

with $\bar{\eta}$ = a random disturbance to the state vector caused by execution errors, and X_u = a (3×2) matrix of partials:

$$X_u = \frac{\partial \bar{x}}{\partial \bar{u}} = \begin{bmatrix} \frac{\partial T}{\partial v} & \frac{\partial T}{\partial \gamma} \\ \frac{\partial h_p}{\partial v} & \frac{\partial h_p}{\partial \gamma} \\ \frac{\partial \omega}{\partial v} & \frac{\partial \omega}{\partial \gamma} \end{bmatrix} \quad (30)$$

These components of the X_u matrix are obtained by differentiating the elements of vector \bar{x}_1 specified by Eqs. (9)–(11) together with the auxiliary variables a_1 , e_1 , and θ_1 of Eqs. (12)–(14) with respect to v and γ . Thus,

$$\frac{\partial T}{\partial v} = 6\pi\mu v \left(\frac{a}{\mu}\right)^{5/2} \quad (31)$$

$$\frac{\partial T}{\partial \gamma} = 0 \quad (32)$$

$$\frac{\partial h_p}{\partial v} = \frac{2a^2(1-e)^2}{vr} \cdot \frac{1 - \cos \theta}{1 + e \cos \theta} \quad (33)$$

$$\frac{\partial h_p}{\partial \gamma} = -\frac{a(1-e^2)}{e} \tan \gamma \quad (34)$$

$$\frac{\partial \omega}{\partial v} = \frac{2 \sin \theta}{ev} \quad (35)$$

$$\frac{\partial \omega}{\partial \gamma} = \frac{1}{e(1 + e \cos \theta)} [2e + (1 + e^2) \cos \theta] \quad (36)$$

Substituting the expression of \bar{x}_1 in Eq. (27) into Eq. (15), the performance index becomes

$$J(\bar{x}_0, \Delta \bar{u}, \theta) = (\bar{x}_0 + \Delta \bar{x} - \bar{x}_d)' W (\bar{x}_0 + \Delta \bar{x} - \bar{x}_d) + f \quad (37)$$

where f is the contribution of the execution errors to the performance index:

$$f = E(\bar{\eta}' W \bar{\eta}) = E(\bar{\epsilon}' X_u' W X_u \bar{\epsilon}) = E(\bar{s}' B' X_u' W X_u B \bar{s}) \quad (38)$$

and is called the stochastic dispersion factor.

Let

$$W_j = B' X_u' W X_u B, \quad (2 \times 2) \quad (39)$$

and assume that the random variables s and p are independent of each other:

$$E[s \cdot p] = 0 \quad (40)$$

Then f is reduced to

$$f = \sigma_s^2 W_{j_{11}} + \sigma_p^2 W_{j_{22}} \quad (41)$$

To minimize the performance index J with respect to $\Delta \bar{u}$, it is differentiated by \bar{u} and equated to zero, using the first-order approximation to \bar{x}_1 :

$$0 \cong \left(\frac{\partial \bar{x}}{\partial \bar{u}} \right)' W \left(\bar{x}_0 + \frac{\partial \bar{x}}{\partial \bar{u}} \delta \bar{u} - \bar{x}_d \right) + \bar{g} \quad (42)$$

where \bar{g} is the column portion of $\partial f / \partial \bar{u}$. The solution of this becomes

$$\delta \bar{u} = - (X_u' W X_u)^{-1} [X_u' W (\bar{x}_0 - \bar{x}_d) + \bar{g}] \quad (43)$$

To begin with, the true anomaly is fixed at θ_{0i} , $i = 1, 2, \dots, N$, along the initial orbit. Then, $\delta \bar{u}$ is evaluated at \bar{x}_0 and \bar{u}_0 , which are the state and the velocity vectors before any correction, and is denoted by $\delta \bar{u}(1)$. A new velocity vector $\bar{u}_0(1)$ is computed by

$$\bar{u}_0(1) = \bar{u}_0 + \delta \bar{u}(1) \quad (44)$$

Also, a new state vector $\bar{x}_0(1)$ and the true anomaly $\theta_{0i}(1)$ are computed by means of Eqs. (9)–(14).

It should be noted that this $\delta \bar{u}(1)$ is not the optimal control to be carried out, but is only an initial guess. Having these updated parameters $\bar{x}_0(1)$, $\bar{u}_0(1)$, and $\theta_{0i}(1)$, the next fraction of control $\delta \bar{u}(2)$ is computed by Eq. (43); this is then added to $\bar{u}_0(1)$ to generate $\bar{u}_0(2)$. Thus, the

process is iterated until $\bar{u}_0(i)$ converges to some value \bar{u}_1^* . Hence,

$$\bar{u}_1^* = \bar{u}_0 + \Delta \bar{u}^* \quad (45)$$

with

$$\Delta \bar{u}^* = \sum_{j=1}^m \delta \bar{u}(j) \quad (46)$$

This $\Delta \bar{u}^*$ is the optimal control to be applied at the given true anomaly θ_{0i} , and the resultant orbit \bar{x}_1 and true anomaly θ_{1i} are computed by Eqs. (9)–(14) using the above \bar{u}_1^* .

So far, the constraint on the correction capability has not been considered. In reality, the correction can never exceed the propellant budget c . Therefore, the program computes $\bar{u}_c = [v_c, \alpha]'$ every time the fractional control $\delta \bar{u}(j)$ of Eq. (43), as well as $\Delta \bar{u}(i)$ [the summation of $\delta \bar{u}(j)$], are obtained and verifies whether or not v_c exceeds c . Whenever it does, v_c is fixed at c and the program returns to Eq. (43) to recompute $\delta \bar{u}$. By iterating this process until convergence, the program essentially searches for an optimal direction of maneuver while retaining its magnitude at c (Fig. 21a).

6. General Description of Single-Stage Program

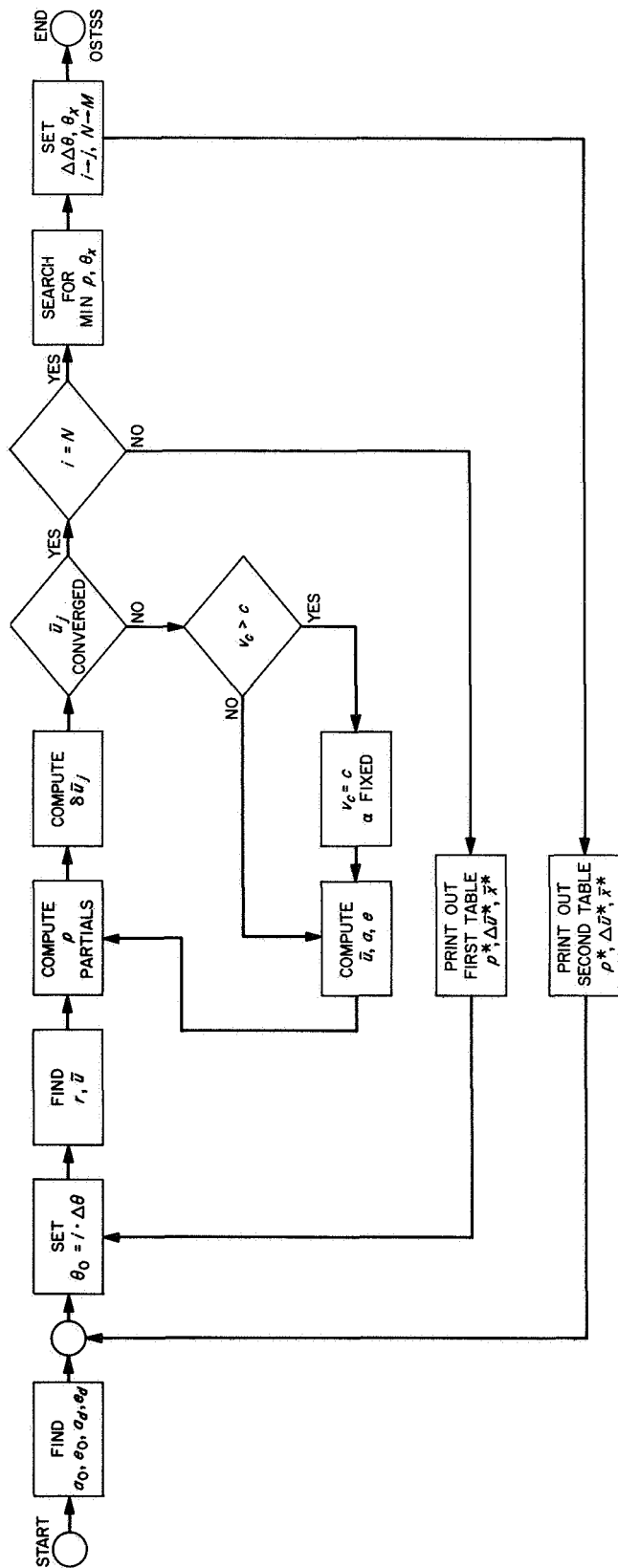
The procedure described in the preceding sections provides the optimal control at a specific location (true anomaly) along the orbit. In order to acquire the overall optimal maneuver, a search program for the minimum performance index along the orbit is formulated. This subroutine essentially constructs two tables, one for a rough mesh of θ_0 and the other for a fine mesh of θ_0 . The first table is a collection of $p_1(\bar{x}_0, \theta_0)$ supplied by the minimization subroutine at the rough-mesh points $\theta_0 = i \cdot \Delta \theta$, $i = 1, 2, \dots, N$, e.g., $\Delta \theta = 10$ deg.

The program searches for the minimum p_1 in the first table and the associated true anomaly θ_x . Then, the second table of a fine-mesh $\Delta \Delta \theta$ (e.g., 1 deg) is obtained around this θ_x within the range of $\pm \Delta \theta$, and the overall minimum point is derived from that table. This process is mathematically described as

$$p_1^*(\bar{x}_0) = \min_{\theta_0} p_1(\bar{x}_0, \theta_0) \quad (47)$$

This program of finding the optimal control through a single maneuver which involves two minimization steps (first by $\Delta \bar{u}_0$, then by θ_0) described by Eqs. (16) and (47) is called the "optimal stochastic transfer single-stage

(a)



(b)

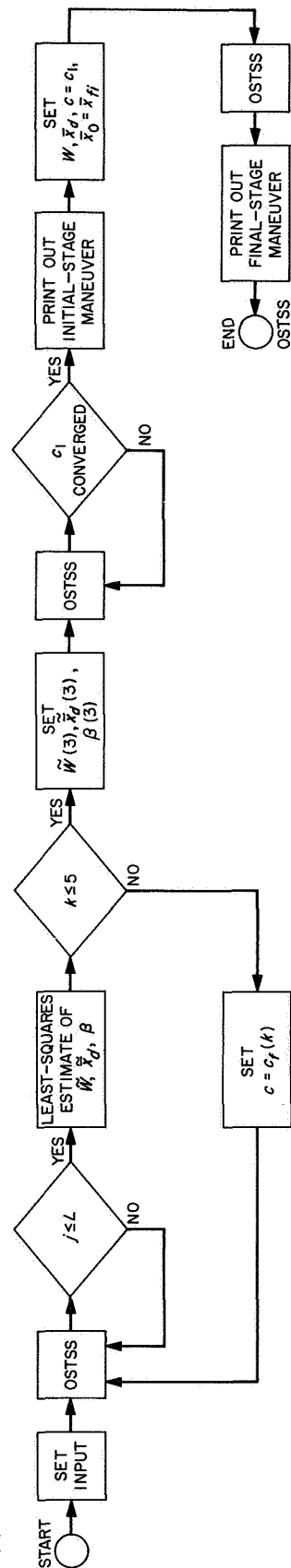


Fig. 21. Optimal stochastic transfer programs: (a) OSTSS program, and (b) OSTTS program

program." A flow chart of the OSTSS program is given in Fig. 21a.

7. Two-Stage Program: Dynamic Programming Formulation

When two maneuvers, $\Delta \bar{u}_0$ and $\Delta \bar{u}_1$, are permitted, the transition of states takes place in the order of

$$\bar{x}_0 \xrightarrow{\Delta \bar{u}_0} -\bar{x}_1 \xrightarrow{\Delta \bar{u}_1} \bar{x}_2$$

The guidance strategy is to minimize the mean-squared distance between the final state \bar{x}_2 and the target state \bar{x}_d .

$$\begin{aligned} p_2^*(\bar{x}_0) &= \min_{\theta_0, \Delta \bar{u}_0, \theta_1, \Delta \bar{u}_1} E[(\bar{x}_2 - \bar{x}_d)' W(\bar{x}_2 - \bar{x}_d)] \\ &= \min_{\theta_0, \Delta \bar{u}_0, \theta_1, \Delta \bar{u}_1} J(\bar{x}_1, \theta_1, \Delta \bar{u}_1) \end{aligned} \quad (48)$$

According to the procedure of the dynamic programming, this is first minimized with respect to $\Delta \bar{u}_1$ and θ_1 (final-stage control). This can be accomplished by means of the single-stage program described above. Then, shifting indices in Eqs. (16) and (47) as $\bar{x}_0 \rightarrow \bar{x}_1$, $\bar{x}_1 \rightarrow \bar{x}_2$, $\Delta \bar{u} \rightarrow \Delta \bar{u}_1$, and $\theta_0 \rightarrow \theta_1$ and combining these two equations yields

$$p_1^*(\bar{x}_1) = \min_{\theta_1, \Delta \bar{u}_1} J(\bar{x}_1, \theta_1, \Delta \bar{u}_1) \quad (49)$$

The basic assumption adopted in the two-stage program is that this $p_1^*(\bar{x}_1)$ may be approximated by a quadratic function of \bar{x}_1 :

$$p_1^*(\bar{x}_1) \simeq (\bar{x}_1 - \tilde{\bar{x}}_d)' \tilde{W}(\bar{x}_1 - \tilde{\bar{x}}_d) + \beta \quad (50)$$

The new weighting matrix \tilde{W} , target vector $\tilde{\bar{x}}_d$, and a constant term β must be determined by some curve-fitting techniques (explained below) after the OSTSS program has been run at the sufficient number of points on the \bar{x}_1 vector space.

Substituting Eq. (50) into Eq. (48) yields, with the aid of Eq. (49),

$$\begin{aligned} p_2^*(\bar{x}_0) &= \min_{\theta_0, \Delta \bar{u}_0} E[p_1^*(\bar{x}_1)] \\ &= \min_{\theta_0, \Delta \bar{u}_0} [(\bar{x}_1 - \tilde{\bar{x}}_d)' \tilde{W}(\bar{x}_1 - \tilde{\bar{x}}_d) + \beta] \end{aligned} \quad (51)$$

It can then be observed that the OSTSS program can be applied to obtain the optimal maneuver $\Delta \bar{u}_0^*$ and true anomaly θ_0^* at the initial stage, because the performance-index function is again quadratic.

This two-stage program is called the "optimal stochastic transfer two-stage program." A flow chart of the OSTTS program is given in Fig. 21b.

8. Least-Squares Curve-Fitting Technique and Fuel Constraint

The least-squares method is employed for fitting a quadratic surface to a collection of points $p_1^*(\bar{x}_1)$ distributed in the three-dimensional space. When the expression of $p_1^*(\bar{x}_1)$ of Eq. (49) is expanded in terms of the elements of vectors and a matrix involved, it may be described as

$$p_1^*(i) = A_i \bar{y} \quad (52)$$

where A_i is a (1×10) -row vector consisting of second- and first-order terms of $\bar{x}_1(i)$, $i = 1, 2, 3$, plus a constant term, and \bar{y} is a (10×1) -column vector whose first six elements are equal to the elements of the \tilde{W} matrix to be identified; the remaining four elements are used to determine the $\tilde{\bar{x}}_d$ vector and β with the aid of the first six elements.

If L points on the \bar{x}_1 vector ($i = 1, 2, \dots, L$) space are picked up for the OSTSS program input to yield the corresponding L points of p_1^* ($i = 1, 2, \dots, L$) and form an L vector \bar{p}_1^* , the latter vector is expressed as

$$\bar{p}_1^* = A \bar{y} \quad (53)$$

where A is an $(L \times 10)$ matrix having the above A_i , $i = 1, 2, \dots, L$, as its rows. Then the least-squares estimate of \bar{y} is obtained as, when $L \geq 10$,

$$\hat{\bar{y}} = (A'A)^{-1} A' \bar{p}_1^* \quad (54)$$

From this estimate $\hat{\bar{y}}$, the performance-index parameters \tilde{W} , $\tilde{\bar{x}}_d$, and β can be determined uniquely. In the actual program, certain normalization is introduced in order to evade numerical problems of matrix inversion.

As for correction capability, initially five levels of propellant budget $c_f(k)$, $k = 1, \dots, 5$, which are separated by intervals Δc , are assigned to the final-stage maneuver. Then, for every $c_f(k)$, the performance-index parameters \tilde{W} , $\tilde{\bar{x}}_d$, and β are computed following the procedure described in the preceding sections and are tabulated. At first, the OSTSS program finds the optimal control $\bar{u}_{c0} = (v_{c0}, \alpha_0)'$, using the medium values $\tilde{W}(3)$, $\tilde{\bar{x}}_d(3)$, and $\beta(3)$ of the performance-index parameters. It then

computes the remaining fuel c_1 by subtracting v_{e0} from the initial budget c :

$$c_1 = c - v_{e0} \quad (55)$$

By means of linear interpolation, new performance-index parameters are now computed. If it is supposed that c_1 falls between $c_f(k)$ and $c_f(k+1)$, then

$$\tilde{W}(c_1) = \tilde{W}(k) + [\tilde{W}(k+1) - \tilde{W}(k)] \cdot \frac{c_1 - c_f(k)}{\Delta c} \quad (56)$$

Similar relationships hold for \tilde{x}_d , as well as for β . When c_1 hits outside the range covered by $c_f(k)$, the program is capable of extrapolating these parameters on both sides by the amount Δc . Beyond that, they are fixed at the extreme values, namely, the values at either $c_f(1) - \Delta c$ or $c_f(5) + \Delta c$, because an excessive extrapolation is not dependable. Actually, in such cases where c_1 hits outside the above range, the initial assignment of $c_f(k)$ should be modified so that c_1 comes inside the range.

Through the use of this new $\tilde{W}(c_1)$ computed by Eq. (56) as well as $\tilde{x}_d(c_1)$ similarly obtained, v_{e0} and c_1 are furnished by the OSTSS program. The process is then iterated until it converges.

9. Status of Development

Two computer programs, OSTSS and OSTTS, aimed at numerical solutions of stochastic orbit-transfer problems with the aid of the dynamic programming technique have been described. Since emphasis was placed on the description of the analytical aspects of these programs, no experimental results were reported here. Currently, the OSTSS program is performing satisfactorily, but the OSTTS program requires some modifications. An extension of the program to an insertion maneuver, making a three-stage program, is under consideration. The further progress in developing this program, as well as experimental results using the OSTSS and OSTTS programs (especially the latter), will be reported in a future article in the SPS, Vol. II.

H. Navigation Technology: Continuous Estimation of the State of a Distant Spacecraft During a Single Pass of Data, J. F. Jordan

1. Introduction

In recent months, some effort has been devoted to determining a data compression scheme to represent,

with estimates of a few parameters, the information content of a single pass of earth-based doppler data. Hamilton and Melbourne (SPS 37-39, Vol. III, pp. 18-23) have compressed the content of a single pass into estimates of three parameters related to the spacecraft geocentric range rate, its right ascension, and its declination. In their analysis, it was assumed that the observed space probe moves directly away from the center of the earth, and, therefore, any effects that lateral velocities might have on the accuracies of the estimates were neglected. Curkendall (SPS 37-47, Vol. II, pp. 15-21) has added the effects of lateral velocities to the Hamilton-Melbourne compression scheme, thereby increasing the number of estimated parameters to five, since the two components of lateral velocity can also be estimated.

This article presents the results of applying the CEP (SPS 37-48, Vol. II, pp. 23-27) to the problem of estimating the state of a distant probe from a 12-h pass of data. The advantages of using the CEP for this problem are: (1) the time histories of the estimation accuracies can be observed during the pass itself, and (2) the variations of the accuracies with the probe declination can easily be seen. In addition, the CEP can compute navigational accuracies for a probe subject to a stochastic forcing function. The results presented here for the case when this function is zero will serve as a basis of comparison for a study, to be published subsequently, which considers the effects of process noise.

It should be noted that the coordinate system in which the results of the CEP are presented is cartesian and is not exactly equivalent to the polar system used by Hamilton and Melbourne or Curkendall. Also, the CEP obtains the accuracy of estimates of the instantaneous time-varying state of the probe, rather than the accuracy of the state at some epoch. Nevertheless, the results presented here are similar in some cases to those of Hamilton-Melbourne and Curkendall, and comparisons between their results and those presented here will be made when appropriate.

2. Problem Geometry

Consider a tracking station located on the earth's equator observing a distant space probe traveling with constant geocentric velocity. The probe state and station location can be specified in the coordinate system illustrated in Fig. 22 with the following definitions:

$$\left. \begin{array}{l} x \\ y \\ z \end{array} \right\} \text{geocentric position components of probe}$$

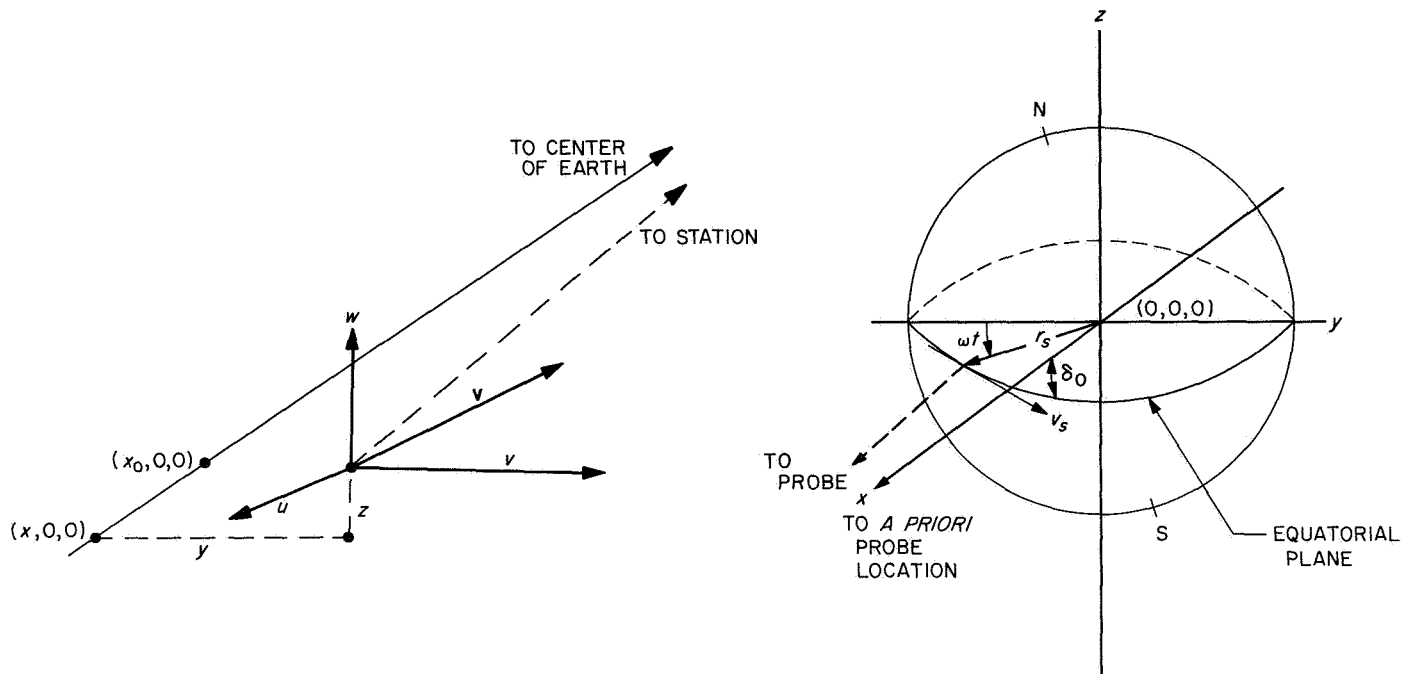


Fig. 22. Problem geometry

$$\left. \begin{array}{l} u = \dot{x} \\ v = \dot{y} \\ w = \dot{z} \end{array} \right\} \text{geocentric velocity components of probe}$$

$$\left. \begin{array}{l} x_s \\ y_s \\ z_s \end{array} \right\} \text{geocentric position components of station}$$

$$\left. \begin{array}{l} u_s = \dot{x}_s \\ v_s = \dot{y}_s \\ w_s = \dot{z}_s \end{array} \right\} \text{geocentric velocity components of station}$$

It should be noted that the x -axis of the coordinate system extends from the center of the earth through the *a priori* position of the probe at the beginning of the pass, a known direction. The y -axis is perpendicular to the x -axis and lies on the equatorial plane, and the z -axis completes the right-handed system.

The station position and velocity during the pass can be expressed in terms of geophysical constants by

$$\left. \begin{array}{l} x_s = r_s \cos \delta_0 \sin \omega t \\ u_s = \omega r_s \cos \delta_0 \cos \omega t \\ y_s = -r_s \cos \delta_0 \\ v_s = \omega r_s \sin \omega t \\ z_s = -r_s \sin \delta_0 \\ w_s = -\omega r_s \sin \delta_0 \cos \omega t \end{array} \right\} \quad (1)$$

where

t = time measured from the beginning of the pass

ω = angular velocity of the earth

δ_0 = *a priori* geocentric declination of probe

r_s = equatorial radius of the earth

The observational data type obtained by the station is counted doppler, or integrated range rate, contaminated by gaussian exponentially correlated noise. Hence, the observable $\phi(t)$ can be expressed as

$$\phi(t) = \int_0^t \dot{\rho}(\tau) d\tau + \eta(t) \quad (2)$$

where the station-probe range is related to the probe state by

$$\rho^2 = (x - x_s)^2 + (y - y_s)^2 + (z - z_s)^2 \quad (3)$$

and $\eta(t)$ has the following properties:

$$\left. \begin{array}{l} E[\eta(t)] = 0 \\ E[\eta(t_1)\eta(t_2)] = (\sigma_\eta^2)^{-(1/\tau)} |t_2 - t_1| \\ \dot{\eta}(t) = -\frac{1}{\tau} \eta(t) + w(t) \end{array} \right\} \quad (4)$$

with

σ_η^2 = the variance of $\eta(t)$

τ = the correlation time

$w(t)$ = white noise with autocorrelation coefficient $2\sigma_\eta^2/\tau$

The information content of the data is unchanged if the derivative of the counted doppler is regarded as the observable. Using Eq. (4), this derivative is

$$\dot{\phi}(t) = \dot{\rho}(t) - \frac{1}{\tau} \eta(t) + w(t) \quad (5)$$

Thus, the observable can be thought of as the station-probe range rate contaminated by exponentially correlated noise, which can be estimated, and white noise.

The analytical expression for the station-probe range can be differentiated to obtain the range rate:

$$\begin{aligned} \dot{\rho} = & \frac{x - x_s}{\rho} \frac{d}{dt} (x - x_s) + \frac{y - y_s}{\rho} \frac{d}{dt} (y - y_s) \\ & + \frac{z - z_s}{\rho} \frac{d}{dt} (z - z_s) \end{aligned} \quad (6)$$

Letting $r = x - x_s$ and noting that ρ is extremely large compared with y , z , y_s , and z_s , ρ in the denominator of the above expression can be approximated with r . Thus, Eq. (6) can be written as

$$\rho = u - u_s + \frac{y - y_s}{r} (v - v_s) + \frac{z - z_s}{r} (w - w_s) \quad (7)$$

The partials of $\dot{\rho}$ with respect to the probe state parameters are as follows:

$$\left. \begin{aligned} \frac{\partial \dot{\rho}}{\partial x} &= -\frac{(y - y_s)(v - v_s)}{r^2} - \frac{(z - z_s)(w - w_s)}{r^2} \approx 0 \\ \frac{\partial \dot{\rho}}{\partial u} &= 1 \\ \frac{\partial \dot{\rho}}{\partial y} &= \frac{v - v_s}{r} \\ \frac{\partial \dot{\rho}}{\partial v} &= \frac{y - y_s}{r} \\ \frac{\partial \dot{\rho}}{\partial z} &= \frac{w - w_s}{r} \\ \frac{\partial \dot{\rho}}{\partial w} &= \frac{z - z_s}{r} \end{aligned} \right\} \quad (8)$$

It is seen from the partials that the primary parameter that can be estimated is u , the velocity component along the *a priori* earth-probe line. There is also a secondary estimation capability for the lateral velocities v and w and the lateral positions y and z . The range x cannot be effectively estimated. It should be noted that the partials with respect to the lateral positions y and z depend upon the lateral velocities of the probe and station. These are the so-called "velocity parallax" terms, which make possible the estimation of the lateral position of the probe. The partials with respect to the lateral velocities v and w depend upon the lateral position components of the probe and station. These are "position parallax" terms, which make possible the estimation of the lateral velocity components of the probe state.

3. Covariance Matrix of Errors in the State Estimates

The accuracy to which the state components of the probe can be estimated is expressed in terms of the covariance matrix of the errors in the estimates. This covariance matrix can be written as

$$\Lambda = E \begin{bmatrix} (u - \hat{u})^2 & (u - \hat{u})(v - \hat{v}) & . & . & . \\ (v - \hat{v})(u - \hat{u}) & (v - \hat{v})^2 & . & . & . \\ . & . & (w - \hat{w})^2 & . & . \\ . & . & (x - \hat{x})^2 & . & . \\ . & . & (y - \hat{y})^2 & . & . \\ . & . & . & (z - \hat{z})^2 & . \end{bmatrix} \quad (9)$$

where $\hat{\cdot}$ denotes the minimum-variance estimate. The square roots of the diagonal terms of the covariance matrix are taken as the rms accuracies of the individual state components. These terms can be stated as

$$\left. \begin{aligned} \sigma_x &= [E[x - \hat{x}]^2]^{1/2} \\ \sigma_u &= [E[u - \hat{u}]^2]^{1/2} \\ \sigma_y &= [E[y - \hat{y}]^2]^{1/2} \\ \sigma_v &= [E[v - \hat{v}]^2]^{1/2} \\ \sigma_z &= [E[z - \hat{z}]^2]^{1/2} \\ \sigma_w &= [E[w - \hat{w}]^2]^{1/2} \end{aligned} \right\} \quad (10)$$

In the original formulation of the CEP, the covariance matrix was obtained as a solution to the following matrix Riccati differential equation:

$$\dot{\Lambda} = F\Lambda + \Lambda F^T - \Lambda G\Lambda + H \quad (11)$$

(SPS 37-48, Vol. II, pp. 23-27). It has been found convenient, for numerical reasons, to deal with the inverse

of the covariance matrix in the program. This inverse matrix obeys the following equation:

$$\frac{d}{dt}(\Lambda^{-1}) = (-F^T)\Lambda^{-1} + \Lambda^{-1}(-F) - \Lambda^{-1}H\Lambda^{-1} + G \quad (12)$$

which is also Riccati in form.

Theoretically, the inverse of the covariance matrix can be integrated over the time of a complete pass with the initial condition $\Lambda^{-1}(0) = 0$, and the matrix solution can then be inverted to yield the covariance matrix and sigmas specifying the information content of the pass. For numerical reasons, however, the following *a priori* sigmas have been used as input to the program:

$$\left. \begin{aligned} \sigma_{u_0} &= \sigma_{v_0} = \sigma_{w_0} = 1 \text{ km/s} \\ \sigma_{x_0} &= \sigma_{y_0} = \sigma_{z_0} = 10^6 \text{ km} \end{aligned} \right\} \quad (13)$$

These *a priori* values of the probe state accuracies are sufficiently large so as not to affect the final sigmas

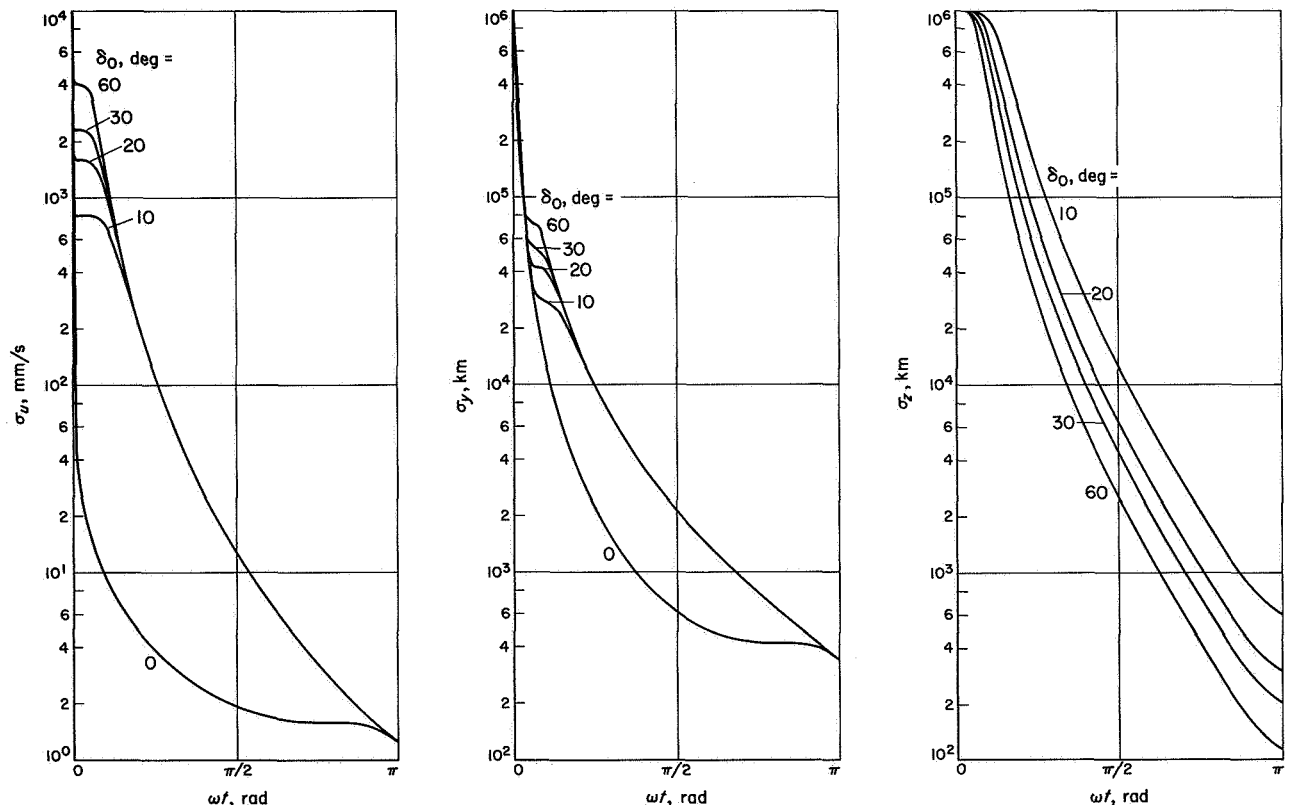


Fig. 23. Probe state accuracy time histories for three-parameter model: $\sigma_\eta = 10$ m

significantly, while, at the same time, the program has experienced few numerical problems.

4. Results of the Three-Parameter Model

For the three-parameter model presented here, the effects of uncertainties in the lateral velocities will be neglected, and the space probe being observed will be restricted to travel directly away from the center of the earth. The observable partial derivatives with respect to the parameters to be estimated become, for this case,

$$\left. \begin{aligned} \frac{\partial \dot{\rho}}{\partial u} &= 1 \\ \frac{\partial \dot{\rho}}{\partial y} &= -\frac{\omega r_s}{r} \sin \omega t \\ \frac{\partial \dot{\rho}}{\partial z} &= \frac{\omega r_s \sin \delta_0}{r} \cos \omega t \end{aligned} \right\} \quad (14)$$

The primary parameter being estimated is u , with y and z also being estimated with the aid of the velocity parallax terms in the two latter partials of Eq. (14).

The time histories of σ_u , σ_y , and σ_z are given in Figs. 23 and 24 for observations with *a priori* data-noise standard-deviation $\sigma_\eta = 10$ m and 1 m, respectively. The observed probe is at a distance of 10^8 km from the earth, and the correlation time of the data noise has been taken to be 1000 s, which is of the same order of magnitude as the round-trip light travel time between the earth and the probe.

In both the 10- and 1-m data cases, the curves for σ_u and σ_y show variation with different values of the declination δ_0 during the pass time interval, with convergence of the curves at the end of the pass. This effect is primarily due to the odd nature of the function $\cos \omega t$ over the span $0 < \omega t < \pi$. In effect, this says that, no matter what the probe declination is, the observing station begins and ends each pass on the y -axis. The curves for σ_z show extreme variation to δ_0 due to the term $\sin \delta_0$ in the partial with respect to z .

It should be noted that the parameters estimated here can be converted into the polar coordinate system used by

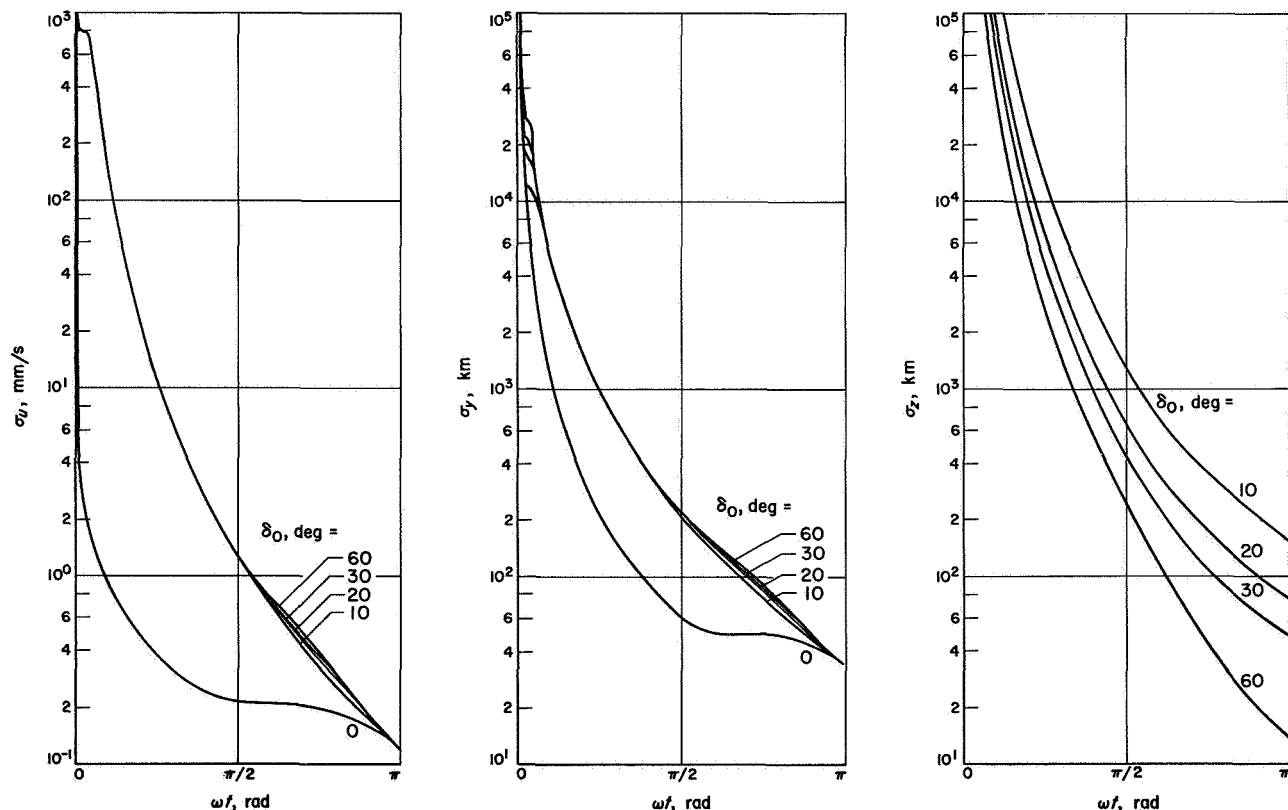


Fig. 24. Probe state accuracy time histories for three-parameter model: $\sigma_\eta = 1$ m

Hamilton and Melbourne by the following substitution:

$$\left. \begin{aligned} u &= \dot{r} \\ y &= r \cos \delta_0 \Delta\alpha \\ z &= r \Delta\delta \end{aligned} \right\} \quad (15)$$

For the 1-m data case when $\delta_0 = 30$ deg, the following approximate values for $\sigma_{\dot{r}}$, σ_{α} , and σ_{δ} are found:

$$\left. \begin{aligned} \sigma_{\dot{r}} &\approx 0.1 \frac{\text{mm}}{\text{s}} \\ \sigma_{\alpha} &\approx \frac{0.35 \times 10^5 \text{m}}{r \cos \delta_0} \approx 3.5 \times 10^{-7} \text{ rad} \\ \sigma_{\delta} &\approx \frac{0.5 \times 10^5 \text{m}}{r} \approx 5.0 \times 10^{-7} \text{ rad} \end{aligned} \right\} \quad (16)$$

These values are seen to correspond closely to the values given by Hamilton and Melbourne in their SPS article.

5. Results of the Five-Parameter Model

For the five-parameter model presented here, the effects of uncertainties in the lateral velocities will be included in the analysis, but the *a priori* velocity of the probe will still be directed along the earth-probe line. The partial derivatives of the observable $\dot{\rho}$ with respect to the parameters which can be estimated are

$$\left. \begin{aligned} \frac{\partial \dot{\rho}}{\partial u} &= 1 \\ \frac{\partial \dot{\rho}}{\partial v} &= \frac{r_s \cos \omega t}{r} \\ \frac{\partial \dot{\rho}}{\partial w} &= \frac{r_s \sin \delta_0 \sin \omega t}{r} \\ \frac{\partial \dot{\rho}}{\partial y} &= -\frac{\omega r_s \sin \omega t}{r} \\ \frac{\partial \dot{\rho}}{\partial z} &= \frac{\omega r_s \sin \delta_0 \cos \omega t}{r} \end{aligned} \right\} \quad (17)$$

The primary parameter being estimated is u , with velocity parallax terms facilitating the estimation of y and z , and position parallax terms making possible the estimation of v and w .

The time histories of σ_u , σ_v , σ_w , σ_y , and σ_z are given in Figs. 25 and 26 for 10-m and 1-m data, respectively. It is seen in these figures that the convergence of the sigmas for different probe declinations does not occur at $\omega t = \pi$, as it does in the three-parameter case. This is due primarily to the feeding of the lateral position uncertainties by the lateral velocity uncertainties during the time in which data is taken. It is also seen that the accuracies in the estimates of u , v , and y are best when the probe is near the equatorial plane, but that w and z are virtually unobservable if the probe is in this region.

It should be noted that the five parameters estimated here do not correspond to the five estimated parameters of Curkendall's model. There is, however, a close similarity between the two sets of parameters, and, in fact, the parameters estimated here can be related to a set of polar variables as follows:

$$\left. \begin{aligned} u &= \dot{r} \\ y &= r \cos \delta_0 \Delta\alpha \\ z &= r \Delta\delta \\ v &\approx r \cos \delta_0 \dot{\alpha} \\ w &\approx r \dot{\delta} \end{aligned} \right\} \quad (18)$$

Using these transformations, the following sigmas are obtained for a 12-h pass with 1-m data when the declination of the probe is 30 deg:

$$\left. \begin{aligned} \sigma_{\dot{r}} &= 2.6 \frac{\text{mm}}{\text{s}} \\ \sigma_v &= 7 \frac{\text{m}}{\text{s}} \\ \sigma_w &= 70 \frac{\text{m}}{\text{s}} \\ \sigma_{\alpha} &= 1.3 \times 10^{-5} \text{ rad} \\ \sigma_{\delta} &= 1.5 \times 10^{-5} \text{ rad} \\ \sigma_{\dot{\alpha}} &= 8.1 \times 10^{-11} \text{ rad/s} \\ \sigma_{\dot{\delta}} &= 7 \times 10^{-10} \text{ rad/s} \end{aligned} \right\} \quad (19)$$

It is seen from a comparison of the accuracies of the five-parameter models and those of the three-parameter models that the inclusion of lateral velocity uncertainties causes a degradation in the estimates of \dot{r} , α , and δ by a factor of about 40.

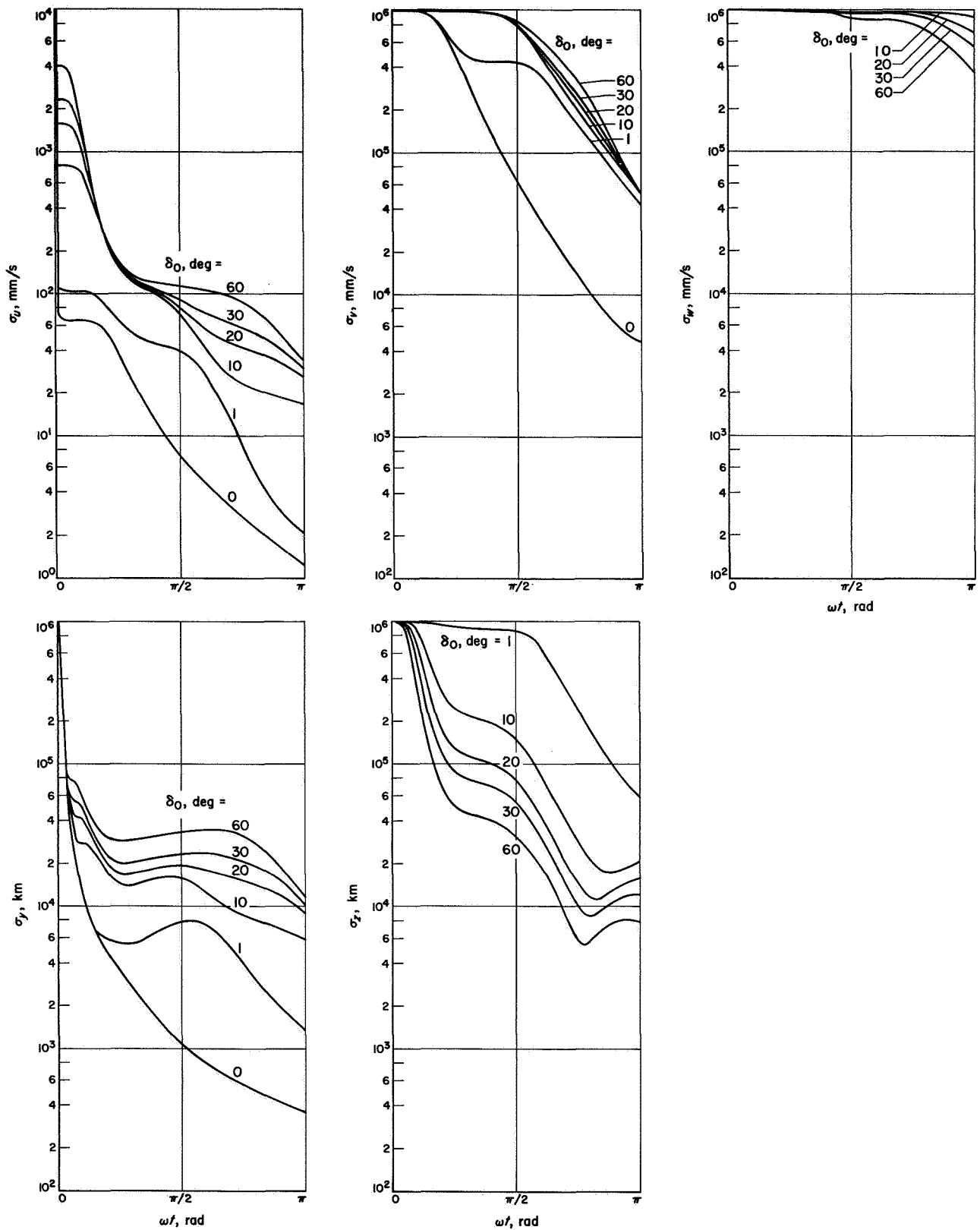


Fig. 25. Probe state accuracy time histories for five-parameter model: $\sigma_\eta = 10$ m

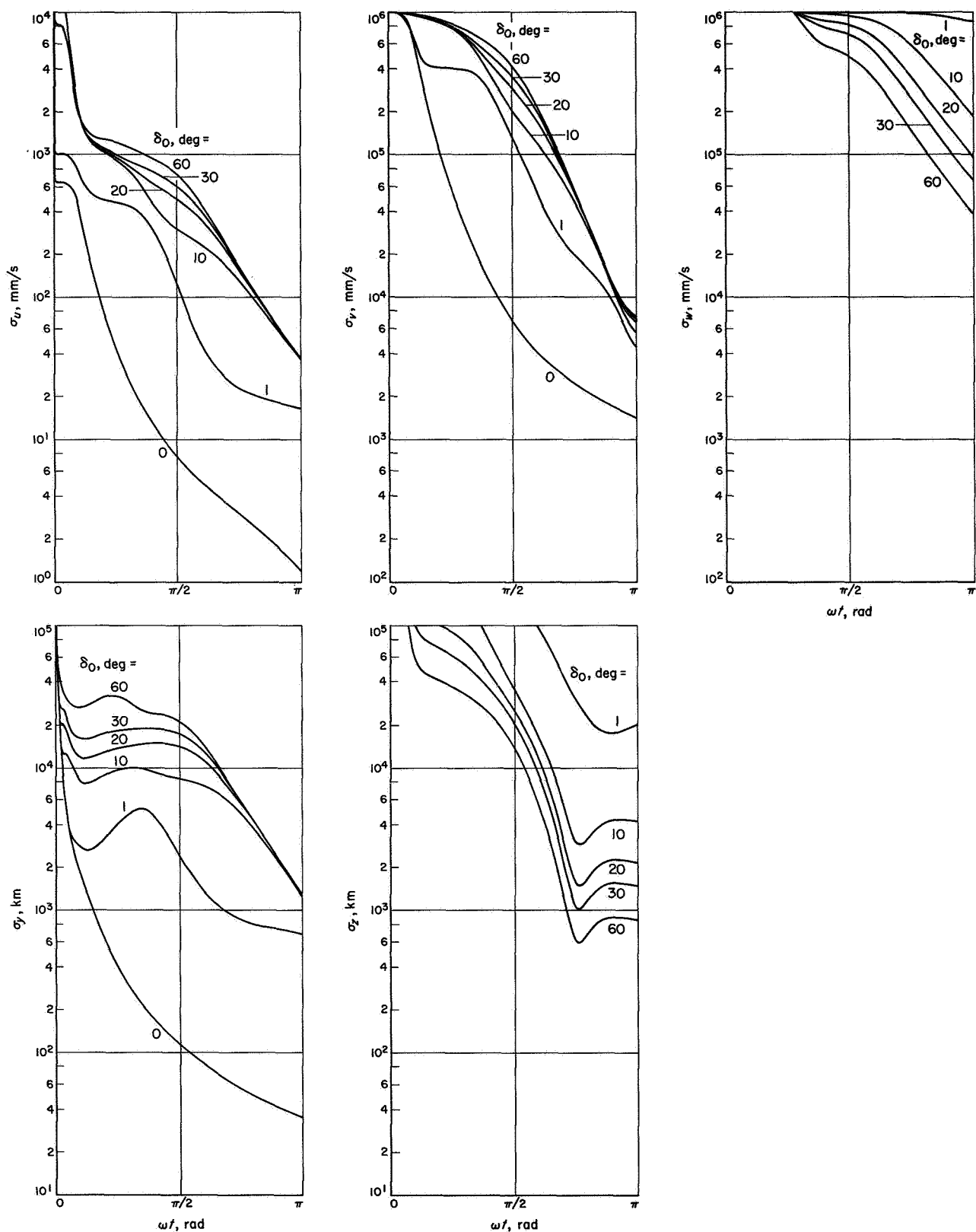


Fig. 26. Probe state accuracy time histories for five-parameter model: $\sigma_\eta = 1$ m

6. Effects of Large Lateral Velocities

In the results presented thus far, the space probe being tracked has been assumed to be traveling more or less directly away from the center of the earth, since, although there have been large uncertainties in the components of lateral velocity, the *a priori* values are zero. If the probe is thought to have non-zero lateral velocity components v_0 and w_0 before data is taken, the partials of $\dot{\rho}$ with respect to the parameters to be estimated become:

$$\left. \begin{aligned} \frac{\partial \dot{\rho}}{\partial u} &= 1 \\ \frac{\partial \dot{\rho}}{\partial v} &= \frac{v_0 t + r_s \cos \omega t}{r} \\ \frac{\partial \dot{\rho}}{\partial w} &= \frac{w_0 t + r_s \sin \delta_0 \sin \omega t}{r} \\ \frac{\partial \dot{\rho}}{\partial y} &= \frac{v_0 - \omega r_s \sin \omega t}{r} \\ \frac{\partial \dot{\rho}}{\partial z} &= \frac{w_0 + \omega r_s \sin \delta_0 \cos \omega t}{r} \end{aligned} \right\} \quad (20)$$

It has been found that the parameters whose accuracy is significantly affected by the inclusion of non-zero *a priori* lateral velocities are the range rate, u , and the component of lateral velocity in the ecliptic plane, v . The accuracies of the other state variables are not significantly affected.

Figure 27 illustrates the effects of a lateral velocity component in the ecliptic plane on σ_u and σ_v . Curves are presented for $v_0 = 0, 10$, and 20 km/s. It is also interesting to note the effects of a single 1-m ranging point at the beginning of the pass on the accuracies of the estimates when lateral velocities are present. The dashed curves in Fig. 27 yield the accuracy time histories when a single ranging point is included in the data. It is seen that σ_u is degraded by the lateral velocities $v_0 = 10$ and 20 km/s by about two orders of magnitude, and that the inclusion of a ranging point does not significantly aid the range-rate estimates. In the case of σ_v , the degradation by the lateral velocities is about one order of magnitude. However, the inclusion of a ranging point in the data decreases σ_v to approximately 1 cm/s. Thus, it is seen that the inclusion of a ranging point significantly aids the estimation of v if v_0 is non-zero.

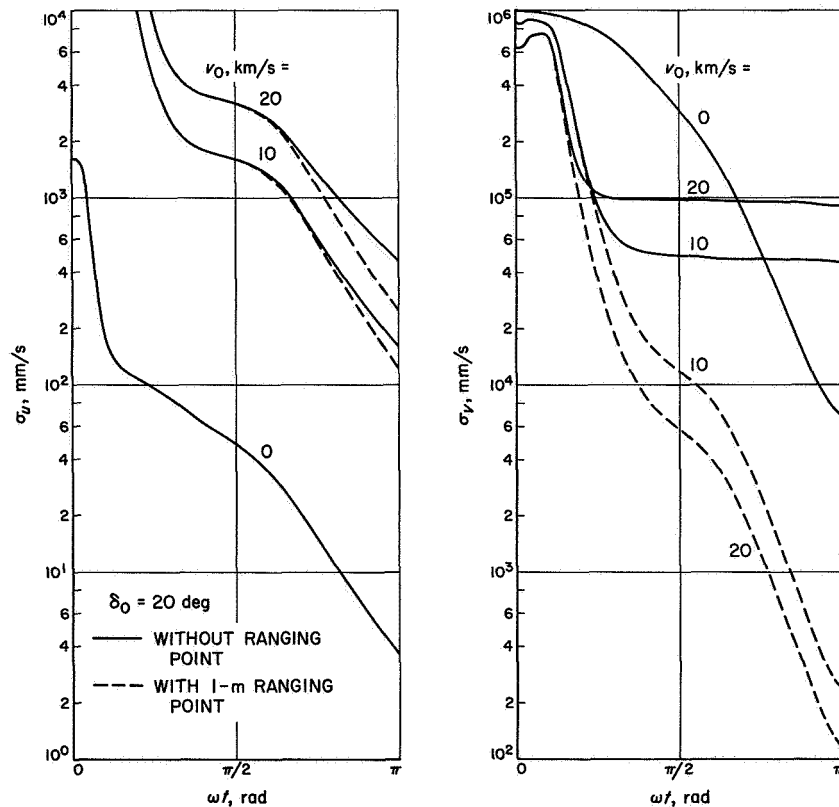


Fig. 27. Effects of lateral velocity component in the ecliptic plane on σ_u and σ_v : $\sigma_\eta = 1$ m

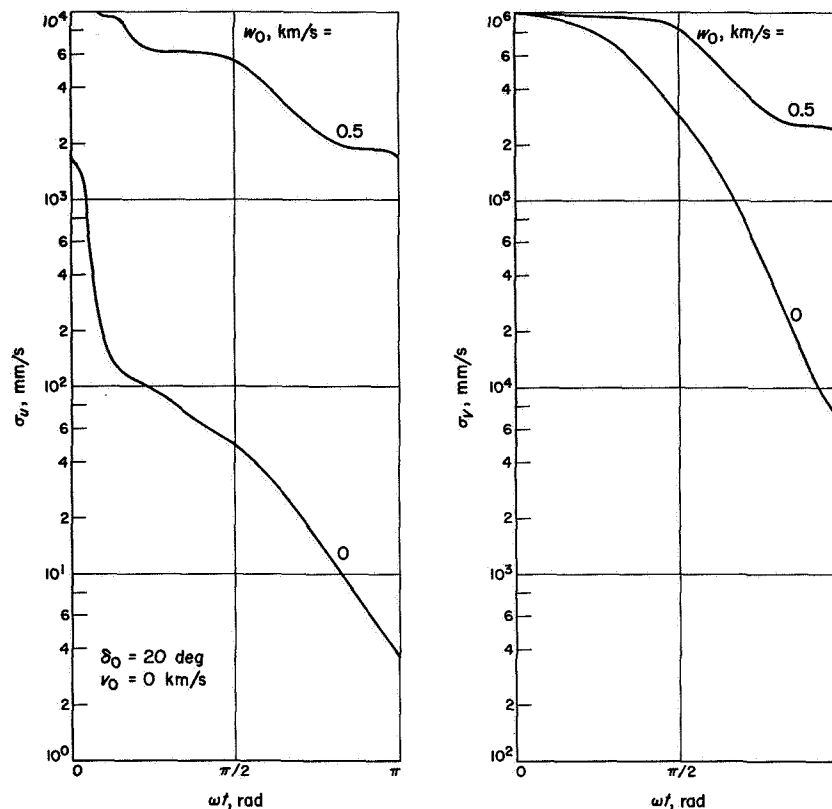


Fig. 28. Effects of lateral velocity component perpendicular to the ecliptic plane on σ_u and σ_v ; $\sigma_\eta = 1$ m

Figure 28 illustrates the effects of a lateral velocity component perpendicular to a line in the ecliptic plane. Curves are shown for $w_0 = 0$ and 0.5 km/s; $v_0 = 0$ for this case. By the presence of a non-zero w_0 , σ_u is seen to be degraded by almost three orders of magnitude and σ_v by almost two orders of magnitude. Ranging data does not aid the estimates.

It can be concluded that: (1) the presence of large lateral velocities seriously degrades the accuracy of the estimates of u and v , but (2) if $v_0 \neq 0$, the inclusion of a ranging point greatly increases the power of the position parallax effect, which aids in estimating v .

I. Double-Precision Trajectory Program:

DPTRAJ, A. R. Khatib

1. Introduction

The increasingly complex nature of current and future space missions has led to the need for extended capabilities and generality of the spacecraft trajectory computations, coupled with the need for modeling and calculation

accuracies to match those of current and predicted tracking accuracies of the DSN. In response to these requirements, a double-precision trajectory program called DPTRAJ has been developed. The initial (Phase I) version of the program is now being used for production computer runs.

General guidelines used in the development of DPTRAJ were:

- (1) General models and methods reflecting the advanced state-of-the-art should be introduced to replace or complement existing models in the single-precision trajectory program (Ref. 1).
- (2) Separability of functions should exist to allow phase 1 of the development to be established on a sound logical structure that will permit straightforward evolution through the follow-on phases.
- (3) Double-precision arithmetic should be used consistently in all computations.
- (4) DPTRAJ should be an integral part of the DPODP (SPS 37-38, Vol. III, pp. 24-26).

2. General Description

DPTRAJ is a four-link program written in Fortran IV language for the IBM 7094 (DCOS). Its main functions are to perform a transformation of coordinate systems, write an integrated spacecraft ephemeris, and display trajectory information. The four links are:

- (1) ODINA, an input organizer that sets up and arranges parameters, constraints, and options to be utilized in the program.
- (2) TRIC, the coordinate transformation link.
- (3) PATH, the trajectory calculator link.
- (4) POST, the output processor link.

Each link, or portions thereof, can be extended for special usage in other programs.

a. Fundamental reference system. The desirability of a truly inertial coordinate system enabling all computations to be carried out uniformly and efficiently, coupled with the availability of lunar and planetary ephemerides in the same system, prompted the use of the rectangular coordinate system referenced to the mean equinox and equator of 1950.0. In addition, the need for a uniform invariable time system to be the independent variable in the equations of motion predicated the use of ET as the fundamental time system for the probe ephemeris and the tabulation of the planetary and lunar ephemerides. Routines are coded for conversion from or to any other time system necessitated by the different input or output data types, which include: UT1, necessary to compute space-fixed positions of the tracking stations, and UTC, the standard broadcast time reference. The above time systems are transformed to ET, using atomic time (A.1) as an intermediary because of its semi-uniform properties. (A discussion of these time systems is given in SPS 37-39, Vol. III, pp. 36-38.)

b. Equations of motion. The Newtonian acceleration of a probe (P) referenced to the central body i (where i is any of the planets, the sun, or the moon) is:

$$\ddot{\mathbf{r}}_{ip} = -u_i \frac{\mathbf{r}_{ip}}{r_{ip}^3} - \sum_{j \neq i} u_j \left(\frac{\mathbf{r}_{ip} - \mathbf{r}_{ij}}{|\mathbf{r}_{ip} - \mathbf{r}_{ij}|^3} + \frac{\mathbf{r}_{ij}}{r_{ij}^3} \right) + \ddot{\mathbf{r}}_{ip}(\text{OBL, IND}) + \ddot{\mathbf{r}}_{ip}(\text{SP, AC, Pf})$$

where the first two terms are the central two-body and n -body perturbative accelerations, respectively, and

u_k = gravitational coefficient for body k

$\ddot{\mathbf{r}}(\text{OBL, IND})$ = direct and indirect perturbative accelerations due to the oblateness of the planets; computed from the generalized potential function expressed in terms of Legendre's polynomials and associated functions

$\ddot{\mathbf{r}}(\text{SP, AC, Pf})$ = accelerations due to solar pressure, low-thrust (control-jet leakages), and high-thrust (powered flight); computed from polynomials which express these forces in the proper orientation

(A discussion of the mathematical model is presented in SPS 37-41, Vol. III, pp. 24-31.)

c. The integrator. The integrator portion of DPTRAJ utilizes a modified Cowell-Adams method of numerical integration of the probe's total acceleration. A brief description of that method follows:

Let h be the step size and ∇ the backward difference operator. Also, let the difference line of $\ddot{\mathbf{X}}_K$ at t_n spanning the interval $(t_n - mh) \leq t \leq t_n$ (where m is the highest order of difference to be retained) be represented by the array

$$D_{t_n, h} = [\nabla^{-i} \ddot{\mathbf{X}}_K(t_n)], \quad i = -2, \dots, m$$

One can compute $\ddot{\mathbf{X}}_K(t1)$ by interpolation:

$$\ddot{\mathbf{X}}_K(t+sh) = \sum_{i=0}^m \beta_i(s) \nabla^{i-1} \ddot{\mathbf{X}}_K(t), \quad -m \leq s \leq 0$$

$\mathbf{X}_K(t1), \dot{\mathbf{X}}_K(t1)$ by integration:

$$\mathbf{X}_K(t+sh) = h^2 \sum_{i=0}^{m+2} \beta_i''(s) \nabla^{i-2} \ddot{\mathbf{X}}_K(t)$$

$$\dot{\mathbf{X}}_K(t+sh) = h \sum_{i=0}^{m+1} \beta_i'(s) \nabla^{i-1} \ddot{\mathbf{X}}_K(t)$$

and jerk $\dddot{\mathbf{X}}_K(t1)$ by differentiation:

$$\dddot{\mathbf{X}}_K(t+sh) = h^{-1} \sum_{i=1}^m \dot{\beta}_i(s) \nabla^i \ddot{\mathbf{X}}_K(t)$$

where β'' , β' , β , and $\dot{\beta}$ are coefficients of the integrated polynomials replacing the derivative of the function over the interval.

The procedures may be summarized as follows:

- (1) A procedure for starting or restarting to compute $D_{t_{0+g,h}}$ which utilizes a Taylor series expansion for starting and extrapolation for restarting.
- (2) A procedure for stepping the solution to $D_{t_{n+g,h}}$ from $D_{t_{n,h}}$.
- (3) A procedure for halving the step size, i.e., $D_{t_{n,h/2}}$.
- (4) A procedure for doubling the step size, i.e., $D_{t_{n,2h}}$.
- (5) A reversal procedure for backward integration, i.e., $D_{t_{n-m,-h}}$.
- (6) An automatic step-size control.

(A discussion on the integrator is given in SPS 37-33, Vol. IV, pp. 33-35.)

3. Existing Capabilities

The following capabilities are incorporated in phase 1 of DPTRAJ:

(1) A lock file is incorporated that contains nominal values for most parameters in the program to minimize the input for standard runs, with the capability to override any or all by input.

(2) Initial conditions can be expressed in cartesian, spherical, classical elements, energy asymptote, or pseudo-asymptote coordinates.

(3) Coordinate systems can be expressed in, or transformed to, any of the systems shown in Table 11.

(4) A capability exists to do forward or backward integration and to hold the central body for integration constant throughout the trajectory or allow it to change according to its predominance in the equation of motion. Also, the flexibility is available to vary method (predictor-corrector, predictor only, or pseudo-predictor-corrector, where X, \dot{X} are corrected), step size (supplied step size or automatic step control), order of differences, and error control, all of which affect accuracy and running time.

(5) Trajectory output is tailored to satisfy questions regarding when to start output, what kind of output, at which event, and when to terminate output. Concerning when to start output, the start of output processing is user-controlled at any time along the probe's ephemeris. As for the kind of output, seven print lists are allowed, of which six can be used with the occurrence of specified

Table 11. Coordinate systems used in phase 1 of DPTRAJ

Center	Reference planet	Reference plane				Equinox	
		Mean	True	Equatorial	Orbital	1950.0	Of date
Space-fixed coordinate systems ^a							
Any of the nine planets plus the sun and moon	Earth	✓		✓		✓	
		✓			✓	✓	
		✓		✓			✓
		✓			✓		✓
			✓	✓			✓
			✓		✓		✓
	Mars	✓		✓			✓
		✓			✓		✓
			✓	✓			✓
			✓		✓		✓
	Moon		✓	✓			✓
Body-fixed coordinate systems ^b							
Earth	Earth		✓	✓			✓
Mars	Mars		✓	✓			✓
Moon	Moon		✓	✓			✓

^aSpace-fixed implies that the x-axis is along the ascending node of the orbital plane on the equatorial plane.

^bBody-fixed implies that the x-axis is pointing toward the prime meridian, and the x-y plane is the body's true equator of date.

^aSpace-fixed implies that the x-axis is along the ascending node of the orbital plane on the equatorial plane.

^bBody-fixed implies that the x-axis is pointing toward the prime meridian, and the x-y plane is the body's true equator of date.

output events. Each print list allows the output of information organized under the following groups:

- (a) *Body group*, which includes user-specified ephemeris bodies and trajectory parameters referenced to the plane and epoch specified. A maximum of three body-centered coordinate systems, each with two ephemeris bodies for additional print, is allowed. The parameters include the state vector of the probe and several scalar values such as the probe altitude and shadow parameters.
- (b) *Conic group*, which includes osculating orbital elements and closest approach and impact parameters. In addition, a maximum of four coordinate systems for plane-dependent conic print is allowed.
- (c) *Angle group*, which contains a series of probe position angles referenced to the earth, sun, moon, reference star, and two user-requested bodies.

As to which event, output occurrence is classified under three main categories:

- (a) *Phase output for phase-dependent events.* Seven phase lists are allowed which reflect seven natural changes based on the dominance of an ephemeris body in the equation of motion, or seven artificial phase changes independent of the natural change and whose terminating events are user-controlled. Each phase list specifies output at (1) uniform times and distances, (2) proximity to a specified ephemeris body, and (3) closest approach to the list's physical central body. Any of these events or a natural phase change can serve as a terminating event for the phase list. In addition, events such as geocentric and heliocentric occultations are included.
- (b) *Unique events.* User-specified epochs, distances from ephemeris bodies, start of attitude control, start and end of motor burn, and terminal events are included in this category.
- (c) *Fixed output.* Information on indirect oblateness is an example of fixed output.

Regarding when to terminate output, termination is achieved by the first occurrence of any of the following: closest approach to, or a distance from, a user-specified ephemeris body, a specified epoch, and naturally the end of the spacecraft ephemeris.

(6) Additional features such as the display of optional extra information concerning intermediate steps used in

the transformation of coordinates; options on time formats such as vigesimal representation of an epoch, Julian date, or seconds past a reference Julian date; and the type of time supplied and the type of time requested.

4. Capabilities Planned for Follow-On Phases

As can be seen, phase 1 of DPTRAJ has a wide base that lends itself to future additions and refinement. Some of the desired capabilities planned for follow-on phases are:

- (1) Topocentric coordinates, view period computations and summary, and a landed probe ephemeris capability.
- (2) Search capability for targeting integrated trajectories and parameter study features.
- (3) Introduction of relativity and aerodynamic accelerations to the equations of motion.
- (4) Addition of equator and orbits for all planets and the inclusion of planetary satellites as reference and/or perturbing bodies.
- (5) Introduction of ENCKE and VARIATION-OF-PARAMETER versions of the integrator.

Reference

1. White, R. J., et al., *Space-Single Precision Cowell Trajectory Program*, Technical Memorandum 33-198. Jet Propulsion Laboratory, Pasadena, Calif., Jan. 15, 1965.

III. Communications Engineering and Development

A. Rotating Linear Polarization Modification of the DSS 14 Receiver, G. S. Levy and B. L. Seidel

1. Introduction

Recently, an experiment was conducted at the AAS (DSS 14) to convert the receiving system from circular polarization to rotating linear polarization. Since *Pioneer*-type spacecraft transmit linear polarization, a properly aligned, linearly polarized, receiving antenna is optimum for the ground station. The modification was made in such a manner as to allow the receiving system to be switched between linear and circular polarization with a set of IF relays.

2. Recent Work

On November 1, 1967, a modification was made to the DSIF receiver at DSS 14 to convert the system from circular polarization to rotating linear polarization. It can be shown (Ref. 1) that the sum of RCP and LCP is indeed LP. This was accomplished by connecting the second (back-up) maser to the LCP port on the feed and to an angle channel of the receiver. The other maser was connected to the RCP port and to the reference channel of the receiver. The outputs of the two coherent receiver channels were then combined in a hybrid junction (at the 10-MHz IF) and the sum was injected back into the

reference channel of the receiver. The difference voltage, which is also available from the hybrid, was injected back into the angle channel of the receiver and is used to indicate when the polarization is correctly aligned with the spacecraft. A simplified block diagram of the receiving system is shown in Fig. 1.

Since the signal is fully correlated in the two receiver channels, the signal output of the sum arm of the hybrid is, with proper receiver phasing, the sum of the signals in the two receiver channels. This corresponds to proper alignment of the transmitter and receiver polarizations. However, the noise in the two receiver channels is, at least to a first order, completely uncorrelated. The noise in each of the outputs of the hybrid is therefore equal to the arithmetic mean of the noise in each of the receiver channels. Since the signal-to-noise ratio is nominally the same in both receiver channels, the correlation that occurs in the hybrid junction will ideally produce a 3-dB improvement in the final signal-to-noise ratio.

The signal from the difference arm of the hybrid is processed in one of the receiver's standard angle error detectors. Proper phasing of the receiver is accomplished when the output of the detector is nulled (proper care must be exercised in setting the phasing of the detector's reference signal).

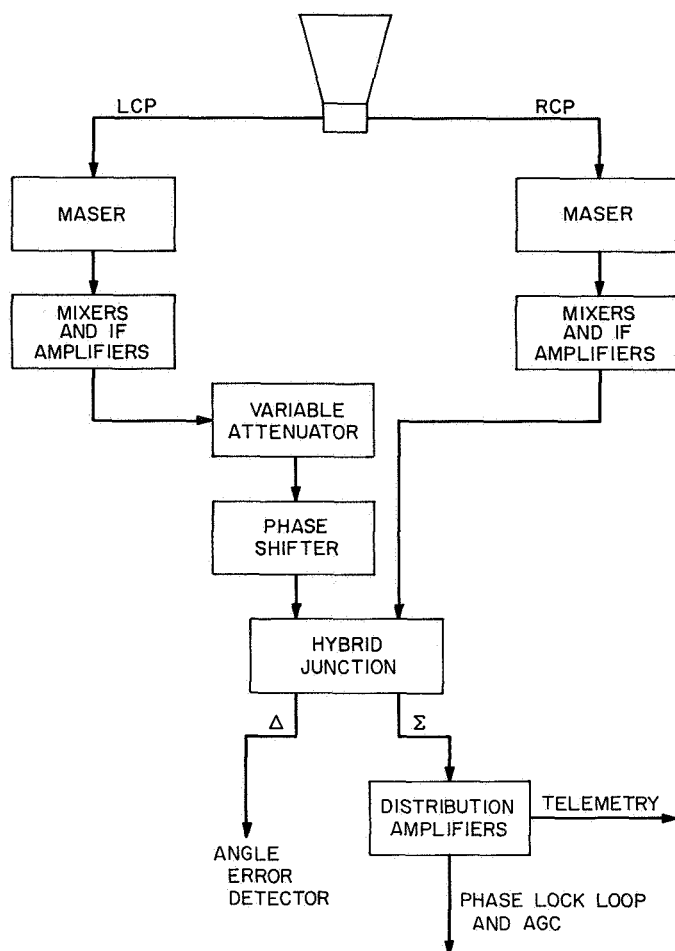


Fig. 1. Simplified block diagram of DSS 14 receiving system modified for rotating linear polarization

3. Results

On November 1, 1967, receiver 1 at DSS 14 was modified as described above to provide linear receive capability. Since this was a first test of the compatibility of the modification to the receiver, no IF relays were installed and the parity error rate was compared between receiver 1 (modified) and receiver 2 (standard). The *Pioneer VI* spacecraft was commanded to transmit at a rate of 16 bits/s. Table 1 is a tabulation of the results of this experiment.

Lindsey (Ref. 2) has shown the relationship between parity error rate and signal-to-noise ratio. Unfortunately, there was not enough time available to collect statistically significant data on the parity error rates and use Lindsey's analysis to confirm the improvement in signal-to-noise ratio. Suffice it to say that at a transmission rate of 16 bits/s, the standard receiver configuration produced a

Table 1. *Pioneer VI*—parity error rate with modified and standard receiver configurations

Time, GMT	Receiver No.	Received power, ^a dBm	Bit rate, bits/s	Parity error rate ^b
14:44	1 (mod)	−159.9	16	0.000
14:56	↓	↓	↓	0.000
15:08	↓	↓	↓	0.000
15:20	↓	↓	↓	0.000
15:32	↓	↓	↓	0.039
15:56	2 (std)	−163.0	16	0.420
16:08	↓	↓	↓	0.430
16:16	Computer lost lock—questionable data			Bad > 1.000
16:20	↓	↓	↓	0.339
16:31	↓	↓	↓	0.427
16:50	1 (mod)	−159.5	16	0.000
17:02	↓	↓	↓	0.000
17:16	↓	↓	↓	0.000
17:28	↓	↓	↓	0.000
End of test time—start of standard track—noncontrolled data				
18:16	1 (std)	−162.4	16	0.587
19:04	↓	↓	↓	0.806
20:16	↓	↓	↓	0.691

^aAs determined from AGC level.
^b0.109 = 1 error in 1000.

higher-than-acceptable parity error rate while the modified configuration produced a completely acceptable parity error rate.

References

1. Kraus, J. D., *Antennas*. McGraw-Hill Book Co., Inc., New York, 1950.
2. Lindsey, W. C., *Performance of Phase-Coherent Receivers Preceded by Bandpass Limiters*, Technical Report 32-1162. Jet Propulsion Laboratory, Pasadena, Calif., Sept. 15, 1967.

B. Ultracone Rotatable Linear Polarization Modifications, F. E. McCrea

1. Introduction

The ultracone (SPS 37-46, Vol. III, p. 63), which has been demonstrated to operate with a total zenith receive system noise temperature of 16.8°K on the DSS 13 85-ft reflector, is being modified by the installation of three rotary joints. It will now be possible to select one of three polarizations: RCP, LCP, and rotatable linear polarization.

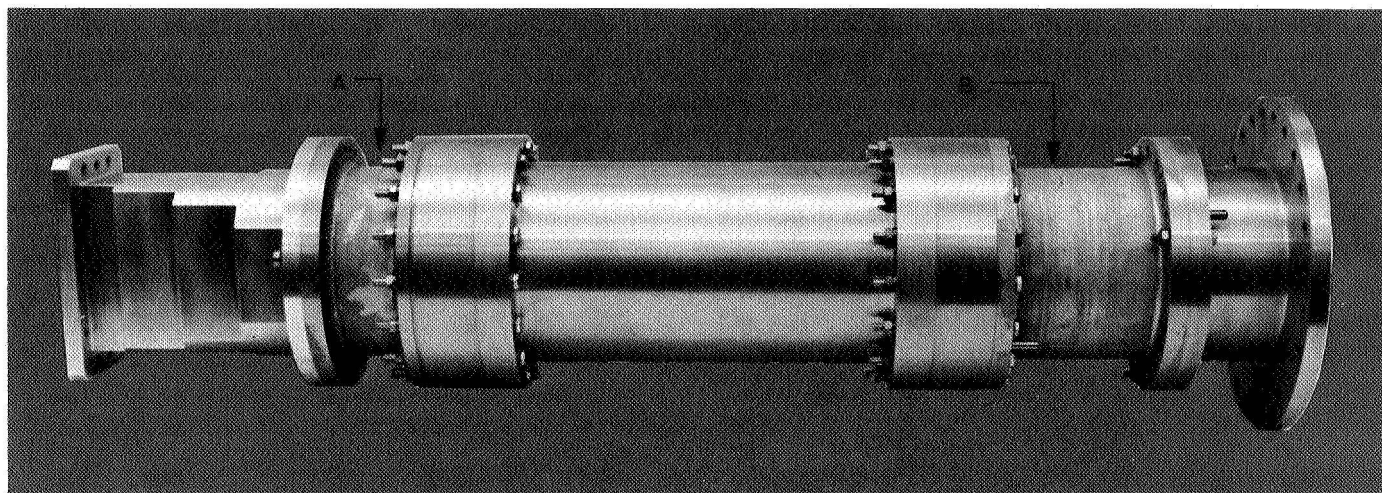


Fig. 2. Ultracone polarization components

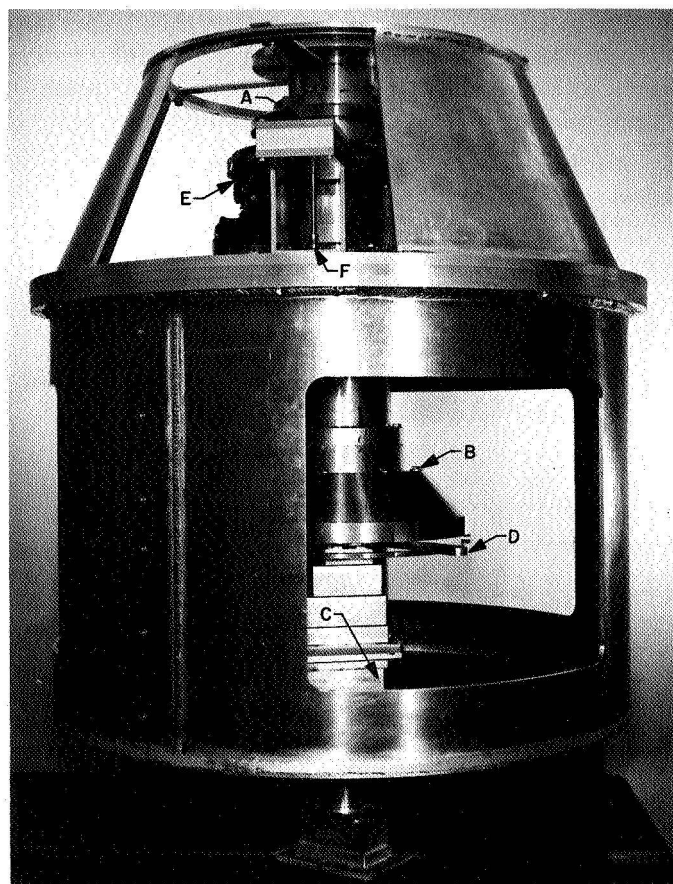


Fig. 3. Rotating linear polarization components

A 3-dB gain will be realized in tracking a linearly polarized spacecraft over tracking with a circularly polarized antenna. The ultracone will retain the versatility of tracking RCP and LCP spacecraft.

2. Recent Work

By replacing phasing sections A and B in the original feed (Fig. 2) with circular waveguide rotary joints of appropriate lengths (Fig. 3, items A and B) and by the addition of a rectangular rotary joint (Ref. 1) (Fig. 3, item C), it is now possible to manually change the position of the broadband rectangular transition (Ref. 2) in relation to the quarter wave plate (SPS 37-46, Vol. III, p. 63), giving RCP, LCP, or linear polarization. When linear polarization is selected and locked in place by an indexing device (Fig. 3, item D), the feed is then driven by a dc motor and worm reduction (Fig. 3, item E) between rotary joints A and C (Fig. 3). The feed can be rotated to maximum signal by observing the receiver AGC voltage. Angle readout is obtained through a synchro transmitter (Fig. 3, item F) with a resolution of 15' of arc.

The installation of these components in the ultracone is expected to produce a total receive system noise temperature of 18°K at zenith. The possibility of adding further diversity to the ultracone, in the form of a separate maser capable of operating in a diplexed mode, is being investigated.

References

1. Stevens, R., and Victor, W. K., *Radar Exploration of Venus: Goldstone Observatory Report for September-December 1962*, Technical Report 32-396. Jet Propulsion Laboratory, Pasadena, Calif., June 30, 1965.
2. Bathker, D. A., "A Stepped Mode Transducer Using Homogeneous Waveguides," *Transactions IEEE Microwave Theory and Technique*, pp. 128-129, Feb. 1967.

C. Low-Noise Receivers: Microwave Maser Development, Second Generation TWM, R. C. Clauss

1. Introduction

The equivalent input noise temperature of the second generation TWM has been measured from 2267 to 2305 MHz. The measurement technique involved the use of broadband noise sources in conjunction with a swept-frequency receiver. An x - y recorder was used to provide a continuous display of noise ratios, which are used to compute system temperature at any point within the TWM passband.

2. Instrumentation

A block diagram for noise measurement instrumentation is shown in Fig. 4. Excess noise, from an argon-filled noise source, is coupled into the TWM through a directional coupler. Calibration of the excess noise is accomplished by measuring the noise level difference when the noise source is turned on and off. Noise power ratios are

obtained on each of the three reference terminations. The measured noise power ratio $Y(\text{dB})$ is used as follows:

$$\frac{T_e + T_m + T_L}{T_m + T_L} = R \quad (1)$$

where $Y = 10 \log R$, T_e = excess noise coupled from noise source to TWM input, T_m = TWM equivalent input noise temperature, and T_L = reference termination temperature. Simultaneous solution of equations with ratios obtained when using two reference terminations at different temperatures results in values for T_e and T_m . The receiver noise temperature is determined by T_m . The maser operates at $45\frac{1}{2} \pm \frac{1}{2}$ dB net gain between 2267 and 2305 MHz, and noise contributions from the mixer following the maser are insignificant.

The cooled reference termination temperatures are referred to the maser input by adding the temperature increase caused by interconnecting waveguide components to the reference termination bath temperature.

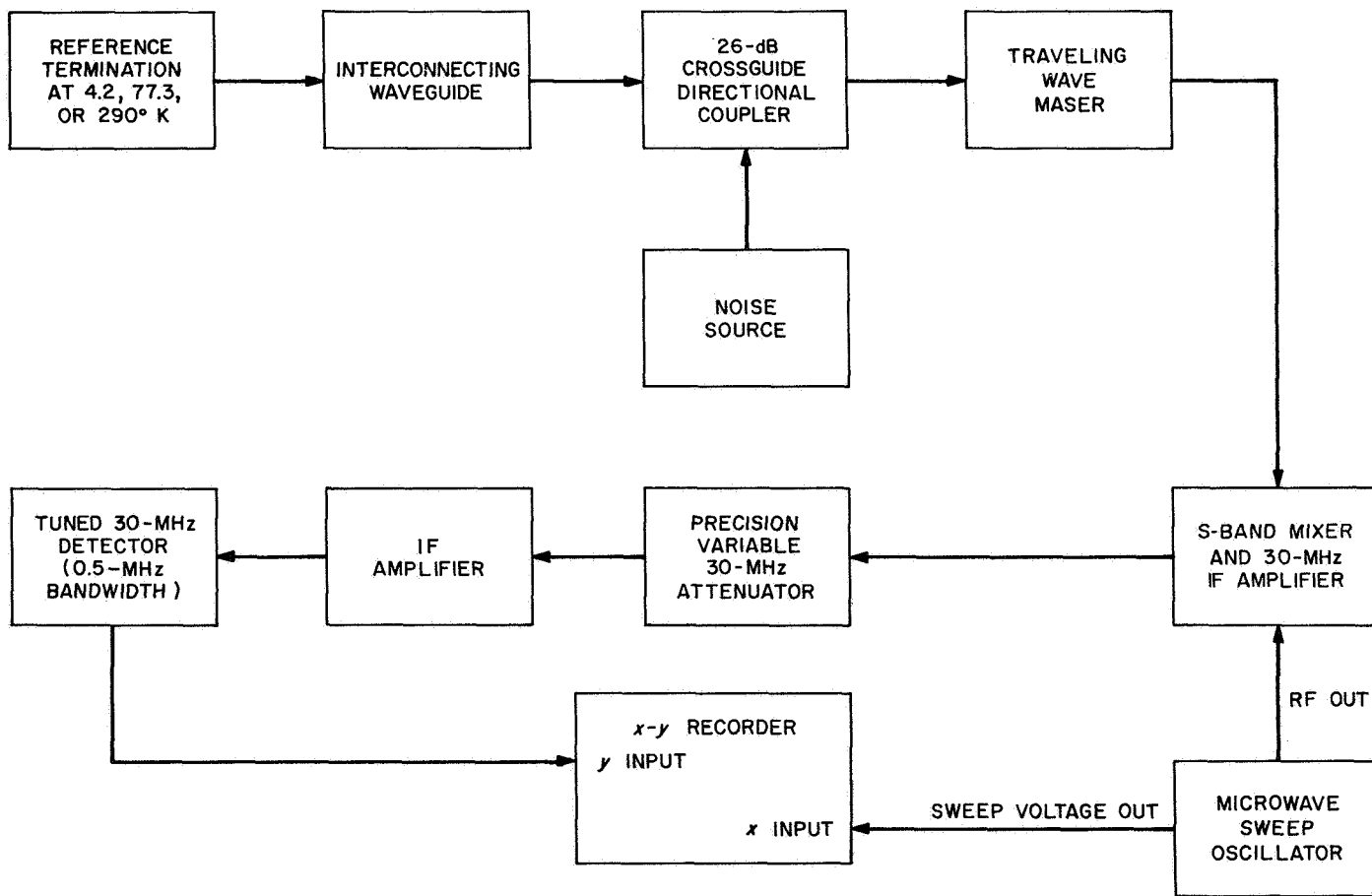


Fig. 4. Noise measurement instrumentation

Noise power ratios are measured with the precision 30-MHz variable attenuator, using the *x-y* recorder as an indicator of the rectified total system noise power.

Sweeping the local oscillator of the S-band mixer produces a graph of noise power versus frequency on the *x-y* recorder. The sweep rate used requires 100 s to cover the TWM pass band. The slow sweep rate permits use of a 1-s time constant filter to be used with the ½-MHz bandwidth detector. Filtering reduces the recorded rms noise jitter to less than 0.01 dB.

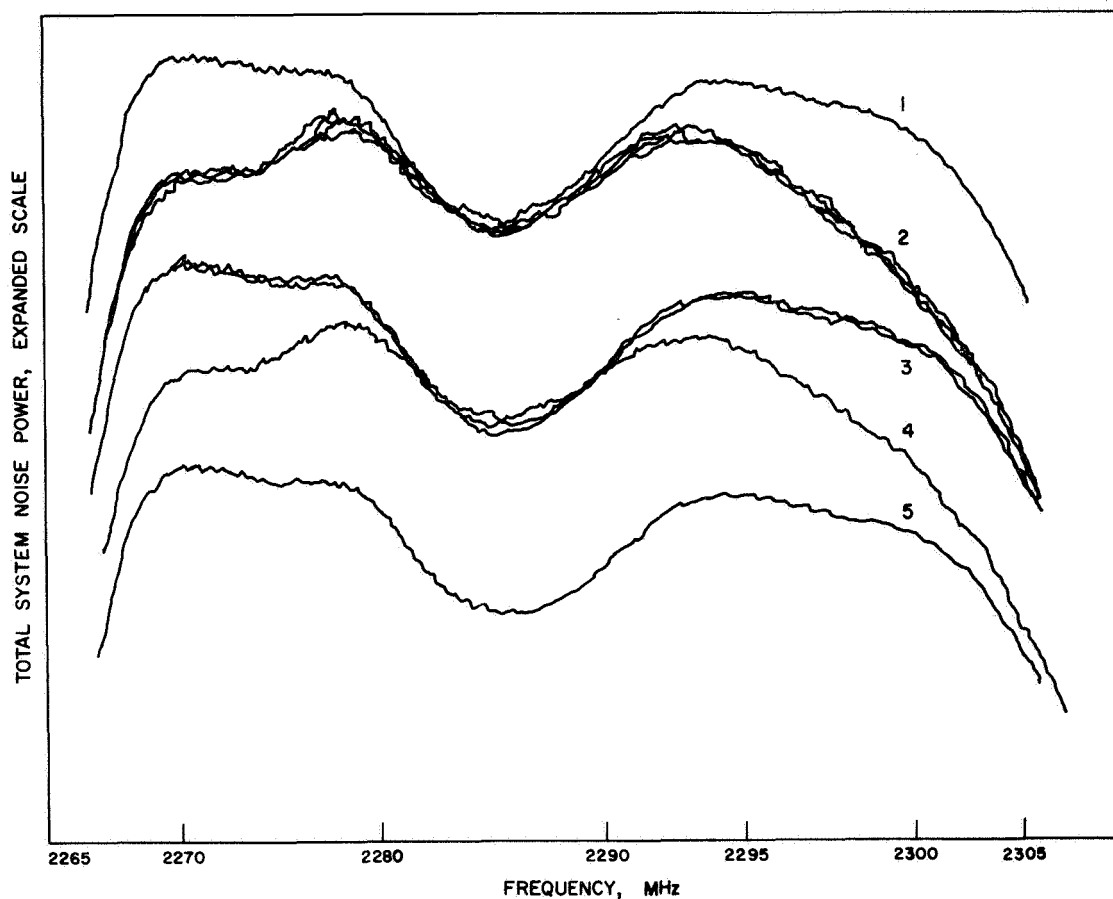
Superimposed *x-y* plots show a continuous display of noise power ratios in the frequency range under evalu-

ation. The ratios are used to determine system temperature at any point in the TWM pass band.

Errors caused by instability, receiver linearity, and attenuator inaccuracy are directly proportional to the total system temperature. Best resolution and accuracy are obtained by terminating the TWM with a matched load at the lowest possible temperature. For these reasons a liquid-helium-cooled waveguide termination is used.

3. Results

Noise source calibration data were taken using three reference terminations. The value of excess noise, 23.6°K,



1. NOISE SOURCE OFF. ATTENUATOR SETTING 11.50 dB.
2. NOISE SOURCE ON. FOUR CONSECUTIVE RUNS. ATTENUATOR SETTING 16.42 dB.
3. NOISE SOURCE OFF. TWO RUNS, BEFORE AND AFTER RUN 2. ATTENUATOR SETTING 12.00 dB.
4. NOISE SOURCE ON. ATTENUATOR SETTING 16.94 dB.
5. NOISE SOURCE OFF. ATTENUATOR SETTING 12.50 dB.

Fig. 5. Recorded data for swept noise measurement

was used with the liquid-helium-cooled termination to measure the change in TWM noise temperature from 2267 to 2305 MHz. Fig. 5 shows the x - y recording used to measure system temperature. A total of nine recordings are shown. Repetition is used to demonstrate system stability. A calibrated change in system gain is recorded at 0.5-dB intervals (see runs 1, 3, and 5). The precision 30-MHz attenuator is used for calibration and measurement of the power change when the noise source is on or off. Curve 3 is recorded before and after the 4 runs of curve 2. The difference, in dB, between curves 2 and 3 is added to the change in attenuator setting (4.42 dB). These Y factors vary with frequency as determined by the system temperature. The Y factor ratio R is used to compute system temperature:

$$\frac{T_s + T_e}{T_s} = R \quad (2)$$

where $T_s = T_m + T_L$.

A plot of T_m , the measured equivalent input temperature of the TWM, is shown in Fig. 6. The width of this curve shows the maximum and minimum values obtained from the repeated data runs of Fig. 5. The computed curve

shown on Fig. 6 represents the theoretical noise temperature of this TWM. The prediction differs from measured values due to input transmission line loss and TWM input mismatch. The peak-to-peak deviations in measured values should not be interpreted as a tolerance on the absolute accuracy of the measurement. The deviation is representative of relative point-to-point accuracy.

D. Improved RF Calibration Techniques: Ultracone-on-Ground Noise Temperature Calibrations, T. Y. Otoshi

1. Introduction

This article presents the results of component noise temperature calibrations made at 2297 MHz on the S-band Cassegrain ultracone receiving system. The purpose of these calibrations is to evaluate component performance as well as to analyze the total system temperature in terms of its basic noise temperature components. For this receiving system, the basic components which contribute to system temperature are (1) the antenna assembly, (2) the antenna-to-maser interconnecting transmission line, (3) the maser assembly, and (4) the follow-up receiver. Although for most operational purposes only total

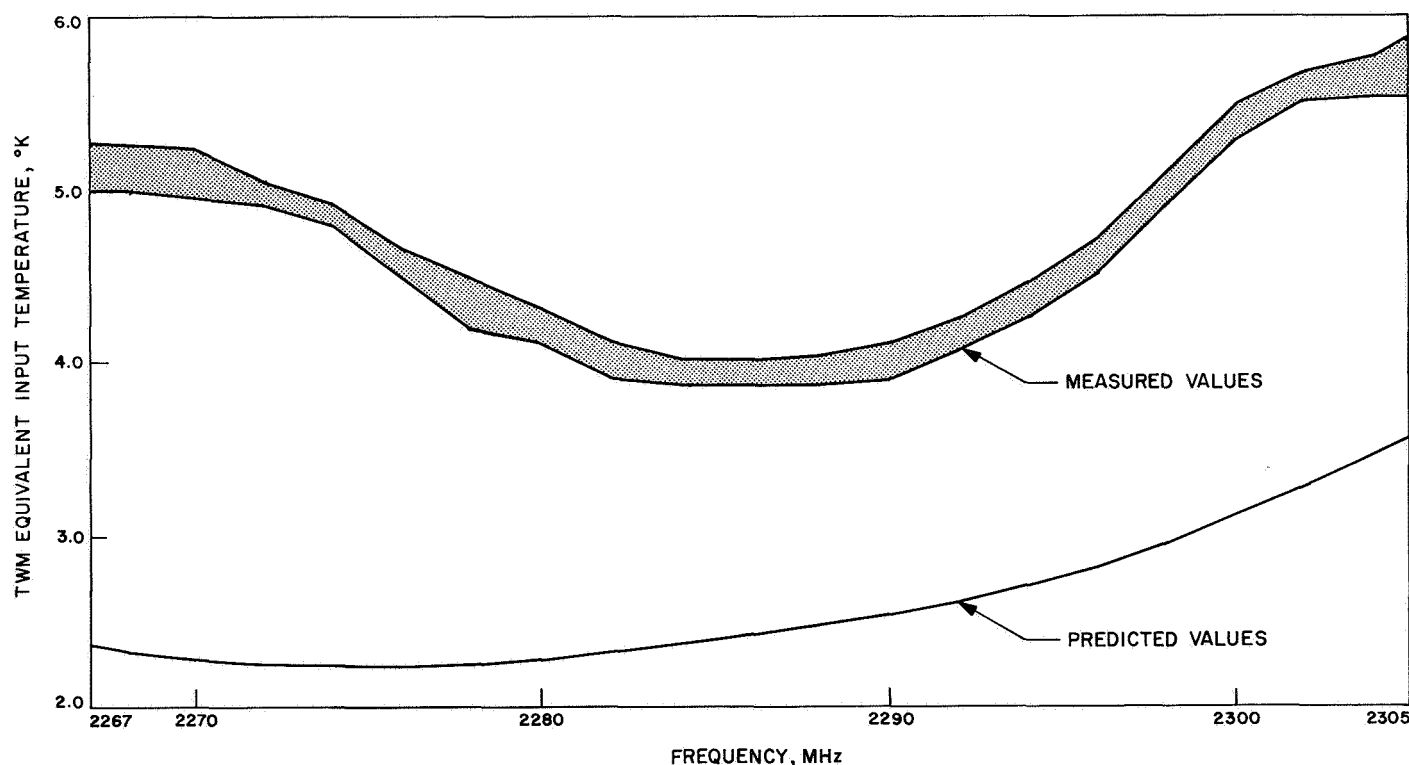


Fig. 6. TWM equivalent input temperature

system temperature is of major concern, periodic component calibration data are necessary for system diagnosis, system design, and component evaluation purposes.

Calibrations on the S-band Cassegrain ultracone were made both at JPL and at DSS 13. The results presented in this article apply to the cone-on-ground test configuration. Similar calibration tests for the cone-on-paraboloid configuration are being planned for the future. Comparisons of antenna temperature data obtained from the two test configurations should provide information concerning the effects of quadripod blockage, dish surface tolerances, spillover, hyperboloid focusing, etc.

2. Description of Ultracone System

Figure 7 shows a block diagram of the ultracone receiving system components and also the instrumentation

associated with noise temperature calibrations. A detailed description of the system may be found in SPS 37-46, Vol. III, p. 63.

The antenna output reference point is the output of the broadband transition (point Δ in Fig. 7), while the maser input reference flange is the output of the 33-dB waveguide coupler (point Δ in Fig. 7). The antenna-to-maser transmission line consists of a three-position waveguide switch and the 33-dB waveguide coupler.

The line losses between points Δ and Δ indicated in Fig. 7 are presently being evaluated so that the effective antenna temperature can be defined closer to the horn aperture in the future.

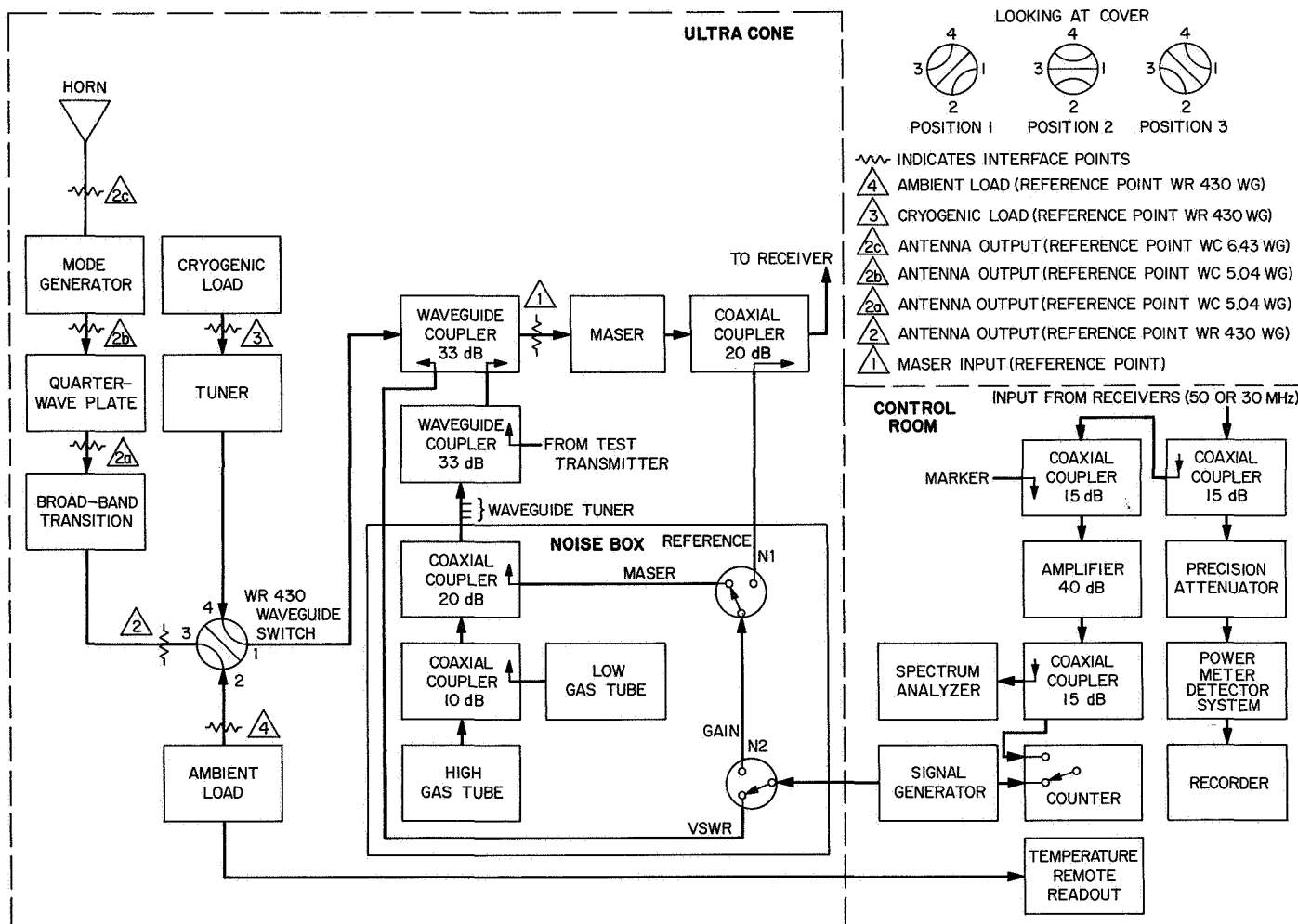


Fig. 7. Block diagram of the S-band Cassegrain ultracone noise temperature calibration system

Table 2. Average noise temperatures of S-band Cassegrain ultracone at 2297 MHz

Test description	Calibration period (1967 GMT day number)	Air temperature at ground level, °F	Relative humidity at ground level, %	Zenith T_A' , °K	T_{Lr} , °K	T_M'' , °K	T_F'' , °K	T_{SA}'' , °K ^a	T_{EL}'' , °K	T_{EH}'' , °K	T_{02r} , °K
Cone-on-ground (JPL) WR 430 LHe load, ^c 12 runs	201	71	65	6.2 ±0.3 (pe) _r	1.2	4.6 ±0.3 (pe) _r	0.06 ±0.01 (pe) _r	12.1	0.7	6.7	296.2
Cone-on-ground (JPL) ultracone 1N load, ^d 16 runs	214-215	79.3 ±1.7 (pe) _b	48.3 ±2.7 (pe) _b	5.8 ±0.07 (pe) _b ±0.6 (pe) _r	1.2	6.2 ^b ±0.05 (pe) _b ±0.6 (pe) _r	0.07 ±0.01 (pe) _r	13.1 ^b ±0.04 (pe) _b	0.6 ±0.02 (pe) _b	6.7 ±0.04 (pe) _b	299.0 ±0.8 (pe) _b
Cone-on-ground (DSS 13) ultracone 1N load, ^d 13 runs	255	77.0 ±1.1 (pe) _b	26.5 ±0.6 (pe) _b	5.6 ±0.04 (pe) _b ±0.6 (pe) _r	1.2	5.7 ±0.05 (pe) _b ±0.6 (pe) _r	0.09 ±0.01 (pe) _r	12.6 ±0.01 (pe) _b	0.7 ±0.02 (pe) _b	6.6 ±0.04 (pe) _b	299.1 ±0.3 (pe) _b

^aDifference between T_{SA}'' and sum of component temperatures is due to roundoff and weighting.
^bThe maser pump power was set too high for these runs, causing increased maser temperature.
^cRFT Part No. 271.
^dMMC Model SR 8135, SN003.

3. Measurement Techniques

The method used for absolute noise temperature calibrations of the individual components of system temperature is the Y-factor technique involving the use of two thermal noise standards and calibrated line loss data. This measurement technique has been previously discussed in detail in SPS 37-39, Vol. III, pp. 86-91 and in SPS 37-40, Vol. IV, pp. 202-209.

Temperature symbols used in this article are defined below. Double-primed symbols indicate temperatures defined at the maser input reference flange; all single-primed symbols refer to temperatures defined at the antenna output reference flange. The double- and single-primed temperatures are related by the dissipative loss of the transmission line which connects the antenna to the maser.

T'_A = antenna temperature, °K

T_L = temperature contributed by the dissipative loss of the transmission line between the antenna output and the maser input reference flanges, °K

T''_M = maser temperature, °K

T''_F = follow-up receiver temperature contribution, °K

$T''_{SA} = T'_A + T_L + T''_M + T''_F$ = system temperature when the maser input is switched to the antenna, °K

T''_{EL} = excess noise temperature of the low gas tube injected into the maser, °K

T''_{EH} = excess noise temperature of the high gas tube injected into the maser, °K

T_{02} = physical temperature of the receiving system transmission lines, °K

4. Calibration Results

The calibrated component noise temperatures associated with the S-band Cassegrain ultracone receiving system are summarized in Table 2. Weighted averages obtained with a liquid helium (LHe) load as the cryogenic noise standard are compared with those obtained with the S-band Cassegrain ultracone WR 430 liquid nitrogen load. A detailed analysis of the data and associated errors

indicates that the temperature values calibrated with the LHe load are the most accurate values.

For calculations of the total probable errors $(pe)_T$, considerations were given to the measurement dispersion errors $(pe)_D$, and the bias probable error $(pe)_B$ caused primarily by uncertainties in the cryogenic load reference temperature, ambient load temperature, Y-factor ratios, and mismatches.

The major sources of noise temperature calibration errors are believed to be the uncertainties associated with the cryogenic thermal reference loads. The dependence of the thermal load noise temperature upon cryogenic liquid level, line loss and reflection coefficient stability, and cryogenic liquid temperature stability are problem areas which need to be investigated.

E. Efficient Antenna Systems: X-Band Gain Measurements, D. A. Bathker

1. Introduction

The 85-ft az-el reflector at DSS 13 has been operated at X-band, 8448 MHz, for the purpose of evaluating large ground antenna performance at extended frequency. A selected celestial source, Cygnus A (3C405), has been observed on two occasions, during November 1966 and June 1967. This reporting will discuss results obtained during both test periods.

2. Recent Work

As reported in SPS 37-45, Vol. III, pp. 42-48, the excess system temperature referenced to the maser input flange was $15.5 \pm 2.3^\circ\text{K}$, 3σ , on Cygnus A during the November 1966 tests. This result was qualified as being applicable for elevation angles between 40 and 70 deg. Also mentioned in the above referenced SPS was the uncertainty in focusing the system. During the June 1967 tests, our knowledge of the main reflector in terms of change in focal length and mechanical hysteresis as functions of elevation angle was substantially improved as shown in Fig. 24 of SPS 37-47, Vol. II, pp. 77-80. Since the focus data (Fig. 24 of referenced SPS) indicates no appreciable focal length change over 60-90 deg of elevation angle, a selected fixed focus of 0.125 in. during the June 1967 tests was expected to produce optimum antenna gain at high elevation angles.

Figure 8 shows 371 measured excess system temperatures referenced to the maser input flange for Cygnus A

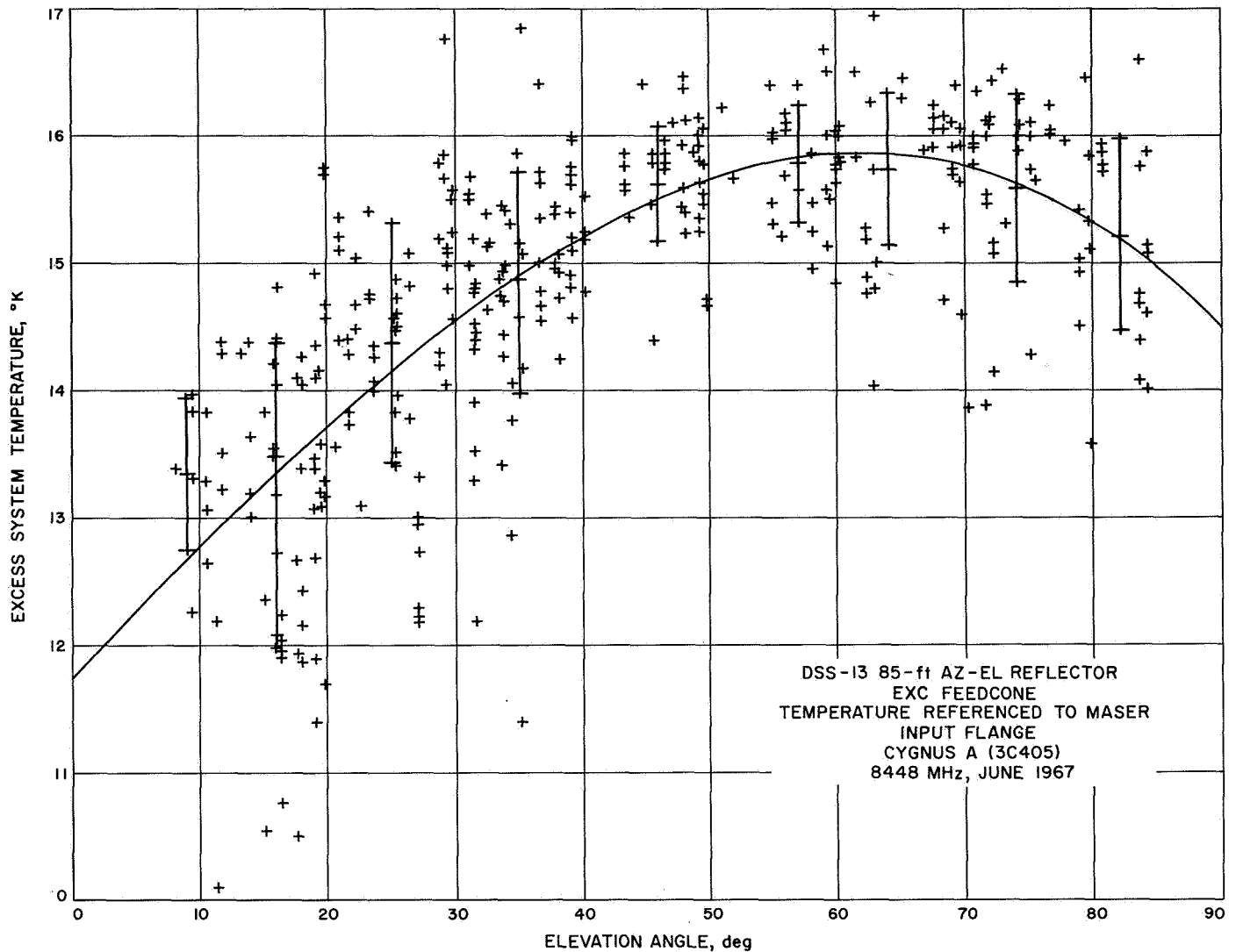


Fig. 8. Excess system temperature as a function of elevation angle

during June 1967, with the antenna focused as discussed above. All data were obtained through the cooperation of DSS 13 personnel. Each measurement is the mean of differencing five determinations of ambient load to antenna Y-factor on source with five determinations of ambient load to antenna Y-factor off source. Off-source system temperature measurements are made by alternately slewing ± 2.0 deg from the source in elevation when the source is above 45 deg and ± 2.0 deg in azimuth when the source is below 45-deg elevation. Only 2-3% of the total data was rejected as blunder points.

Figure 8 includes a third-order polynomial curve which was fit to the data without weighting. Also, a sample interval of 10-deg elevation angle was selected. The

center of each vertical bar in Fig. 8 represents the sample mean excess system temperature (at the sample mean elevation angle) in that 10-deg elevation angle increment. The bars represent the square root of the sample variance, which is essentially \pm one standard deviation about the sample mean except for the lowest elevation increment. A fourth-order polynomial curve was fit to the data with each point weighted inversely to the probable error. The probable error was taken as the root sum square of the probable errors of the individual on-source and off-source temperature measurements. No significant difference exists between that curve and Fig. 8. Indeed, the apparently anomalous low temperatures observed between 10- and 35-deg elevation were individually examined; the probable errors of the on-source and off-source

temperatures for those data are not unlike any of the data and therefore appear to be real. It was expected that poor pointing or radiometer gain changes would be indicated by increased jitter among the individual determinations. Possibly significant is the fact that data between 40- and 60-deg elevation exhibits the smallest jitter.

The peak temperature observed at 60-deg elevation is thought to be due to (1) the paraboloid surface, which was adjusted to be optimum at 45-deg elevation and (2) the focus setting, which was adjusted to be optimum at 75-deg elevation as discussed. Because atmospheric extinction is thought to have a very small effect at these elevation angles, it is not unreasonable to expect the highest temperatures to be observed between 45- and 75-deg elevation.

The weighted mean of the data between 40- and 70-deg elevation is $15.7 \pm 3.0^\circ\text{K}$, 3σ , which is nearly identical to the November 1966 result of $15.5 \pm 2.3^\circ\text{K}$, 3σ . An improved value for the efficiency, defined at the maser input flange and applicable over 40–70 deg elevation is $46.2 \pm 11.2\%$, 3σ , where the tolerance is taken as the root sum square of the standard deviations of the selected flux density for Cygnus A and the measurement scatter. For the data reported here, the measurement scatter exceeds the flux density uncertainty.¹ As a scale factor for the convenience of the reader, the mean system efficiency during June 1967 is greater than 40% (13.6°K excess system temperature in Fig. 8) for elevation angles greater than 20 deg.

Data presented in the form of Fig. 8 are useful to a deep space communications system designer, i.e., several effects such as microwave dissipation loss, antenna defocusing, and atmospheric extinction are automatically included in the observations. Of interest to the antenna designer and/or radio astronomer is to separate the various contributions. To date, only the defocusing effect due to paraboloid focal length change has been evaluated. Based on focus data mentioned earlier, we can expect nearly 0.4λ axial misalignment of the Cassegrain subreflector at 10 deg elevation angle for the 85-ft az-el at DSS 13. This axial misalignment, if corrected, would increase the observed excess system temperature approximately 1.9°K at 10 deg elevation. Preliminary work indicates atmospheric extinction is less than half the defocusing loss.

¹The selected value for flux density of Cygnus A is based on a uniquely calibrated 4-m paraboloid (Ref. 1).

Reference

1. Lastochkin, V. P., Sorin, Yu. M., and Stankevich, K. S., "Spectrum of Radio Emission from Cygnus-A," *Soviet Astronomy-AJ*, Vol. 8, No. 4, pp. 613–614, Jan.–Feb. 1965.

F. Prototype Frequency Agile Receiver (Wide-Band Receiver System), K. D. Schreder

1. Introduction

The wide-band receiver system is a prototype S-band receiver system suitable for use in the DSN and/or MSFN. The system is capable of changing the S-band frequency in 1-Hz increments over the entire DSN and MSFN frequency ranges. The system is also capable of being switched to any frequency in the above-mentioned bandwidth independent of the channel and of achieving two-way phase lock without any tuning adjustments. The system configuration has been previously reported in SPS 37-30, Vol. III, pp. 86–91, and SPS 37-33, Vol. III, pp. 96–107. A system block diagram is shown in SPS 37-33, Vol. III, p. 101.

Special modules which were designed for this system to provide the desired performance are cited in SPS 37-40, Vol. III, pp. 13–21, and SPS 37-41, Vol. III, pp. 69–71. The wideband multiplier (SPS 37-40, Vol. III, pp. 13–21) provided the desired S-band bandwidth necessary for changing to any frequency within the S-band frequency range without any adjustments. (This was one of the goals of the system.)

In this article, system characteristics and techniques for measuring the characteristics are presented and discussed.

2. System Analysis

The analysis used in defining the receiver system has been given in SPS 37-17, Vol. III, pp. 24–27 and SPS 37-18, Vol. III, pp. 53–64. (Equations will be taken from the previously mentioned reports without any explanation or definition of terms.) The equations used to describe the reference and ranging receiver system are shown below with the calculated system values.

a. Threshold. Threshold is defined where the noise and signal powers are equal, i.e.,

$$P_S = P_N = 10 \log KT (2\beta_L)$$

The receiver noise figure NF is 11.4 dB (2871°K). The threshold level for the various closed-loop bandwidths is shown in Table 3.

Table 3. Threshold level

$2\beta_L$, Hz	Threshold power, dBmW
0.8	-165.0
4.0	-158.0
5.0	-157.0
12.0	-153.2
16.0	-152.0
48	-147.2
152	-142.2

b. Limiter suppression factor. The limiter suppression factor α is defined to be the limited output voltage for an ideal bandpass limiter.

$$\alpha = \left[1 + \frac{4}{\pi} \left(\frac{P_N}{P_S} \right) \right]^{-1/2}$$

and the predetection noise bandwidth for the receiver is 2 kHz. The value of α for various received signal powers is shown in Fig. 9.

c. Closed-loop noise bandwidth. The closed-loop noise bandwidth $2\beta'_L$ is a function of the limiter suppression factor (signal strength). The defining equation is:

$$2\beta'_L = \frac{2\beta_L}{3} \left(1 + 2 \frac{\alpha}{\alpha_0} \right)$$

where $2\beta_L$ is the threshold closed-loop bandwidth and α_0 is the threshold limiter suppression factor. The values of $2\beta'_L$ for the various received signal powers are shown in Fig. 10.

3. System Performance

a. System characteristics. The performance data for the frequency agile receiver will consist of (1) the system closed-loop tracking bandwidths, (2) the AGC closed-

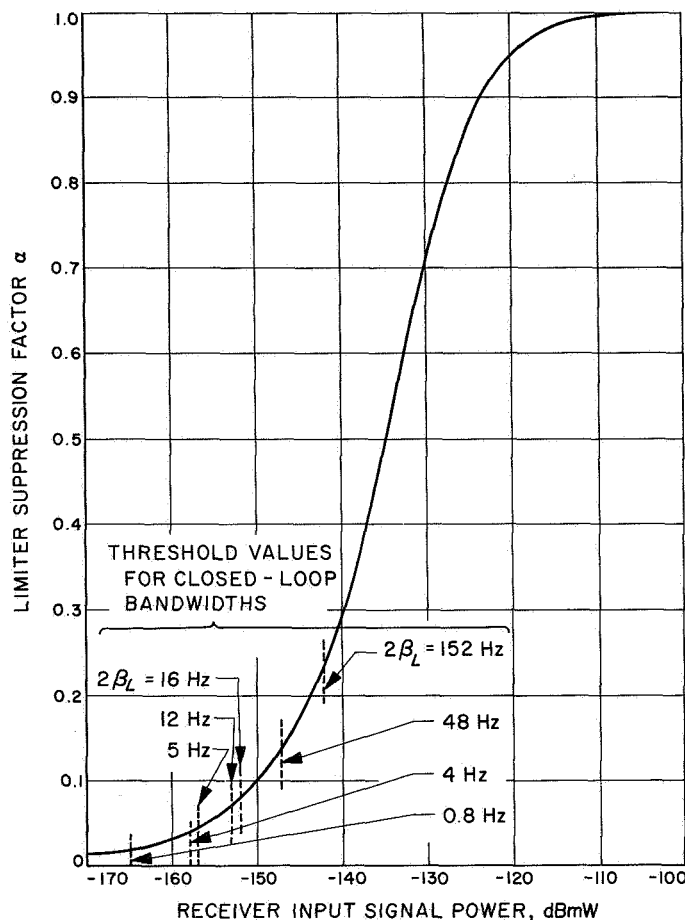


Fig. 9. Values of limiter suppression factor for received input signal power

loop bandwidths, (3) the system RF bandwidths, and (4) the reference receiver sensitivity characteristic.

RF carrier reference receiver. The -1-dB bandwidth is 28 MHz for the reference receiver at the antenna terminals (Fig. 11). The local oscillator chain has a -1-dB bandwidth of 34 MHz (Fig. 12). The difference between the bandwidth of the reference receiver and the local oscillator is caused by the filtering in the diplexer and in the preselector which are encountered before the S-band mixer.

The curves for the optimal bandwidth of the closed-loop transfer function response of the receiver are shown in Fig. 13. (The closed-loop bandwidths are 5, 16, 48, and 152 Hz.) The measured data is shown plotted over the optimal curves for the various bandwidths. The 5-Hz curve is shown for an $\alpha = 0.150$, which is 10.5 dB above threshold as indicated in Fig. 9. Measuring the 5-Hz

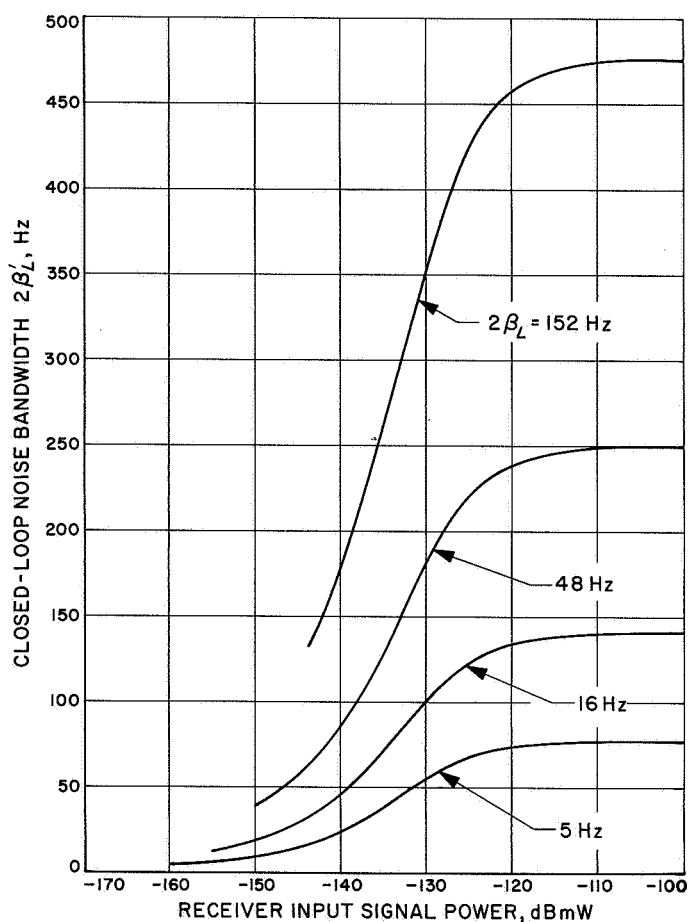


Fig. 10. Values of reference receiver closed-loop bandwidth for received input signal power

closed-loop response at a point above threshold was necessary due to the noise at threshold which prevented the loop from remaining in lock throughout the measuring time. All the other closed-loop measurements were made at threshold.

A curve showing the 5-Hz closed-loop response for various values of α is shown in Fig. 14.

Receiver AGC loop. The block diagram used for measuring the AGC closed-loop transfer function response is shown in Fig. 15. This is a direct method for measuring the closed-loop response. The measurement uses a low-frequency oscillator which amplitude-modulates a coherent 50-MHz signal from the synthesizer section of the system. The signal is a phase coherent amplitude-modulated signal which is injected into the 50-MHz IF signal amplifier to lock up the AGC loop. The loop tracks the low-frequency modulation and a point on the loop response curve is obtained for each frequency setting of the low-frequency oscillator.

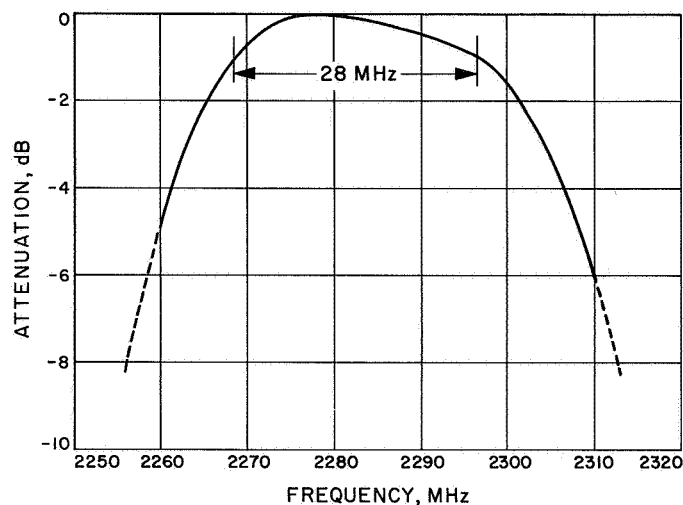


Fig. 11. Receiver bandwidth at antenna

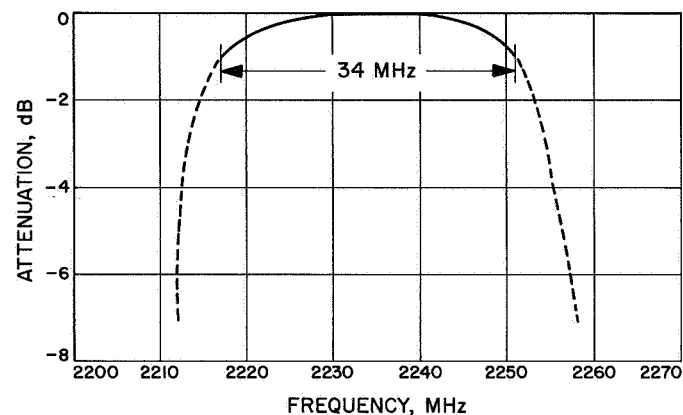


Fig. 12. Local oscillator bandwidth at S-band mixer

The optimal system closed-loop characteristic for the three desired loop parameters is shown in Fig. 16. The measured data is plotted over the optimal curves.

The AGC sensitivity characteristic is the curve from which the power level of an unknown received input signal can be determined, noting only the AGC voltage is developed. The AGC sensitivity characteristic for the frequency agile receiver is shown in Fig. 17.

Exciter loop. The transmitter bandwidth is shown in Fig. 18. The -1-dB bandwidth is 45.5 MHz, which has been widened slightly by having a traveling-wave tube amplifier in the exciter chain. The closed-loop bandwidth response for the exciter loop is shown in Fig. 19 with the associated data points plotted on it.

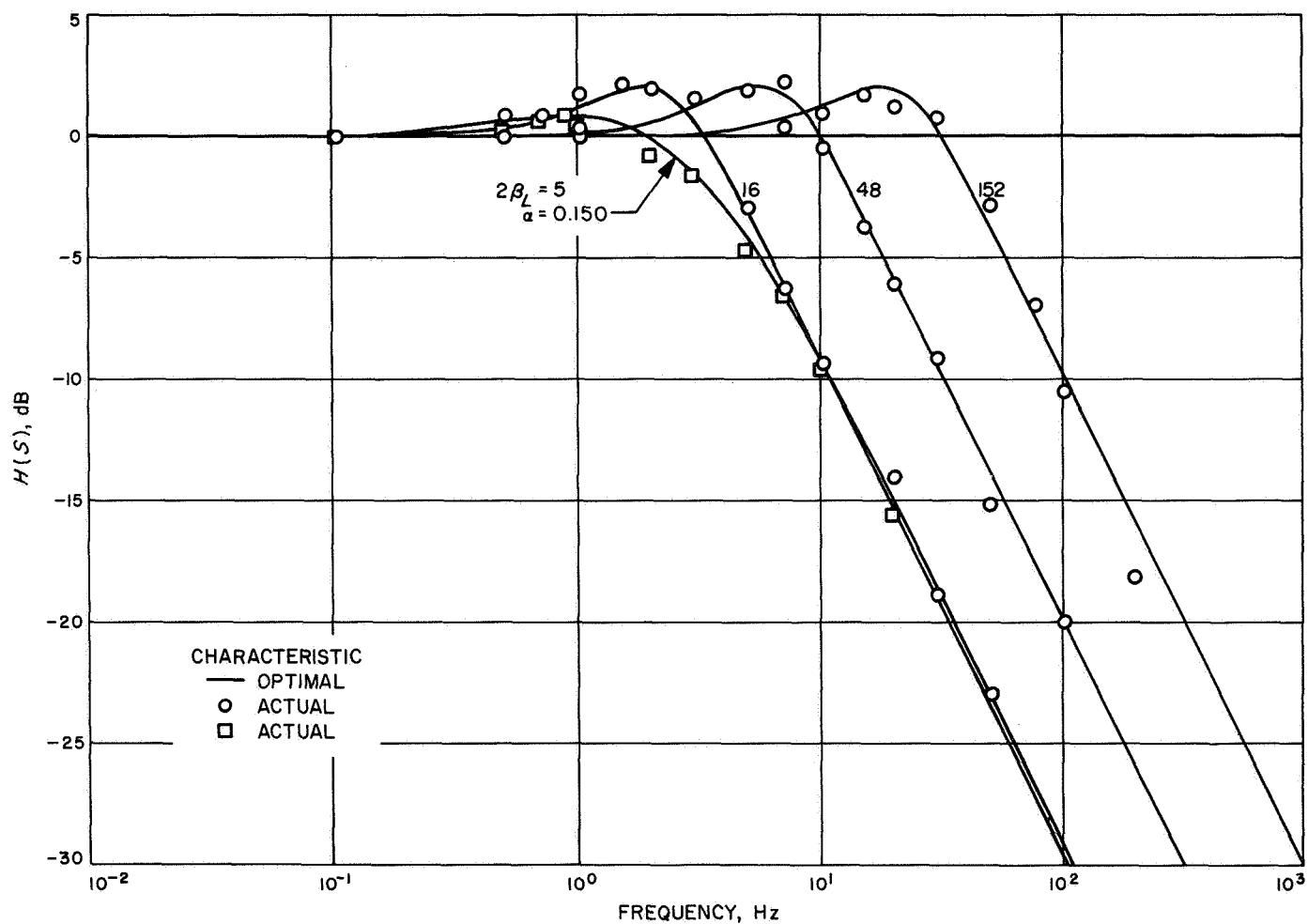


Fig. 13. Reference receiver closed-loop transfer function response

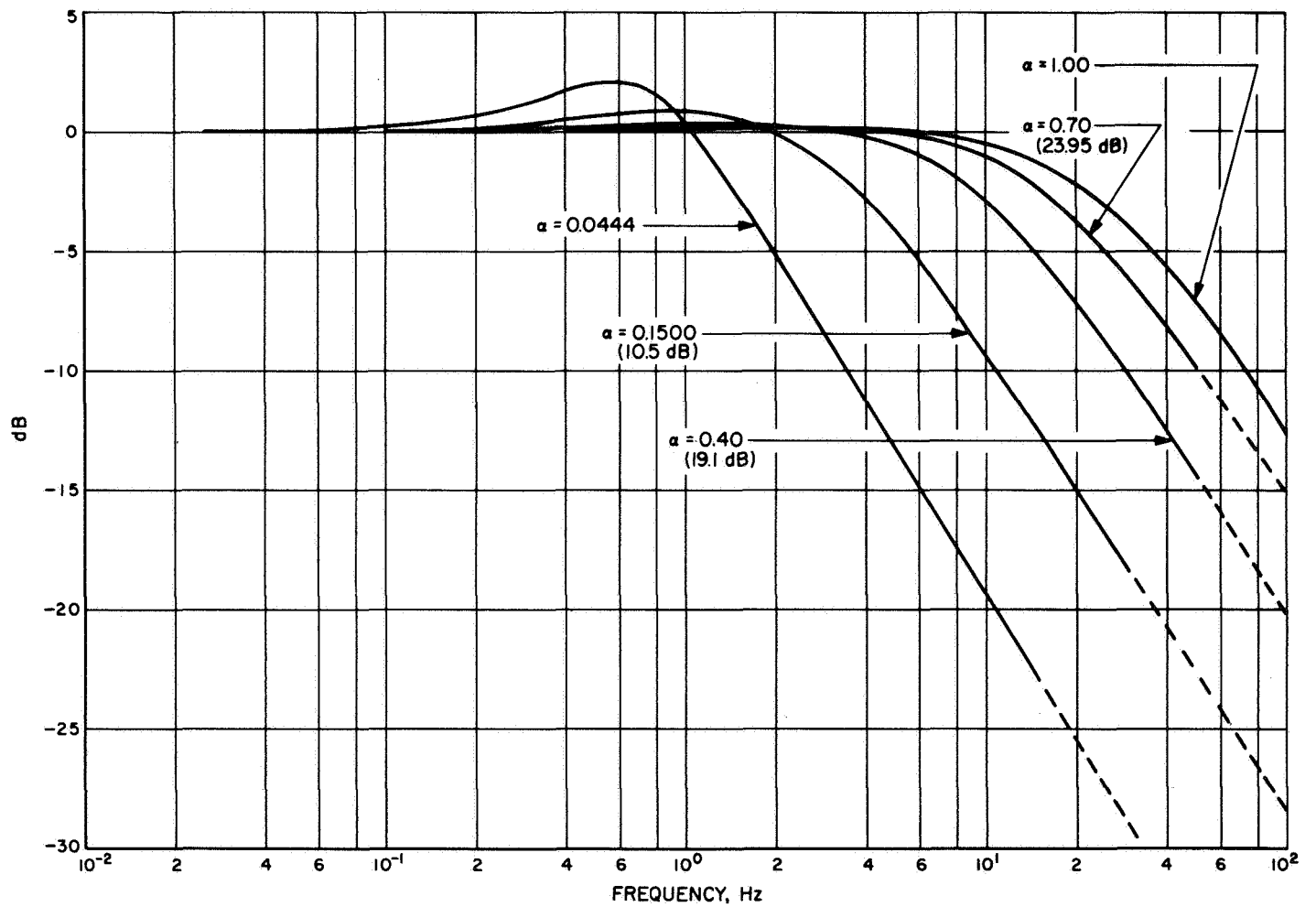


Fig. 14. Closed-loop transfer function for various suppression factors

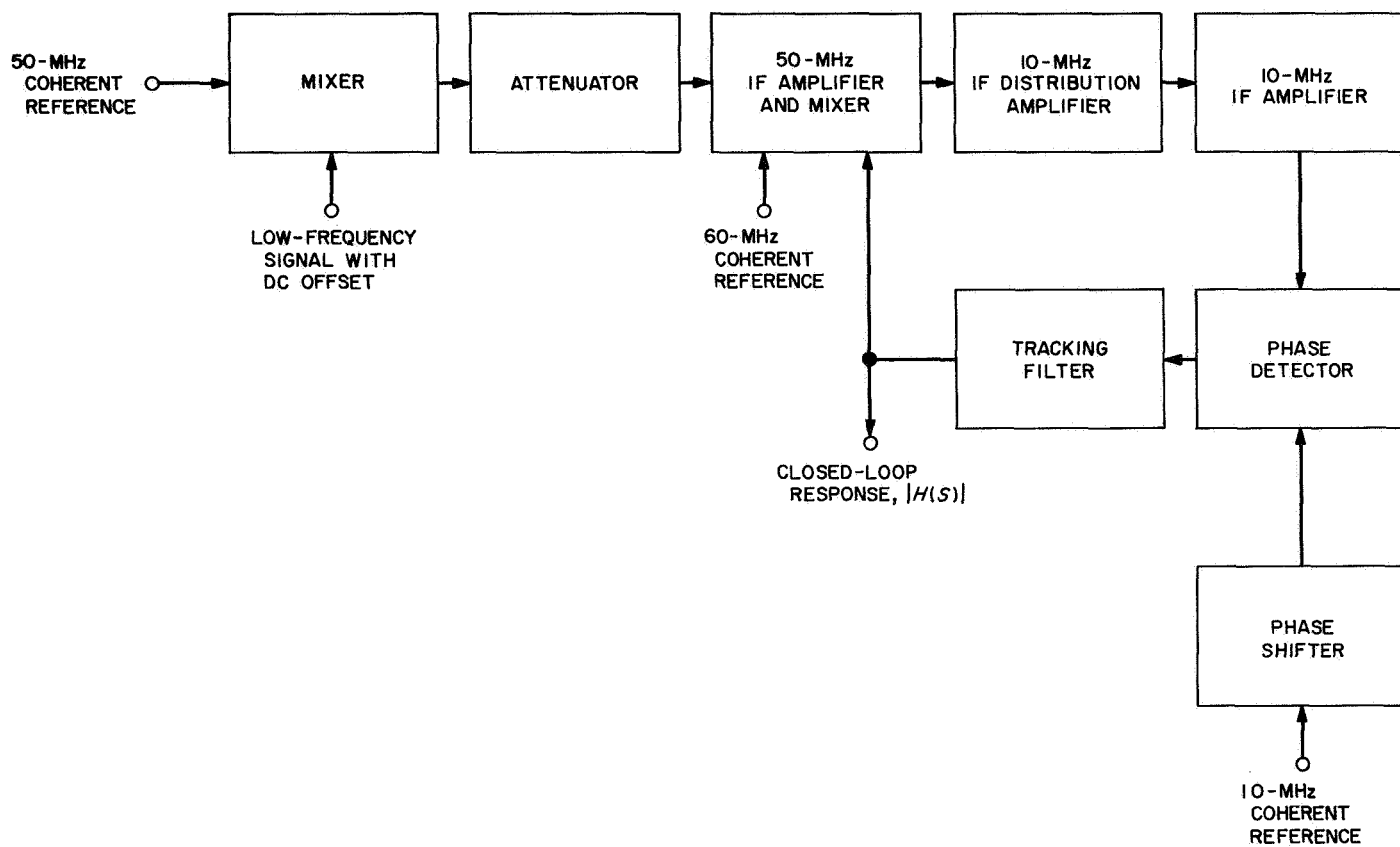


Fig. 15. Block diagram for measuring AGC closed-loop response

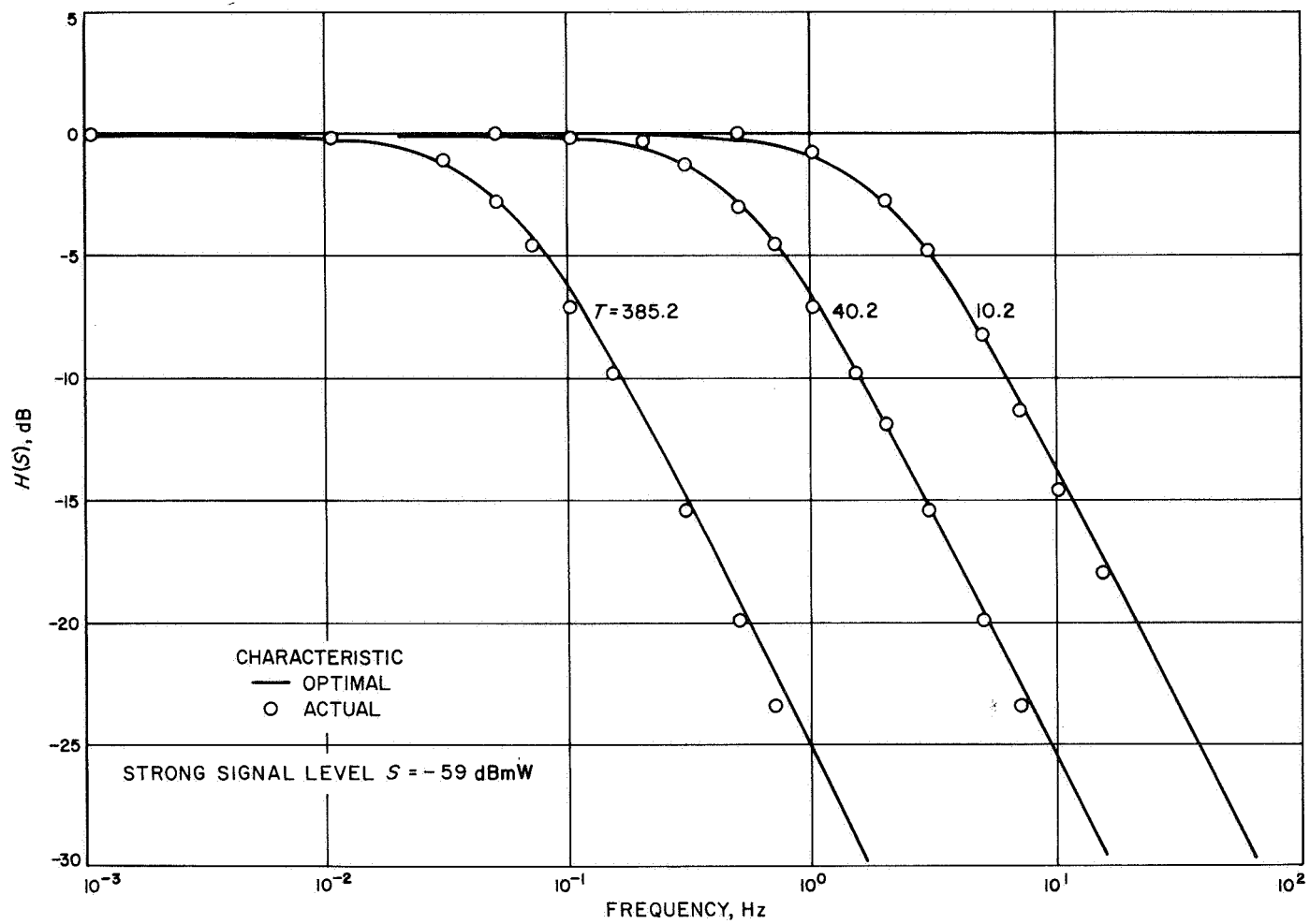


Fig. 16. Receiver AGC loop transfer function response

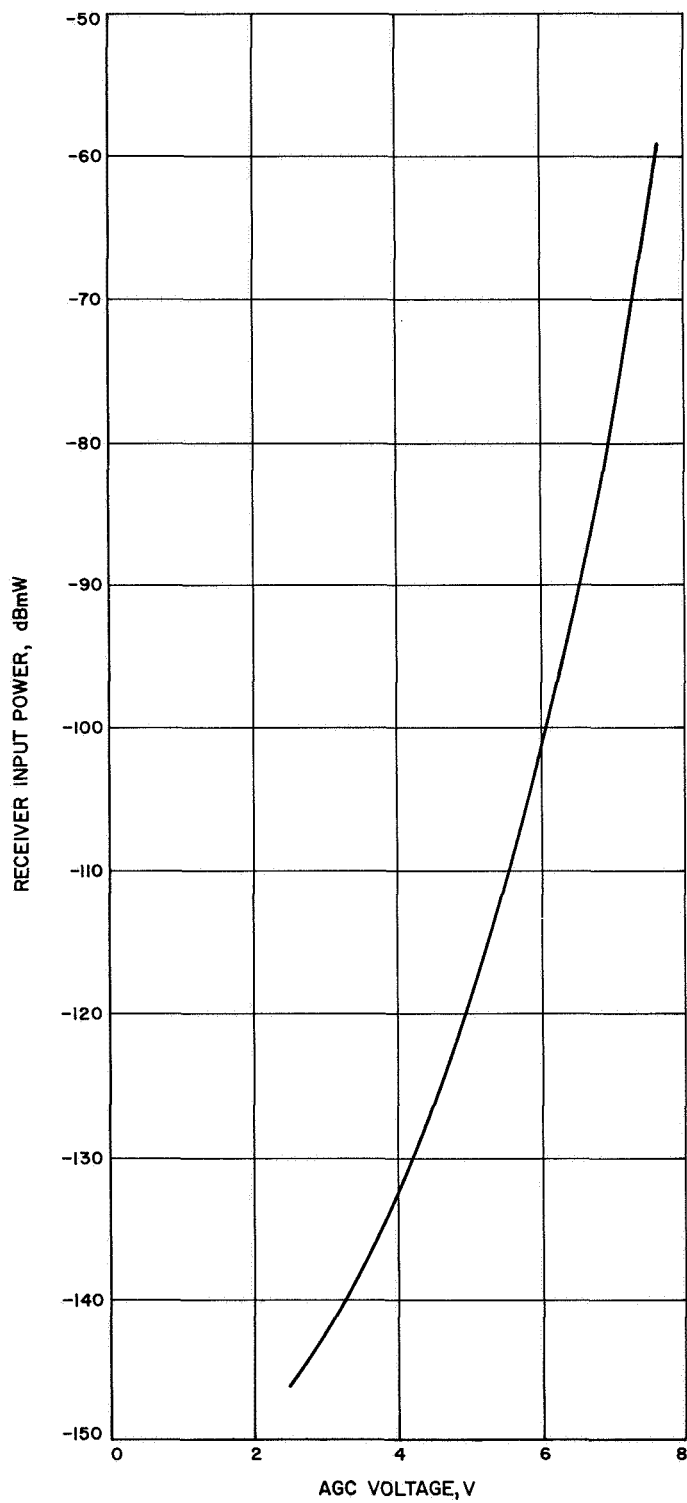


Fig. 17. AGC sensitivity characteristic

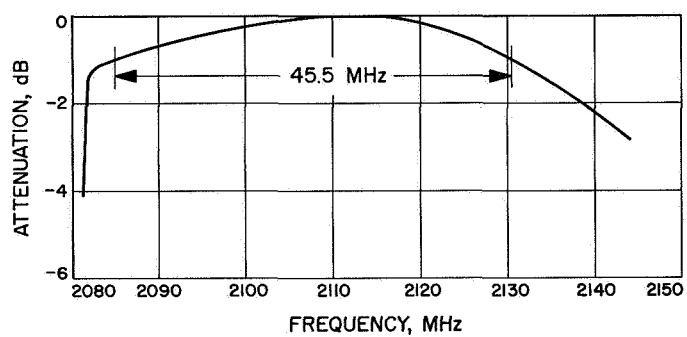


Fig. 18. Transmitter bandwidth at antenna

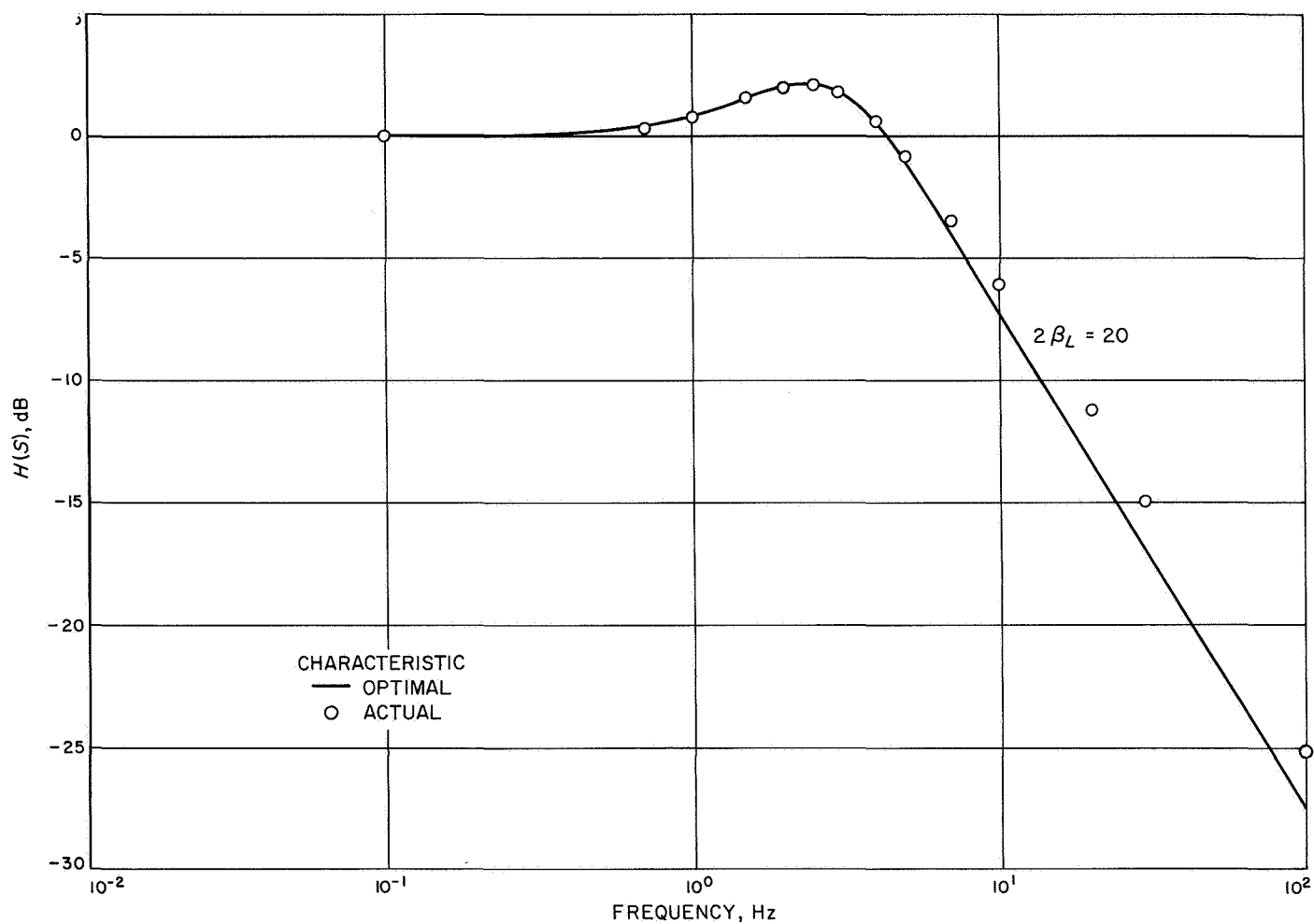


Fig. 19. Exciter closed-loop transfer function response

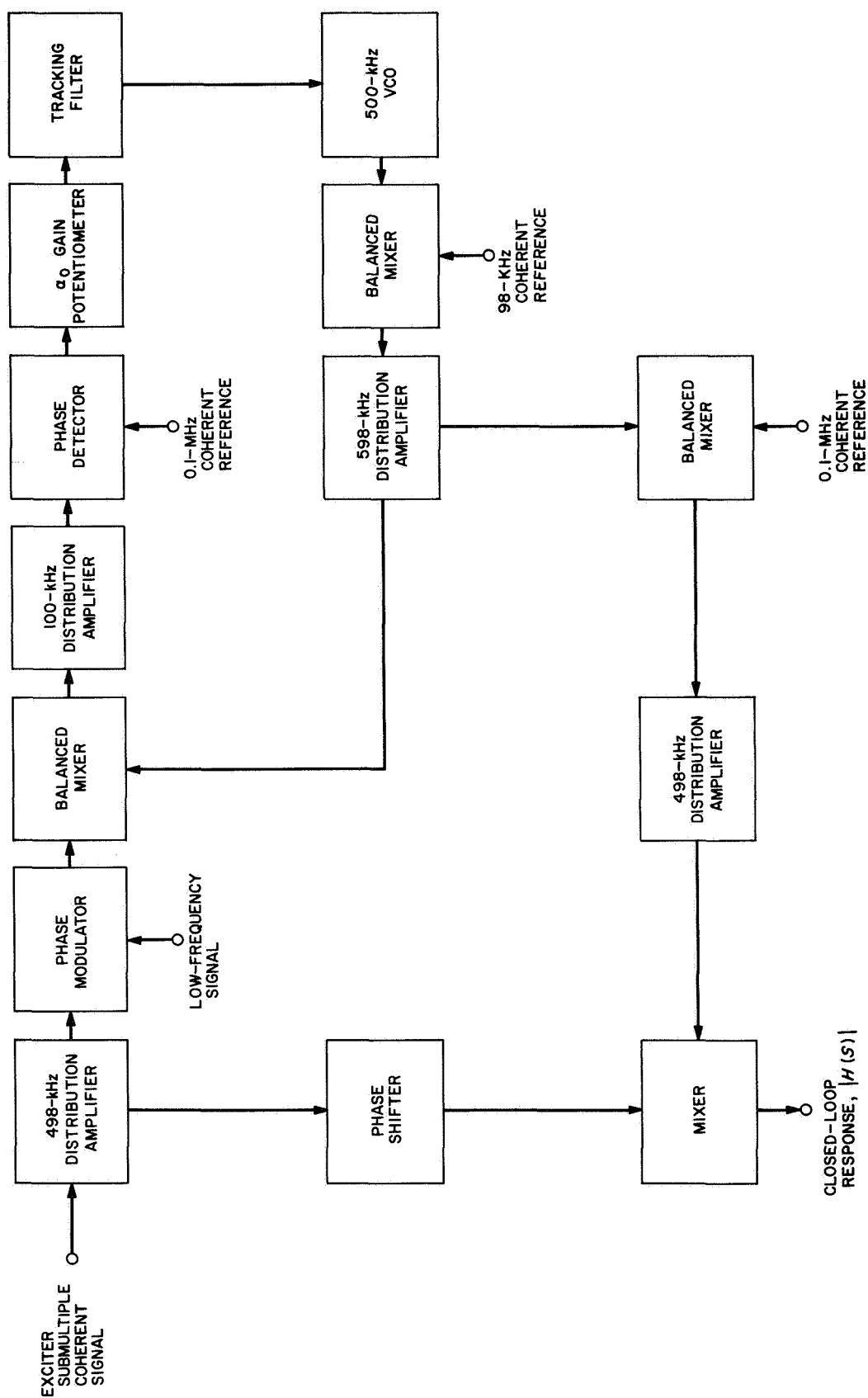


Fig. 20. Block diagram for measuring ranging receiver closed-loop response

Ranging receiver loop. The method for measuring the ranging receiver closed-loop response, as well as the response for the code clock, is shown in Fig. 20. The optimal threshold closed-loop response for the three different bandwidths is shown in Fig. 21. The threshold bandwidths were measured by adjusting the α_0 gain potentiometer to the threshold limited suppression factor value shown in Fig. 9.

Code clock transfer loop. The optimal and actual code clock transfer loop response is shown in Fig. 22. The block diagram used for measuring the response of the loop is the same as the ranging receiver with the α_0 gain potentiometer shorted out. (The code clock loop is a strong signal loop.)

b. System agility. The use of the word agility in this connotation will refer to the capability of coherently

switching from any discrete frequency to any other discrete frequency within the system bandwidth. This switching is accomplished by programming the receiver and exciter synthesizers. A list of the specified preprogrammed frequencies for coherent operation of all the DSN and MSFN channels is shown in Table 4.

System agility configuration. The block diagram for testing frequency agility is shown in Fig. 23. This diagram shows how the transmitter and receiver are coherently locked through a transponder. The number of transponders between which one may switch is limited only by the predetection bandwidth of the receiver, i.e., the frequency separation for adjacent transponders should not be closer than the receiver predetection noise bandwidth. Other requirements, such as telemetry or ranging data bandwidths, may require further frequency separation. The experiment for verifying system frequency agility used two transponders whose center frequency

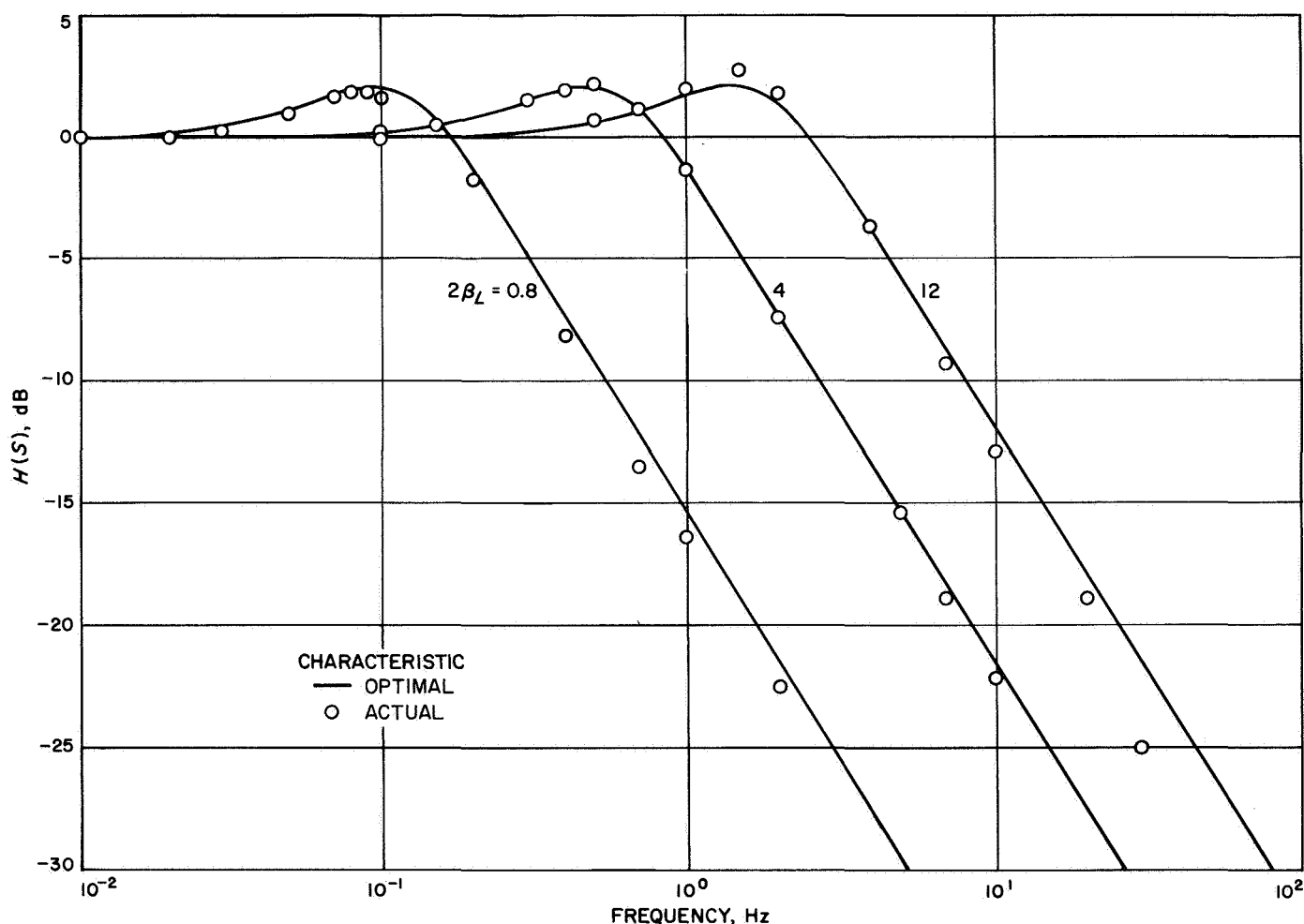


Fig. 21. Ranging receiver closed-loop transfer function response

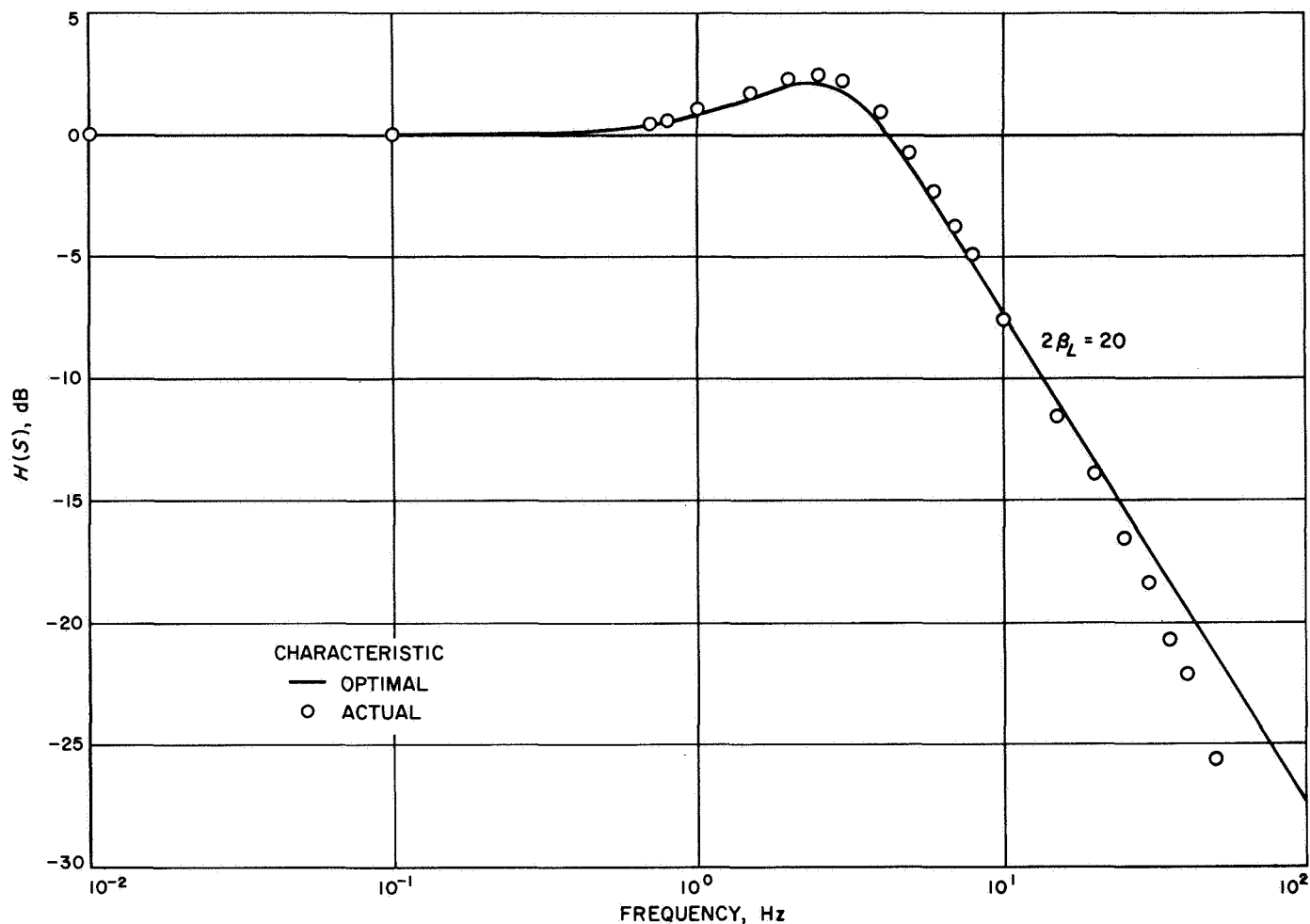


Fig. 22. Code clock closed-loop transfer function response

was near the bandwidth edges of the system. (Referring to Table 4, transponder 1 required exciter channel MSFN-1b and receiver channel MSFN-3a for two-way lock and transponder 2 required exciter channel 24b and receiver channel 24a for two-way lock.)

Verifying data of system agility. For a system to be frequency agile, two-way lock must be accomplished rapidly after switching, to achieve coherent operation. To verify the frequency agile receiver capability to achieve coherent operation after switching, the following pictures show the time after switching for two-way lock to be achieved by monitoring the dynamic phase error of the reference receiver and the 0-deg RF doppler simultaneously.

(1) Figure 24 shows the time to lock when switched from a medium power signal (-111 dBmW) transponder 1 to a strong signal (-79 dBmW) transponder 2.

The time to achieve coherent operation again was less than 50 ms. The RF carrier reference receiver was set for a closed-loop bandwidth of 5 Hz and a low AGC loop bandwidth.

(2) Figure 25 shows the time to lock when switched from a weak signal (-143 dBmW) to a weak signal (-138 dBmW). Since both signals are near threshold conditions, it is not possible to tell when two-way lock is achieved from the dynamic phase error picture, but lock is readily seen from the 0-deg RF doppler. The time to achieve lock was less than 30 ms. The same system configuration was used for this picture as in Fig. 24.

(3) Figure 26 shows the time to lock when switched from a strong signal (-70 dBmW) to a strong signal (-70 dBmW). Two-way lock is achieved within 20 ms. A 5-Hz closed-loop bandwidth was set on the reference receiver.

Table 4. Preprogrammed synthesizer frequencies for DSN and MSFN channels

Exciter channel number	Exciter frequency synthesizer $\left(90 - \frac{F_s}{32}\right)$, MHz	Transmitter frequency F_s , MHz	Receiver channel number	Receiver frequency synthesizer $\left(90 - \frac{F_s \left(\frac{240}{221}\right) - 50}{32}\right)$, MHz	Received frequency $F_s \left(\frac{240}{221}\right)$, MHz
—	—	—	1a	19.994,219	2290.185
—	—	—	2a	19.982,656	2290.555
—	—	—	3a	19.971,094	2290.925
—	—	—	4a	19.959,500	2291.296
5b	24.054,906	2110.243	5a	19.947,938	2291.666
6b	24.044,250	2110.584	6a	19.936,344	2292.037
7b	24.033,594	2110.925	7a	19.924,781	2292.407
8b	24.022,938	2111.266	8a	19.913,219	2292.777
9b	24.012,281	2111.607	9a	19.901,625	2293.148
10b	24.001,625	2111.948	10a	19.890,063	2293.518
11b	23.990,969	2112.289	11a	19.878,500	2293.888
12b	23.980,313	2112.630	12a	19.866,906	2294.259
13b	23.969,656	2112.971	13a	19.855,344	2294.629
14b	23.959,000	2113.312	14a	19.843,750	2295.000
15b	23.948,344	2113.653	15a	19.832,188	2295.370
16b	23.937,688	2113.994	16a	19.820,625	2295.740
17b	23.927,031	2114.335	17a	19.809,031	2296.111
18b	23.916,375	2114.676	18a	19.797,469	2296.481
19b	23.905,719	2115.017	19a	19.785,906	2296.851
20b	23.895,063	2115.358	20a	19.774,313	2297.222
21b	23.884,406	2115.699	21a	19.762,750	2297.592
22b	23.873,750	2116.040	22a	19.751,188	2297.962
23b	23.863,094	2116.381	23a	19.739,594	2298.333
24b	23.852,438	2116.722	24a	19.728,031	2298.703
25b	23.841,750	2117.064	25a	19.716,438	2299.074
26b	23.831,094	2117.405	26a	19.704,875	2299.444
27b	23.820,438	2117.746	27a	19.693,313	2299.814
28b	23.809,781	2118.087	—	—	—
29b	23.799,125	2118.428	—	—	—
30b	23.788,469	2118.769	—	—	—
31b	23.777,813	2119.110	—	—	—
32b	23.767,156	2119.451	—	—	—
33b	23.756,500	2119.792	—	—	—
—	—	—	MSFN-1a	20.546,875	2272.500
—	—	—	MSFN-2a	20.390,625	2277.500
MSFN-1b	24.318,686	2101.802	MSFN-3a	20.234,375	2282.500
MSFN-2b	24.174,813	2106.406	MSFN-4a	20.078,125	2287.500

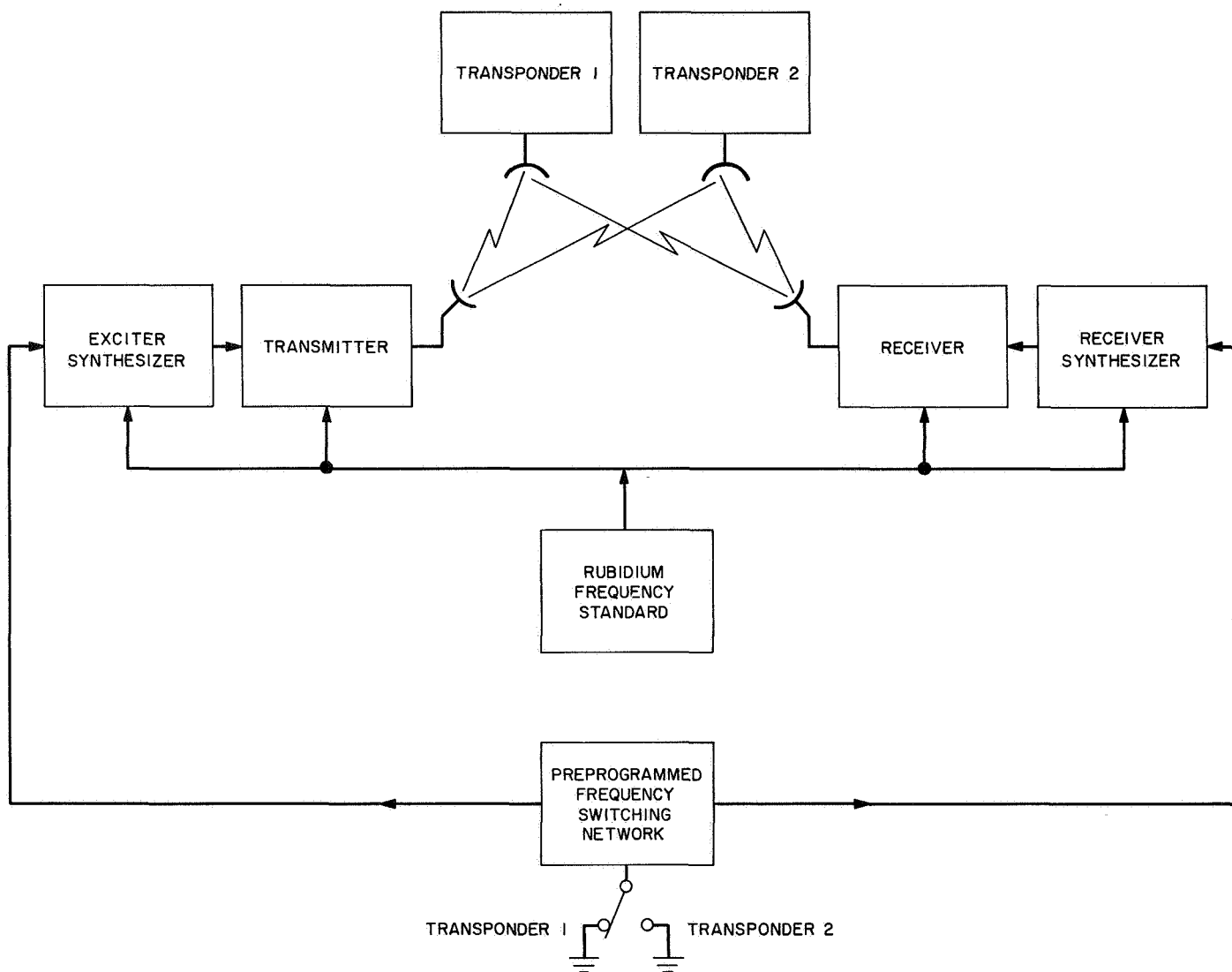
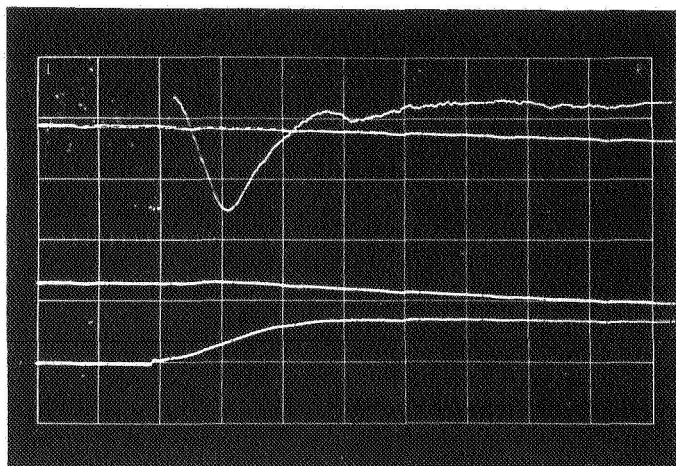
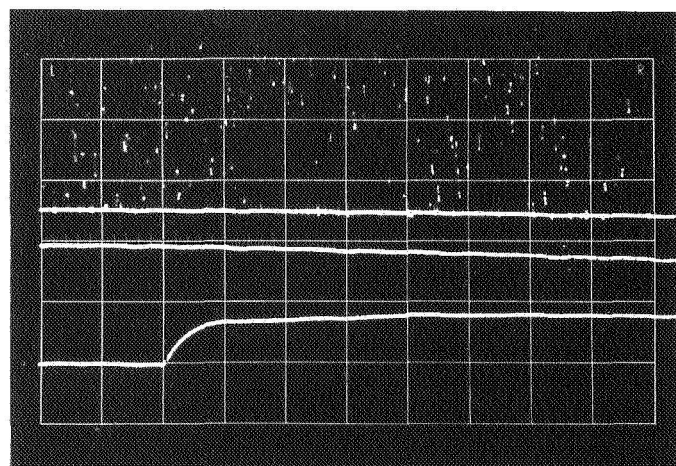


Fig. 23. Frequency agile testing block diagram



TRACE 1: REFERENCE RECEIVER DYNAMIC PHASE ERROR
TRACE 2: TRANSPONDER 2 AGC
TRACE 3: REFERENCE RECEIVER AGC
TRACE 4: 0° RF DOPPLER
TIME BASE: 10 ms/DIVISION

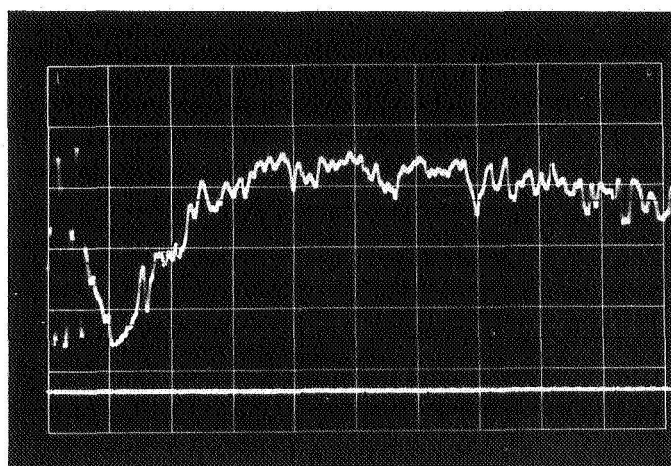
Fig. 24. Two-way lock for medium-to-strong signal



TRACE 1: REFERENCE RECEIVER DYNAMIC PHASE ERROR
TRACE 2: REFERENCE RECEIVER AGC
TRACE 3: TRANSPONDER 2 AGC
TRACE 4: 0° RF DOPPLER
TIME BASE: 10 ms/DIVISION

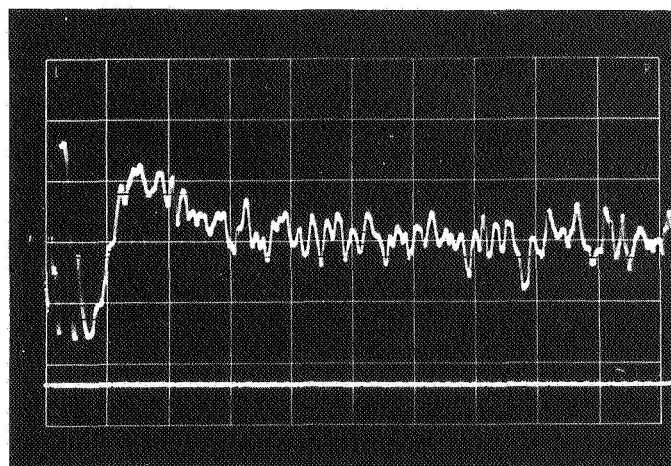
Fig. 25. Two-way lock for weak-to-weak signal

(4) Figure 27 shows the time to lock when switched from a strong signal (-70 dBmW) to a strong signal (-70 dBmW). Coherent operation with the new signal was achieved within 15 ms. A 152-Hz closed-loop bandwidth was set on the reference receiver.



TRACE 1: REFERENCE RECEIVER DYNAMIC PHASE ERROR
TRACE 2: REFERENCE RECEIVER AGC
TIME BASE: 5 ms/DIVISION

Fig. 26. Two-way lock for 5-Hz closed-loop bandwidth



TRACE 1: REFERENCE RECEIVER DYNAMIC PHASE ERROR
TRACE 2: REFERENCE RECEIVER AGC
TIME BASE: 5 ms/DIVISION

Fig. 27. Two-way lock for 152-Hz closed-loop bandwidth

4. Conclusions

The prototype frequency agile receiver remains coherent after switching from transponder 1 to transponder 2 or vice versa without any operator adjustments. The data shows that the time required to achieve coherency when switching is independent of the received signal strength (compare Figs. 24 and 25) and of the receiver closed-loop bandwidth (compare Figs. 25, 26, and 27).

The parameter which does change the time interval between being coherent with one transponder and another when switching is the preprogrammed frequency switching network. This network adjusts the frequency of the exciter and receiver synthesizers. To achieve the minimum out-of-lock time after switching, the voltage-controlled oscillator of the transponder which is providing the new two-way lock must not change frequency from the out-of-lock (free running) operation to the phase-locked operation. When the above condition is satisfied, the exciter and receiver synthesizers know precisely the center frequencies they must have after switching, thereby minimizing the out-of-lock time.

G. Solution to Phase Jitter Problem in MSFN

Range Receiver, R. W. Tappan and J. H. Wilcher

The receiver-exciter-ranging subsystem in the MSFN was recently modified to operate with a fixed ranging clock frequency (Block IIB configuration described in SPS 37-42, Vol. III, pp. 77-83). This modification caused phase jitter to appear in the range receiver clock and clock code transfer loops during ranging code acquisition and range tracking. The prototype receiver-exciter-ranging subsystem located at JPL was converted to the MSFN configuration and tested to determine the origin of the interference. Periodic phase jitter with an amplitude of 20 deg peak-to-peak (3.3 deg rms) was noted during code acquisition (in program states p3 and p4) and during range tracking (in program state p7). The frequency of the phase jitter was measured and found to be equal to the difference between the 10.496 MHz that is derived from the atomic frequency standard and the 10.496 MHz that is derived from the 20-MHz oscillator.

An increase in the phase jitter in the range clock loop raises the noise power level in the range receiver, thereby increasing the acquisition error probability for a given signal-power-to-noise-power ratio. It also increases the scatter of the individual points in the range data about the mean or average value.

Figure 28 shows that one of the inputs to the balanced detector is a 10.496-MHz signal from the reference receiver. The 496-kHz portion of this signal is the ranging clock frequency that is derived by multiplying the 1.0-MHz signal from the atomic frequency standard by 496/1000. The other input to the balanced detector is the local model of the ranging code modulated on a

10-MHz carrier by the phase switch. This local model of the code contains square-wave components of the code, including a 496-kHz component, and also harmonics that are related to the length of the code. When one of the harmonic frequencies of the code length occurs at a frequency near 10.496 MHz, it is combined with the received ranging signal in the balanced detector to produce periodic phase jitter on the 496-kHz output of the phase detector.

The ranging subsystem uses the A code component in program states p3, p4, and p7 to generate the $\bar{X}A$ and \bar{X} ($AB + BC + AC$) code component combinations, respectively. The length of the A code is 31 bits. At a clock frequency of 496 kHz, the bit frequency is 992 kHz, and the repetition rate of the code is 32.000 kHz. The 328th harmonic of this frequency is 10.496 MHz, the frequency of the clock component of the received ranging signal. The A component of the code does not appear separately in the code transmitted to the phase switch; however, it is present at the input to the code combiner, and can influence the digital clock and the dc power during the combining operation. A slight phase and amplitude distortion will appear on the code output of the ranging subsystem.

The $\bar{X}A$ code, which is generated in program states p3 and p4, also generates a harmonic frequency of 10.496 MHz. The $\bar{X}A$ code has a length of 11×31 bits. At a bit frequency of 992 kHz, the code repetition rate is 2.90909 kHz, which is a submultiple of 10.496 MHz.

The power in these interference signals is quite small; however, if it is as large as 76 dB below the power level of the ranging code, the interference signal power is equal to the incoming ranging signal power.

Two solutions to this problem are being implemented, an interim solution and a permanent solution. The interim solution offsets the frequency of the 20-MHz reference oscillator in the receiver-exciter to place the beat frequency well outside the loop noise bandwidth of the range receiver. The oscillator frequency must be monitored and returned to the required offset, when necessary. The permanent solution changes the ranging clock frequency to place the harmonic products of the ranging code length outside the bandwidth of the range receiver by replacing the 496/1000 frequency multiplier with a 495.833/1000 frequency multiplier. Figures 29 and 30 illustrate the differences between the two frequency multipliers.

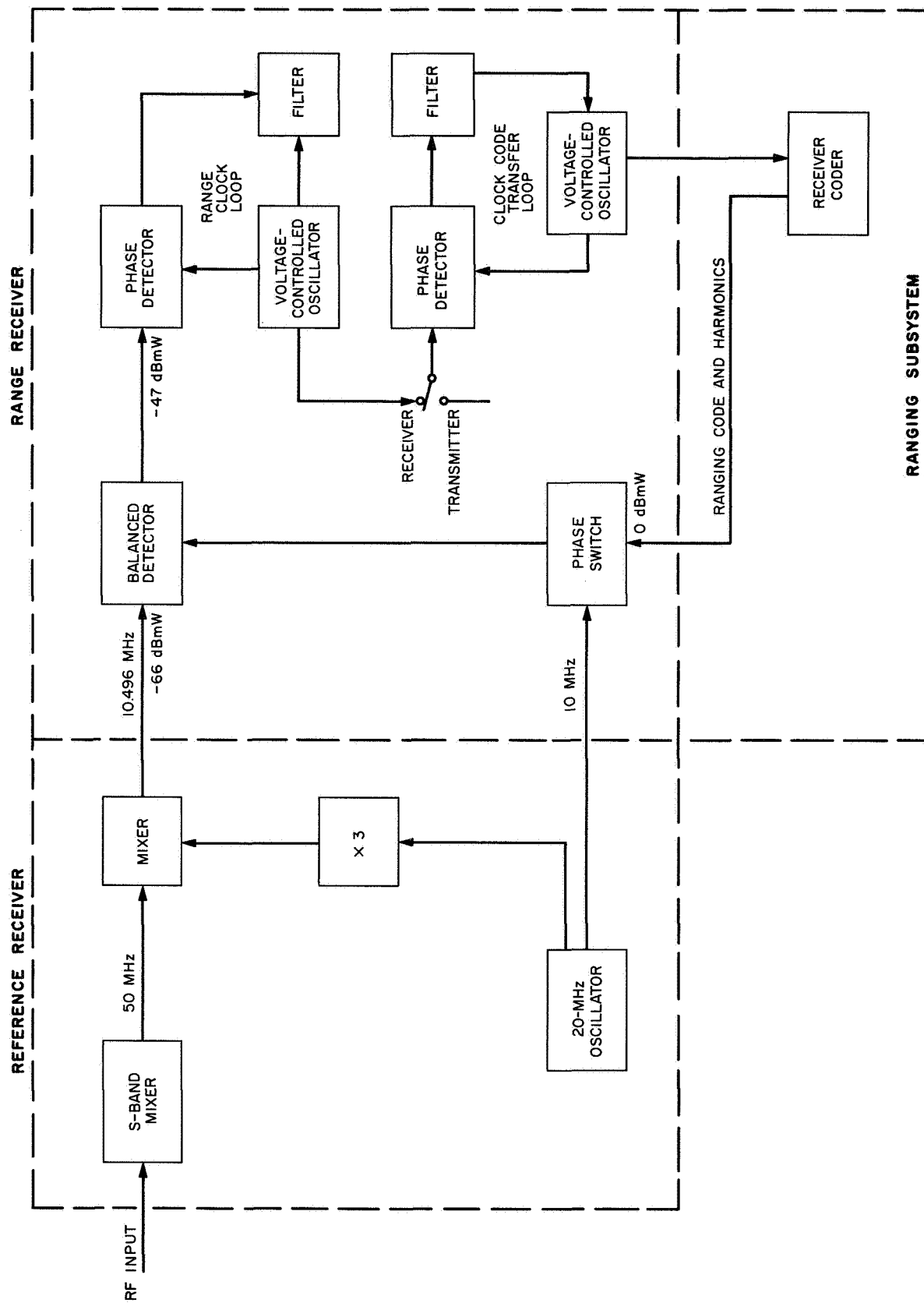


Fig. 28. Ranging simplified block diagram

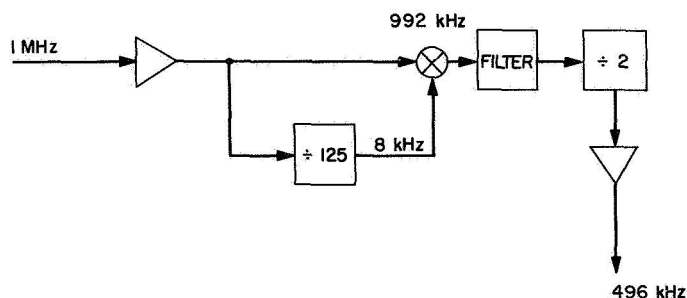


Fig. 29. 496-kHz frequency multiplier

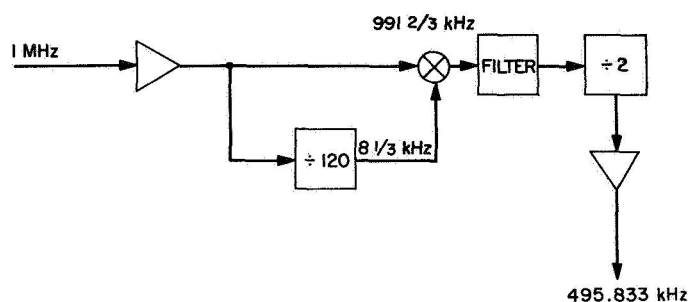


Fig. 30. 495.833-kHz frequency multiplier

H. 450-kW 2.388-GHz Transmitter,

C. P. Wiggins and R. L. Leu

1. Introduction

Testing of the high-power transmitter was started during this reporting period, using a non-radiating type RF calorimetric load. Development of the various components has been in process for approximately one and one-half years; this is the first time they have been operated as a system. The tests are being conducted at the DSS 13 high-power test facility.

2. Transmitter

The transmitter, shown in Fig. 31 with doors closed, contains the klystron and waveguide components behind the doors, coolant distribution and monitoring in the right compartment, and electrical instrumentation and wiring in the left side. The doors have been opened in Figs. 32 and 33 to show the klystron mounted on the focus magnet and filament supply, and the waveguide directional coupler.

3. Klystron

The performance of the klystron has been better than previously anticipated (SPS 37-43, Vol. III, pp. 108-111).

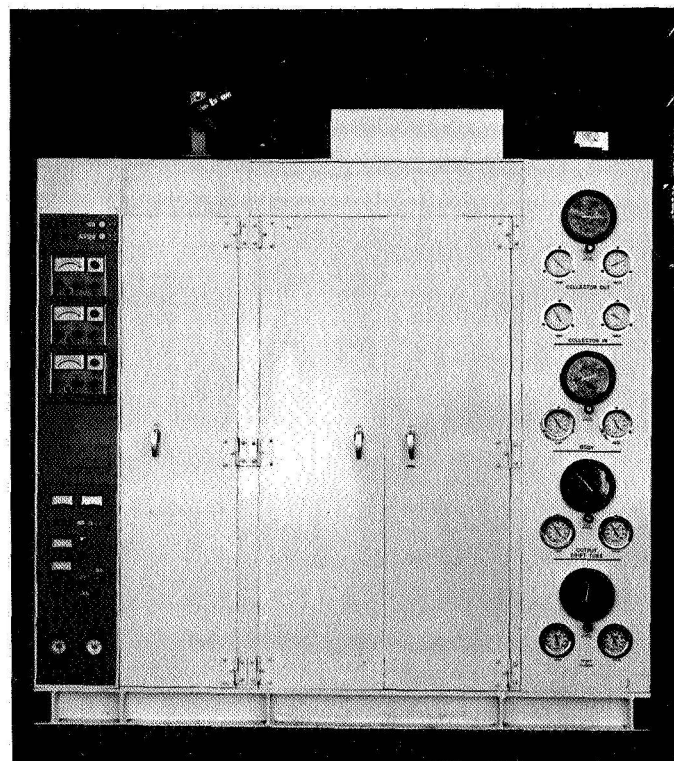


Fig. 31. 450-kW transmitter (front view, doors closed)

The contractor reported power outputs as high as 560 kW at 56% beam efficiency (RF output power/dc beam power) and during the acceptance tests, demonstrated to JPL, power outputs up to 510 kW at 54.5% efficiency. At 20-MHz bandwidth (1 dB points), the gain was 57 dB. However, the contractor has advised JPL that the klystron is rated for only 450-kW power output. At this reduced level, the beam efficiency was measured by JPL to be 49.7%.

Klystron power output as a function of RF drive level is illustrated by Fig. 34. Saturation occurs at 1.1-W drive for 450-kW output. The beam voltage was 62 kV, the center frequency was 2.388 GHz, and the bandwidth 20 MHz.

The effects of beam voltage on bandwidth and power output are shown in Figs. 35 and 36. In both cases, the klystron tuning was fixed; in Fig. 35 the drive was maintained at 1.1 W, and in Fig. 36 the klystron was resaturated at center frequency for each successively lower beam voltage.

4. RF Calorimetric Load

The RF load is used as the primary standard for measurement of transmitter power output. It also provides a

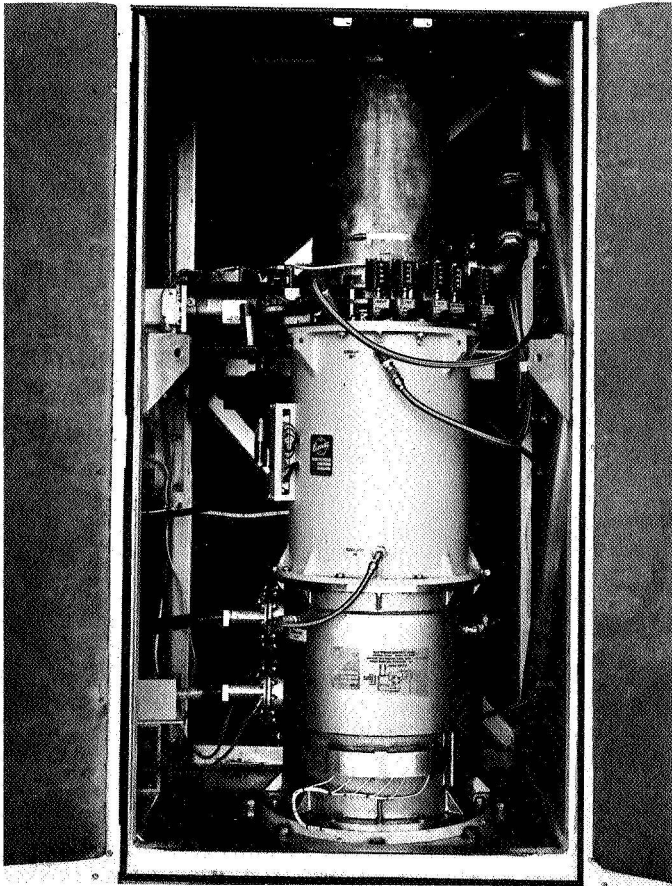


Fig. 32. 450-kW transmitter (door open, showing klystron, magnet, and filament supply)

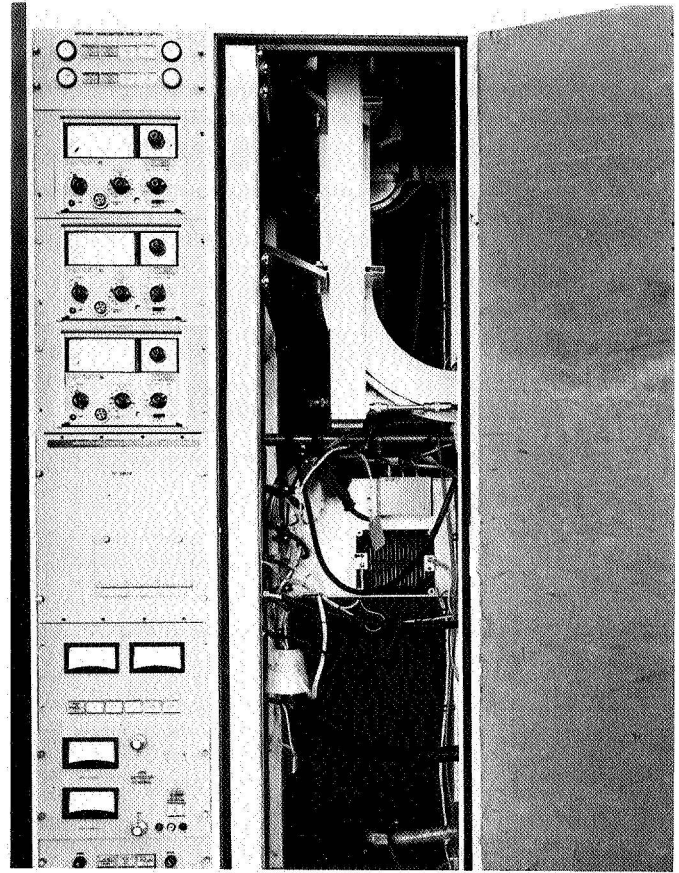


Fig. 33. 450-kW transmitter (door open, showing directional coupler)

non-radiating termination for the klystron output waveguide. The high-power loads used at JPL have employed the technique of coupling the RF power into circulating water. By measurement of the flow and the rise in temperature of the water, the energy absorbed by the water can be determined. These loads consist of an RF waveguide and matching transformer, an RF window, and a water tank. The window is transparent to RF but blocks the water from entering the waveguide. It is necessary that the load be well matched, as mismatches distort the bandpass characteristics of the klystron.

Two 500-kW loads were procured to JPL specifications, but under test these loads were unstable at powers above 150 kW and developed water leaks into the waveguide. They have been returned to the vendor. Tests are proceeding using a different type load loaned by the klystron manufacturer. It was not designed to meet the JPL VSWR specification of 1.07:1 over a frequency range of 2.303 to 2.473 GHz and inlet water temperature of 0° to 62°C.

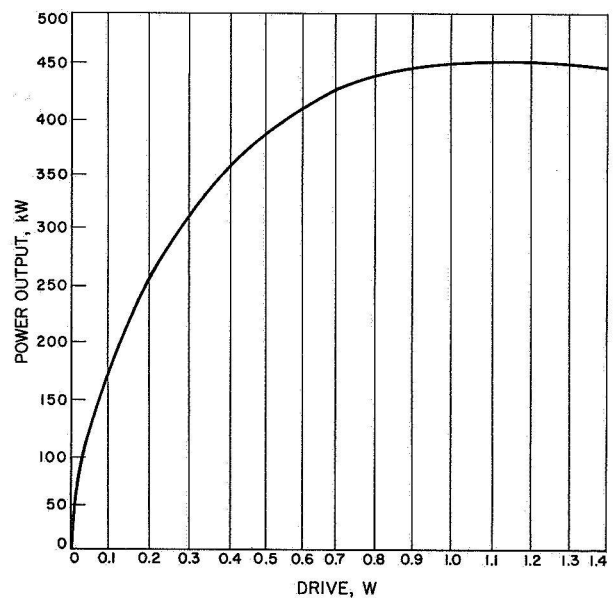


Fig. 34. RF power output vs RF drive [center frequency = 2.388 GHz; 20-MHz bandwidth (1 dB)]

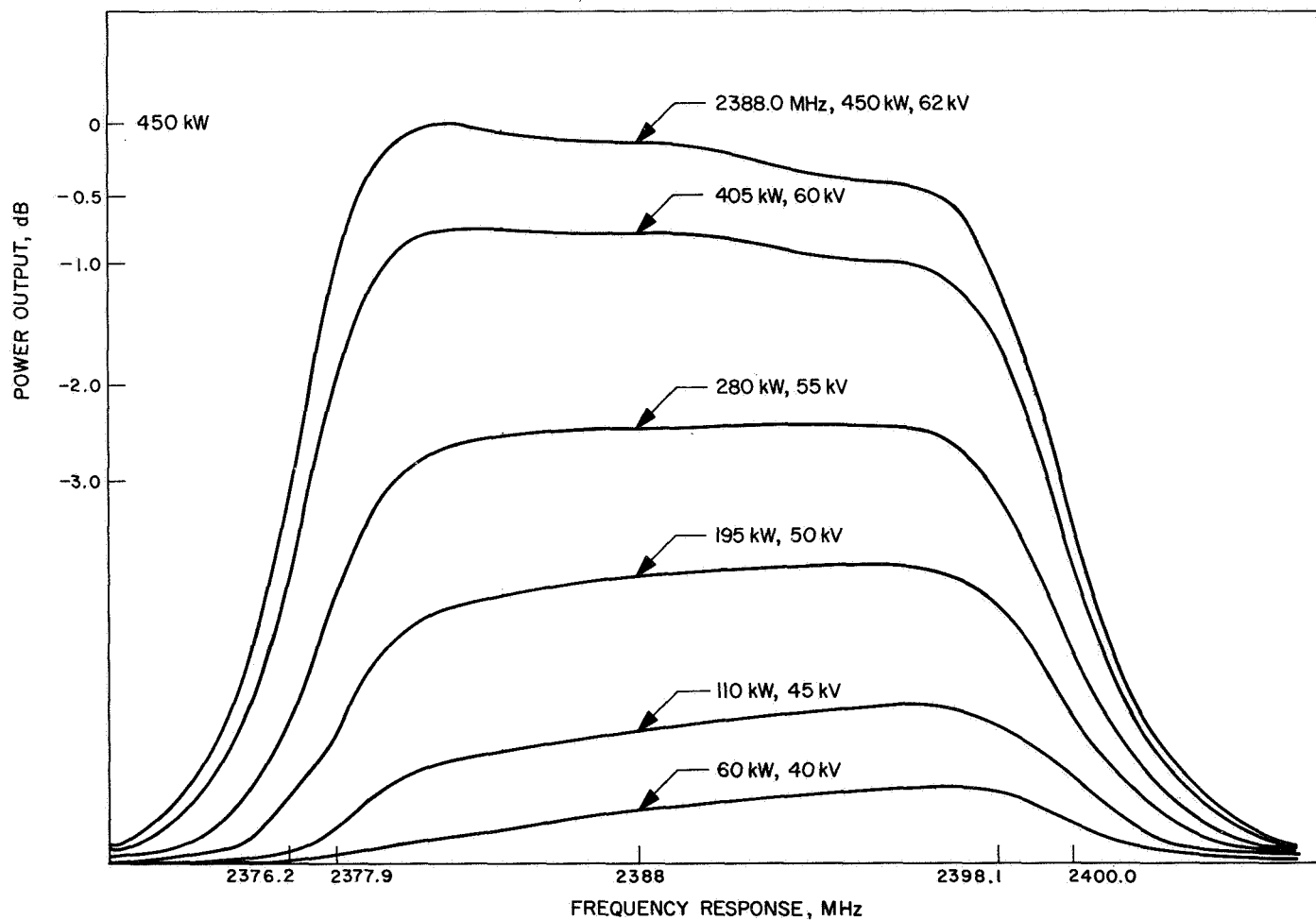


Fig. 35. Power output vs frequency response as a function of beam voltage for constant drive

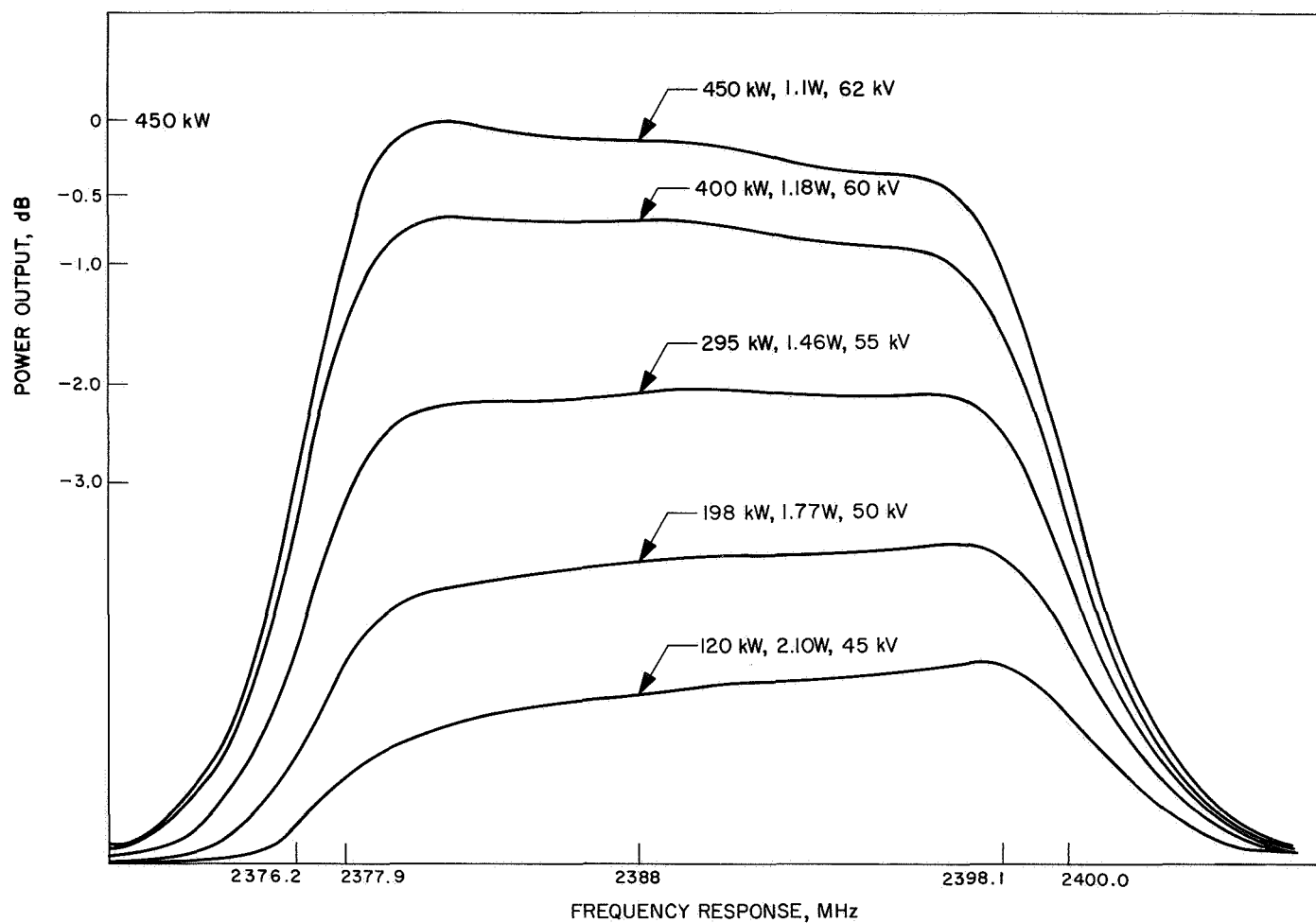


Fig. 36. Power output vs frequency response as a function of beam voltage at saturation drive

5. Future Plans

Tests on the system are continuing. During the next reporting period, the transmitter will be installed on the 85-ft antenna at DSS 13.

1. DSN 20-kW Transmitter, B. W. Harness

1. Introduction

The seven DSN 20-kW transmitters have been redesigned to effect improvement in the following areas:

- (1) Increase the accuracy of forward, reflected, and drive power metering.
- (2) Provide more convenient operating conditions on the klystron cabinet and control panels.
- (3) Substitute an improved device for the resistive loop couplers.

Three major areas included in the subject transmitter alteration are:

- (1) Installation of a newly developed 60-kW broad-wall waveguide directional coupler.
- (2) Klystron cabinet modification, including remote control panels.
- (3) Water load flow and temperature monitor installation.

2. 60-kW Broadwall Multihole Waveguide Directional Coupler

The DSN transmitters presently use a resistive loop waveguide directional coupler for forward and reflected power monitoring. Although the resistive loop type of coupler has the advantage of compactness, it is inferior to the multihole coupler in bandwidth and directivity and is susceptible to loss of calibration due to accidental movement of the loops. A waveguide multihole direc-

tional coupler developed for use in the 20-kW transmitter subsystem was installed in transmitter 2 at DSS 11 in place of the resistive loop coupler. At the three DSN dual transmitter stations it is possible to couple the outputs of both transmitters through the combiner with a maximum resultant output of 54 kW. For this reason, the newly developed directional coupler was designed for 60 kW.

The new waveguide multihole dual coupler has two separate arms: one arm for forward power monitoring and one arm for reflected power monitoring. The secondary arms include waveguide-to-coaxial transitions equipped with type N female connectors. Since the RF loads were designed for maximum directivity, there are no adjustments to achieve the design directivity of greater than 45 dB at center frequency. Table 5 presents the critical specifications for the unit, and Fig. 37 is a photograph of the unit. Table 6 shows the test results for the directional coupler installed at DSS 11.

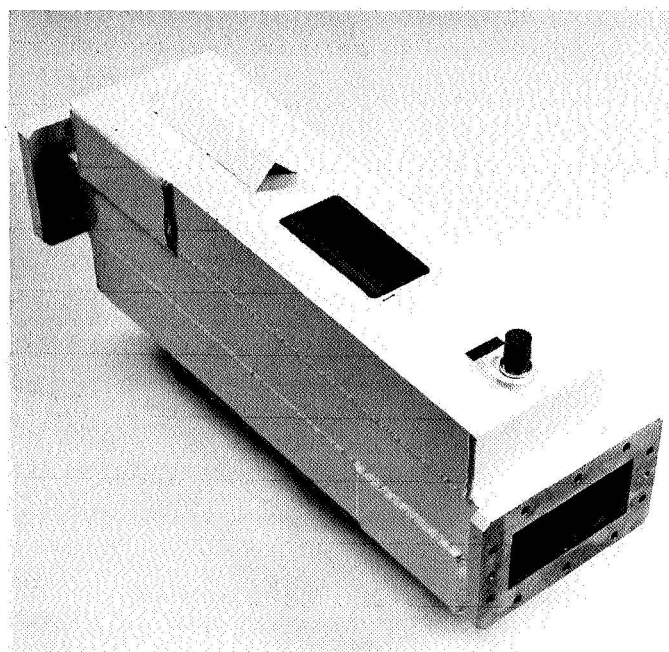


Fig. 37. Waveguide directional coupler

Table 5. Design specifications for waveguide directional coupler

Coupling coefficient, dB	Maximum coupling coefficient variation, dB	Power rating, kW	Band center frequency, GHz	Directivity, dB	Maximum VSWR
Forward 50 ± 1.0	0.20	60	2.110	30	1.03:1.0
Reverse 40 ± 1.0	0.20	—	—	40	—

Table 6. Test results for SN 001 waveguide directional coupler

Frequency, GHz	Coupling coefficient, dB		Directivity, dB		VSWR	Maximum coupling variation, dB
	Forward	Reverse	Forward	Reverse		
2.090	50.13	40.29	37.89	41.00	<1.03:1.00	0.10
2.100	50.22	40.37	41.77	42.00	<1.03:1.00	
2.110	50.20	40.38	45.92	41.90	<1.03:1.00	
2.120	50.22	40.39	43.82	40.10	<1.03:1.00	
2.130	50.22	40.37	39.70	41.60	<1.03:1.00	

3. Transmitter Klystron Cabinet Modification

The klystron cabinet modification affects the klystron cabinet in the antenna room, the power supply cabinet control panel, and the control panel assembly located in the station control room. Figure 38 shows the configuration of the klystron cabinet before modification. The control panels in the power supply cabinet and the control room cabinet are identical in appearance to control panel assembly A1 in the klystron cabinet. Before modification, the RF power was monitored using crystal detectors in the klystron cabinet whose outputs were applied to three sets of remote meters in the three control panels. The crystal detector outputs were nonlinear with respect to input power and the panel meter scales were marked 0-1, making it difficult to determine the actual power level. Forward and reflected power were monitored (switch-selectable) on one microwave power meter in the RF calibration panel in the klystron cabinet. The transmitter upgrade allows deletion of the crystal detectors and application of the sampled forward, reflected, and drive power to *three* microwave power meters whose recorded outputs are applied to three sets of calibrated panel meters substituted for those mentioned above. The existing power meter (and associated filter and thermistor mount) from the RF calibration panel was re-used in the modified subsystem along with two new microwave power meters and thermistor mounts, all mounted in a new RF calibration panel along with an attenuator at the input of each power meter. The attenuators are used for calibration of the forward, reflected, and drive power meters. The new RF calibration panel was located in the top of bay 1 of the klystron cabinet. The other spaces in bay 1 were replaced with a new hinged panel (for klystron tuning accessibility), a card holder panel (for klystron tuning curve), and a new blank panel.

The flow indicators for RF load, klystron, magnet, and body flow, along with inlet and outlet pressure and temperature, were mounted in a new flow indicator panel.

The new flow indicator panel was located in the top of bay 3 in the space vacated by deletion of the old RF calibration panel. The plumbing and wiring for the relocated flow meter, pressure gauges, and thermometer were rerouted with the copper plumbing being partially replaced by teflon-lined stainless steel flexible tubing to simplify field installation. The modified transmitter klystron cabinet assembly is pictured in Fig. 39.

4. Water Load Flow and Temperature Monitor

The flow and temperature monitors provide remote RF power instrumentation for the 20-kW RF loads. The temperature and flow readout is located in the transmitter rack in the station control room. This permits an absolute power calibration at any time it is possible to switch the transmitter into the load. Previously, it was necessary to discontinue tracking, move the antenna to zenith, and send a man up to the electronics room to perform the calibration. In order to accomplish this instrumentation change, it was necessary to install temperature sensors in the inlet and outlet of each water load, and place a turbine flow meter in the outlet of each water load. A junction box was installed in the antenna room to contain the temperature bridges and amplifiers and to serve as a central cabling point for the sensors. A twenty-four conductor cable transmits the flow and delta temperature data to the control room where it is possible to read the flow and temperature differential on a digital voltmeter. The water load monitor panel in the control room also contains a multiplier to combine flow and temperature measurements to enable the operator to read the RF power in the water loads directly in kilowatts. The water load flow and temperature power measurement technique will be described in detail in a future article.

5. Conclusion

The 20-kW transmitter redesign has been accomplished at DSS 11, transmitter 2, with very satisfactory results.

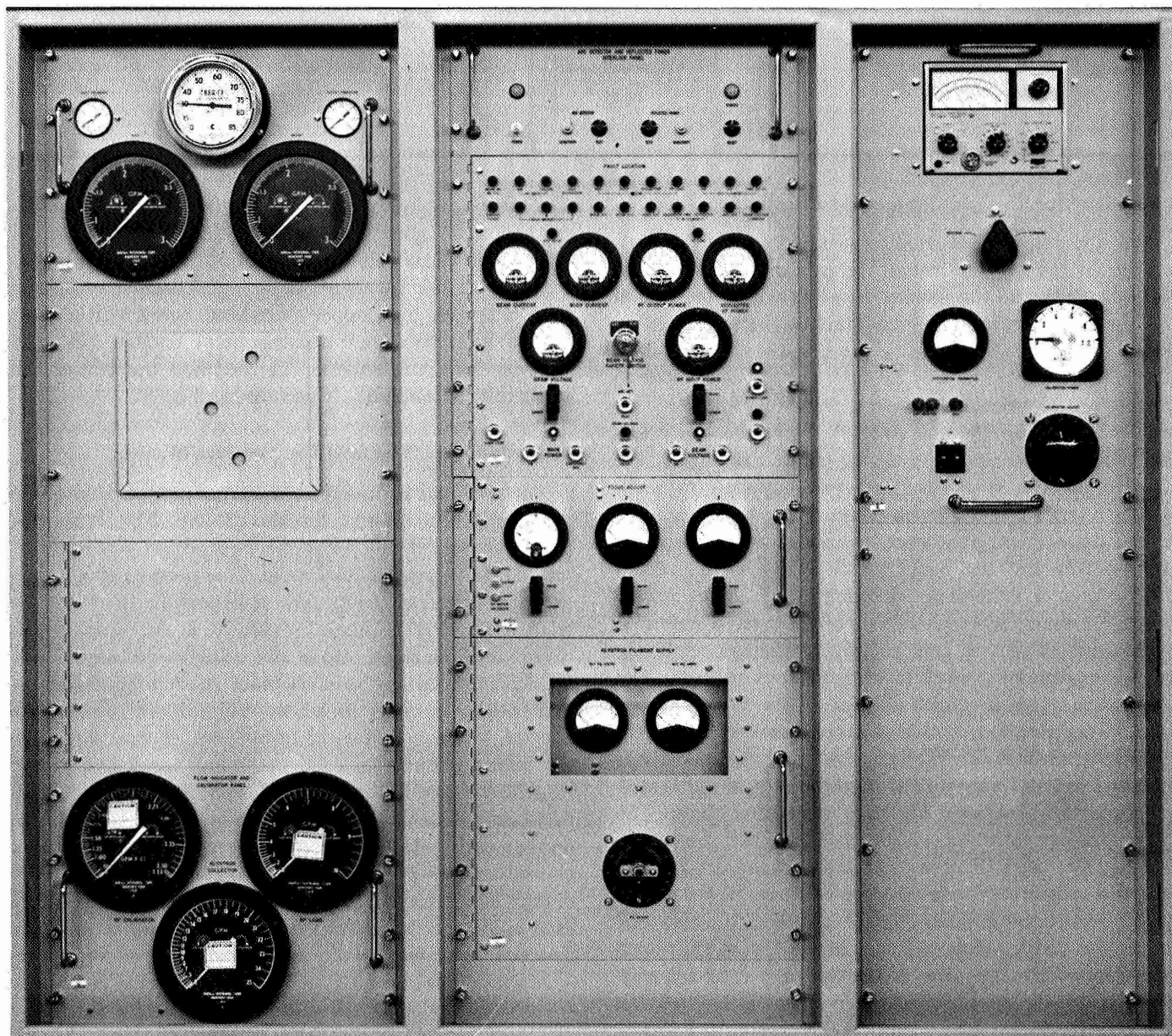


Fig. 38. Klystron cabinet before modification

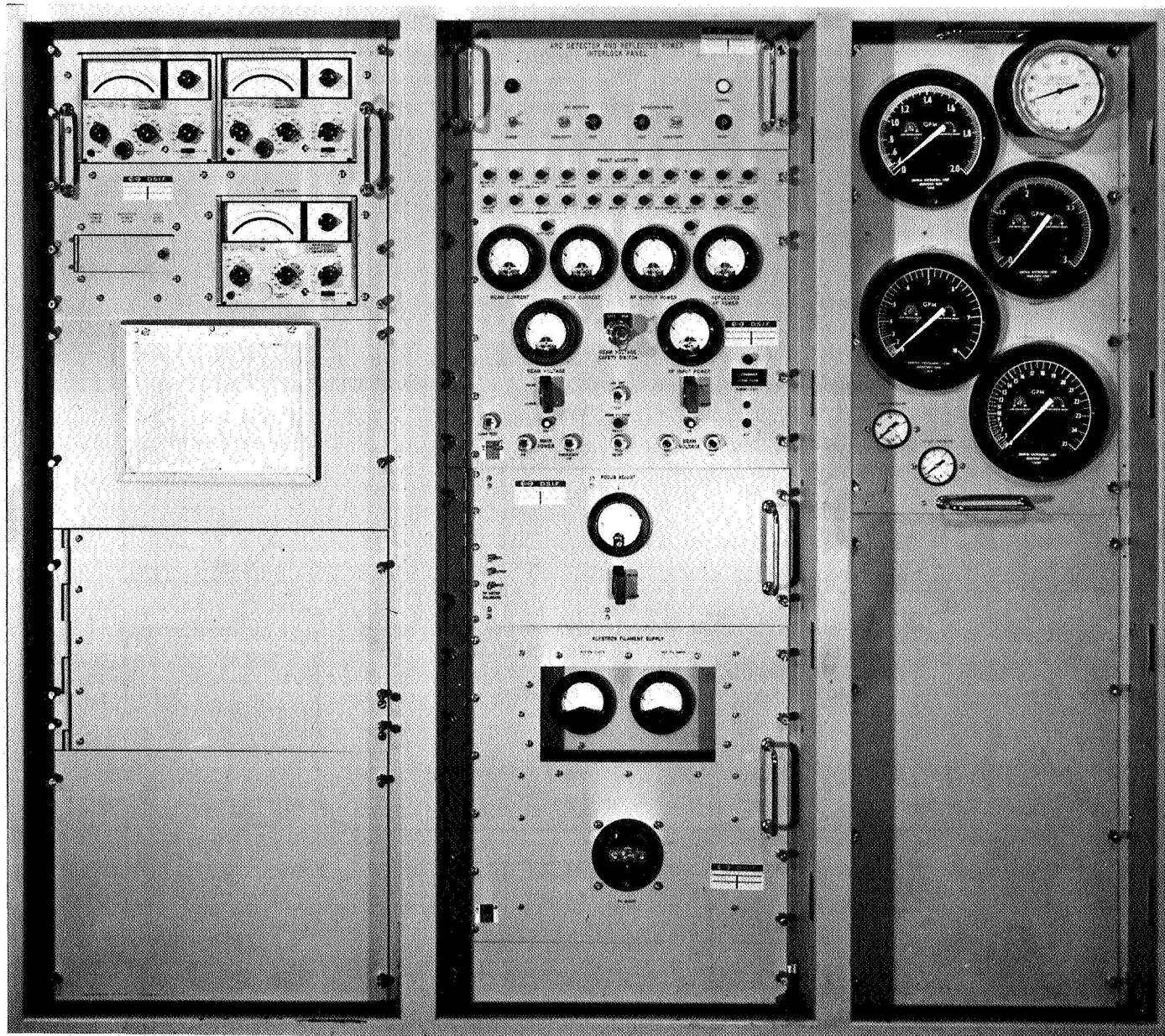


Fig. 39. Klystron cabinet after modification

Since the modification was completed, the transmitter has been successfully operated at output power levels up to 20 kW.

6. Future Plans

The modification kits necessary to accomplish the redesign at the other six 20-kW transmitters are presently being fabricated. It has been scheduled to complete the 20-kW transmitter redesign at DSS 14, DSS 42, and DSS 61 as soon as the kits are available.

J. 500-kW (CW) WR-430 Waveguide Switch Tests, B. W. Harness

1. Introduction

A 500-kW (CW) waveguide switch for the WR-430 waveguide has been developed for use in the S-band high-power development program. The switch is a four-port configuration that will transmit at least 500 kW (CW) in a waveguide system filled with nitrogen at 1.0 atm pressure. The switch stator and rotor are both water-cooled, using a rotary joint in order to prevent differential

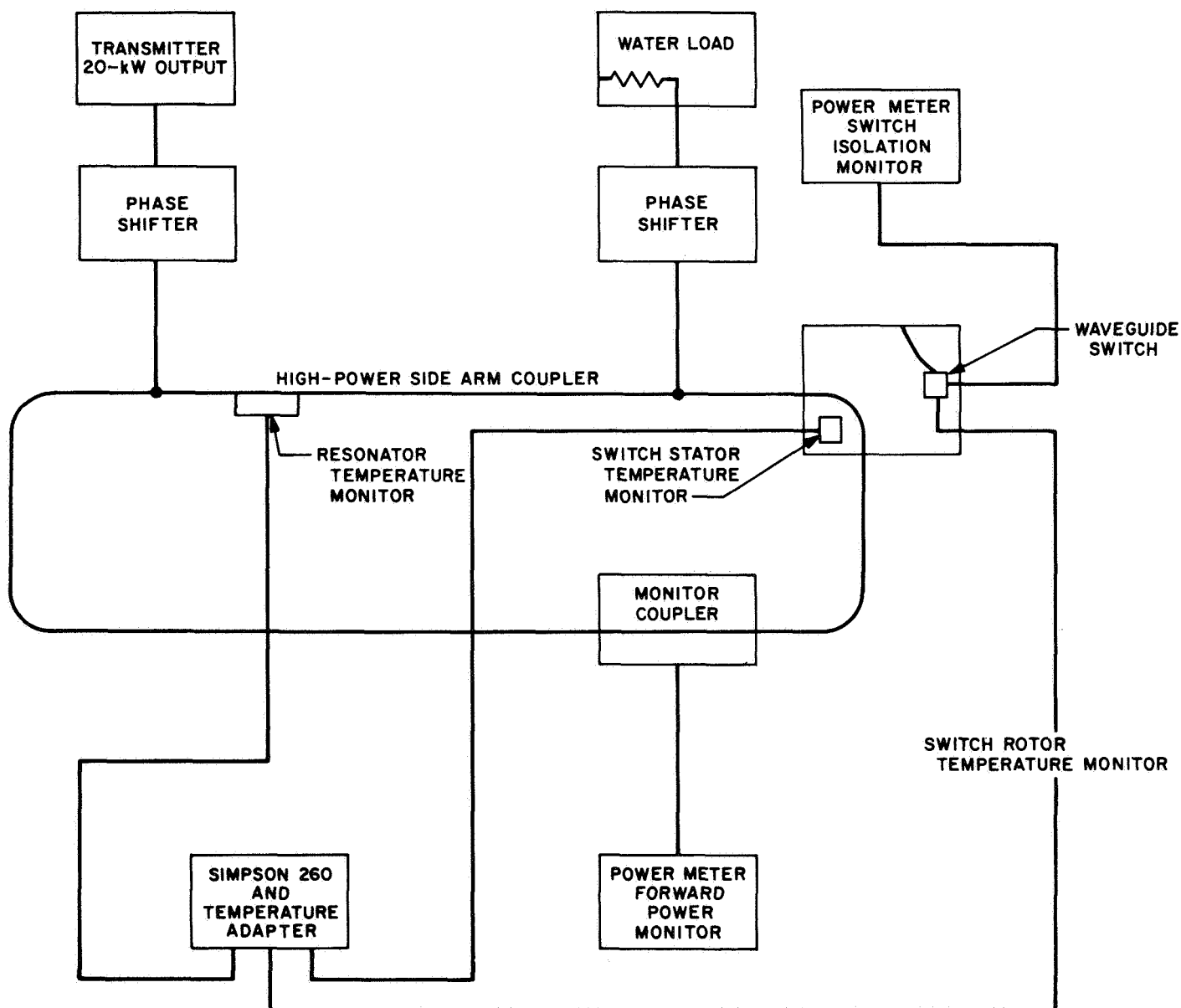


Fig. 40. Microwave switch test configuration

expansion which would result in a change of the air gap. There is to be no RF breakdown or significant deterioration in electrical or mechanical performance at the 500-kW level. The switch was fabricated from OFHC copper and was designed for at least 100,000 cycles of operation between overhaul. Table 7 presents the critical specifications for the waveguide switch.

2. RF Acceptance Tests

The required tests that were performed for RF acceptance were as follows:

- (1) VSWR—measured for all four-port pairs, using the sliding load method as described in Ref. 1.
- (2) Isolation—measured for both switch positions.
- (3) Mechanical operation—switching time measured before and after RF power applied.
- (4) Transmit RF power—at levels of 100 through 500 kW for various periods of time.

The high-power level testing of the microwave switch was accomplished using a traveling-wave resonator, some-

times called a "resonant-ring." The traveling-wave resonator used to test the isolation and power handling capabilities of the 500-kW microwave switch was developed at the JPL microwave test facility and has been discussed in detail in SPS 37-40, Vol. III, pp. 24-26. Figure 40 is a block diagram of the switch test configuration. Figures 41 and 42 are photographs of the resonator with test unit installed.

One microwave switch was tested for a total period of 8 h. The isolation was measured prior to test and at completion of test, and was found to exceed 100 dB each time. Immediately after removal of power, the switch operating time was compared to the operating time prior to test, and no degradation was observed. Tables 8 and 9 present the complete test results of this switch.

3. Conclusion

In addition to testing at 100 through 400 kW, the switch was run continuously for 5 h at 500 kW. During the continuous run, there were no excessive temperatures monitored in the switch. After removal of power, the switch operated in a satisfactory manner.

Table 7. Design specifications for waveguide switch

Bandwidth, GHz	Maximum VSWR	Maximum insertion loss, dB	Minimum isolation, dB	Maximum switching time, ms
2.100-2.400	1.02:1.00	0.020	80	150

Table 9. VSWR test results of microwave switch

Frequency, MHz	Position 1	Position 2	Position 1	Position 2
	Input 1	Input 1	Input 2	Input 2
2085	1.0254	1.026	1.0266	1.0253
2115	1.0244	1.0262	1.0262	1.0250
2388	1.0090	1.0088	1.0087	1.00948
2473	1.0049	1.0050	1.00449	1.00424

Table 8. Test results of microwave switch

Traveling-wave resonator			Microwave switch					
Transmitter power, kW	Forward, kW	Ring temperature, °F	Water inlet temperature, °F	Rotor water outlet temperature, °F	Rotor temperature, °F	Isolation, dB	Switching time, ms	Application of RF power, h
4.9	100	141	132	134	139	110	510	0.5
8.4	200	145	133	135	142	110	510	0.5
12.6	300	147	133	137	144	110	510	0.5
16.8	400	149	134	138	145	110	510	0.5
21.0	500	155	128	133	148	110	510	1
21.0	500	155	128	133	148	110	510	5

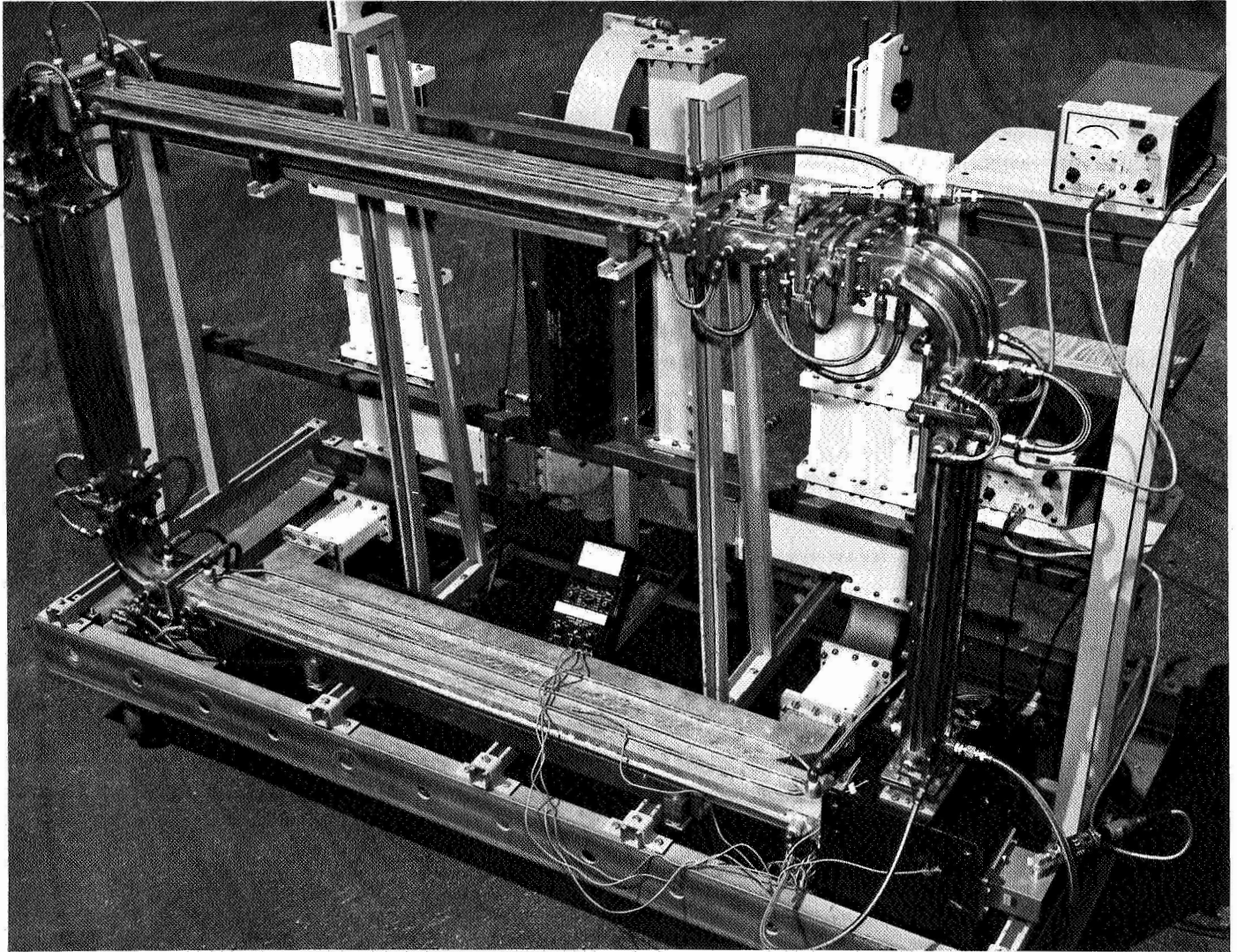


Fig. 41. Traveling-wave resonator

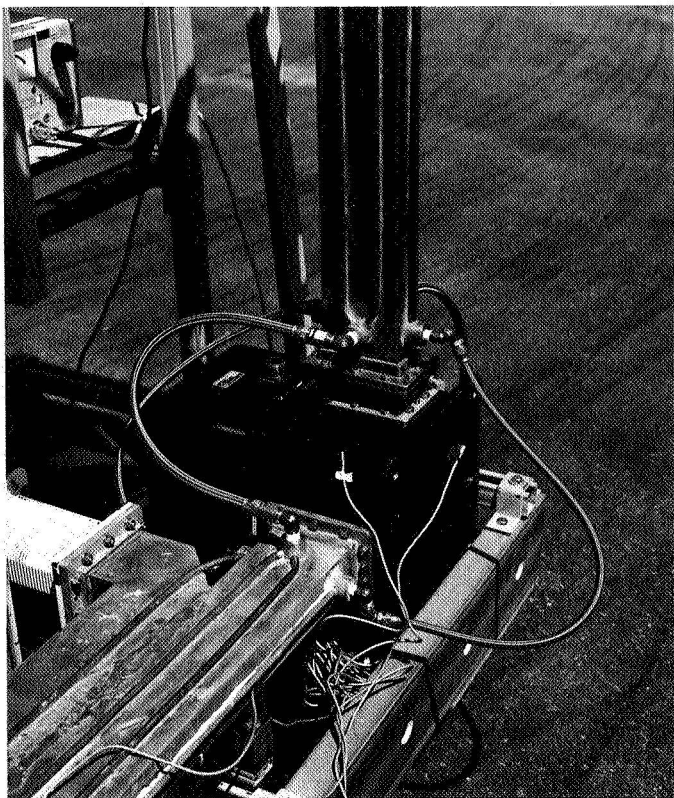


Fig. 42. Microwave switch

4. Future Plans

Testing of three additional microwave switches will begin in the near future. Along with the high-power operation, one switch will be operated until a failure occurs in order to evaluate the switch cooling system and the seals in the rotary joint.

Reference

1. *Microwave Theory and Measurements*, Hewlett-Packard Engineering Staff. Prentice-Hall, Inc., New York, 1962. [This test contains all the material in Hewlett-Packard Application Note No. 38, *Microwave Measurements for Calibration Laboratories* (now out of print).]

K. DSS 13 Mariner Venus 67 Occultation and CW Signal Power Calibration Receiver, C. F. Foster

1. Introduction

The *Mariner* Mars 1964 encounter receiver (SPS 37-35, Vol. III, pp. 42-45) has been modified to provide the *Mariner* Venus 67 occultation experiment with a back-up receive capability at DSS 13. Also, the control room portion of the Mod IV (SPS 37-21, Vol. III, pp. 49-63)

was joined to the *Mariner* Venus 67 receiver to support the CW signal power calibration experiment.

2. Implementation and Requirements

Modification of the *Mariner* Mars 1964 receiver required that, with the exception of the multiplier chain, the modules in the control room portion be replaced. The new modules were designed, built and tested at JPL, then taken to DSS 13 where they were installed and retested as a system. A plot of the total receiver bandwidth is shown in Fig. 43. The design goal was a 3-dB bandwidth of 100 kHz, with the carrier frequency suppressed 15 dB or greater. The 30-MHz bandpass amplifier, using a crystal bandpass filter, provides a carrier rejection of 14 dB. This rejection was improved by more than 30 dB with the second conversion mixer. This mixer incorporates a transformer in the output, which has a passband of 8 to 600 kHz.

The *Mariner* Venus 67 occultation receiver is a manually tuned, constant gain, double conversion, upper sideband, superheterodyne with a 3-dB passband of 94 kHz. It amplifies and frequency-translates the S-band input signal to the audio frequency region and records it on magnetic tape (Fig. 44).

The local oscillator signals are derived from the rubidium frequency standard, which drives a central frequency synthesizer and two manually-steppable frequency synthesizers, one of which is multiplied $\times 64$ to produce the first LO. This is stepped to keep the received signal in the receiver passband. The central frequency synthesizer produces the second LO, and the other synthesizer is used as a reference for the test transmitter. The CW signal power calibration receiver (Fig. 44) is a triple-conversion, phase-locked superheterodyne receiver, constructed and operated in a non-standard configuration. The 30-MHz signal is split off in the *Mariner* Venus 67 occultation receiver described above, sent to the 30-MHz input of the Mod IV, mixed to 455 kHz, injected into a phase detector, and filtered to drive a stable 24-MHz VCO. (The 24-MHz VCO replaced the 31.44-MHz VCO of Mod IV.) The VCO output is then sent to a frequency synthesizer where it replaces the synthesizer's internal 24 MHz. The synthesizer, in effect, offers selectable center frequency of the VCO so that, when multiplied by 64 and mixed with the incoming S-band signal, the resulting frequency is 30 MHz, completing the phase-locked loop. The AGC voltage is derived from a synchronous amplitude detector which is filtered and read out on a digital voltmeter. The AGC voltage is calibrated versus received signal strength by means of a calibrated test transmitter mounted in the antenna structure.

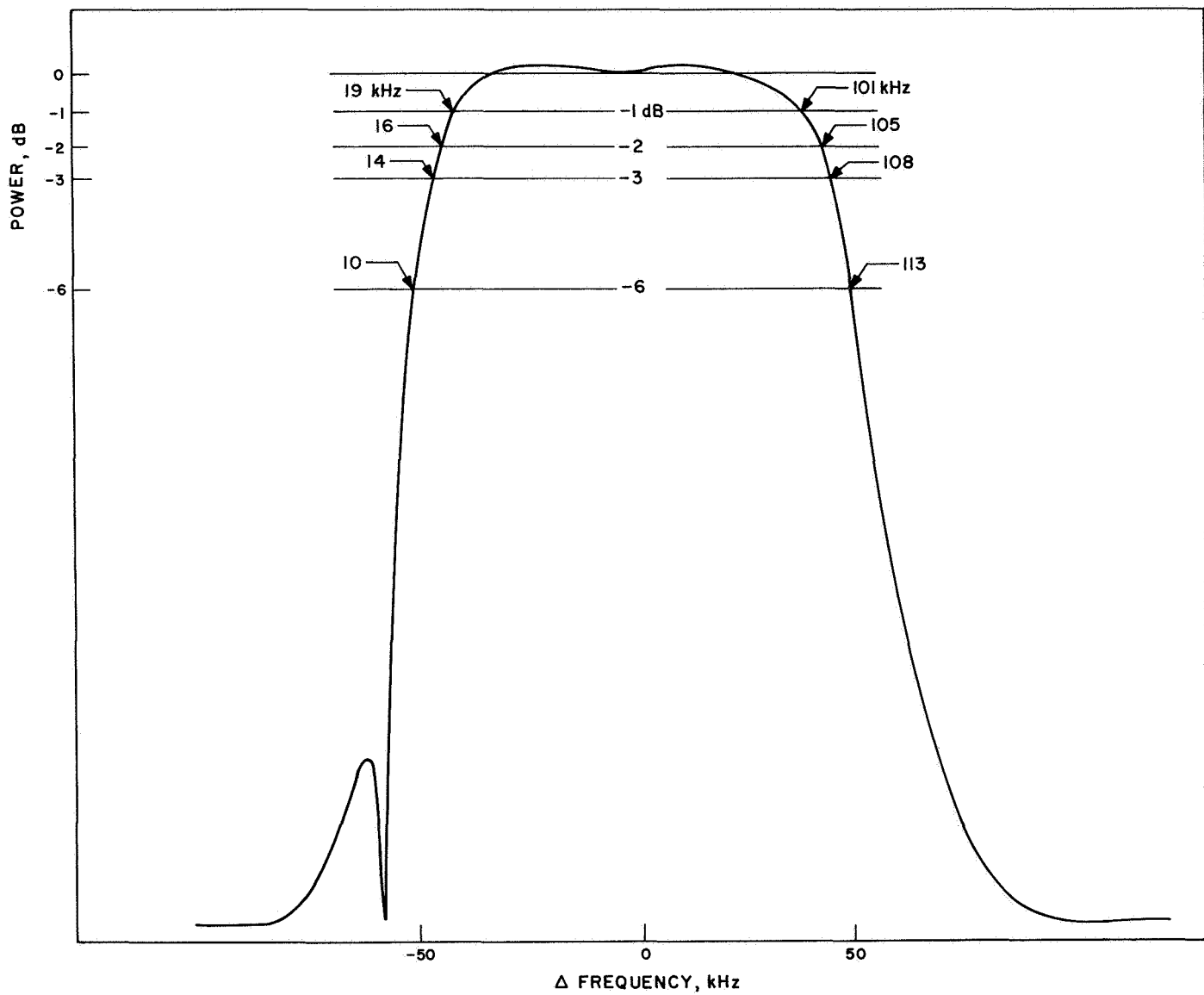


Fig. 43. Occultation receiver bandpass

The modifications have been completed, and both receivers were used successfully in support of *Mariner* Venus 67 occultation and CW signal power calibration experiments. The data taken with the aid of these receivers are now being analyzed and will be reported in the future.

L. Multiple-Mission Telemetry System,

*W. S. Baumgartner, W. Frey, J. K. Woo, R. G. Petrie,
J. E. Stelzried, and M. H. Brockman*

1. Introduction

SPS 37-46, Vol. III, pp. 175-243 gave a detailed description and analysis of the system, and SPS 37-47, Vol. II, pp. 138-142 outlined the project status as of August 1967. The purpose of this article is to report on changes to system specifications, capabilities, and design and to present a complete analysis on the final design of the subcarrier demodulator. The DSN implementation schedule is included.

Changes in spacecraft commitments have made it both desirable and feasible to use identical subcarrier demodulators on the multiple-mission telemetry system and the high-rate telemetry system. Simplified operator control also was possible, and to meet these requirements the subcarrier demodulator assembly was redesigned.

SPS 37-46, Vol. III, listed 20 kHz as the lowest subcarrier frequency to be used. It now becomes desirable to handle subcarrier frequencies of 2 kHz and 150 Hz to accommodate existing spacecraft, and design changes have been made to operate at these frequencies (perhaps with some degradation in performance).

Testing and fabrication of the systems is progressing satisfactorily, and, while there are some problem areas and the schedule is very tight, it appears at this time that both schedule and specifications will be met.

2. Project Status

An updated schedule and functional block diagram have been generated for the multiple-mission telemetry project.

Figure 45 provides an implementation schedule of the subcarrier demodulator assemblies, the telemetry and command processor IIc configuration (includes memory expansion), and the multiple-mission telemetry test equipment rack. The schedule also contains appropriate notations and installation periods for each of the DSIF

stations. If additional stations are to be equipped with this system, their operational dates will be in March 1969.

Figure 46 provides an updated functional block diagram of the multiple-mission telemetry system equipment. The primary area of change from previous block diagrams is in the subcarrier demodulator assembly. While the modifications have not significantly changed the subcarrier demodulator assembly operational capabilities, the changes have resulted in the following advantages:

- (1) Extended range of capability (the new block diagram can support both multiple-mission telemetry and high-rate telemetry requirements).
- (2) Simplified operator control (eliminated operator frequency search control and reduced number of loop bandwidth settings).
- (3) Improved performance (loop error channel modified to include a narrow-band IF filter, a more stable VCO, and an automatic gain adjustment).
- (4) Provide acceptable in-lock indicator.

A description of the modifications to the subcarrier demodulator assembly and status of the telemetry and command processor IIc and test equipment follow.

3. Computer and Digital Equipment

The TCP II expansion equipment consists of: (1) additional magnetic core memory for the TCP computers; and (2) a set of analog equipment consisting of multiplexers, analog-to-digital converters, and special interface logic. This equipment will be added to each TCP computer in support of the multiple-mission telemetry project and will become the TCP-IIc configuration.

The prototype TCP expansion equipment (single-channel implementation) will be integrated to the *Mariner* Mars 1969 computer (SDS 920 W/16K memory) in CTA 21 for the system compatibility test. Installation of the dual-channel TCP-IIc expansion equipment into the DSN will be performed by a team of field engineers from the equipment vendor (see Fig. 45 for schedule).

4. Digital Phase Shifter

The first prototype digital phase shifter, using the Hi-Rel digital modules, has been fabricated (Fig. 47) and installed in the telemetry development laboratory. Evaluation of performance indicates that all design goals and

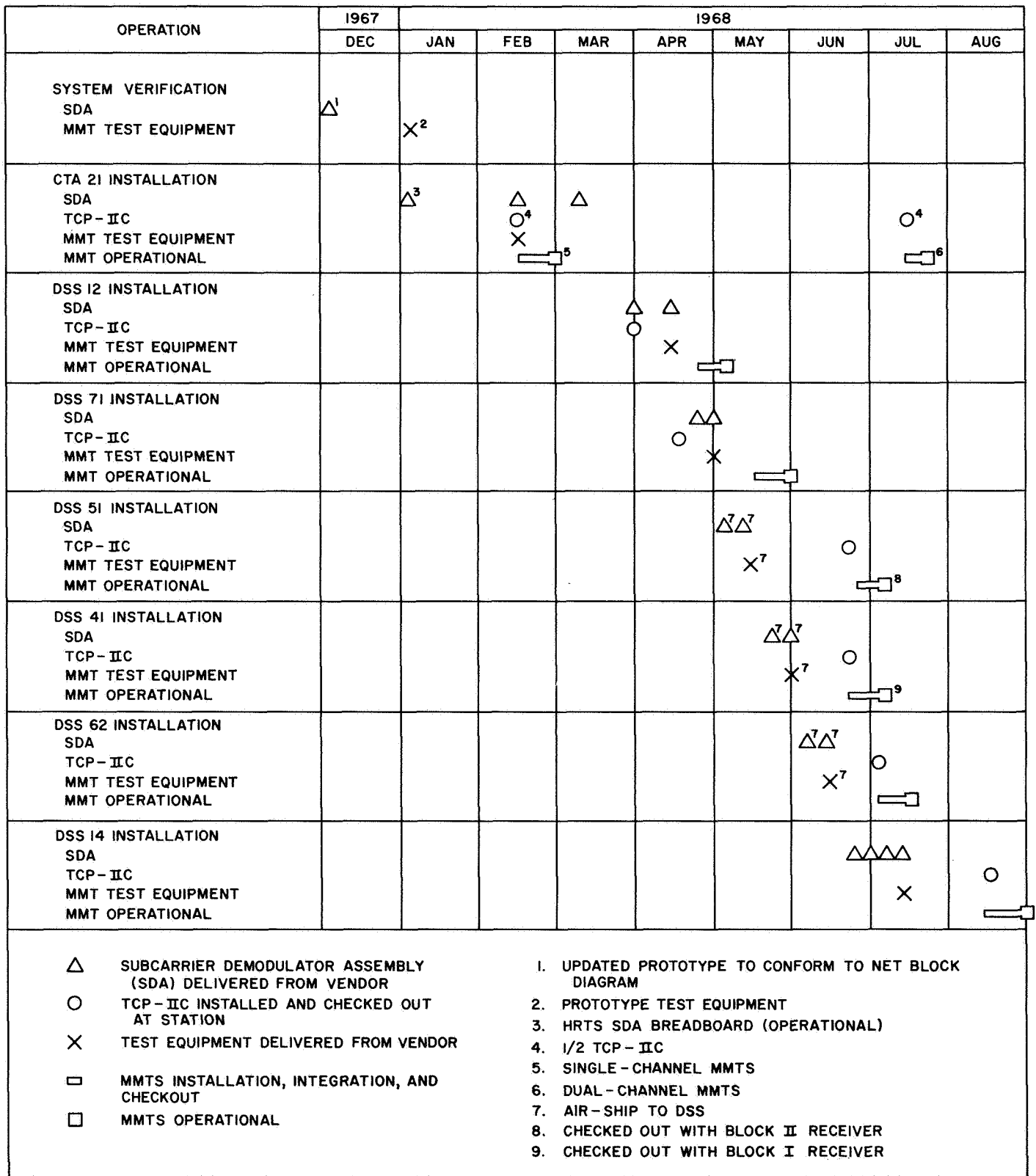


Fig. 45. Multiple-mission telemetry project schedule

constraints have been met and that no electrical interface problems exist with the SDS 920 computer.

In order to accommodate the SDS equipment rack, into which digital phase shifter is to be mounted, a new packaging design became necessary. This design has been completed and the new hardware is presently being fabricated, with completion in time for CTA 21 implementation.

5. Test Equipment

The detail design of the multiple-mission telemetry system test equipment is continuing and fabrication of the first prototype unit has been started. In order to meet schedule requirements, as well as technical specifications, a dual effort approach is being followed.

The first effort is directed toward supplying the telemetry development laboratory with an abbreviated version of the test equipment as soon as feasible. The abbreviation is in the areas of control and redundancy and not in the functional capabilities of the equipment. It is necessary to pursue this effort in order to properly evaluate the test equipment design and performance, and to make changes in the design as required, before the first GSDS version is completed.

Simultaneously with the above activity, the second effort is directed toward solving known circuit problems, primarily in the interface circuits, and in generating the necessary packaging and control hardware for the final GSDS version test equipment.

6. Subcarrier Demodulator Assembly

a. Equipment changes. The updated subcarrier demodulator assembly block diagram (Fig. 48) reflects all the latest equipment definitions. Some of these changes were discussed in SPS 37-48, Vol. II, pp. 124-129. The most recent changes include:

- (1) Addition of a selectable time constant high-pass filter in the data output for purposes of blocking any dc drift caused by the wide-band amplitude detector subassembly.
- (2) Redesign of the quadrature generator subassembly for multiplication of data estimate signal with the subcarrier estimate prior to demodulation of the error signal. A third output was also added to feed the quadrature data channel. This technique eliminates the need for the 10-MHz reference phase switch and includes the function previously pro-

vided by the 10-MHz signal phase switch. This approach allows the error channel to be narrow-banded.

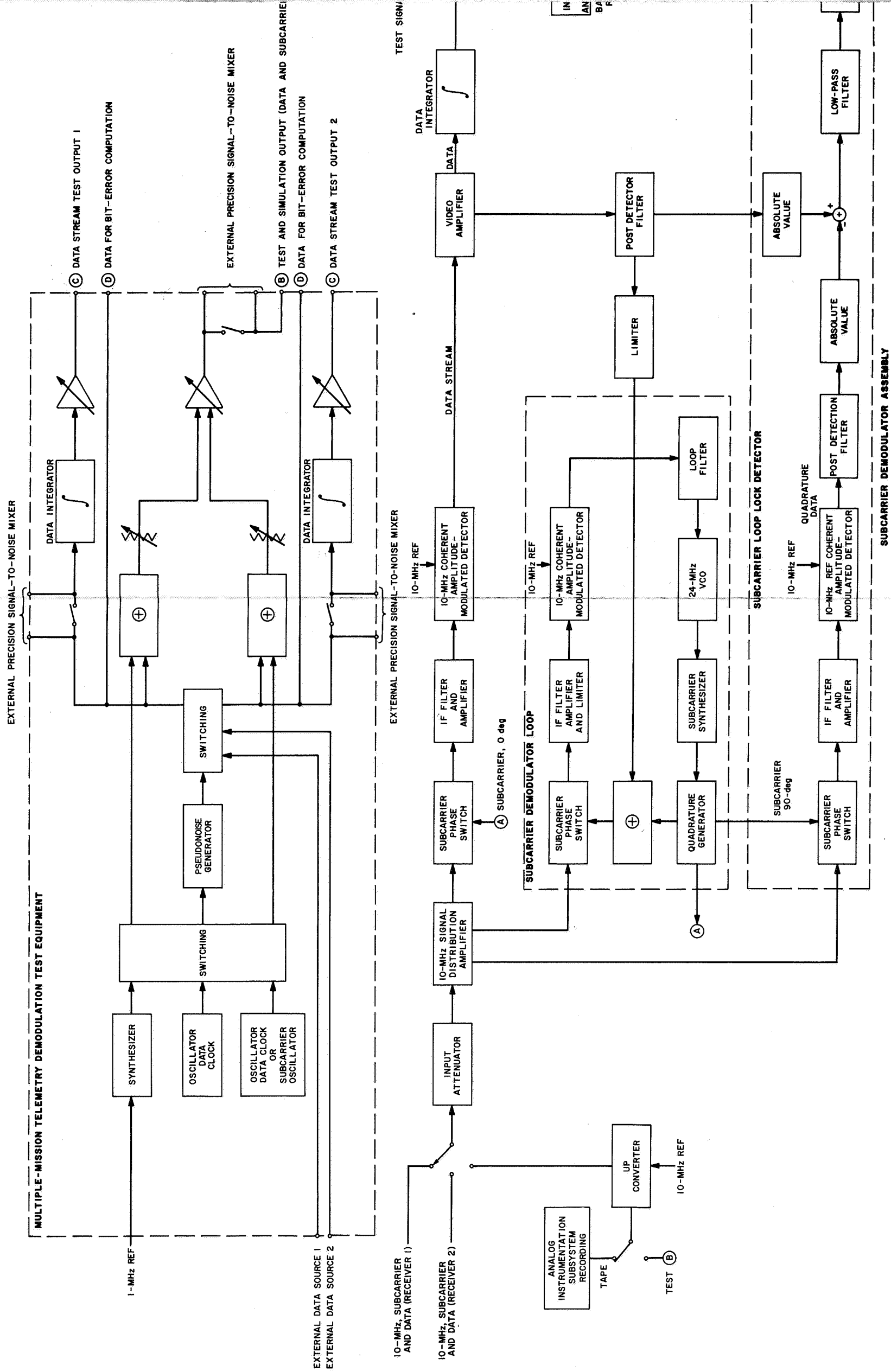
- (3) Redesign of the in-lock detector to provide absolute value detection rather than the previous squaring technique. A separate quadrature data channel, which includes a 10-MHz selectable bandwidth filter and a 10-MHz wideband amplitude detector, provides a signal in quadrature to the data signal for absolute value comparison. The correlation of these absolute value signals is used to determine the in-lock condition.
- (4) Redesign of the 10-MHz signal distribution amplifier to provide an extra output to the quadrature generator and also to provide selectable gains in order to optimize operation of the quadrature generator.
- (5) Redesign of the loop filter and lock indicator units to eliminate the acquisition control and to add an acquisition loop-widening circuit. Control and monitoring circuits for the Hewlett-Packard model H30-5103A synthesizer were also added.
- (6) Redesign of the 10-MHz narrow-band amplifier to provide a fixed 500-Hz bandwidth filter and an output bandpass limiter for purposes of enhancing dynamic range capabilities of the loop.
- (7) Redesign of the 10-MHz selectable bandwidth filter. This unit incorporates both selectable bandwidths and gains in order to optimize the operation of the 10-MHz wide-band amplitude detector. This approach eliminates the need of the 10-MHz IF amplifier as a separate module.

b. Equipment configuration. The subcarrier demodulator assembly equipment configuration has been modified to incorporate the block diagram changes. The optional 100-kHz module drawers have been eliminated and the HP-H30-5103A synthesizer has replaced the Fluke-type 314B-7. A separate data condition drawer has been added. The control panel has been modified by elimination of the acquisition control and the acquisition meter indicator.

7. Subcarrier Demodulator Analysis

a. General analysis.

Functional description. Figure 49 is a functional block diagram for the multiple-mission telemetry subcarrier demodulator. The input signal is an RF signal at the IF frequency of the DSIF receiver which is at a fixed phase.



101A Fig. 46A

101-B Fig. 46B

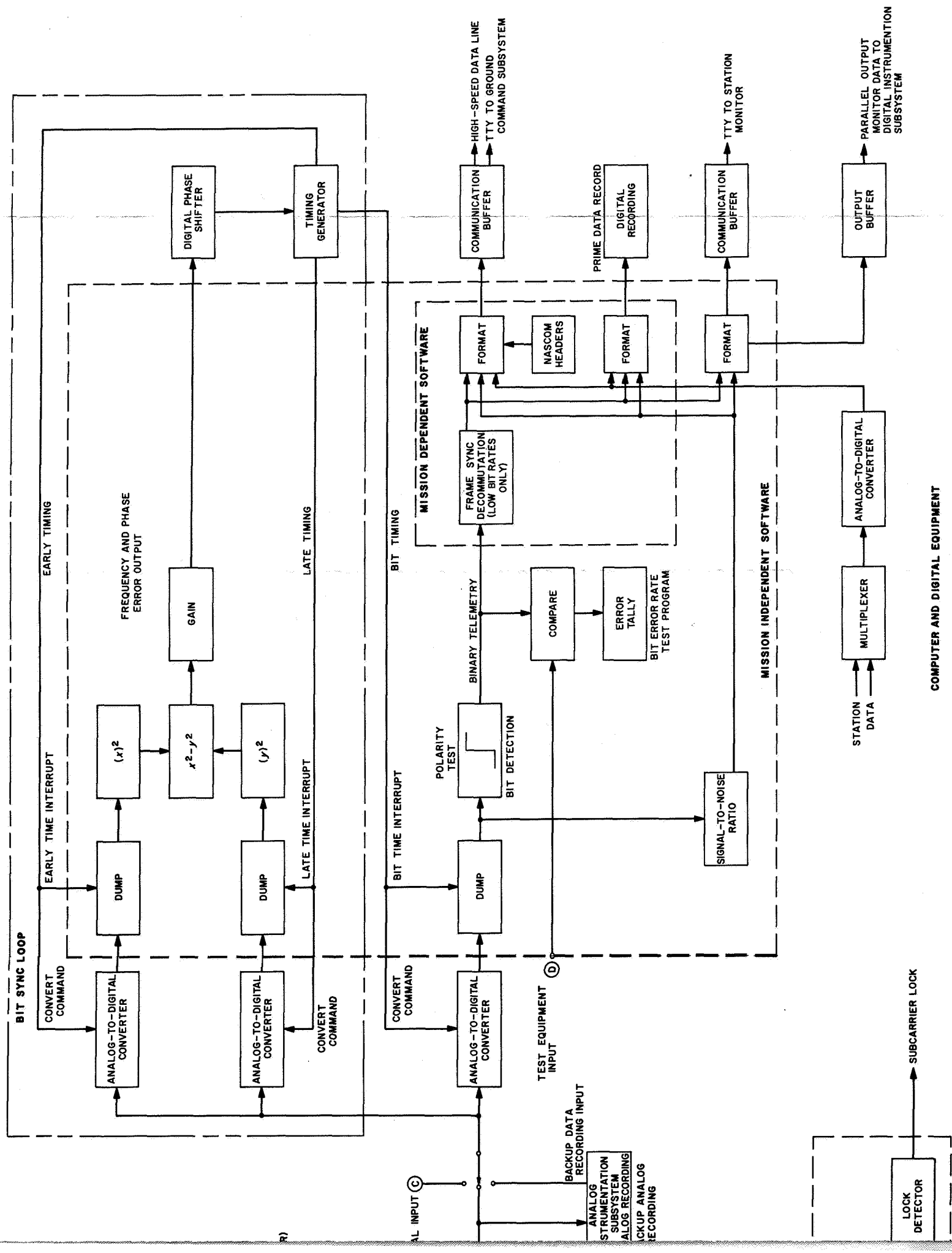


Fig. 46 Multiple-mission telemetry system functional block diagram

PRECEDING PAGE BLANK NOT FILMED.

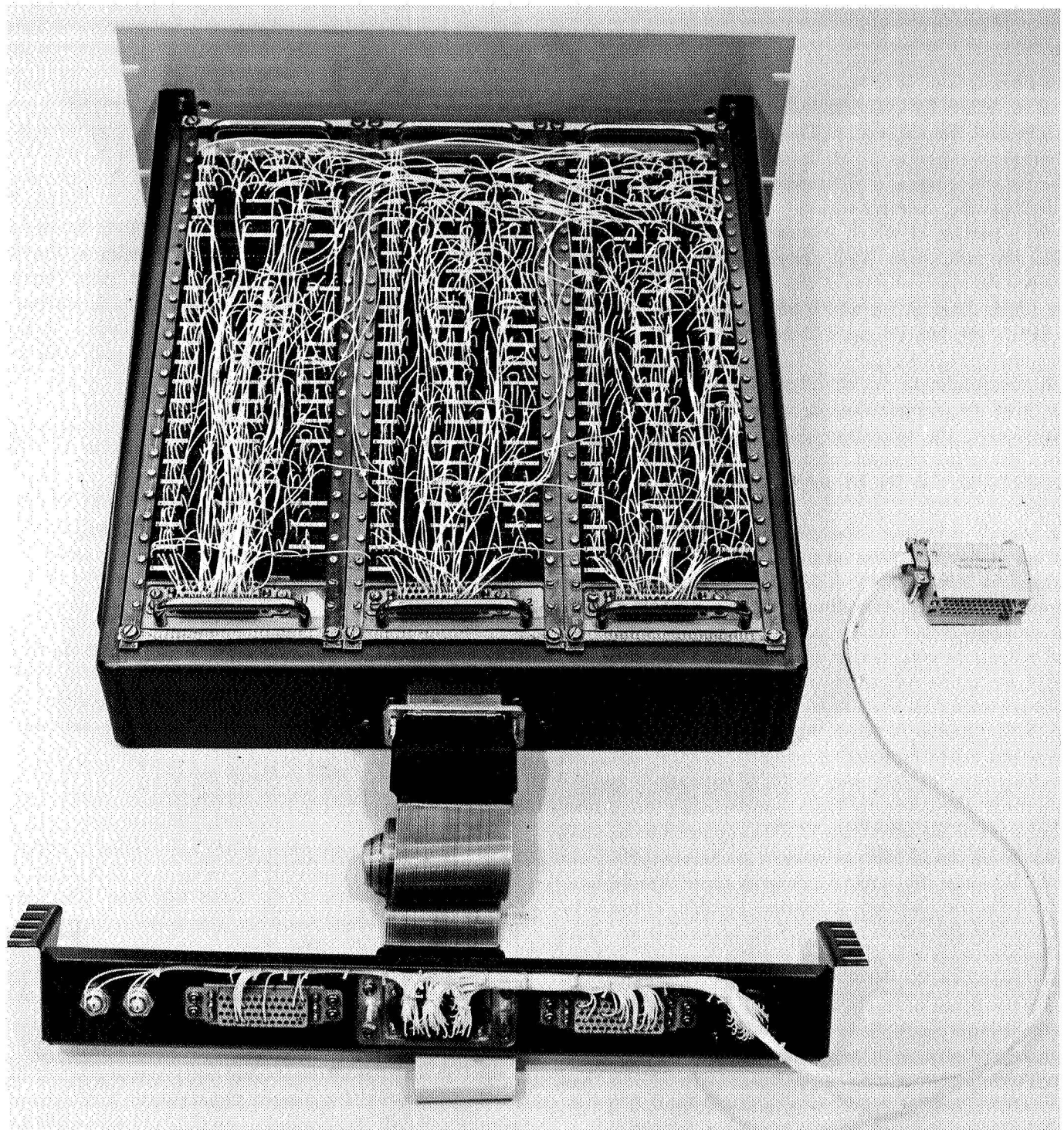


Fig. 47. Prototype digital phase shifter

The received signal contains telemetry data in the form of a binary waveform which biphase-modulates a square-wave subcarrier. The modulated subcarrier, which is also a binary waveform, in turn phase-modulates the carrier. The purpose of the multiple-mission telemetry subcarrier demodulator is to recover the original binary telemetry waveform by synchronously demodulating both the carrier and the subcarrier. The DSIF receiver provides a reference signal at 10 MHz to demodulate the carrier. The reference signal to demodulate the subcarrier is provided by the multiple-mission telemetry demodulator, itself, a portion of which acts as a phase-locked loop to track the subcarrier. Both demodulation processes take place in the upper channel of Fig. 49. Figure 49 differs from the block diagram for which an analysis was presented in SPS 37-46, Vol. III, pp. 175-243 as described below.

In recapitulation, for circuitry reasons associated with the need to accommodate a wide range of subcarrier frequencies, the subcarrier demodulation is performed first. The upper channel functions the same as described in SPS 37-46, Vol. III. Its output is the recovered binary waveform which is sent to another part of the system for overall detection. The effect of phase error in the subcarrier tracking loop on the demodulated output was treated in SPS 37-48, Vol. II, pp. 124-129. The output (upper channel) is also filtered and limited to provide an estimate of the binary waveform to the lower channel which, in conjunction with the tracking filter and VCO, forms the subcarrier tracking loop. A basic difference between Fig. 49 and SPS 37-46, Vol. III, pp. 175-243 lies in the manner in which the filtered and limited binary waveform (data estimate) is injected into the subcarrier tracking loop. In this case, the data estimate is injected into the tracking loop by biphase-modulating the quadrature phase of the subcarrier VCO (as opposed to biphase-modulating the 10-MHz reference). As before (SPS 37-46, Vol. III), since the original telemetry waveform biphase-modulates the received subcarrier, the data estimate injection has the effect of providing a quadrature phase subcarrier loop output which, on the average, matches the phase reversals of the received subcarrier to provide the error signal in the loop. In addition, since the lower channel input multiplier needs only to provide the error signal (CW portion of its output) to the coherent linear amplitude detector, the noise bandwidth of the predemodulation filter F_{A_2} can be made as narrow as circuitry design permits. This reduced bandwidth permits higher gain operation of the coherent linear amplitude

detector which, in turn, reduces the effect of circuit imperfections (unwanted dc detection components) on loop performance. Also, the bandpass limiter shown in Fig. 49 permits accommodation of a large range of data rates (both uncoded and coded) with a relatively simple tracking filter design.

It should be noted that in the following analysis the bandpass limiter is treated as (and operates as) an ideal (hard) limiter at the design point. For the low and medium data rates considered later in this article, the bandpass limiter also operates as a hard (infinite gain) limiter at minimum operating condition. The bandpass limiter shown in Fig. 49 is actually a soft (finite gain) limiter which, at high data rates or high signal levels, operates as a linear device. Analysis of the overall effect of the soft limiter on the subcarrier demodulator performance will be presented in a later article.

A detailed analysis of the upper channel presented in SPS 37-46, Vol. III provides reference material for the following analysis. This analysis relates to the lower channel and the subcarrier tracking loop in Fig. 49. The linear model of the subcarrier tracking loop presented in SPS 37-46, Vol. III also provides reference material for this article. In addition, the assumptions made in SPS 37-46, Vol. III apply herein.

Predemodulation signal and noise. The input signal is an RF signal (at IF frequency f_2 Hz or ω_2 rad/s) phase-modulated with a square-wave telemetry subcarrier ω_{sc} which is, in turn, biphase-modulated with the data $m(t)$.

$$(2)^{1/2} A \cos [\omega_2 t + m(t) \times m_{ps} \times \cos (\omega_{sc} t + \theta)] + n_2(t) \quad (1a)$$

where m_{ps} is the peak phase-modulation index in radians (due to telemetry) and $m(t)$ is +1 or -1, depending on the data. The term θ is the input telemetry subcarrier phase which is considered as non-time-varying in this simplified analysis. The term $n_2(t)$ represents input receiver noise (gaussian and white) for the receiver bandwidth at this point in the system which has a double-sided noise spectral density of $N_0/2$. $N_0/2 = (k \times T \times 1)/2$ W/Hz where k is Boltzmann's constant, 1.38×10^{-23} joule/°K, and T is the equivalent noise temperature of the receiving system. Total input signal power is A^2 (an impedance of unity is assumed to simplify the expression for power), where $A \ll 1$. Because the modulation waveform is binary, Expression (1a) can be written as

$$\underbrace{2^{1/2} A \cos m_{ps} \cos \omega_2 t}_{\text{carrier}} + \underbrace{2^{1/2} A \sin m_{ps} \times m(t) \times \cos (\omega_{sc} t + \theta) \times \sin \omega_2 t}_{\text{sidebands}} + n_2(t) \quad (1b)$$

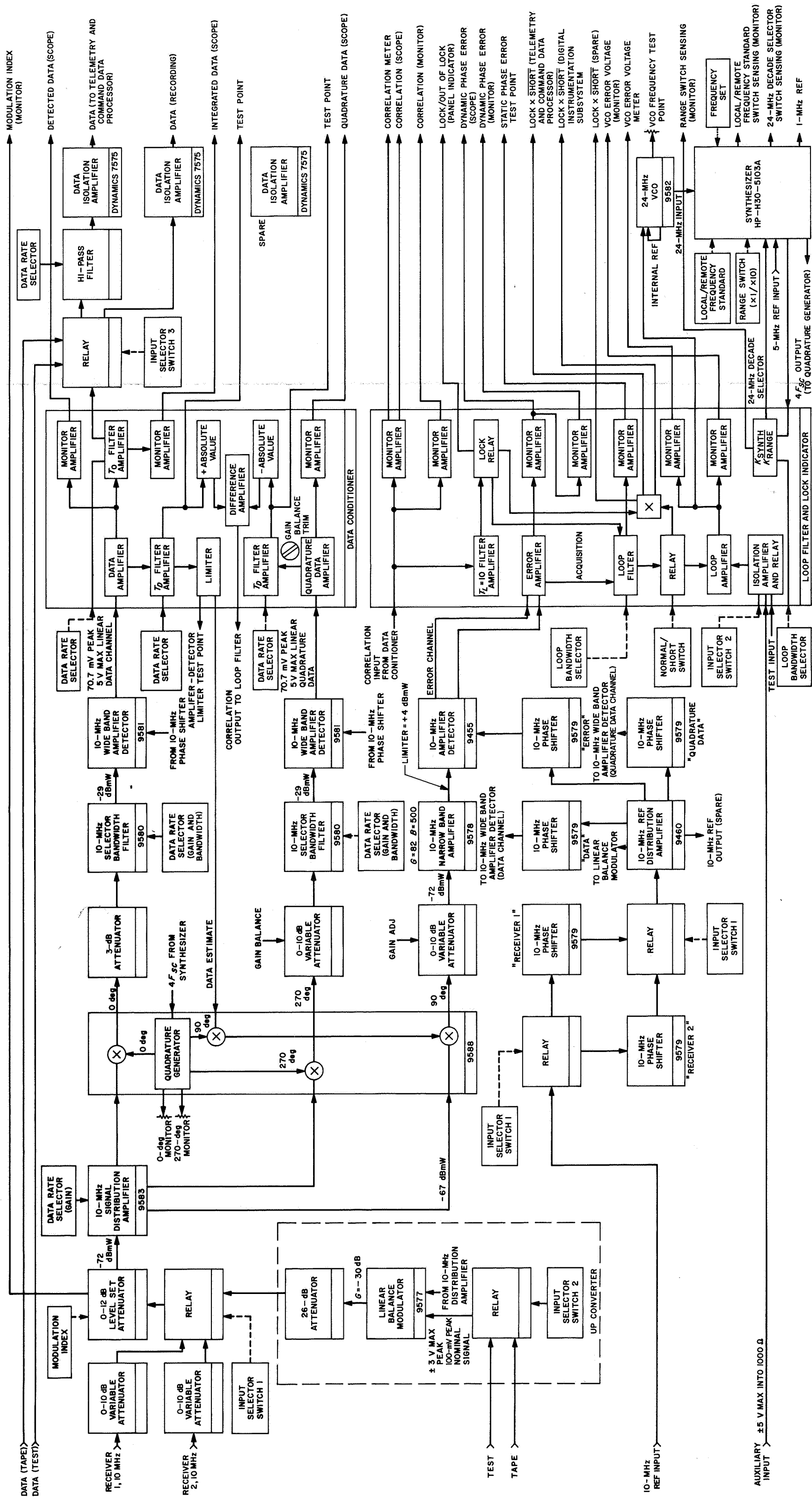


Fig. 48. Subcarrier demodulator assembly block diagram

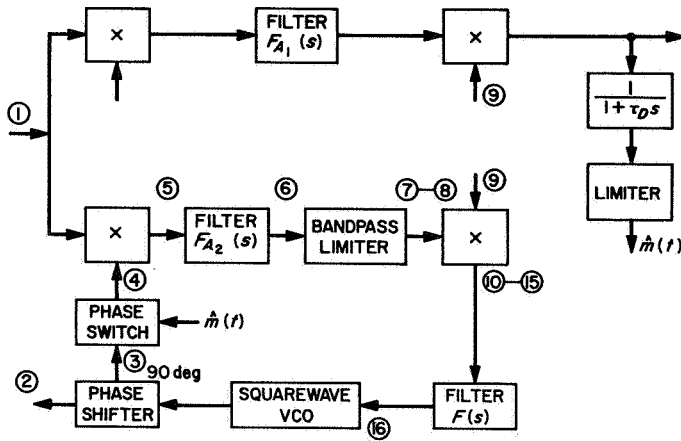


Fig. 49. Telemetry subcarrier demodulator functional block diagram

The signals obtained from the square-wave subcarrier VCO at ② and ③ in Fig. 49 are

$$\cos[\omega_{sc} t + \hat{\theta}(t)] \quad (2)$$

and

$$\sin[\omega_{sc} t + \hat{\theta}(t)] \quad (3)$$

The data symbol stream estimate $\hat{m}(t)$ biphase-modulates the square-wave sine subcarrier VCO at ③ + and $-\pi/2$ rad, which provides Expression (4);

$$\hat{m}(t) \sin[\omega_{sc} t + \hat{\theta}(t)] \quad (4)$$

The input signal, Expression (1b), is multiplied in the lower multiplier in Fig. 49 by the square-wave sine subcarrier signal biphase-modulated with $\hat{m}(t)$, Expression (4), to provide Expression (5):

$$\begin{aligned} & \hat{m}(t) (2)^{1/2} A \cos m_{ps} \sin[\omega_{sc} t + \hat{\theta}(t)] \cos \omega_2 t + m(t) \hat{m}(t) (2)^{1/2} \\ & \times A \sin m_{ps} \cos(\omega_{sc} t + \theta) \sin[\omega_{sc} t + \hat{\theta}(t)] \sin \omega_2 t + n_5(t) \end{aligned} \quad (5)$$

where the noise term $n_5(t)$ is $n_2(t)$ in Expression (1b), multiplied by $\hat{m}(t) \sin[\omega_{sc} t + \hat{\theta}(t)]$.

Assumption. The assumption is made here that the relative broadening in the noise spectrum due to this multiplication is small enough to be ignored. Therefore, the noise term of $n_5(t)$ at ⑤ in Fig. 49 has a double-sided noise spectral density of $N_0/2$. This is a conservative assumption. Note also that in the upper channel, the input noise is

multiplied by $\cos[\omega_{sc} t + \hat{\theta}(t)]$, which determines $\hat{m}(t)$. In the lower channel, the input noise is multiplied by $\sin[\omega_{sc} t + \hat{\theta}(t)]$, which provides noise which is statistically independent of $\hat{m}(t)$, which is, in turn, multiplied by $\hat{m}(t)$.

After passing through the lower filter F_{A2} , Expression (5) becomes

$$\begin{aligned} & F_{A2} \{ \hat{m}(t) (2)^{1/2} A \cos m_{ps} \sin[\omega_{sc} t + \hat{\theta}(t)] \cos \omega_2 t + \alpha' (2)^{1/2} \\ & \times A \sin m_{ps} \cos(\omega_{sc} t + \theta) \sin[\omega_{sc} t + \hat{\theta}(t)] \sin \omega_2 t \} + n_6(t) \end{aligned} \quad (6)$$

where $\alpha' = \overline{m(t)\hat{m}(t)}$ (SPS 37-46, Vol. III, pp. 175-243). The noise term $n_6(t)$ represents the receiver noise at the lower filter (F_{A2}) output with a double-sided noise spectral density of $N_0/2$. The ratio of noise powers represented by $n_6(t)$ and $n_2(t)$ is equal to the ratio of noise bandwidths at ⑥ and ① in Fig. 49. The noise term $n_6(t)$ is centered about f_2 . For the condition that the noise bandwidth of F_{A2} is much less than $2f_{sc}$, the first term of Expression (6) is effectively zero.

The signal plus noise [last two terms of Expression (6)] is applied to the bandpass limiter whose output in the frequency interval centered about f_2 saturates at V_L (rms amplitude). Note that for this case, $V_L = 2\pi \times L$, where L is the rms level at which the bandpass limiter saturates (SPS 37-35, Vol. IV, pp. 307-309). Designate the ratio ν as

$$\nu = \frac{V_L}{A \sin m_{ps}} \quad (7)$$

where $\nu < 1$. At high signal levels, where the soft bandpass limiter operates as a linear device, ν becomes unity. The output of the bandpass limiter in the frequency interval centered about f_2 becomes

$$\begin{aligned} & \nu A \sin m_{ps} \{ \alpha' (2)^{1/2} \times \cos(\omega_{sc} t + \theta) \\ & \times \sin[\omega_{sc} t + \hat{\theta}(t)] \sin \omega_2 t + n_{sL}(t) \} \end{aligned} \quad (8)$$

where α is the bandpass limiter signal-voltage suppression factor (Ref. 1).

Coherent detection of error signal and noise. The reference signal at ⑨ in Fig. 49 is

$$(2)^{1/2} \sin \omega_2 t \quad (9)$$

Assumption. It is assumed for the present that the received carrier power is such that the phase noise error in

the RF carrier tracking loop is small enough so that it can be ignored.

The output of the lower coherent linear detector is the multiplication of Expression (8) by Expression (9), which provides (ignoring double frequency terms which are filtered out and orthogonal terms)

$$\nu A \sin m_{ps} \{ \alpha \alpha' \cos(\omega_{sc}t + \theta) \sin[\omega_{sc}t + \hat{\theta}(t)] + n_{10L}(t) \} \quad (10)$$

As developed in SPS 37-46, Vol. III, for the condition that $\theta - \hat{\theta}(t)$ is less than $\pi/2$ rad, the portion of the product of the square-wave cosine and sine terms centered about dc is proportional to $[\theta - \hat{\theta}(t)]/(\pi/2)$ (where the phase difference is expressed in radians. This dc component is positive in sign when $\theta > \hat{\theta}(t)$ and negative in sign when $\theta < \hat{\theta}(t)$. The double frequency square-wave resulting from the square-wave sine and cosine product is filtered out by tracking filter $F(s)$.

For the case of no bandpass limiter, conversion of rms noise voltage at the lower coherent amplitude detector to equivalent phase noise was accomplished by normalizing the noise voltage to the signal voltage (SPS 37-46, Vol. III). For this case, with a bandpass limiter, the resultant expression becomes

$$\frac{\pi}{2} \times \frac{\sigma_{nv10}}{\alpha \alpha' \nu A \sin m_{ps}} \text{ rad rms} \quad (11)$$

or

$$\frac{\pi}{2} \times \frac{(N_0/2)^{1/2}}{\alpha \alpha' \nu A \sin m_{ps}} \times (NBW_{FA_2})^{1/2} \times \Gamma^{1/2} \text{ rad rms} \quad (12)$$

The term Γ is the limiter performance factor (Refs. 1 and 2) which is closely approximated by the expression

$$\Gamma = \frac{1 + 0.345 \times \left(\frac{P_S}{P_N} \right)_{FA_2}}{0.862 \times 0.690 \left(\frac{P_S}{P_N} \right)_{FA_2}} \quad (13)$$

where

$$\left(\frac{P_S}{P_N} \right)_{FA_2} = \frac{(\alpha' A \sin m_{ps})^2}{\frac{N_0}{2} \times 2 NBW_{FA_2}} \quad (14)$$

It should be noted that in this analysis, the limitation is imposed (for the present) that the ratio

$$\frac{\frac{N_0}{2}}{\nu^2 \times (\alpha' A \sin m_{ps})^2} \times 2 NBW_{FA_2} > 1 \quad (15)$$

After passing through the filter $F(s)$, the signal plus noise represented by Expression (10) controls the output phase of the subcarrier VCO.

$$F(\omega) (\nu A \sin m_{ps} \{ \alpha \alpha' \cos(\omega_{sc}t + \theta) \times \sin[\omega_{sc}t + \hat{\theta}(t)] + n_{10L}(t) \}) \quad (16)$$

Since $\theta = \int \omega dt$, the VCO functions as an integrator.

Figure 50 shows the suppression factor due to data α' as a function of ST_{SY}/N_0 , the ratio of signal energy per symbol to noise spectral density. This figure, which was presented in SPS 37-46, Vol. III, is included here for reference.

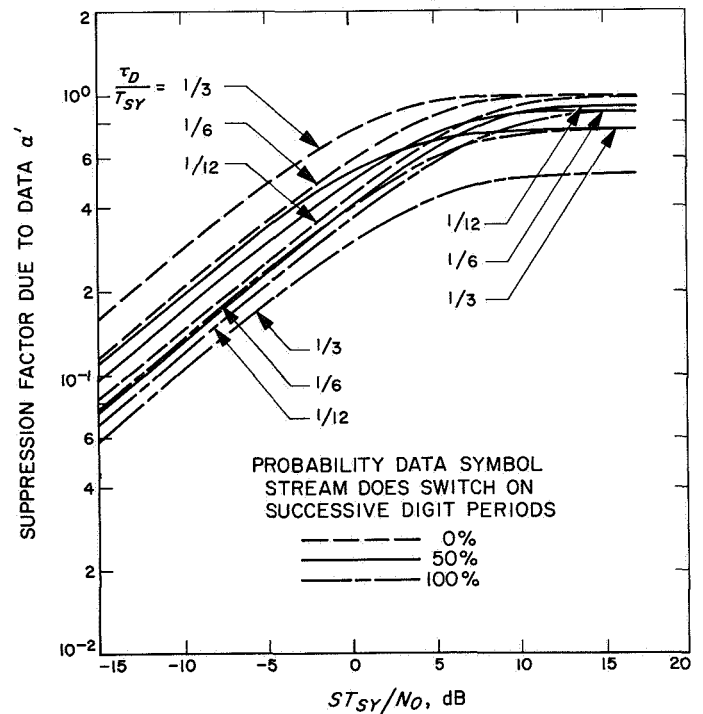


Fig. 50. Multiple-mission telemetry system subcarrier demodulator suppression factor due to data vs ratio of signal energy per symbol to noise spectral density

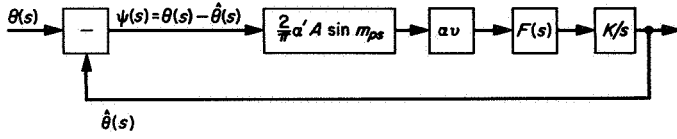


Fig. 51. Linear model of subcarrier phase tracking loop

Linear model of the subcarrier tracking loop. As in SPS 37-46, Vol. III, the lower loop in Fig. 49 can be treated as a linear model of the phase-locked loop (Ref. 3) with the constraint that at minimum signal level the probability of the phase noise exceeding 90 deg $\ll 1$. Figure 51 shows the resulting linear model of the subcarrier phase-tracking loop. The transfer function of the loop is

$$H(s) = \frac{\hat{\theta}(s)}{\theta(s)} = \frac{(\alpha_v) \times \frac{2}{\pi} K \alpha' A \sin m_{ps} \times F(s)}{s + (\alpha_v) \times \frac{2}{\pi} K \alpha' A \sin m_{ps} \times F(s)} \quad (17)$$

The two-sided noise bandwidth of the subcarrier phase-tracking loop is

$$BW_{sc} = \frac{1}{2\pi j} \int_{-j\infty}^{+j\infty} |H(s)|^2 ds \text{ Hz} \quad (18)$$

and the variance of phase noise at the output of the loop is

$$\sigma_{\theta n}^2 = \Gamma \times \frac{\frac{N_0}{2}}{(\alpha_v)^2 \times \left(\frac{2}{\pi} \alpha' A \sin m_{ps}\right)^2} \times BW_{scL} \text{ rad}^2 \quad (19)$$

Note that $A \sin m_{ps} = S^{1/2}$ (SPS 37-46, Vol. III).

First-order subcarrier tracking loop. The first-order loop is considered here so that it can be related to performance characteristics presented in SPS 37-46, Vol. III. For this case, $F(s) = 1$ so that Expression (19) becomes

$$H(s) = \frac{(\alpha_v) \times \frac{2}{\pi} K \alpha' A \sin m_{ps}}{s + (\alpha_v) \times \frac{2}{\pi} K \alpha' A \sin m_{ps}} \quad (20)$$

and the two-sided, closed-loop noise bandwidth becomes, from Expression (18)

$$BW_{scL} = \frac{(\alpha_v) \times \frac{2}{\pi} K \alpha' A \sin m_{ps}}{2} \quad (21)$$

The equivalent time constant of the first-order loop is

$$\tau_L^L = \frac{1}{(\alpha_v) \times \frac{2}{\pi} K \alpha' A \sin m_{ps}} \quad (22)$$

The term (α_v) represents the effect of the bandpass limiter on loop gain and, hence, loop bandwidth. At design point,

$$\tau_{L_0}^L = \frac{1}{(\alpha_{0v}) \times \frac{2}{\pi} K \alpha_0' A \sin m_{ps}} \quad (23)$$

Designate the ratio of $\tau_{L_0}^L$, design point equivalent time constant, to T_{SY} , time duration of a symbol, as γ_0^L , then

$$\tau_{L_0}^L = \gamma_0^L T_{SY} \quad (24)$$

Now for a given ST_{SY}/N_0 , the variance of the phase noise at the output of the first-order loop at the design point is [from Expression (19)]

$$\sigma_{\theta n}^2 = \Gamma \times \left(\frac{1}{\alpha_0'}\right)^2 \times \left(\frac{\pi}{2}\right)^2 \times \frac{N_0}{ST_{SY}} \times \frac{T_{SY}}{2} \times \frac{1}{2\gamma_0^L T_{SY}} \times \left(\frac{1}{\alpha_{0v}}\right)^2 \text{ rads} \quad (25)$$

Note that the above expression can be compared to Expression (62) (SPS 37-46, Vol. III) by rewriting the above (since $\gamma_0^L = \gamma_0/\alpha_{0v}$) as

$$\sigma_{\theta n}^2 = \Gamma \times \left(\frac{1}{\alpha_0'}\right)^2 \times \left(\frac{\pi}{2}\right)^2 \times \frac{N_0}{ST_{SY}} \times \frac{1}{4\gamma_0} \times \frac{1}{\alpha_{0v}} \text{ rad}^2 \quad (26)$$

Expression (26) shows the two effects produced by the bandpass limiter; first, the limiter performance factor Γ which relates to the change in signal-to-noise ratio, and, second, the effect of the limiter $1/\alpha_{0v}$ on noise bandwidth at design point.

Second-order subcarrier tracking loop. For a second-order loop with a passive integrator, the filter $F(s)$ is of the form

$$F(s) = \frac{1 + \tau_2 s}{1 + \tau_1 s} \quad \begin{array}{c} \text{---} R_1 \text{---} \\ | \\ \text{---} R_2 \text{---} \\ | \\ \text{---} C \text{---} \end{array} \quad \begin{array}{l} \tau_1 = (R_1 + R_2)C \\ \tau_2 = R_2 C \end{array} \quad (27)$$

Therefore, from Expression (17), the transfer function of a second-order loop becomes

$$H(s) = \frac{(\alpha\nu) \times \alpha' \frac{2}{\pi} K A \sin m_{ps} \times \left(\frac{1 + \tau_2 s}{1 + \tau_1 s} \right)}{s + (\alpha\nu) \alpha' \frac{2}{\pi} K A \sin m_{ps} \times \left(\frac{1 + \tau_2 s}{1 + \tau_1 s} \right)}$$

which can be rewritten as:

$$H(s) = \frac{1 + \tau_2 s}{1 + \left\{ \tau_2 + 1 / \left[(\alpha\nu) \alpha' \frac{2}{\pi} K A \sin m_{ps} \right] \right\} s + \left\{ \tau_1 / \left[(\alpha\nu) \alpha' \frac{2}{\pi} K A \sin m_{ps} \right] \right\} s^2} \quad (28)$$

Define a quantity r' as

$$r' = (\alpha\nu) \alpha' \frac{2}{\pi} K A \sin m_{ps} \times \frac{\tau_2^2}{\tau_1} \quad (29)$$

and the transfer function becomes

$$H(s) = \frac{1 + \tau_2 s}{1 + \tau_2 \left(1 + \frac{\tau_2}{r' \tau_1} \right) s + \frac{\tau_2^2}{r'} s^2} \quad (30)$$

The two-sided noise bandwidth of the second-order subcarrier tracking loop is (from Expression 18) (Ref. 1)

$$\begin{aligned} BW_{SCL} &= \frac{1}{2\pi j} \int_{-j\infty}^{+j\infty} |H(s)|^2 ds \\ &= \frac{r' + 1}{2\tau_2 \left(1 + \frac{\tau_2}{r' \tau_1} \right)} \end{aligned} \quad (31)$$

At the design point,

$$BW_{SCL_0} = \frac{r'_0 + 1}{2\tau_2 \left(1 + \frac{\tau_2}{r'_0 \tau_1} \right)} \quad (32)$$

The variance of the phase noise at the output of the second-order loop is (from Expression 19)

$$\begin{aligned} \sigma_{\theta n}^2 &= \Gamma \times \left(\frac{1}{\alpha'} \right)^2 \times \left(\frac{\pi}{2} \right)^2 \times \frac{N_0}{ST_{SY}} \times \frac{T_{SY}}{2} \\ &\times \frac{r' + 1}{2\tau_2 \left(1 + \frac{\tau_2}{r' \tau_1} \right)} \times \left(\frac{1}{\alpha\nu} \right)^2 \text{ rad}^2 \end{aligned} \quad (33)$$

At the design point, set the two-sided noise bandwidth of the second-order loop equal to that of the first-order loop (see the preceding part). From Expressions (21), (23), and (24),

$$BW_{SCL_0} = \frac{1}{2\gamma_0^L T_{SY}} \quad (34)$$

For a given ST_{SY}/N_0 , the variance of the phase noise at the output of the second-order loop at the design point is

$$\sigma_{\theta n}^2 = \Gamma \times \left(\frac{1}{\alpha'_0} \right)^2 \times \left(\frac{\pi}{2} \right)^2 \times \frac{N_0}{ST_{SY}} \times \frac{1}{4\gamma_0} \times \frac{1}{\alpha_0\nu} \text{ rad}^2 \quad (35)$$

Consequently, for a given τ_D/T_{SY} , γ_0 , $\alpha_0\nu$, and probability that the data symbol stream does switch on successive symbols, the rms phase error $\sigma_{\theta n}$ can be calculated from Expression (35), where α'_0 is obtained from Fig. 50.

Having selected a design point noise bandwidth, it is now necessary to determine how $\sigma_{\theta n}^2$ varies with ST_{SY}/N_0 for the second-order loop. Expressions (31) and (32) can be rewritten as

$$BW_{SCL} = \frac{\tau_1 r' + \tau_1}{2\tau_2 \tau_1 \left(1 + \frac{\tau_2}{r' \tau_1}\right)} \quad (36)$$

and

$$BW_{SCL_0} = \frac{\tau_1 r'_0 + \tau_1}{2\tau_2 \tau_1 \left(1 + \frac{\tau_2}{r'_0 \tau_1}\right)} \quad (37)$$

respectively. Inspection of Expression (29) shows that

$$r' = \frac{\alpha \nu}{\alpha_0 \nu} \times \frac{\alpha'}{\alpha'_0} r'_0 \quad (38)$$

Using Expression (38), Expression (36) becomes

$$BW_{SCL} = \frac{\frac{\alpha}{\alpha_0} \times \frac{\alpha'}{\alpha'_0} r'_0 \tau_1 + \tau_1}{2\tau_2 \tau_1 \left(1 + \frac{\tau_2}{\frac{\alpha}{\alpha_0} \times \frac{\alpha'}{\alpha'_0} r'_0 \tau_1}\right)} \quad (39)$$

For the condition that $\tau_2 \ll r'_0 \tau_1$,

$$BW_{SCL} = \frac{\frac{\alpha}{\alpha_0} \times \frac{\alpha'}{\alpha'_0} r'_0}{2\tau_2} + \frac{1}{2\tau_2} \quad (40)$$

which becomes

$$BW_{SCL} = \frac{\alpha}{\alpha_0} \frac{\alpha'}{\alpha'_0} r'_0 \left(\frac{BW_{SCL_0}}{r'_0 + 1} \right) + \frac{BW_{SCL_0}}{r'_0 + 1}$$

or

$$BW_{SCL} = \frac{BW_{SCL_0}}{r'_0 + 1} \left(1 + r'_0 \frac{\alpha \alpha'}{\alpha_0 \alpha'_0} \right) \quad (41)$$

Consequently, for the second-order loop, $\sigma_{\theta n}^2$ is

$$\sigma_{\theta n}^2 = \Gamma \times \left(\frac{1}{\alpha'} \right)^2 \left(\frac{\pi}{2} \right)^2 \times \frac{N_0}{ST_{SY}} \times \frac{1}{4\gamma_0} \times \frac{1}{\alpha_0 \nu} \times \left(\frac{1 + r'_0 \frac{\alpha \alpha'}{\alpha_0 \alpha'_0}}{(r'_0 + 1)} \right) \quad (42)$$

where

$$BW_{SCL_0} = \frac{1}{2\gamma_0} \times \frac{1}{\alpha_0 \nu}$$

b. Subcarrier phase tracking loop design. The multiple-mission telemetry system subcarrier demodulator is designed as a second-order loop with three closed-loop noise bandwidths—narrow, medium, and wide—which have nominal values of 0.03, 0.375, and 1.5 Hz, respectively (two-sided), at the design point with $r'_0 = 2$ (0.707 damping). A bandwidth of 0.3 Hz, which is used to insure acquisition during operation in the narrow 0.03-Hz bandwidth, is also provided. The predemodulation filter F_{A_2} has a nominal noise bandwidth of 500 Hz. The resultant bandpass limiter signal voltage suppression factor α is shown plotted in Fig. 52 versus signal-to-noise spectral density S/N_0 .

The design point parameters for the subcarrier tracking loop are summarized in Table 12 (see preceding analysis for explanation of terms). The design point open loop gain shown here as G'_0 relates to the preceding analysis (see Expression 29) as follows:

$$G'_0 = (\alpha_0 \nu) \times \alpha'_0 \frac{2}{\pi} KA \sin m_{ps} \quad (43)$$

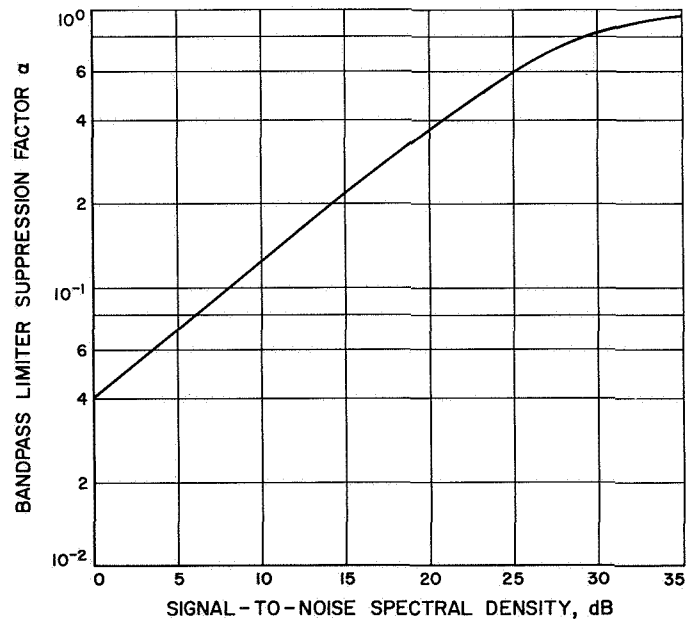


Fig. 52. Bandpass limiter signal suppression factor

Table 12. Subcarrier loop design point parameters

Design point noise band- width, Hz	S/N_0 , dB	Bandpass limiter			Data suppression α'_0 ratio	G_0 , 1/s	r'_0 ratio	τ_1 , s	τ_2 , s
		α_0 ratio	ν ratio	Γ ratio					
0.03	+8	0.10	0.50	1.20	0.49	10	2.0	12500	50
0.375	+16.5	0.25	0.50	1.11	0.49	250	2.0	2000	4
1.50	+23	0.50	0.50	1.0	0.49	500	2.0	250	1

8. Low- and Medium-Rate Telemetry

The low- and medium-rate telemetry for the *Mariner* Mars 1969 mission will be uncoded ($T_B = T_{SY}$). At minimum operating condition ($5/10^3$ bit error rate), ST_B/N_0 (m.o.c.) is +5.2 dB (Ref. 4). This results in a suppression factor due to data $\alpha' = 0.69$ for $\tau_D/T_{SY} = 1/3$ and 50% probability that the data symbol stream switches on successive bit periods (Fig. 50).

Consider use of the narrow subcarrier loop bandwidth at minimum operating condition. The resultant subcarrier phase noise error $\sigma_{\theta n}$ is shown plotted in Fig. 53 as a func-

tion of data rate (8 to 270 bits/s). Degradation in ST_B/N_0 due to rms phase noise error in the subcarrier loop is represented by Expression (44) (SPS 37-48, Vol. II):

$$\frac{\text{Demodulated } \frac{ST_B}{N_0}}{\text{Input } \frac{ST_B}{N_0}} = \left[1 - \left(\frac{2}{\pi} \right)^{3/2} \sigma_{\theta n} \right]^2 \quad (44)$$

Figure 54 shows degradation in ST_B/N_0 for the range of data rates from 8 to 270 bits/s at minimum operating condition ($ST_B/N_0 = +5.2$ dB).

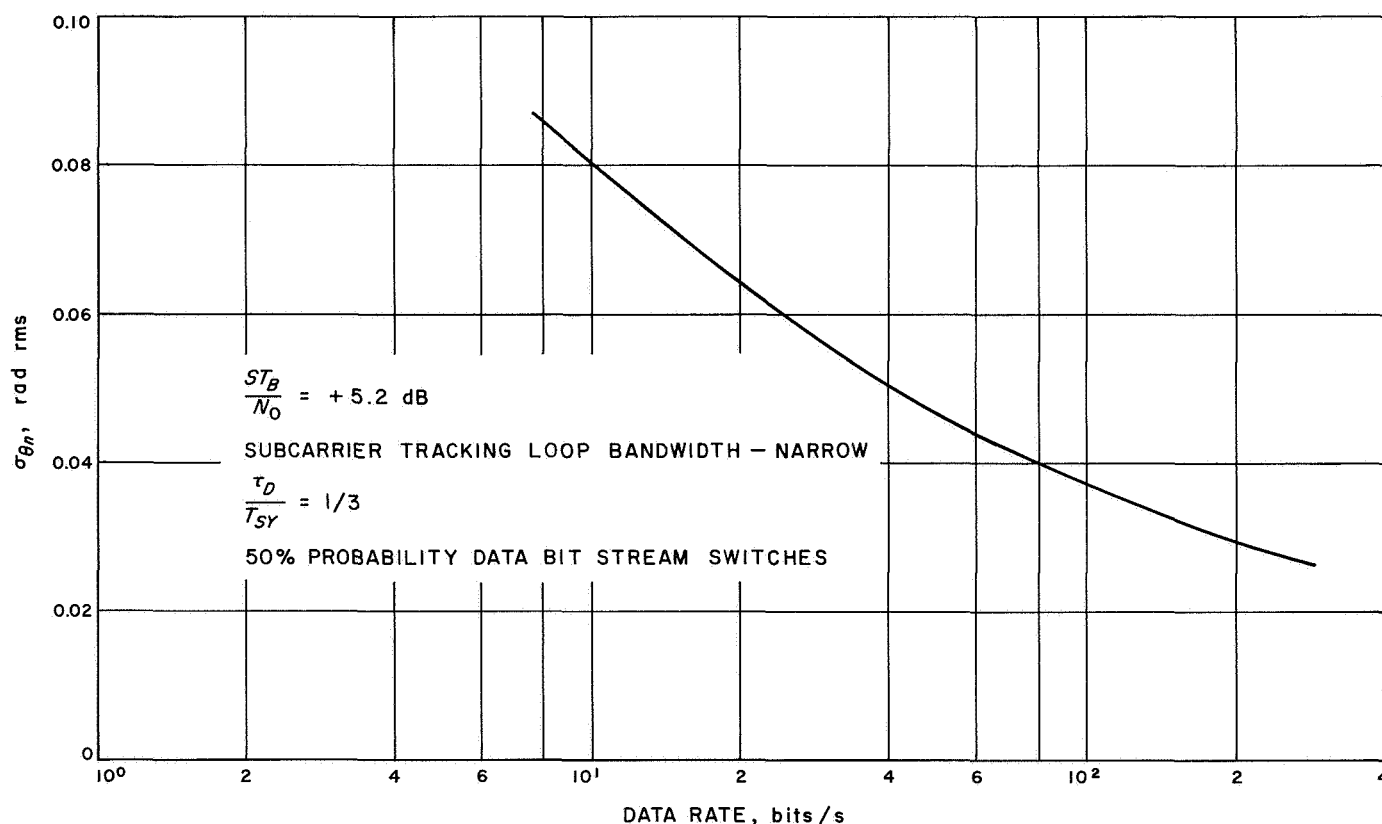


Fig. 53. Subcarrier demodulator rms phase noise error vs data rate

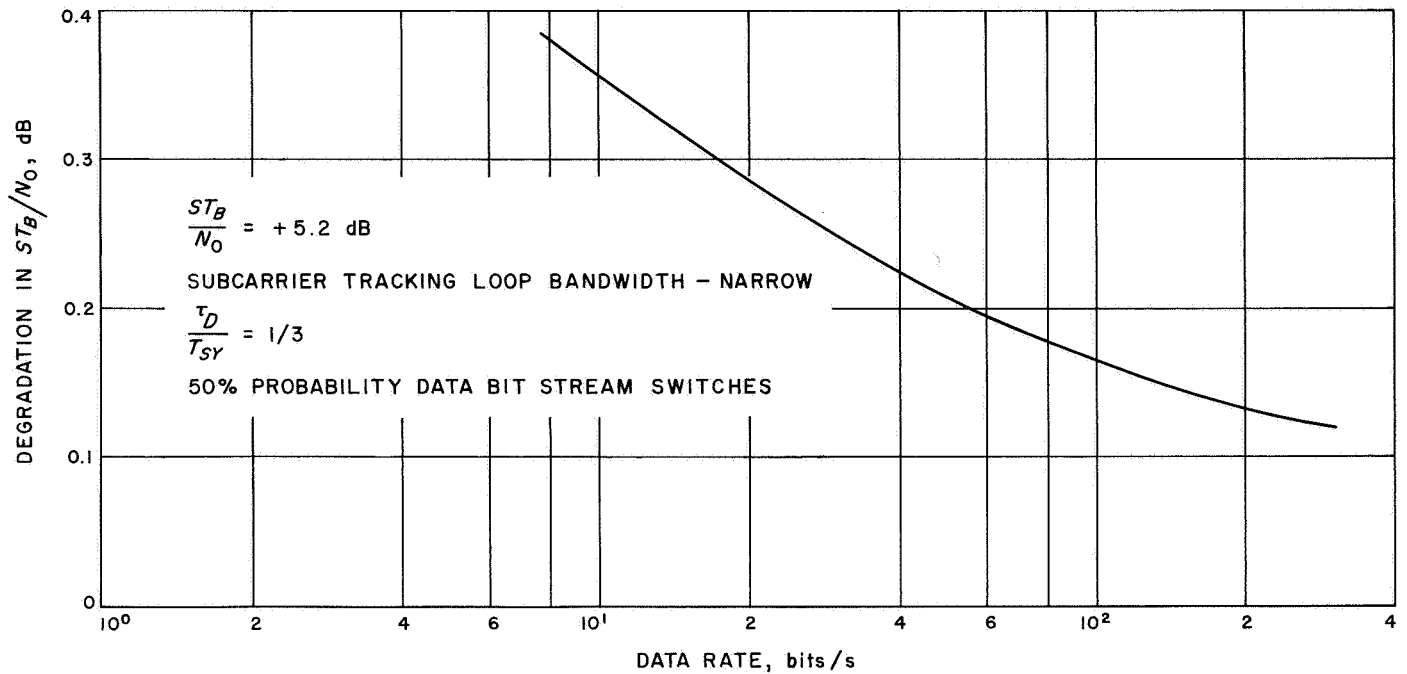


Fig. 54. Degradation in ST_B/N_0 due to phase noise error vs data rate

References

1. Tausworthe, R. C., *Theory and Practical Design of Phase-Locked Receivers, Vol. I*, Technical Report 32-819. Jet Propulsion Laboratory, Pasadena, Calif., Feb. 15, 1966.
2. Davenport, W. B., "Signal-to-Noise Ratios in Bandpass Limiters," *J. Appl. Phys.*, Vol. 24, No. 6, pp. 720-727, June 1953.
3. Jaffe, R. M., and Rechtin, E., "Design and Performance of Phase-Lock Circuits Capable of Near Optimum Performance Over a Wide Range of Input Signals and Noise Levels," *IRE Transactions on Information Theory*, Vol. 1T-1, pp. 66-76, March 1955.
4. Golomb, S. W., et al., *Digital Communications*. Prentice-Hall, Inc., Englewood Cliffs, N.Y., 1964.

IV. High-Rate Telemetry Project

A. Introduction, R. C. Tausworthe

This set of articles is a continuation of the reporting of progress on the HRT described in SPS 37-48, Vol. II, pp. 83-130. It consists of a description of: (1) the test code generator used to check various parts of the telemetry demodulator or the entire telemetry function of a tracking station, (2) the details and construction of the cross-correlator field sets, and (3) the telemetry system verification test procedure. The final article investigates the reference jitter degradation of the error rate.

B. Test Equipment, R. I. Greenberg

1. Purpose

The purpose of the HRT test equipment is to generate signals to functionally test and determine the operational status of the high-rate telemetry subsystem. The HRT test equipment provides test signals that are electrically equivalent to those of the received telemetry data stream and can be sent to any of several inputs of the high-rate telemetry subsystem for performing telemetry system checks.

2. Outputs

The outputs are essentially a series of comma-free code words consisting of 32 code symbols per word derived

from 6-bit data words. There are two types of symbols represented by two voltage levels, and are operated on to provide the following type of outputs:

a. Types of output

Integrated data stream. This is a series of comma-free code symbols operated on by an integrating circuit. The time constant of the circuit is 85 μ s.

Modulated data stream. This is a series of comma-free code symbols modulating a square wave subcarrier. There are three subcarrier cycles per symbol, and the rising edge of the first subcarrier cycle in the symbol is coincident with the start of the symbol.

Each of the above outputs may be operated on by a signal-to-noise mixer. The outputs are used, in accordance with Fig. 1, as follows:

b. Uses of output

The integrated data stream to the cross-correlator. This is a fixed signal output with a 2-V infinite bit. The signal, which may be mixed with the noise, is then processed for injection into the cross-correlator. This provides a check of the correlator-computer subsystem.

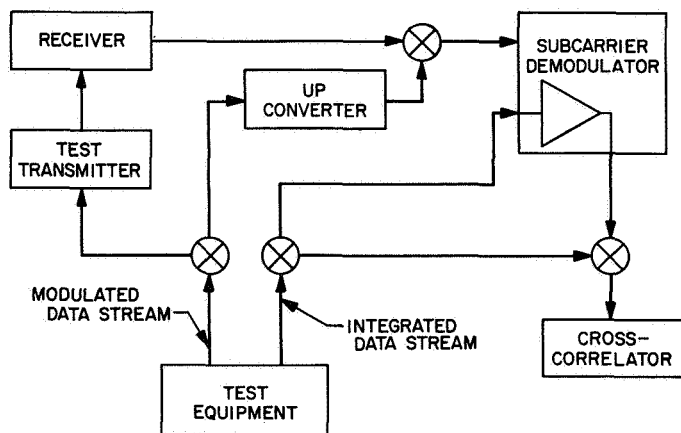


Fig. 1. Distribution of HRT signals

The integrated data stream to the subcarrier demodulator. This is a fixed signal with an 800-mV infinite bit. The signal, which may be mixed with noise, is amplified in the SDA to provide a 2-V infinite bit to be sent to the cross-correlator for decoding as above.

The modulated data stream to the test transmitter. This is a signal which may be varied between 1.5 and 0.15 V by means of an attenuator and may be mixed with noise. The signal is to be injected into the modulator of the test transmitter for testing the entire telemetry function from the S-band receiver to data output.

The modulated data stream to the subcarrier demodulator assembly. This is a fixed signal of 200 mV peak-to-peak, and may be mixed with noise. It is the same signal as the preceding one, except for the level. It is injected into the SDA up-converter to test the telemetry demodulator without the need for the receiver.

The equipment is capable of generating a 6-bit code word at 16,200 bits/s, and converted to a 32-symbol comma-free code word at 86,400 symbols/s.

The test equipment is to be installed in half-size mobile racks for movement to any convenient location. The outputs are through TNC connectors. BNC connectors are used to connect to the S/N mixer.

3. Detailed Block Diagram

The test equipment will operate in accordance with the following (Fig. 2):

a. Sine-wave oscillator. This is the source of the basic testing frequency. The frequency is chosen in accordance with the following equation.

$$\begin{aligned} \text{Oscillator frequency} &= 2 \left[\frac{\text{symbols/data word}}{\text{data bits/data word}} \right] \\ &\quad \times [\text{subcarrier cycles/symbol}] \\ &\quad \times [\text{data bit frequency}] \end{aligned}$$

Therefore

$$\text{Oscillator frequency} = 2 \left[\frac{32}{6} \right] [3] [16,200] = 518.5 \text{ kHz}$$

The oscillator amplitude must exceed 1 V rms in order to provide enough input to the pulse shaper.

b. Pulse shaper. The pulse shaper converts the sine wave into a series of pulses at the same frequency.

c. The square wave generator. This is actually only a flip-flop. The state of the flip-flop is changed at each pulse time. Since the pulses are equally spaced, the output of the flip-flop is a symmetrical square wave of half the oscillator frequency. The output provides the basic clock pulse CL_0 to the test equipment. CL_0 is also the subcarrier which will be modulated by the comma-free code symbols.

d. Divider register R_0 and R_1 . This is a two-stage divide-by-three counter needed to provide the three subcarrier cycles per symbol. Once during each counting cycle the symbol pulse CL_1 is generated at the required rate

$$\frac{518.4 \text{ kHz}}{2 \times 3} = 86,400 \text{ pulses/s}$$

e. State counter C_0 through C_4 . This register counts in free-running natural binary. The register will recycle every 32 CL_1 pulses. The word pulse, CL_2 , is generated once each counting cycle and is coincident with the beginning of the all zero state of the register.

$$\text{The rate is } 86,400/32 = 86,400 \text{ pulses/s}$$

f. Pseudorandom word generator D_0 through D_8 and D_9 . This is a 9-bit modified PN generator which provides a series of states in a sequence which repeats every 512 word times. A new bit state is put into the D_8 end. Shifting is done in the D_0 direction. A 6-bit word is chosen from D_5 through D_0 , and a new word appears every CL_2 time. Each 6-bit word will appear pseudorandomly 8 times during every 512-word sequence.

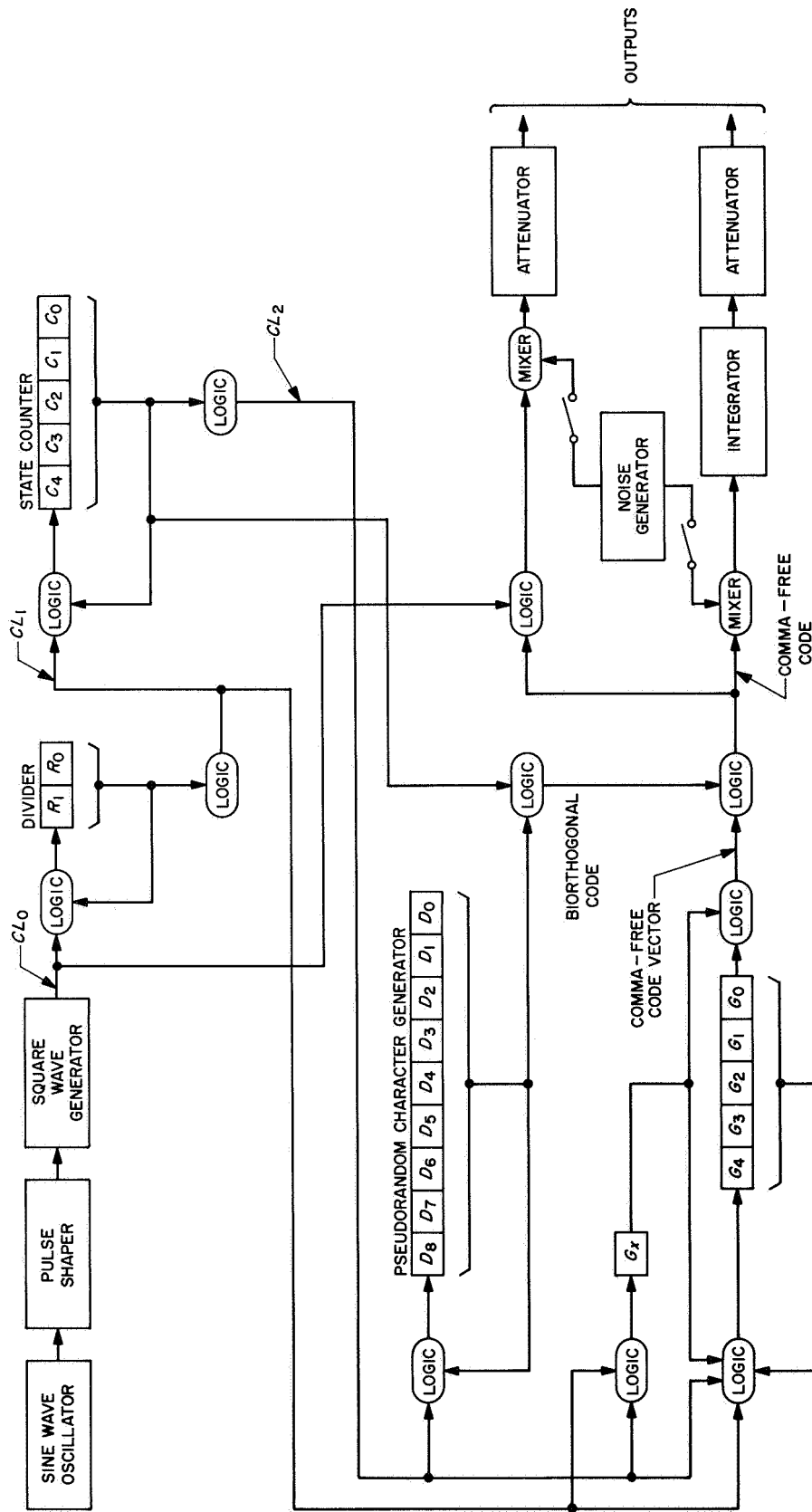


Fig. 2 HRT test equipment for field units

g. *Comma-free code vector generator, G_0 through G_{31} , and G_{32} .* This vector is as follows:

$$C = \underbrace{10001101110101000010010110011111}_{\text{PN code of 31 symbols}}$$

$t_0 \xrightarrow{\text{time}} t_{31}$

It is provided by a 5-bit PN generator for a 31-bit sequence plus a flip-flop to fill out the 32-bit sequence required for the vector.

h. *Formation of the biorthogonal code.* This code is formed by logically combining the states of the appropriate bits of the pseudorandom word generator and the states of the state counter. The dictionary is in accordance with Table 1.

i. *Formation of the comma-free code.* This code is formed by the modulo 2 addition of the biorthogonal code and comma-free vector streams.

j. *Modulated code.* Exclusive Or logic is used to modulate the subcarrier with the comma-free code. The output of the logic is biased in order to provide plus and minus voltages which are symmetrical about zero volts before going to the attenuator.

k. *Integrator.* The comma-free code to the integrator is biased as in j above to provide a symmetrical input. The so-called integrator is not a true integrator but provides an exponential response at the output to the symbol inputs. Its time constant is 85 μ s.

l. *Noise insertion.* Noise may be inserted into either the modulated code stream or into the integrated code stream by means of a noise selector switch. There are three positions. The choices are:

- (1) No noise in either channel.
- (2) Noise on the integrator channel and no noise on the other.
- (3) Noise on the modulated channel and none on the other.

4. Field Unit/Laboratory Unit Differences

The preceding is essentially a description of the field units. The laboratory unit, which is now being checked for compatibility with the high-rate telemetry subsystem, differs in several respects from the field units now being built. The laboratory unit is capable of providing:

- (1) A variable number of subcarrier cycles per symbol.
- (2) Variable integrator time constants.
- (3) Limited control over data word size.

Table 1. Data word/biorthogonal code correspondence

Word No.	Data Word	Coded Word															
		$t_0 \xrightarrow{\text{Time}} t_{31}$															
0	00 00 00	00	00	00	00	00	00	00	00	00	00	00	00	00	00	00	00
1	00 00 01	01	01	01	01	01	01	01	01	01	01	01	01	01	01	01	01
2	00 00 10	00	11	00	11	00	11	00	11	00	11	00	11	00	11	00	11
3	00 00 11	01	10	01	10	01	10	01	10	01	10	01	10	01	10	01	10
4	00 01 00	00	00	11	11	00	00	11	11	00	00	11	11	00	00	11	11
5	00 01 01	01	01	10	10	01	01	10	10	01	01	10	10	01	01	10	10
6	00 01 10	00	11	11	00	00	11	11	00	00	11	11	00	00	11	11	00
7	00 01 11	01	10	10	01	01	10	10	01	01	10	10	01	01	10	10	01
8	00 10 00	00	00	00	00	11	11	11	11	00	00	00	00	11	11	11	11
9	00 10 01	01	01	01	01	10	10	10	10	01	01	01	01	10	10	10	10
10	00 10 10	00	11	00	11	11	00	11	00	00	11	00	11	11	00	11	00
11	00 10 11	01	10	01	10	10	01	10	01	01	10	01	10	10	01	10	01
12	00 11 00	00	00	11	11	11	11	00	00	00	00	11	11	11	11	00	00
13	00 11 01	01	01	10	10	10	10	01	01	01	01	10	10	10	10	01	01
14	00 11 10	00	11	11	00	11	00	00	11	00	11	11	00	11	00	00	11
15	00 11 11	01	10	10	01	10	01	01	10	01	10	10	01	10	01	01	10
16	01 00 00	00	00	00	00	00	00	00	00	11	11	11	11	11	11	11	11

Table 1. (contd)

Word No.	Data Word	Coded Word															
		f_0 ————— Time ————— f_{31}															
17	01 00 01	01	01	01	01	01	01	01	01	01	10	10	10	10	10	10	10
18	01 00 10	00	11	00	11	00	11	00	11	11	00	11	00	11	00	11	00
19	01 00 11	01	10	01	10	01	10	01	10	10	01	10	01	10	01	10	01
20	01 01 00	00	00	11	11	00	00	11	11	11	11	00	00	11	11	00	00
21	01 01 01	01	01	10	10	01	01	10	10	10	10	01	01	10	10	01	01
22	01 01 10	00	11	11	00	00	11	11	00	11	00	00	11	11	00	00	11
23	01 01 11	01	10	10	01	01	10	10	01	10	01	01	10	10	01	01	10
24	01 10 00	00	00	00	00	11	11	11	11	11	11	11	11	00	00	00	00
25	01 10 01	01	01	01	01	10	10	10	10	10	10	10	10	01	01	01	01
26	01 10 10	00	11	00	11	11	00	11	00	11	00	11	00	00	11	00	11
27	01 10 11	01	10	01	10	10	01	10	01	10	01	10	01	01	10	01	10
28	01 11 00	00	00	11	11	11	11	00	00	11	11	00	00	00	00	11	11
29	01 11 01	01	01	10	10	10	10	01	01	10	10	01	01	01	01	10	10
30	01 11 10	00	11	11	00	11	00	00	11	11	00	00	11	00	11	11	00
31	01 11 11	01	10	10	01	10	01	01	10	10	01	01	10	01	10	10	01
32	10 00 00	10	01	01	10	01	10	10	01	01	10	10	01	10	01	01	10
33	10 00 01	11	00	00	11	00	11	11	00	00	11	11	00	11	00	00	11
34	10 00 10	10	10	01	01	01	01	10	10	01	01	10	10	10	10	01	01
35	10 00 11	11	11	00	00	00	00	11	11	00	00	11	11	11	11	00	00
36	10 01 00	10	01	10	01	01	10	01	10	01	10	01	10	10	01	10	01
37	10 01 01	11	00	11	00	00	11	00	11	00	11	00	11	00	11	00	11
38	10 01 10	10	10	10	10	01	01	01	01	01	01	01	01	10	10	10	10
39	10 01 11	11	11	11	11	00	00	00	00	00	00	00	00	11	11	11	11
40	10 10 00	10	01	01	10	10	01	01	10	01	10	10	01	01	10	10	01
41	10 10 01	11	00	00	11	11	00	00	11	00	11	11	00	00	11	11	00
42	10 10 10	10	10	01	01	10	10	01	01	01	01	10	10	01	01	10	10
43	10 10 11	11	11	00	00	11	11	00	00	00	00	11	11	00	00	11	11
44	10 11 00	10	01	10	01	10	01	10	01	01	10	01	10	01	10	01	10
45	10 11 01	11	00	11	00	11	00	11	00	00	11	00	11	00	11	00	11
46	10 11 10	10	10	10	10	10	10	10	10	01	01	01	01	01	01	01	01
47	10 11 11	11	11	11	11	11	11	11	11	00	00	00	00	00	00	00	00
48	11 00 00	10	01	01	10	01	10	10	01	10	01	01	10	01	10	10	01
49	11 00 01	11	00	00	11	00	11	11	00	11	00	00	11	00	11	11	00
50	11 00 10	10	10	01	01	01	01	10	10	10	10	01	01	01	01	10	10
51	11 00 11	11	11	00	00	00	00	11	11	11	11	00	00	00	00	11	11
52	11 01 00	10	01	10	01	01	10	01	10	10	01	10	01	01	10	01	10
53	11 01 01	11	00	11	00	00	11	00	11	11	00	11	00	00	11	00	11
54	11 01 10	10	10	10	10	01	01	01	01	10	10	10	10	01	01	01	01
55	11 01 11	11	11	11	11	00	00	00	00	11	11	11	11	00	00	00	00
56	11 10 00	10	01	01	10	10	01	01	10	10	01	01	10	10	01	01	10
57	11 10 01	11	00	00	11	11	00	00	11	11	00	00	11	11	00	00	11
58	11 10 10	10	10	01	01	10	10	01	01	10	10	01	01	10	10	01	01
59	11 10 11	11	11	00	00	11	11	00	00	11	11	00	00	11	11	00	00
60	11 11 00	10	01	10	01	10	01	10	01	10	01	10	01	10	01	10	01
61	11 11 01	11	00	11	00	11	00	11	00	11	00	11	00	11	00	11	00
62	11 11 10	10	10	10	10	10	10	10	10	10	10	10	10	10	10	10	10
63	11 11 11	11	11	11	11	11	11	11	11	11	11	11	11	11	11	11	11

3. Symbol Timing Loop

Operation of the cross-correlation detector is predicated on the occurrence of the analog-to-digital conversion signal at the exact beginning of each symbol time. To ensure this condition, blocks (5) through (9), together with the computer, are used to form a phase-locked loop called the symbol timing loop. Block (5) acts upon the signal in the same manner as block (1) with the exception that the conversion signal occurs at the midpoint of each symbol time. The resultant integral value is the sum of the last half of the previous symbol and the first half of the current symbol. When a transition occurs between two symbols, and the conversion signal is exactly centered, the resultant integral value will be zero, neglecting noise. Departure from this exact timing will result in an error signal proportional to the phase error. The sign logic (6) inhibits the output of (5) when there is no transition and inverts the sign of (5) when the transition is negative.

Integral values are accumulated in block (7) for 128 symbol times. The computer reads in this accumulated number at the same time it reads in the numbers from the cross-correlator detector. After digitally filtering the numbers read from (7), the computer controls the search oscillator in the Hewlett Packard synthesizer (9) through the digital-to-analog converter (8) in order to maintain the error value at zero. A more detailed discussion of the various blocks in the digital equipment may be found in SPS 37-48, Vol. II.

4. Construction

The digital equipment for laboratory set A is housed in one cabinet. Digital logic within the equipment is contained in three slide-out drawers, each occupying 7.5 in. of panel height, as shown in the photograph of Fig. 4. Within the drawers are ten printed circuit cards, each mounting a maximum of 66 microcircuits. Some of the 66 microcircuit positions on selected cards are not used, in order to provide spare positions for possible equipment modification in the future.

Figure 5 shows a card on an extender. Integral levers at the top of each card are used for insertion, removal, and the secure retention of the card. Interconnections between the microcircuit positions are made using the wire-wrap technique. The printed pattern shown beneath the wiring is a ground plane which helps suppress pickup of noise and extraneous signals. Figure 6 shows the opposite side of the card, known as the microcircuit side. Microcircuits are mounted on a grid labeled A through N

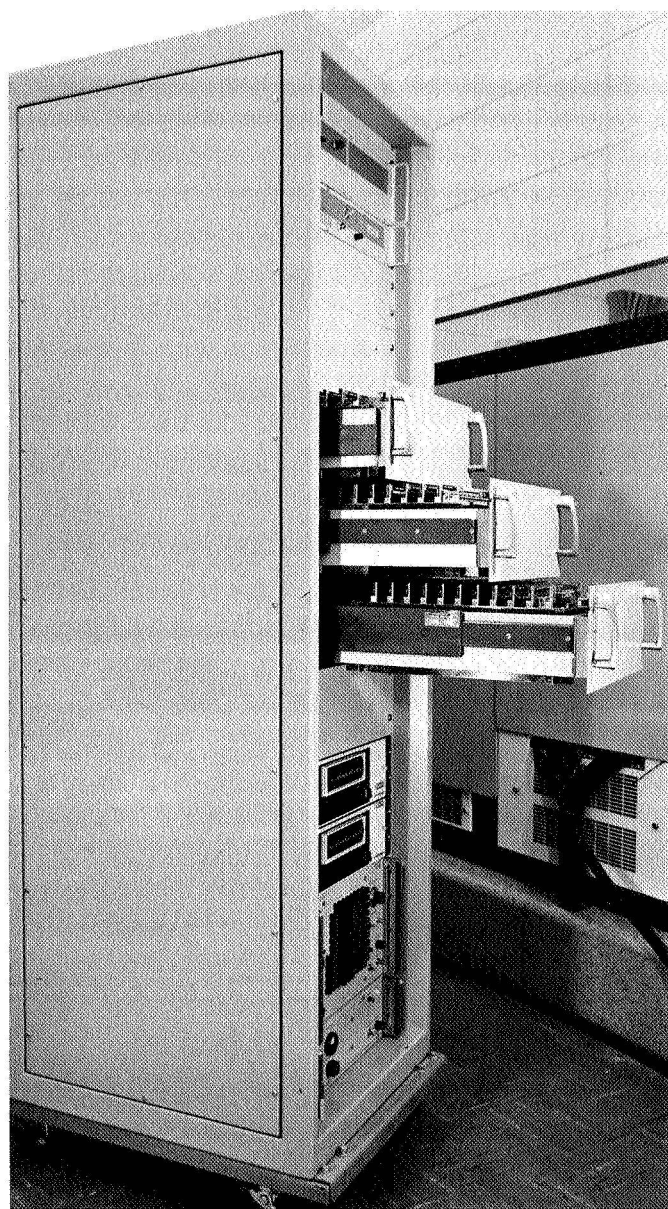


Fig. 4. Digital equipment with drawers extended

horizontally and 1 through 6 vertically. Supply voltages are brought to all usable grid positions by means of the printed circuit grid pattern.

Construction of the digital equipment for laboratory set A is similar to that used by the programmed exciter described in SPS 37-36, Vol. III, pp. 59. However, a significant innovation in the present equipment is the use of retractable printed circuit ribbon cables shown in Fig. 7, the digital equipment cabinet rear view. These cables connect the logic drawers to the cabinet harness wiring. The harness wiring is located in Panduit ducting

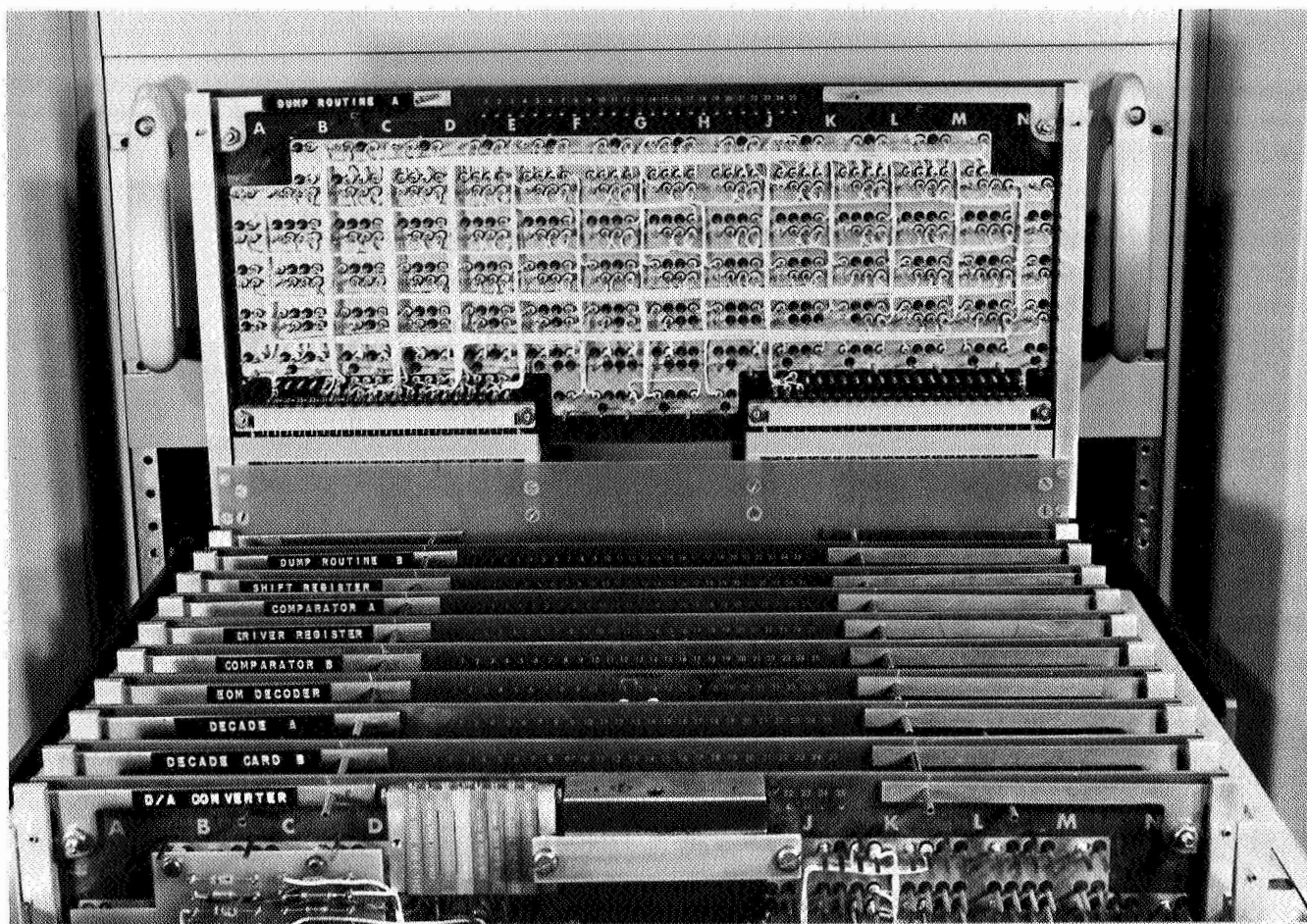


Fig. 5. Microcircuit card on extender

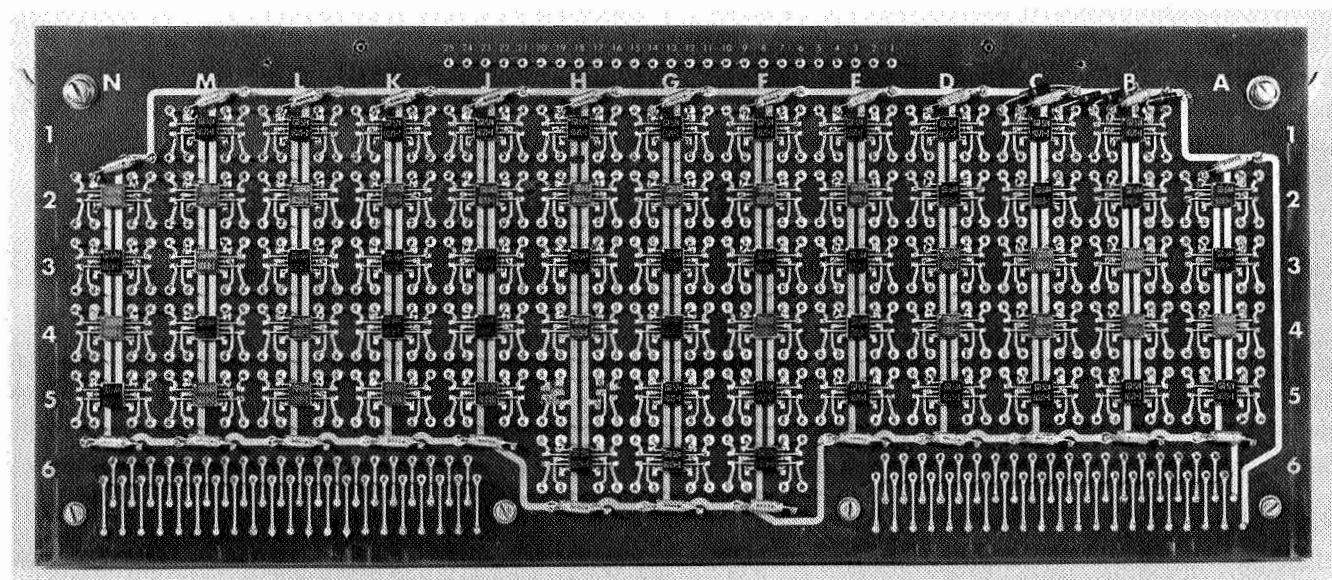
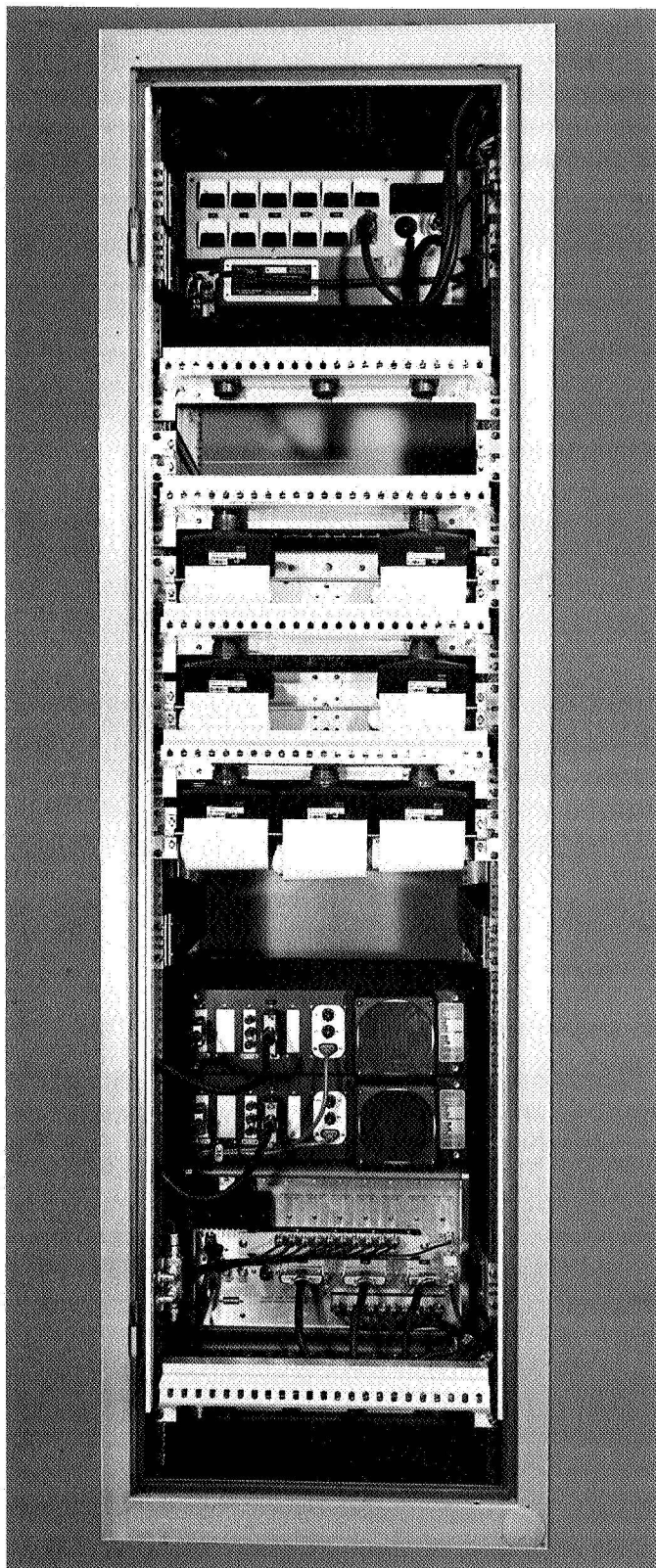


Fig. 6. Microcircuit side of card



**Fig. 7. Digital equipment cabinet
rear view**

around the rear door perimeter and crossing the rear door opening at several selected places.

The entire construction and mechanical design has been oriented to facilitate the initial equipment debugging phase, provide ease in field retrofitting, simplify maintenance procedures for quick failure recovery, and supply a rugged reliable housing for the digital equipment.

D. Verification Tests, R. W. Burt

1. Introduction

The goal of this test is to demonstrate the performance characteristics of the DSIF high-rate telemetry function. The word error rate of the demodulated telemetry and the reliability of correct word acquisition as functions of the RF input signal-to-noise ratio are used as measurements of performance. To exercise the entire high-rate telemetry function the test signal is introduced at the S-band carrier frequency. The carrier is then converted to an intermediate frequency of 10 MHz by the receiver and is further processed by the telemetry demodulator assembly.

The sideband modulation index of the S-band test signal is first adjusted for a specific sideband-to-carrier ratio. Then a signal-to-noise energy per bit is determined which will produce a desired word error rate in the demodulated data. Then, without modulation, the carrier-to-noise ratio is set to give the required sideband-to-noise energy ratio when modulation is applied. Next, modulation is applied, and the performance of the high-rate telemetry function is judged by the word error rate ratios having expected data word error rates of 0.1, 1, and 23.3%. The latter figure is a 10% bit error probability. Finally, the reliability of correct word acquisition is tested at the sideband-to-noise ratio having an expected word error rate of 23.3%. The importance of accurately establishing signal-to-noise ratio and modulation index are discussed in the following paragraphs.

2. Bit Error Degradation

The output demodulated data error rate depends on four fundamental parameters which become evident when the simplified block diagram of the system as shown in Fig. 8 is examined. The general equation for effective sideband signal-to-noise ratio is given in Eq. (1).

$$R = \frac{ST_B}{N_0} (\ell) (m) (n) (p) \quad (1)$$

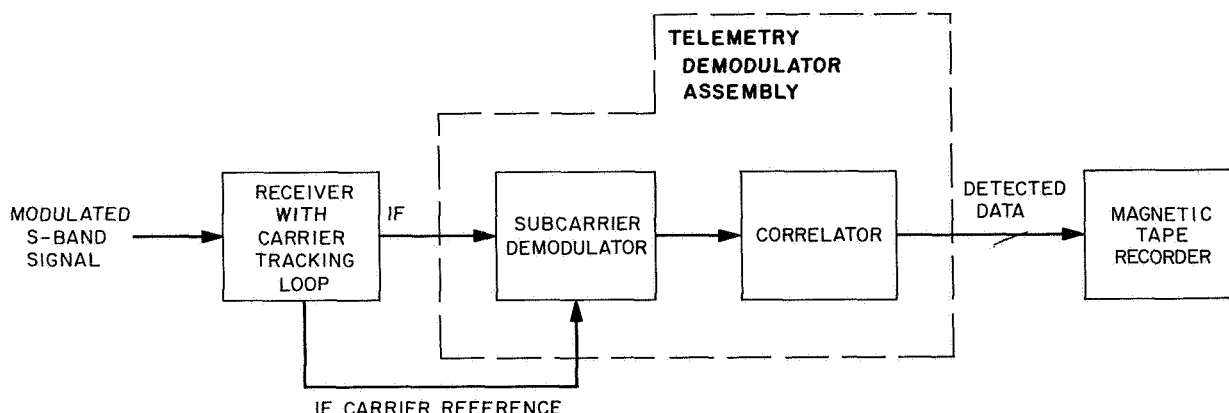


Fig. 8. HRT system block diagram

where

R = effective sideband signal-to-noise energy ratio per bit

$\frac{ST_B}{N_0}$ = input sideband signal-to-noise energy ratio per bit required for the test

l = degradation caused by inaccuracy in setting the carrier-to-noise energy ratio

m = degradation caused by inaccuracy in setting the subcarrier modulation index

n = degradation caused by the IF reference error

p = degradation caused by errors in the telemetry demodulation assembly including: subcarrier reference error, bit synchronization error, and bit detection errors

The parameter p is determined during subsystem testing and has a design goal of 0.2 dB; n , a function of signal level and modulation index, is the result of signal processing between S-band and the telemetry demodulator assembly and has a design goal of 0.1 dB. A test accuracy goal has been established for each of the other two parameters. This goal is 0.1 dB maximum degradation when the probability of word error for the output bit stream is 0.01.

3. Test Setup

Figure 9 is a block diagram of the test setup. The high-rate telemetry test set provides the telemetry subcarrier modulated with data. This is used to modulate a test translator or transmitter. Attenuator A1 controls the subcarrier modulation index, and attenuator A2 controls the signal-to-noise ratio. The resulting S-band test signal is applied

to the receiver and detected in the high-rate telemetry demodulator, where the data error rate is measured. The S-band input signal-to-noise ratio is established at the receiver input by monitoring the heterodyne signal at 50 MHz, using the signal-to-noise ratio measurement assembly. The use of this equipment in CW power calibration is described in SPS 37-48, pp. 54-57. For the high-rate telemetry project this equipment has been further developed to provide the means for precision signal-to-noise calibration at DSSs 14 and 71 and CTA 21. Modulation index is set by observing the carrier suppression by using the HP 302 wave analyzer and HP 355C attenuator, but the conventional method has been improved by substituting the attenuator accuracy for the wave analyzer dial calibration.

4. SNR Measurement Method

The technique used consists of accurately measuring the ratio of carrier-plus-noise power to noise power. First, power indicator M1 is adjusted for full-scale deflection with the RF signal source off. Then, the desired ratio, less the bandwidth of filter F, is inserted in the precision attenuator A3, and, with the unmodulated signal source turned on, A2 is adjusted until the power level at M1 is returned to the same value.

As an example of the method, consider the following: suppose the test requirement is to set up a signal-to-noise ratio yielding a 1% word error rate. For this case

$$\frac{ST_B}{N_0} = 2$$

so that for $1/T_B = 16.2$ kbits

$$S/N_0 = 45.1 \text{ dB}$$

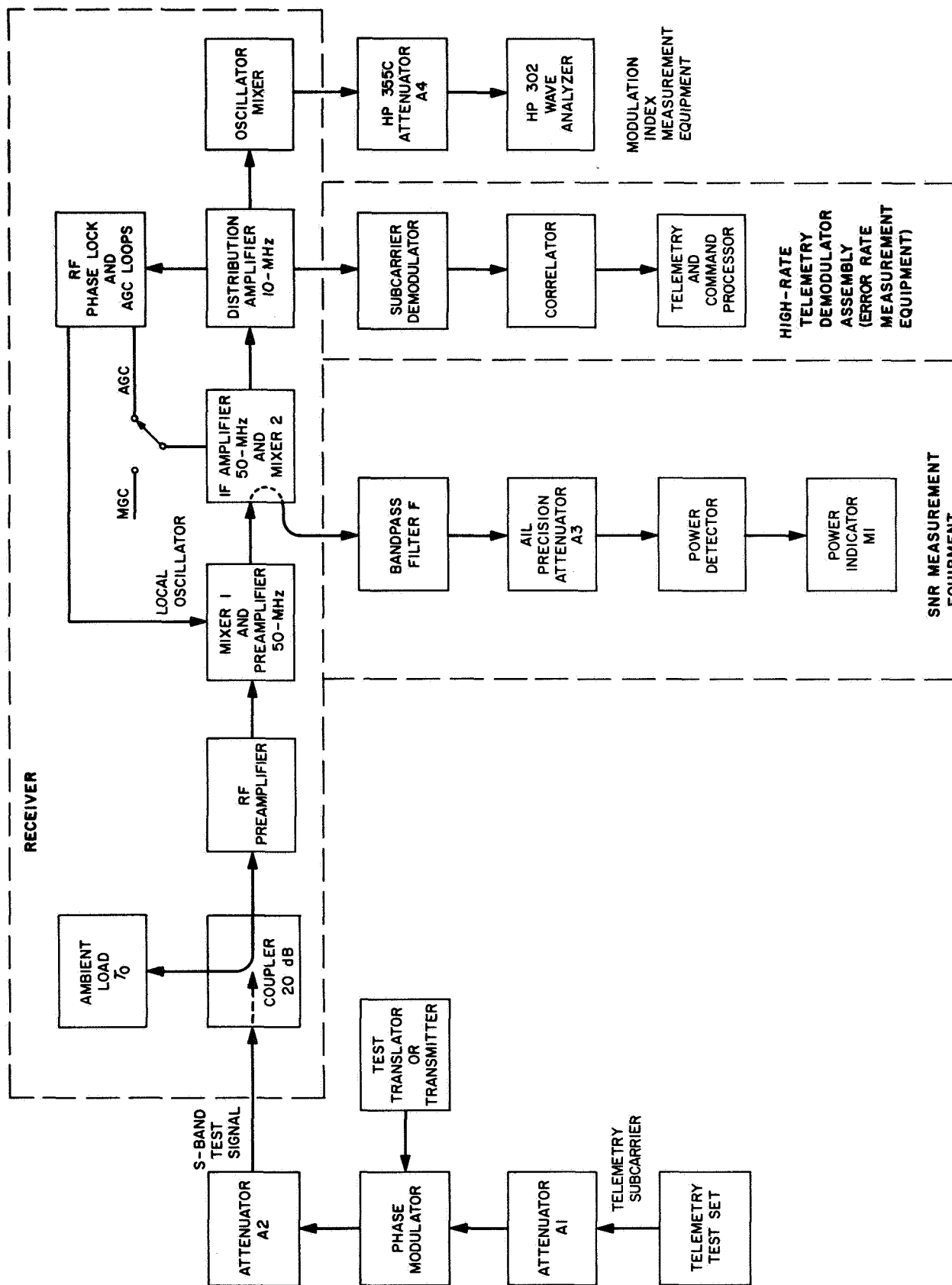


Fig. 9. System verification test setup

Also, assume square wave modulation with carrier suppression given by

$$\frac{P_c}{P_T} = -8 \text{ dB}$$

where

P_c = carrier power at the receiver input

P_T = total signal power at the receiver input
and with modulation index specified by

$$\frac{S}{P_T} = -0.75 \text{ dB}$$

Note that the numbers closely approximate *Mariner* Mars 1969 requirements. Then since

$$\frac{P_T}{P_n} = \frac{S/P_n}{S/P_T} = 45.85 \text{ dB}$$

the ratio required in the noise bandwidth F , for $F = 10 \text{ kHz}$, is 5.85 dB. Thus the difference between signal plus noise and noise only to be set up with attenuator A3 is 6.85 dB. The measurement is expressed by

$$\frac{P_T G(f_0) + k T_0 F G(f_0)}{k T_0 F G(f_0)} = A_3, \text{ dB} \quad (2)$$

or

$$\frac{P_T}{k T_0 F} = A_3 - 1$$

where

$k T_0 F$ = noise power at the receiver input in the bandwidth F

and

$$F = \int_0^\infty g(f) df = \text{bandwidth, Hz}$$

where

$$g(f) = \frac{G(f)}{G(f_0)}$$

= normalized gain response where f_0 is 50 MHz

The accuracy of this measurement establishes the parameter ℓ in Eq. (1), and is determined by attenuator A2 and the bandpass filter F , assuming that response from S-band to the receiver 50-MHz output is flat across F so that $g(f)$ is only a function of the filter F . It is also assumed that

signal level is constant. These assumptions will be checked when tests are run at CTA 21. The accuracy with which F is known is given in Ref. 1 as $\pm 0.01 \text{ dB}$. The accuracy of the precision AIL attenuator is given by the manufacturer as $\pm 0.1 \text{ dB}$ for the worst case. Thus ℓ is $\pm 0.11 \text{ dB}$ for the worst case.

5. Modulation Index

Modulation index is adjusted using the method of carrier suppression. With the receiver in MGC and locked to the incoming carrier at strong signal, a convenient level is set on the HP 302 wave analyzer. Attenuation equal to the desired carrier suppression is inserted in attenuator A4 and a reference level measured on the meter. A4 is then returned to its original setting, and modulation is applied until the reference level is again reached.

Figure 10 illustrates the manner in which the HP 302 wave analyzer observes only the carrier. The 3-Hz band-pass filter excludes the modulation sidebands and all but a negligible amount of noise. Noise contribution to the error is negligible, however, since the carrier-to-noise power in this bandwidth is purposely set high during this measurement. Also, the receiver is assumed linear over the nominal 8-dB range of carrier variation, since it is phase-locked and operating in manual gain control. This assumption will also be checked when tests are run at CTA 21. Another assumption will be that the operator can return exactly to the reference level. For these assumptions, m in Eq. (1) is determined by the accuracy of the HP 355C, which is given by the manufacturer as 0.1 dB.

Reference

1. Stelzried, C. T., and Reid, M. S., *Precision Power Measurements of Spacecraft CW Signal Level With Microwave Noise Standards*, Technical Report 32-1070. Jet Propulsion Laboratory, Pasadena, Calif., (Reprinted from *IEEE Transactions on Instrumentation and Measurement*, Vol. IM-15, No. 4, pp. 318-324, Dec. 1966.)

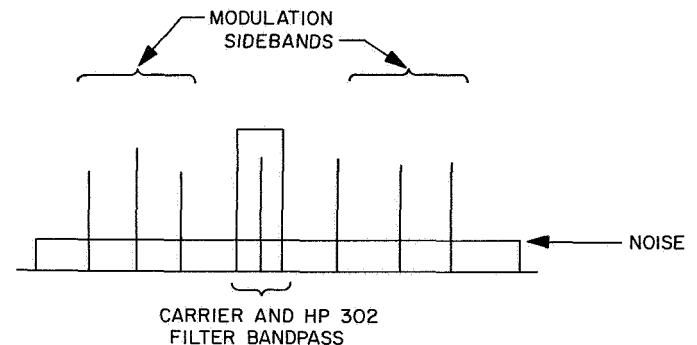


Fig. 10. Wave analyzer observation of carrier

E. Subcarrier Demodulator, M. H. Brockman

1. Introduction

Analysis of the subcarrier demodulator, which provides reference material for the following, is contained in the article relating to the multiple-mission telemetry system, Section III-L. This report provides information on subcarrier phase noise and its resultant degradation of ST_B/N_0 for high-rate telemetry for *Mariner* Mars 1969.

The high-rate telemetry for the *Mariner* Mars 1969 mission will use biorthogonal coding with 6 bits/word and a data rate of 16.2 kbits/s. At minimum operating condition (1% word error rate), ST_B/N_0 (m.o.c.) is +3 dB (Ref. 1) which provides an ST_{SY}/N_0 (m.o.c.) of -4.3 dB (SPS 37-48, Vol. II). This results in a suppression factor due to data $\alpha' = 0.36$ for $\tau_D/T_{SY} = 1/3$ and 50% probability that the data symbol stream switches on successive symbol periods (see Section III-L-7, Fig. 50).

At mission design point (10% bit error rate), $ST_B/N_0 = -1$ dB which provides $ST_{SY}/N_0 = -8.3$ dB and $\alpha' = 0.24$. The resultant signal-to-noise spectral density S/N_0 in the subcarrier loop premodulation bandwidth is

$$\frac{S}{N_0} = \frac{1}{1.26 \times 5.33 \times T_{SY}} = \frac{86,400}{6.72} = 12,860 \quad (1)$$

The resultant signal-to-noise ratio (P_S/P_N) in the 500-Hz noise bandwidth of the subcarrier loop predemodulation filter is

$$\frac{P_S}{P_N} = \frac{12,800}{500} = 25.72 \quad (2)$$

Consequently, for this case, the "soft" bandpass limiter in the subcarrier loop is operating as a linear device (in the MMTS subcarrier analysis, this results in $\Gamma = 1$ and $\alpha = 1$).

For *Mariner* Mars 1969 high-rate telemetry, the medium bandwidth for the MMTS subcarrier demodulator would be selected. The resultant subcarrier phase noise (σ_{θ_n}) is shown in Fig. 11 as a function of ST_B/N_0 . Degradation in ST_B/N_0 due to rms phase noise error in the subcarrier tracking loop is (SPS 37-48), Vol. II):

$$\frac{\text{demodulated } \frac{ST_B}{N_0}}{\text{input } \frac{ST_B}{N_0}} = \left[1 - \left(\frac{2}{\pi} \right)^{3/2} \sigma_{\theta_n} \right]^2 \quad (3)$$

Using the information in Fig. 11 and Eq. (3), the resultant degradation in ST_B/N_0 due to subcarrier phase noise is obtained (Fig. 12) as a function of ST_B/N_0 . Note that at minimum operating condition ($ST_B/N_0 = +3$ dB), the degradation due to subcarrier phase noise is 0.09 dB.

Reference

1. Golomb, S. W., Baumert, L. D., Easterling, M. F., Stiffler, J. J., and Viterbi, A. J., *Digital Communications*. Prentice-Hall, Inc., Englewood Cliffs, N.Y., 1964.

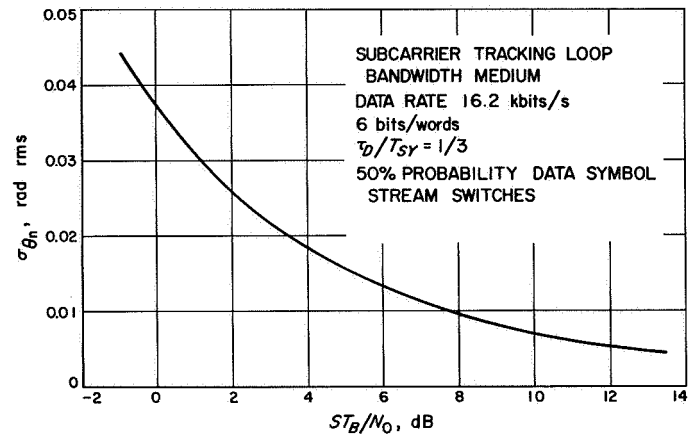


Fig. 11. Subcarrier demodulator rms phase noise error versus ratio of signal energy per bit to noise spectral density

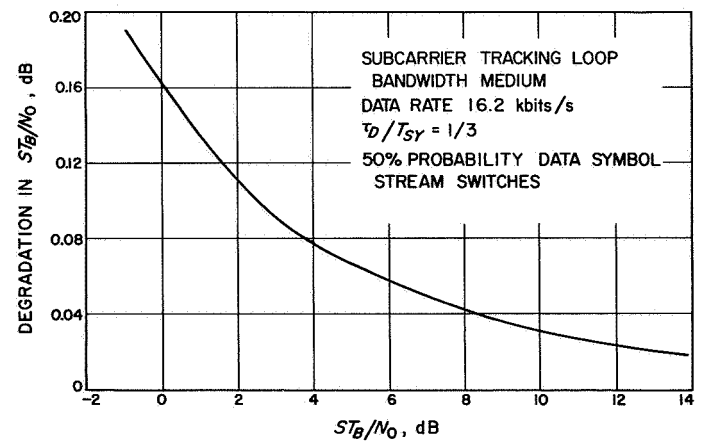


Fig. 12. Degradation in ST_B/N_0 due to phase noise error versus ratio of signal energy per bit to noise spectral density

V. Facility Engineering and Operations

A. Goldstone DSCC Flight Project Support,

W. E. Larkin and R. M. Cuberly

1. Lunar Orbiter Mission

The Echo DSS continued to provide mission support for the sole remaining spacecraft—*Lunar Orbiter V*. The station performed tracking and data command transmissions in support of JPL engineering and scientific experiments.

2. Surveyor Missions

a. Surveyor V. The DSSs attempted unsuccessfully to acquire the spacecraft during the third lunar day. On December 14, 1967, the second day of the fourth lunar day, the Pioneer DSS resumed the search with offsets calculated by station engineers. The spacecraft was reacquired and routine tracking was resumed.

b. Surveyor VI. The spacecraft was launched on November 7, 1967. The Pioneer DSS provided primary tracking and data command transmissions, and processed photographic, engineering, and scientific data transmitted by the spacecraft. More than 24,000 video frames were processed by the station during the first lunar day.

On November 17, the Pioneer DSS transmitted commands for a lunar translation maneuver—a motor burn

which lifted the spacecraft from the lunar surface for a second landing. Mission tracking and data command transmissions were resumed without incident after the maneuver.

c. Surveyor G. The Pioneer DSS performed engineering verification and configuration verification testing in preparation for the *Surveyor G* launch.

3. Mariner Missions

a. Mariner IV. The mission was officially ended on December 20, 1967. Tracking was concluded when the telemetry received at the station had diminished to a few minutes of data per hour. The Mars DSS and Echo DSS were providing the tracking and data transmissions during the final passes, with the Echo DSS processing the spacecraft transmissions. The Mars DSS commanded a retransmission of stored video on November 29, from which the Echo DSS was able to process nine and one-half pictures of the original encounter sequence.

b. Mariner V. The DSSs supported the mission until December 5, when the spacecraft signal strength dropped below demodulator lockup capability. No further tracking is anticipated before September 1, 1968. The Mars DSS and Echo DSS provided the mission support, with the Echo DSS processing the spacecraft telemetry.

c. **Equipment changes.** The Pioneer DSS has disconnected all *Mariner* mission support equipment from the station data command system.

4. Pioneer Missions

a. **Pioneers VI and VII.** The Mars DSS continued to provide primary tracking and command support at the DSCC, and the Echo DSS continued processing the spacecraft telemetry.

b. **Pioneer VIII.** The spacecraft was launched on December 13, 1967. The Echo DSS provided primary tracking and data command transmissions, and processed engineering and scientific data from the spacecraft. Mission support is continuing in a normal manner.

c. **Proposed expansion of support capability.** A solution for increasing spacecraft coverage has been proposed by the Pioneer DSS and has met with tentative approval. The proposal utilizes spare equipment, presently located

at Echo DSS, which would be installed in a portable rack that could be readily relocated to another tracking station. Two configurations are possible as follows:

Full station capability. This configuration is shown in Fig. 1. The demodulator/synchronizer, computer buffer, command encoder, and one power supply are available spare units. The other two power supplies are available in the orientation racks. When the use of the orientation racks is required, these power supplies could be reinstalled. This, of course, would render the portable rack inoperative. The use of the TCP at Pioneer DSS, or the digital instrumentation subsystem at Mars DSS, would enable processing of telemetry and command.

Partial capability. This configuration is shown in Fig. 2. The demodulator synchronizer, command encoder, and one power supply are available in the orientation racks. There would be no computer processing, but demodulation of telemetry and command would be possible. Only cables 7, 12, and 14 are required to implement this system.

Gain in support capability. The advantages of using the proposed rack installation are as follows:

- (1) Ability to track and process data from two spacecraft simultaneously.

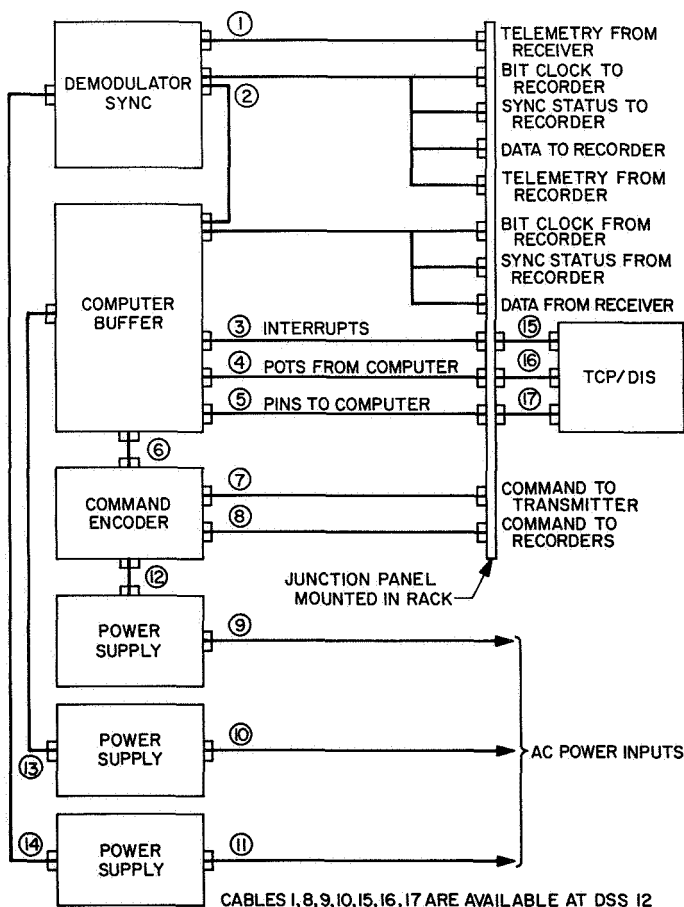


Fig. 1. Pioneer Project full station capability configuration

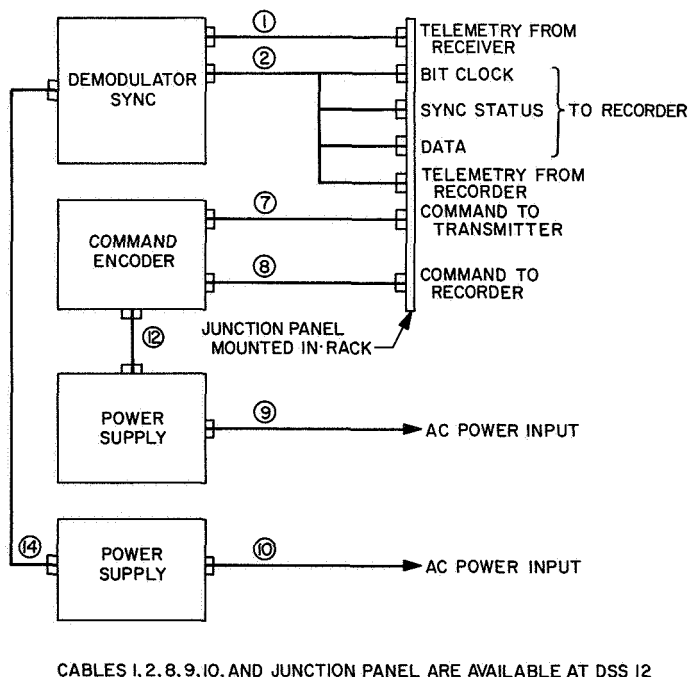


Fig. 2. Pioneer Project partial capability configuration

- (2) Eliminates scheduling problems when using two stations to support one spacecraft.
- (3) Provides a backup station in the event of a major failure to computers, or loss of communication circuits between DSSs.
- (4) Provides tracking by an alternate station when modifications or tests are required at the prime station.

5. Special Tests and Experiments

The DSCC supported various tests and experiments for the development of projects, procedures, and equipment. Most significant were the DSN system development, DSN quasar tracking experiments, bistatic radar experiments, *Mariner Mars 1969* Project system noise temperature experiments, *Pioneer* Project coding tests, and DSIF ranging confidence and time-correlation tests.

B. Multiple-Mission Telemetry Implementation,

R. L. Weber

A description and analysis of the multiple-mission telemetry system appears in SPS 37-46, Vol. III, pp. 175-243. Subsequent design status is reported in SPS 37-47, Vol. II, pp. 138-141; current design status and an implementation schedule appear in this issue on pp. 98-113.

Deep Space Stations 12, 41, 51, 62, 71, and 14 and CTA 21 will receive multiple-mission telemetry equipment. In addition, DSS 14 will receive two high-rate correlator racks and test equipment. These five additional racks are not standard equipment and will be operated on an experimental basis. The Spacecraft Monitoring Station at Cape Kennedy will receive, in addition to the standard MMTS equipment complement, a single experimental high-rate correlator and its test equipment. CTA 21 will have one channel of multiple-mission telemetry and one channel of high-rate telemetry.

C. DSIF Station Control and Data Equipment,

E. Bann, R. N. Flanders, A. T. Burke, P. C. Harrison,
and E. Garcia

1. Introduction

This report gives the status of the DSIF station control and data equipment as of December 1967. This equipment consists of the antenna pointing subsystem, digital instrumentation subsystem, the telemetry and command proces-

sor, station monitor and control, the frequency and timing subsystem, and the multiple-mission support equipment.

2. Antenna Pointing Subsystem Phase I

The APS has been implemented in the DSIF stations to provide the capability of positioning the station antenna via computer control. Implementation has been on an interim basis at DSSs 11, 12, 41, 61, 62, and 72. DSS 14 is operational with APS phase I. Descriptions of IAPS and APS I have been given in previous reports.

Current activity has been coordination of an installation plan for the implementation of APS I at DSSs 12, 41, 42, 51, 61, and 62. Objectives of the plan are to: (1) physically separate the SDS 910 computer which is now part of the digital instrumentation subsystem (at DSSs 41, 51, and 62 only), (2) reconfigure the SDS 910 computer from its present nonstandard form to an SDS standard model configuration, (3) integrate the SDS 910 computer with the APS I interface equipment and provide necessary check-out for complete implementation of APS I at each station, and (4) coordinate with the concurrent implementation plan for DIS II and TCP II so that optimum use can be made of support and checkout personnel at each installation site.

The tentative installation schedule for APS I is:

DSS 12	March 1968
DSS 41	June 1968
DSS 51	June 1968
DSS 62	July 1968
DSS 42	May 1968
DSS 61	April 1968

3. Digital Instrumentation Subsystem Phase II

The digital instrumentation subsystem phase II provides each Deep Space Station in the DSIF with the capability for monitoring the performance and alarm status of the various subsystems at the station. The DIS II, under control of the DSIF phase I monitor program, also prepares a permanent record of station performance on magnetic tape for postmission analysis, and provides real-time alarm and status messages for transmission to the SFOF via high-speed data line and telemetry. At present, the DIS II prototype is being retrofitted by the manufacturer.

The current effort involves the continued definition of the hardware and software interfaces to the DIS II. Data

received by the DIS II from the telemetry and command processor via the parallel data interface is being defined and message formats determined. Formats for station performance and alarm messages to the SFOF are also being established to assure compatibility between the processing programs at the transmitting and receiving ends. The hardware interface with the ground communications facility has been defined to permit GCF functions to be identified for monitoring by the DSIF monitor system phase I program.

4. Telemetry and Command Processor Phase II

The telemetry and command processor phase II provides the DSIF with a mission-independent telemetry and command processing capability for real-time operation. The TCP II is in the process of expansion (TCP II-C) to increase the telemetry data-processing capability to support the DSIF multiple-mission telemetry system.

The contract for fabrication of the expansion equipment is on schedule, with equipment delivery scheduled for early 1968. The first complete subsystem field installation is planned for March 1968 at DSS 12. This installation will serve to test the equipment design and installation procedures to ensure that major problems are not encountered during the overseas installations.

An SDS 920 computer in the TCP II-C configurations is scheduled for delivery in February 1968 and will be installed in CTA 21 to support early *Mariner* Mars 1969 testing. This computer will be installed with the TCP II computer and communications buffer that have been removed from DSS 72.

The early installation of analog-to-digital converters was completed at DSS 11 and DSS 12 to provide *Mariner* Venus 67 direct demodulation support. Additional units will be installed in early 1968 at DSS 42 and DSS 61 to provide direct demodulation support for follow-on *Mariner* Venus 67 tracking. The remaining A/DCs will be installed with the TCP II-C modification.

5. Station Control and Monitor Console Phase II

The SMC II provides for the display of station performance and alarm parameters for inspection by the station manager. The SMC II consists of indicators for visual monitoring of the status of the independent subsystems. Control elements are also supplied to permit the station manager to select the parameters to be output by the digital instrumentation subsystem phase II for display by the SMC II.

The major elements of the SMC II which are to be implemented and their respective status are as follows:

a. Program alarm and control panel. The logic has been documented and hardware procured for fabrication.

b. Countdown clock. The logic has been documented, and hardware acquisition is in process.

c. Remote and local display units. Components have been received and are stored in preparation for assembly.

d. Power supplies and cables. Material delivery is near completion.

Evaluation of the prototype X-Y recorder for the graphical display of station parameters is progressing satisfactorily, with the tests being conducted at Goldstone DSCC. Completion of these tests is anticipated by early January 1968, with the follow-on procurement scheduled for shortly thereafter.

6. Frequency and Timing Subsystem

The functional design of the FTS II has been completed, and a contractor has been selected to assist in the detail design, fabrication, and evaluation of a prototype unit.

The following three tasks have been assigned to the contractor:

a. Evaluation of frequency distribution amplifier. The contractor has evaluated a proposed 5-MHz frequency distribution amplifier. The amplifier under consideration was discovered to have excessive phase shift as a function of temperature. Additional design effort is required to obtain the degree of spectral purity and phase stability required by the station users of the distributed signal.

b. Design and fabrication of a timing pulse generator. The timing pulse generator provides the basic digital timing signals for use throughout the station and for the digital clock. The unit consists of an input phase shifter, pulse shaper, pulse advance and retard circuitry, and a six-decade digital frequency divider. Isolated outputs are provided for distributing the signals throughout the station with timing signals from 1 Hz to 1 MHz provided.

c. Design and fabrication of the digital clock and integration of the FTS II. The digital clock generates the station GMT time signals and distributes these in parallel BCD and serial form. This unit will be integrated with the timing pulse generator and JPL-supplied equipment and evaluated as a subsystem. It is anticipated that this task will be completed in early 1968 with the fabrication of the field units following shortly thereafter.

7. Multiple-Mission Support Area

a. Mission support recording. The mission support recording equipment, installed temporarily at DSS 14 for support of *Mariner* Venus 67 bistatic radar astronomy experiment, has been returned to DSS 12 for continued multiple-mission support of the *Pioneer* Project.

b. Communications interface assembly. Procurement of voltage-controlled oscillator, subcarrier discriminators and monitor test panel, required to meet *Mariner* Mars 1969 multiple-mission support requirements, has been initiated. Delivery of components is expected by March 1968.

D. Venus DSS Operations, J. D. Campbell, M. A. Gregg, E. B. Jackson, and A. L. Price

1. Experimental Activities

During the period of October 16 through December 15, 1967, the 30-ft antenna at the Venus DSS continued to be used in a time-synchronization experiment, and the 85-ft antenna was used with the *Mariner V* spacecraft during and immediately preceding spacecraft encounter with the planet Venus. Additionally, the 30-ft antenna, fitted with 23-GHz radiometric equipment, continued passive observations of the planet Venus, and the 85-ft antenna was utilized for planetary radar (both monostatic and bistatic) until shutdown on November 2, 1967.

Utilizing the ultra cone (installed on the 85-ft antenna on October 12), reception was accomplished from the *Mariner V* spacecraft during the period preceding and during encounter. During the encounter phase, the open-loop data from the receiver was recorded on two wide-band tape recorders for later processing. Preliminary results from brief analysis reveal that equipment worked properly, and good data was recorded.

The monostatic planetary radar experiment, operating from Mars DSS, with command and data processing being effected in real-time from Venus DSS via microwave link, is working well, and approximately 8 h of total spectrum data have been obtained. Signal strength on December 14, at a one-way range of 142×10^6 km, was approximately -170.5 dBmW, compared to a predicted signal strength of -169 dBmW.

2. Subsystem Performance

a. Receiving systems. The 8448-to-30 MHz converter continues to be used as an X-band transmitter output power and modulation monitor on an intermittent basis for the time-synchronization experiment.

The Mod IV planetary receiver, in conjunction with the *Mariner* receiver, was used to track the *Mariner V* spacecraft during the Venus occultation experiment. The final modified configuration of these receivers allowed operation in either the closed-loop or open-loop mode. The open-loop mode was used during occultation, and receiver tuning was accomplished by manually selecting the correct frequency with a frequency synthesizer.

Following occultation, the Mod IV receiver was reconfigured for operation in planetary radar experiments. This involved removing the modifications to the programmed local oscillator and recabling the inputs to the Mod IV receiver.

b. Transmitting systems

R&D 100-kW transmitter. The R&D transmitter was operated during the balance of October for the Venus bistatic and monostatic radar experiments. The R&D cassegrain cone was removed from the antenna on November 2 for antenna modification, so the transmitter has not operated for the balance of this period.

X-band transmitter. The X-band transmitter has been operated for the time-synchronization experiments for a total of 60.5 beam hours, with only very minor interlock failures.

c. Servosystems. On November 2, the 85-ft az-el antenna was shut down, and there were no operations scheduled during the rest of the period due to structural modifications to the antenna.

3. System Improvements

a. Antenna systems. Work is progressing on the transmitter-electronics room (SPS 37-46, Vol. III) for the 85-ft az-el antenna. The counterweights and surface panels have been removed. The box girder is being strengthened, and the elevation bearings have been replaced with greater capacity bearings. Work also continues on rebolting the back-up structure. Modifications are being made to the servoamplifier to allow the use of a JPL-designed, standard-printed circuit card to replace the contractor-supplied boards.

b. Receiving system. Beginning November 1, all the DSS receiving systems were taken out of operation for the start of an extended shutdown period. Advantage will be taken of the shutdown to incorporate all modifications and to perform tests. All receiver modules will be tested and evaluated. Using the same test setup, all

individual modules from all three receivers will be tested before a new test setup is established.

c. Transmitter systems. The new 450-kW klystron RF assembly has been temporarily installed in the cone test area; it has also been connected to the power and cooling systems for evaluation and testing before installation on the antenna. New solid-state supplies have been installed in the hydromechanical building to replace the rotating equipment for field excitation of the motor-generator set. A new heat exchanger has been installed on the X-band system to provide greater heat capacity for this system on the 30-ft antenna.

E. CTA 21 Implementation, R. C. Rydgig

1. Introduction

At one or more steps in the series of events from the beginning of a planetary spacecraft program, through the conceptual design, functional design, detail design, fabrication, testing at the subsystem level, testing at the system level and finally flight operations, it has been necessary to establish that the flight telecommunication subsystems which interface directly with the DSN will, in fact, integrally perform with the DSN as planned. The testing of elements such as the spacecraft radio, and the DSN receiver and group of elements such as the flight telemetry system, and the DSN (including the SFOF computer chain), is identified as telecommunication compatibility testing for the purposes of this report.

In previous JPL spacecraft programs, such as *Ranger*, *Mariner*, *Lunar Orbiter*, and *Surveyor*, compatibility testing between the spacecraft telecommunications subsystem and the DSN has been performed in either one or both of two specific ways, followed by a final compatibility verification at the launch site by DSS 71. The two specific ways in which compatibility testing has been performed prior to this final verification are:

- (1) By installing elements of the ground telecommunication equipment in the spacecraft assembly facility and exercising the spacecraft with this equipment throughout the normal spacecraft SAF system testing phase.
- (2) By transporting a spacecraft or the telecommunications elements of a spacecraft to the spacecraft test facility at Goldstone DSCC. Portions of *Ranger*, *Mariner*, *Surveyor*, and *Lunar Orbiter* compatibility tests were conducted in this manner.

In general, compatibility testing in SAF or prior to SAF delivery with important elements of the telecommunications ground equipment has been marginally satisfactory as the principal method of demonstrating telecommunications compatibility even when supplemented by some testing at Goldstone DSCC. Although these methods of compatibility testing were reasonably economical, they were not timely enough to provide adequate feedback from prototype or proof-test model testing into flight hardware design. The first method of compatibility testing is now becoming increasingly uneconomical, because the current trend is to provide more mission-independent equipment and less mission-related hardware. Software modification is used to provide the necessary flexibility to handle individual mission requirements.

The deficiencies noted in the two general methods of compatibility testing suggest that a better alternative method of compatibility testing is needed. Desirable objectives of such an alternative method are:

- (1) To reduce the overall cost of compatibility testing.
- (2) To reduce the time duration of compatibility testing at an operational tracking station (Goldstone DSCC) by preliminary first-step compatibility testing at JPL.
- (3) To initiate compatibility testing early.
- (4) To provide a true simulation of each DSN interface with which the spacecraft project must mate with a complete standard hardware configuration.
- (5) To detect, identify, and solve telecommunication problems for approved projects before they become critical.
- (6) To allow timely feasibility testing of R&AD spacecraft telecommunications elements with a standard DSIF operating station, the ground communication system, and the SFOF.
- (7) To verify the theoretical performance of new techniques with experimental data so that system tolerances are reduced and system performance is more predictable.
- (8) To provide enough of a DSIF station in the standard operating configuration to effectively tie selected SAF and environmental test laboratory spacecraft system tests through the interface laboratory to SFOF, providing a tactical mission operations system compatibility test of the entire telecommunications link and data stream.

The plan discussed here accomplishes these objectives by providing a single specialized compatibility test facility, eliminating all compatibility test equipment in the SAF; and by minimizing the time required for compatibility testing of spacecraft at Goldstone DSCC.

The flight project/tracking data acquisition interface laboratory, hereinafter referred to as Compatibility Test Area 21, will be capable of performing three basic types of testing. These are:

- (1) Compatibility between the spacecraft transponder and the ground based receiving and transmitting system.
- (2) Compatibility between the spacecraft command and telemetry systems and the associated ground based DSIF telemetry detection and processing equipment and its software.
- (3) Compatibility between the spacecraft elements, the DSIF, the mission-dependent equipment, the GCF, the SFOF, and elements of the mission operations system with single and multiple simultaneous links.

This testing will be performed on four classes of activity: spacecraft subsystem R&AD testing, engineering developmental model testing, proof-test model testing, and flight equipment (full spacecraft and mission-dependent equipment) testing.

The specific tests and the degree of testing will be different for each project and will depend on the previous flight project and DSN experience with the planned hardware implementation, or the degree of risks which the project and the DSN are willing to take, versus the schedule and cost associated with this type of testing. CTA 21 will be operated exclusively as a *test* facility and not as an extension or supplementation of development laboratories and facilities which are presently located elsewhere. It effectively replaces a function previously carried out in SAF. In this context it is proposed that only sufficient space be provided in the facility to house the necessary test equipment to perform compatibility testing and that the projects will provide their own support equipment during the periods they are performing testing. The operational concept is that the facility be scheduled in the same context as the environmental test laboratory, i.e., exclusively for the purpose of performing telecommunication system evaluation and compatibility verification tests. Once the tests are completed, the project equipment will be returned to the appropriate develop-

ment laboratory in some other area, the problems corrected, and a new test period scheduled for verification of the solutions. It is not intended that general-purpose research or development test equipment be provided as a normal part of the facility.

CTA 21 will consist of these elements:

- (1) A DSN terminal area.
- (2) Mission-dependent equipment area.
- (3) One RF shielded enclosure spacecraft test area.
- (4) Passive RF links to the SAF, 10-ft space simulator and the environmental test laboratory, and a hard-line link to the telecommunications laboratory.
- (5) Teletype and high-speed data line links to SFOF.
- (6) Tactical intercom circuits to each of the above areas.

Figure 3 is a simplified block diagram depicting the relationship between CTA 21 and the other JPL facilities. This configuration provides the capability of testing the entire telecommunications system through all its interfaces from the spacecraft through SFOF or across any individual interface within the system.

The DSN terminal area, which corresponds to a DSN control room, mission-independent equipment area is laid out in a circular fashion similar to standard stations. Sub-floor cooling and cabling is achieved by installing 24-in. high computer-type flooring with 2-ft square removable panels. Neither the MDE area nor the spacecraft test area has the raised floor; they have a concrete floor covered with tile.

Figure 4 is a preliminary functional block diagram of CTA 21 DSN terminal area. The equipment represented by the block diagram will be GSDS equipment and after implementation will be placed under DSIF engineering change control to maintain it in a standard configuration.

At the present time, major items of equipment found in a Deep Space Station but not planned for inclusion in CTA 21 are analog instrumentation, antenna mechanical, tracking data handling, angle data subsystem, acquisition aid, transmitter, and station monitor console.

The ranging subsystem with its data system simulator provides a visual readout of the range measurement in octal form. The GSDS receivers utilize one of the built-in

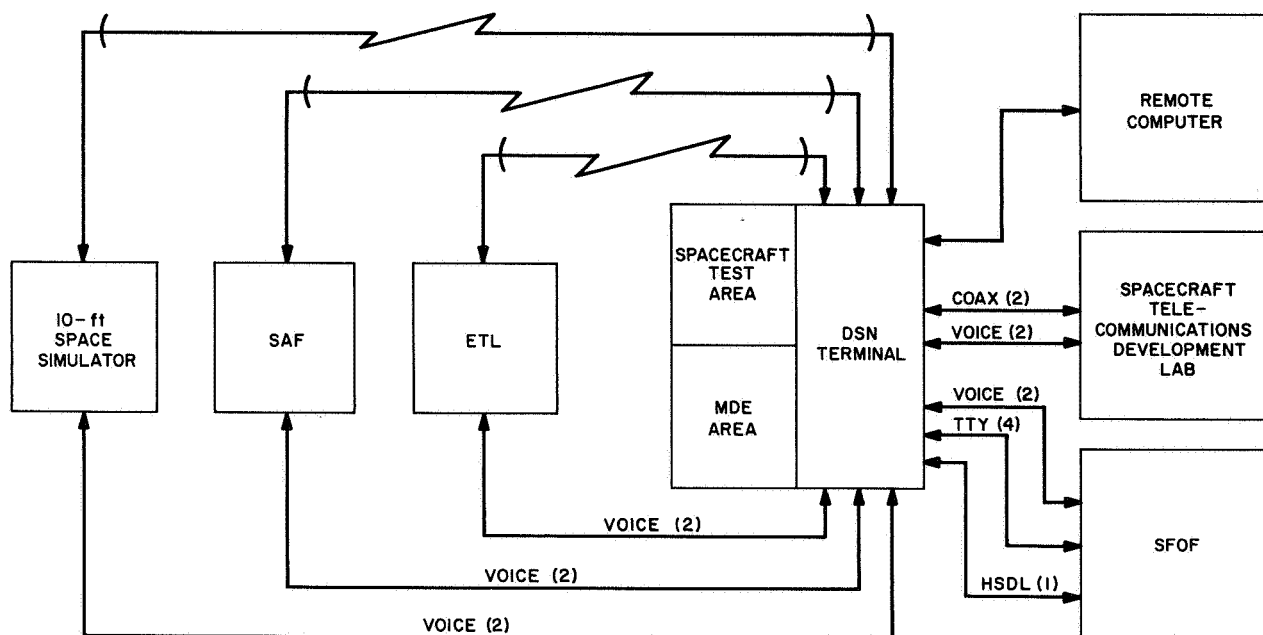


Fig. 3. CTA 21 facility relationship block diagram

counters to present the doppler measurement for visual readout.

The telemetry and command data will be processed and transferred across the appropriate interfaces to the MDE area and SFOF in a manner identical to a DSIF station. The MDE patch rack, the TCP input patch, input and output comm buffers, and the HSDL modems will all be GSDS and fully functional.

It is considered impractical to simulate actual DSIF system temperature conditions for the RF interface. A feasible solution to this problem is to maintain the system temperature reasonably low by the use of a transistorized low-noise amplifier and to define operating conditions in terms of S/N rather than absolute signal level. RF link simulation will be performed with precision attenuators. The selection of the incoming signal from the appropriate test area will be performed with low-loss coaxial switches ahead of the test diplexers. The switching arrangement will allow the use of both receiver channels so that simultaneous testing with two projects can be performed under some conditions. Direct coaxial connections will be made to the shielded enclosure in the facility and to the spacecraft telecommunication subsystem development laboratories. Passive links utilizing 6-ft diam dishes at each end will provide the RF connections to SAF, ETL, and space simulator. The antennas will be connected via waveguide to a suitable location in each building, and the user will determine the method of

interfacing with this junction. All of these facilities will be provided with voice communication stations to allow close coordination between them and the interface laboratory.

A standard interface to the ground communications system will be provided in the facility and will consist of high-speed data line modems and teletype machines for the telemetry and command circuits connected into the SFOF in a manner identical to a DSIF station. Tactical intercom connection to the SFOF intercom system or DSIF intercom stations, as desired, will be provided.

The spacecraft test area will consist of a 12- × 12- × 10-ft-high screen room which provides RF isolation of greater than 100 dB from 14 kHz to 10 GHz. One-hundred amperes of single-phase 60-Hz 110-V power will be provided to the screen room. The screen room will have a controlled environment which is pressurized with filtered air.

The MDE area will be as shown in Fig. 3. Since this area is also for the support of a specific flight project, it will be equipped, staffed, and operated by the project. Sixty-Hz, 110-V three-phase power will be supplied via GSDS outlets on walls surrounding the MDE area.

In late November 1967, the implementation of CTA 21 began. Plant engineering services began the facilities

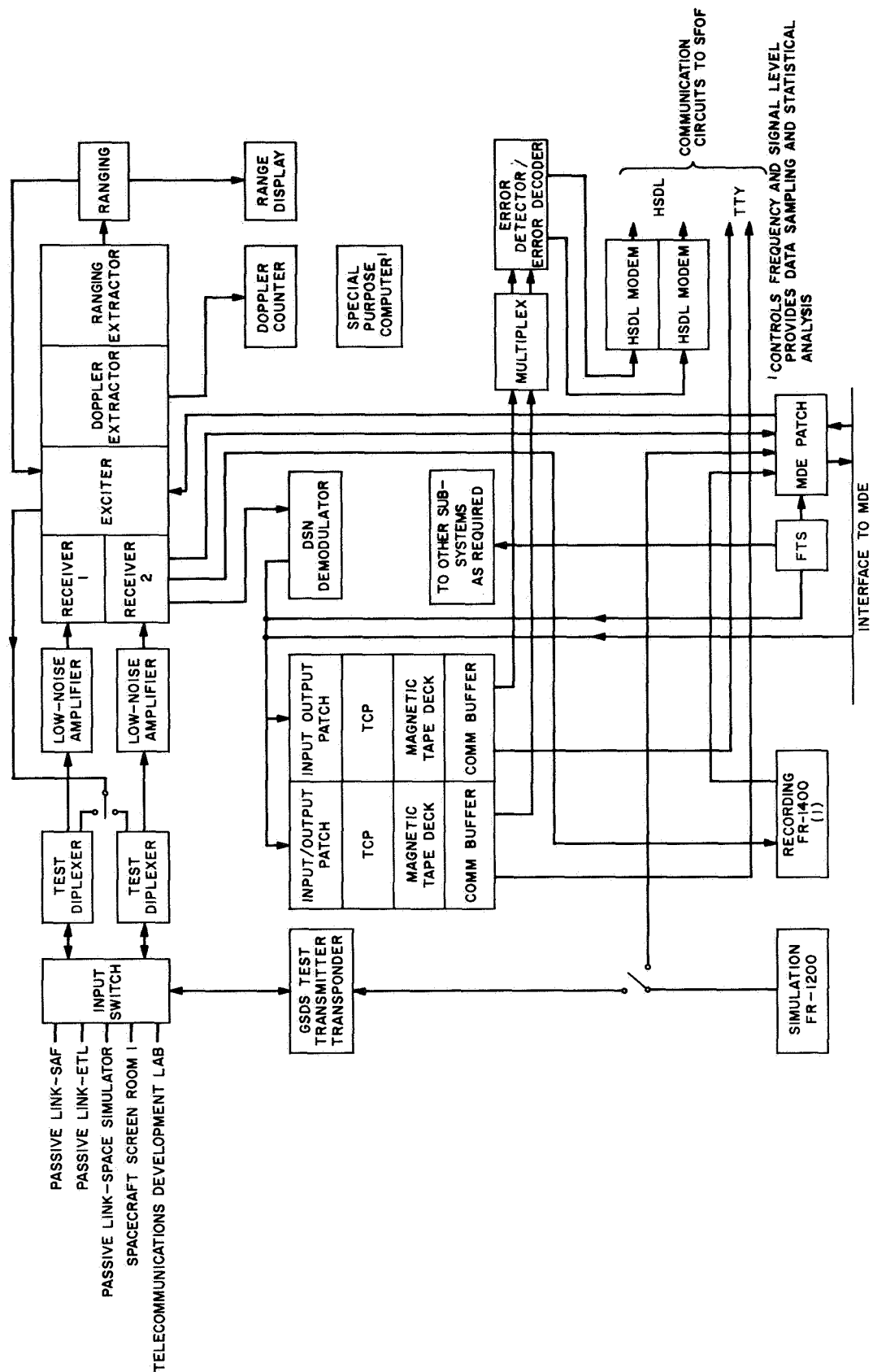


Fig. 4. DSN terminal functional block diagram

design and procurement of needed equipment. By December 4, 1967, the facilities work was sufficiently completed to allow installation of electronic equipment. By December 11, 1967, 50% of the equipment was installed and undergoing subsystem tests. By January 2, 1968, CTA 21 will be operational on a limited basis. Additional equipment is scheduled for installation in January and February, and by March it will be completely operational.

F. High Performance Microwave Link Between DSS 61 and DSS 62, B. Bridges

Two channels of duplex microwave link are being provided to permit multiple-mission cross-support between DSS 61 and DSS 62. A temporary link had been installed while the permanent equipment was being fabricated.

The microwave link installation and checkout was completed on November 4, 1967. All tests met, or exceeded, design specifications, with the exception of the VCOs and discriminators, which will be installed and checked out by December 20, 1967.

G. Ground Instrumentation Configuration for the Mariner Venus 67 (Mariner V) Occultation Experiment, P. L. Parsons and G. S. Levy

1. Introduction

Some knowledge of the characteristics of the atmosphere is required before planetary probes can begin searching the surface of other planets in the solar system. The pressure profile, for example, is necessary to ensure a successful entry capsule design. The success of the occultation experiment on the *Mariner* Mars 1964 mission led to its being included as a prime experiment on the *Mariner* Venus 67 probe. This experiment depends upon the propagation constant of the atmosphere being different from that of free space and changing the frequency of a radio wave traversing it by a measurable amount. The easiest way to send a radio signal through the atmosphere is to plan the trajectory of a fly-by mission so that the probe will pass behind, that is, be occulted by, the planet. This permits two observations of the atmosphere: on entrance to, and exit from, occultation. This was done on October 19 by the *Mariner* V mission, with entrance occurring about 180 deg from the subsolar point and exit occurring near the subsolar point. This geometry gave views of two temperature extremes in the atmosphere, namely midnight and noon, Venus

time. By recording the frequency of the signal and subtracting from this the frequency expected from orbit parameters, one obtains a plot of the atmospheric frequency effect versus time.

2. Instrumentation

The data were collected at the Mars, Echo, Pioneer and Venus DSSs of the Goldstone DSCC. Two methods of collecting data were used. One used the receiver and doppler extraction equipment for normal tracking of deep-space probes. The second method used a form of predetection recording to preserve the data for later, more detailed processing.

Figure 5 is a block diagram of the configuration. The Mars DSS parabolic antenna is 210 ft in diameter on an azimuth-elevation mount. A dual-mode feed horn is used to illuminate the cassegrain optics. The feed system was capable of receiving both orthogonal modes of circular polarization simultaneously. Both were recorded for possible radar echo analysis, but the spacecraft direct signal was received on right circular polarization. The direct signal was initially amplified by a traveling wave maser, having a bandwidth of 20 MHz, a gain of about 42 dB, and operating in a closed cycle cryostat at 4.4°K. The zenith system noise temperature is about 28°K. The receivers are dual-conversion phase-locked loop having IFs of 50 and 10 MHz. The VCO of the PLL is multiplied to S-Band and is used as the first local oscillator. The second LO and detector frequencies are normally derived from a crystal-controlled oscillator.

The station also has two Ampex FR-1400 tape recorders as standard equipment. The normal station equipment was modified by the inclusion of two racks of special equipment designed to process the signal for recording. While the first receiver tracked the signal in its usual manner and returned doppler information to JPL in close to real-time, the second receiver was operated in an open-loop, fixed-tune, triple conversion mode; that is, a fixed frequency was used as the first LO rather than using a VCO controlled by the output of the phase detector. In addition, the crystal oscillator which supplied the second LO and detector frequencies was replaced by an input from the rubidium standard and appropriate multipliers. A synthesizer was used as a first LO frequency source and it was offset from the frequency of the first receiver VCO by an amount sufficient to place the signal (in the IF) about 35 kHz above the nominal IF at the start of atmospheric effects. This frequency was set once, rather than being

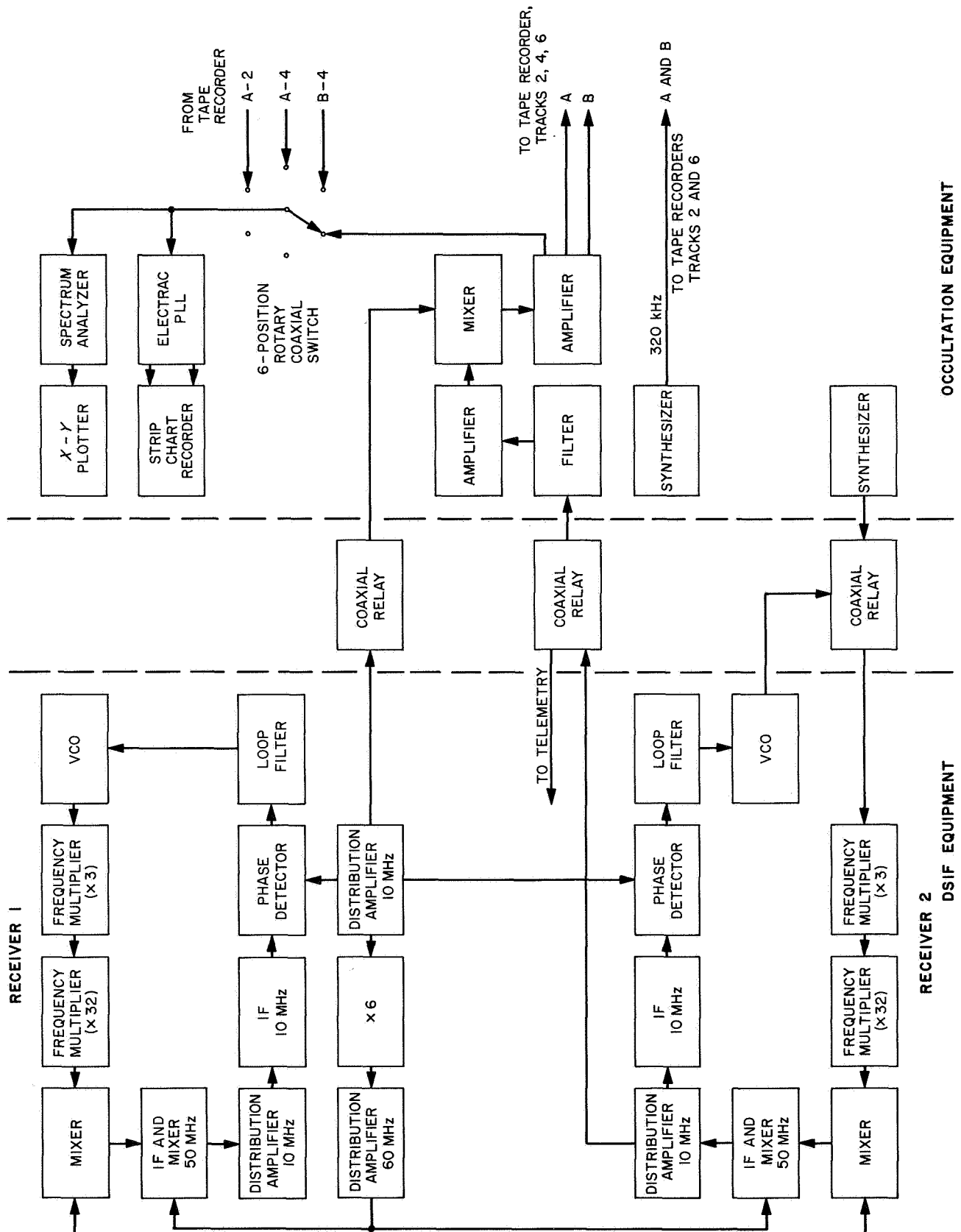


Fig. 5. Occultation experiment equipment block diagram

continually adjusted, and the signal was monitored as it moved in the pass-band. The synthesizer setting was changed at a predetermined time when the spacecraft was directly behind the planet, so that the proper offset in the exit phase was employed. The proper synthesizer frequencies were determined in advance of trajectory predictions. The second IF was filtered and then mixed with a stable 10-MHz signal, which reduced the signal to the previously calculated offset. The filtered pass-band was from 10.01 to 10.2 MHz. This gave an adequate pass-band without folding in any noise during the third conversion. The initial offset of 35 kHz was a compromise between a requirement for a small offset to keep

digitizing requirements low and a larger offset to permit any signals bounced off Venus by the spacecraft to remain in the pass-band.

Included in the open-loop racks was equipment used to monitor various points in the signal path to assure that the signal was being properly recorded. This equipment consisted of an oscilloscope with a plug-in spectrum analyzer, an X-Y plotter, a video phase-lock loop, a strip chart recorder, and a coaxial switch that permitted switching any of the several lines to the video PLL and spectrum analyzer. In this way the input to, and output from, both the recorders could be monitored by a simple switch. Usually the video PLL was left on the recorder input, and its frequency and amplitude outputs were recorded on the strip chart recorder. The video signal resulting from the third conversion was amplified and sent to the magnetic tape recorders. It is interesting to note that the video signal consists of the telemetry sidebands, as well as the carrier and the 200-kHz band of noise. Two tape recorders were used to record the signal, one being started 5 min before the other, so as to have coverage during the tape change. Both recorders were run at 60 in./s, and the video was recorded directly and on the wide-band FM. The digitizing clock of 320 kHz was recorded with the direct video.

The Venus DSS was used as a back-up station and was equipped with a special feed which gave a system zenith noise temperature of 16°K. The special feed was used in an attempt to partially compensate for the reduced gain of the 85-ft antenna from that of the Mars DSS. Although the Venus DSS is not a standard DSIF station, the general configuration was the same as the Mars DSS, except that no closed-loop receiver existed. Although redundant tapes were recorded at both sites, only one set of tapes from the Mars DSS was reduced.

3. Data Reduction

The analog tapes were digitized a few hours after encounter. The reasons for the rush included computer availability and fear of tape degradation as well as scientific interest. Experience has shown that analog tapes degrade noticeably in less than 2 yr. Although degradation in a week's time would probably not be noticeable, it was felt undesirable to take any chances. The tapes were played back at 3.75 in./s, a speed reduction of 16. This permitted sampling at 20 kHz, the limitation of the analog-to-digital conversion system. The periods of interest were determined from the strip chart recordings for both entrance and exit. Each of these turned out to be 7 min long, one starting at 17:36:00 GMT, and the

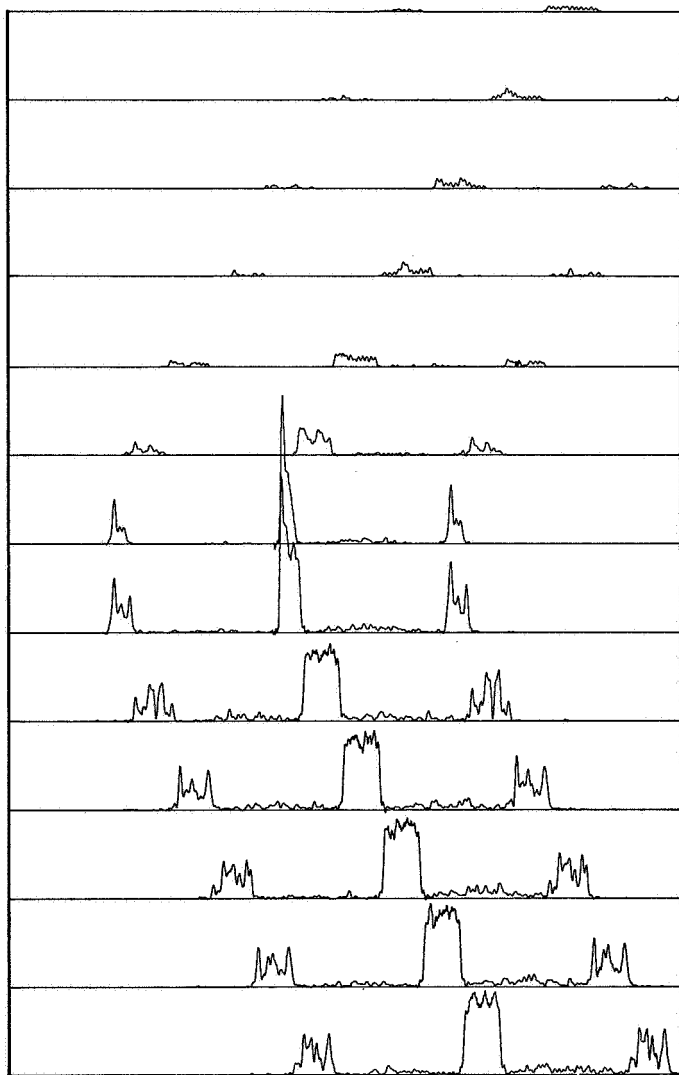


Fig. 6. Frequency spectra of Mariner V radio signals prior to, and at the start of, atmospheric effects

other at 17:55:00. Thirty-nine reels of digital tape were required to record the interesting regions. The digital tapes were reduced at JPL, using a combination of several techniques.

First, spectra were obtained to locate the signal and to determine its rate of change of frequency. The data were then filtered and aliased, using a local oscillator with a rate term to keep the signal centered in the pass-band. After several such passes, a rate-rate term was added, thus giving a second-order fit to the frequency. A phase-locked loop program was then applied to the filtered and aliased data to obtain an accurate, high-resolution picture of frequency and amplitude. It was then possible to fit a third-order polynomial to the PLL output to obtain a fit accurate to within 0.1 Hz. Frequency predictions based on orbit and known spacecraft oscillator changes were then obtained and fit with a polynomial. Actual and predicted frequencies were then differenced, using the two polynomials, to obtain a plot of doppler residuals. These residuals were used to determine atmospheric characteristics.

Figure 6 shows a series of spectra starting at 17:36:00. Here the change in direction of the doppler frequency can be seen at 17:36:11. This is the start of the atmospheric effects. The large doppler rate and spectral broadening are clearly discernible.

H. Advanced Data Systems Project: Proposed Configuration of a Third-Generation SFOF Computing System, A. T. Arcand

1. Introduction

As the central location for real-time monitoring and control of unmanned spacecraft, the SFOF at JPL has grown from a small-scale operation providing single-mission support in the early 1960s to its present large-scale operation providing multimission continuous coverage. Due to planetary mission requirements for increased precision in navigation computations; a larger data-handling capability; a faster, more powerful data system; effective support of large multicenter, multi-contractor projects; and a reduction in estimated annual operations costs, the present system will be inadequate for the flight-project support required in the 1970s.

An Advanced Data Systems Project was formed within the Systems Division to provide the functional analysis and a formal recommendation for a third-generation SFOF scheduled to be operational in 1972. The pre-

liminary configuration which has been proposed is a radical departure in many respects from the existing SFOF equipment, but is in line with the major advances in hardware, software, and system organization that are all elements of the so-called third-generation of computer technology.

To establish and demonstrate the conceptual design of the operational system, to provide measuring and performance standards for sizing this system, and to establish which functional capabilities should be included, a pilot system is planned to be operational by 1969, as part of the new third-generation Scientific Computing Facility (SCF) at JPL. This pilot system, like the Venus DSS prototype of the DSIF, will be maintained and upgraded at regular and appropriate intervals, at least through the 1970s.

2. Anticipated Data System Requirements for the 1970s

a. Increased precision in navigation computations. A 47-bit single-precision capability or an equivalently fast double-precision capability is a minimum requirement for support of planetary orbiter missions. The present methods do not meet these speed and precision requirements.

b. Larger data-handling capability. While it might at first be thought that the increased distance of planetary targets would decrease the overall data-acquisition rates, this is not the case. Planetary orbiter operations will demand at least as much precision and data volume as the present *Lunar Orbiter* operations. In fact, the best present estimates indicate a total 1972 operational load of more than twice our present capabilities. The three functions governing total data rate — telemetry, tracking, and network control — will each require expansion.

Telemetry. Significant advances in coding techniques, significant increases in sensitivity through the use of the 210-ft-diam antennas, increased power associated with the spacecraft transmitter, and an increase in the number of simultaneous targets available, all support the requirement for more total telemetry coverage.

Tracking. Due to the requirement for greater precision at planetary distances, the total volume of tracking data derived from the ground stations will tend to increase.

Network control. The use of communications satellites and high-speed, reliable, two-way contact with overseas stations will allow a reorientation of some functions between the SFOF and the DSIF. Much greater emphasis

will be placed on systems monitoring, performance evaluation, and closed-loop remedial action.

c. Faster, more powerful data system. Because of the increasing cost per launch of the more complex planetary spacecraft of the 1970s, particular attention must be paid to the basic requirements of real-time validation and high-speed trouble correction throughout the DSN. This need for closed-loop operation of the DSN and the operations cost reduction which can be achieved through centralized, real-time control and coordination of DSN activities will require a faster, more powerful data system than that provided by the present SFOF equipment.

d. Effective support of multicenter, multicontractor projects. To minimize the problems of center interdependence in multicenter projects, the third-generation SFOF should incorporate all major advances characteristic of the third generation of computer technology. To effectively support large multicenter, multicontractor projects, it will be necessary to: (1) maintain an easily identified and understood systems/applications interface; (2) share not only applications programs, but also data libraries; and (3) maintain higher reliability standards. None of these requirements can easily be met by the present SFOF configuration.

e. Reduction in estimated annual operations costs. Estimates show that the annual operations costs of maintaining the present SFOF configuration for flight project support in the 1970s will be greater than the costs of converting present equipment and acquiring new equipment for the proposed SFOF configuration. This is due to various factors inherent in the maintenance of obsolete equipment.

3. Physical Characteristics of a Proposed Data System

a. Storage capability. Preliminary estimates indicate a total core memory requirement in excess of 500,000 words. System design will be based upon a capability to expand to at least 512,000 words. The prototype system will include a small subset of this memory applicable to demonstration of systems characteristics. Final determination of memory requirements for the operational system will not be made until estimates of the actual capability required have been refined and preliminary data for the prototype system have been appraised. There is a very important trade-off between word size and the amount of core required if extensive double-precision arithmetic is required.

b. Auxiliary storage capability. The primary memory will be augmented by a hierarchy of slower-speed storage (drum, disk, tapes, and auxiliary mass core) designed to support the entire data base of the SFOF.

c. Word length. The accuracy requirements of navigation during a planetary mission and the active control of orbiters and landers after their arrival at the planets will require at least 47-bit precision for the algorithms. Because of real-time constraints and storage considerations, it is desirable that these 47 bits be in single precision.

d. Speed of operation. The speed of operation required to support the planetary missions of the 1970s, a reflection of the minimum required throughput efficiency, is 10 times the current capability. This processing speed, related to the apparent systems speed as seen by the user and including aspects of inputting, outputting, data transfers, and computation, is easily achievable with available standard equipment and will markedly improve flight operations.

e. Input/output interface. The number of activities to be concurrently supported will be greater; 200 input/output access points have been proposed. Additionally, new types and classes of users must be supported in the proposed operational system.

4. Operational Mode Characteristics of a Proposed Data System

a. Centralized configuration. The advantages of the centralized modular computer will be exploited to the fullest extent possible without degradation of: (1) user capability, (2) noninterference features, (3) functional development flexibility, and (4) maintenance of simple and manageable software interfaces.

b. Multiprogramming features. Multiprogramming will be employed under management direction and control.

c. Multiprocessing features. Advanced multiprocessing features will be employed to minimize the cost of back-up facilities and to improve data systems reliability.

5. Usage Constraints of the Proposed Data System

a. Standardized higher-level language. To simplify programming implementation, checkout, operation, and maintenance, user access to the computer will be restricted to a higher-level language.

b. Standardized hardware and interfaces. A capability will exist to dynamically add or delete input and output units, memory, and central processing units as a function of load. Standardized methods for interface implementation and control will thus be required.

c. Centralized operating system control. The actual running of user programs will be delegated to an effective central operating system designed to operate the total system under the mode and priorities preestablished by management.

d. Noninterference protection. The system must be able to provide adequate protection against users interfering with other users or interfering with the operating system. This will require major aspects of memory protection, message preambles, etc.

6. Advantages Offered by the Proposed Configuration

The configuration described herein will provide the following advantages for the third-generation SFOF:

- (1) Greater operational simplicity and control.
- (2) Alleviation of the management commitment problem.
- (3) Reasonable projects/DSN interface through the solution of the applications/operating system interface problem.
- (4) Cost-saving features of a large centralized, dedicated system.
- (5) Economic advantages of data management concepts.
- (6) Open-ended configuration features, whereby the interfaces and the operating system allow the system elements to be expanded or contracted as a function of project and DSN loading.

I. Advanced Data Systems Project: A Demonstration of Computer-Assisted Entry, K. R. Carter

1. Introduction

The purpose of the Advanced Data System Project is to provide a series of recommendations and standards for the SFOF computing system of the 1970s. To do this requires a major effort of operations research into many areas of computer capabilities. One such area is computer-assisted entry.

CAE is a computer application designed to simplify the man/machine relationship and extend the present range of access and comparative restrictiveness of output format.

Under existing computer entry methods, an occasional user, inexperienced in formatting, requires an operator at an input/output device to extract any use from a computer. Besides the costs of maintaining large numbers of I/O operators the cost of documentation of formatting techniques is great. Any change to any segment of a format program requires revision of a number of manuals. This leads to extreme difficulty when a change or improvement is implemented. These drawbacks tend to limit the scientist or engineer to occasional uses of available computing power.

Several aspects of CAE seem appropriate for possible inclusion into the SFOF future operational system. These include:

- (1) Generation of request messages in a computer-aided conversational mode. With little or no previous operating experience, an engineer or scientist can be guided through the formation of a request by a conversational question and answer interchange with the computer.
- (2) Key word and phrase recognition and completion. The computer can be programmed to interpret initial letters of an input and print this interpreted response for verification.
- (3) Computer recognition of requestor's identity with activation of appropriate capabilities.
- (4) Activation of diagnostic trees for identification and rectification of trouble.
- (5) Management of configuration control and allotment of resources.

While the above capabilities have many obvious advantages, there are also major pitfalls and tradeoffs, such as:

- (1) Cost of programming, overhead, and attendant memory and core needs.
- (2) Relative inefficiency of total computer use as a result of having I/O devices ready for use, but often idle.

- (3) The money costs for additional equipment, communications needs, etc. (as compared to the cost saving by reducing the number of assigned I/O operators).

As a first step in exploring and analyzing CAE for the SFOF, a demonstration of some CAE possibilities has been prepared using a simulated SFOF environment.

2. Purpose of the Demonstration

The main objective of this demonstration is to illustrate some of the facets of CAE as used in retrieving stored data from a large data base. The demonstration was planned to require no training or special knowledge on the part of the operator while allowing complete flexibility in selecting the output format.

Each user of the demonstration will be asked to make comments on its effectiveness, and make evaluations of the possible needs or uses of CAE for the future SFOF system.

These evaluations and the other results from the demonstration will be consolidated into a more detailed major task to evaluate CAE as an SFOF future functional capability. It will lead to a recommendation from the ADS Project as part of its final recommendations for the SFOF of the 1970s.

3. Means of Implementing the Demonstration

JPL, under the cognizance of the Computation and Analysis Section, uses the public time-sharing facilities of Tymshare, Inc., which consist of an SDS 940 computer with time-sharing hardware characteristics, and peripheral equipment. The only output devices at JPL are KSR 35 teletypewriters connected by data-phone to the computer located in Inglewood, California. The ADS Project has leased one portable teletypewriter for the purpose of this demonstration which uses an audio-couple with any telephone handset.

With programming support from the Computation and Analysis Section, the ADS Project has finalized a set of programs requiring some 18,000 words of storage which accomplish the desired demonstration. Since this program is resident on a public system, much of this storage is required for program protection, storing both an object and a source program, etc. Another large portion is the data base itself, and the conversion algorithms needed.

However, our intent was not to illustrate efficiency of CAE programming at this time, but rather to provide a demonstration of some specific features.

4. Features of the Demonstration

The particular aspect of this demonstration is the demonstration of:

a. Conversational access between man and computer.

All that is needed to gain the attention of the computer is to type a special two-character address. From that point, in a series of questions and answers, the user may obtain any desired information to the limit of the demonstration.

b. Computer assistance in automatic completion of key words and phrases. In answering questions put forth by the computer, the user need only type an initial portion of the answer, and the computer completes the input, as soon as the response can be differentiated from other possible responses.

c. Varying levels of capability to selected sets of identified users. In this demonstration, there are five levels of identity — in this case, using only names such as engineer, analyst, etc. Each identity permits a subset of the entire range of options up to project director, who has all capabilities of the demonstration, including revision of the data base, if desired.

5. Use of the Demonstration

The data base consists of telemetry data from ten spacecraft measuring devices, over a 60-min period, one reading per minute from each device. These devices are referred to as parameters. This data base (actually a 60×10 matrix) can be displayed, at the user's option, in any form (raw data or converted data, exponential or decimal output, etc.), over any time range (real-time, starting at time 1, or recalled data, between any two limits of time), for any or all of the parameters, in a completely selectable format. Figures 7 and 8 show two sample outputs.

6. Limitation of the Demonstration

This demonstration has some self-imposed limitations. The relatively slow speed of teletype output, transmission errors on the commercial communications equipment, and the problems of time-sharing on one computer with up to sixty other users simultaneously are difficulties which would not be present in a modern operational system.

THE PARAMETER PRINTOUT WILL BE OF THE FORM:

RECALLED DATA

WITH INITIAL TIME = 15
 FINAL TIME = 30
 INTERVAL = 3

SELECTED FORMAT

ECU DATA

WITH DECIMAL OUTPUT
 LINE COUNT = 6

TIME	TEMPERATURE BAY1	TEMPERATURE BAY3	OXIDIZER PRESSURE	SPACECRAFT VELOCITY	TEMPERATURE BAY5
15	* 8.50	* 13.00	* 112.50	* 1390.00	* -.34
18	* 9.25	* 14.00	* 135.00	* 1270.00	* -.06
21	* 10.00	* 14.50	* 156.00	* 1150.00	* .01
24	* 10.50	* 16.00	* 180.00	* 1030.00	* 1.00
27	* 11.25	* 13.50	* 202.50	* 940.00	* 4.10
30	* 12.00	* 14.00	* 225.00	* 850.00	* 10.65

Fig. 7. Parameter printout of recalled data

THE PARAMETER PRINTOUT WILL BE OF THE FORM:

MODIFIED REAL TIME

WITH FINAL TIME = 10
 SELECTED FORMAT

ECU DATA

WITH DECIMAL OUTPUT
 LINE COUNT = 10

TIME	TH. CHAMBER PRESSURE	SPACECRAFT ACCELERATION	OXIDIZER PRESSURE	ROTATIONAL ACCELERATION	SPACECRAFT VELOCITY
1	* 100.00	-13.31	* 75.00	* .00	* 2000.00
2	* 100.00	-13.31	* 76.50	* .00	* 1950.00
3	* 100.00	-13.31	* 78.00	* .00	* 1900.00
4	* 100.00	-13.31	* 79.50	* -.31	* 1850.00
5	* 100.00	-13.31	* 81.00	* -.31	* 1800.00
6	* 100.00	-13.31	* 87.00	* 3.28	* 1750.00
7	* 100.00	* -9.91	* 88.50	* -.02	* 1710.00
8	* 100.00	* -9.91	* 90.00	* .00	* 1670.00
9	* 100.00	* -9.91	* 91.50	* -.00	* 1630.00
10	* 100.00	* -9.91	* 93.00	* .00	* 1590.00

Fig. 8. Parameter printout of real-time data

7. Performance of the Demonstration

The demonstration is available to all who wish to take it. A brief set of instructions is furnished, along with a glossary of all the program options.

J. Antenna Engineering,

V. B. Lobb, M. Kron, W. J. Kissane, H. D. McGinness,
D. L. Lambdin, C. Lundy, A. Nicula, R. McKee, J. Carlucci, Jr.,
M. S. Katow, W. W. Van Keuren, and M. G. Newsted

1. DSS 13 Trans-Electronics Room Modifications,

V. B. Lobb, M. Kron, and W. J. Kissane

The need for a transelectronic room evolved with the development of the 400-kW transmitter which is to be installed at DSS 13. The installation of the room and the transmitter, and its associated equipment, requires modifications of the existing antenna structure.

a. Final design. The final design which incorporated these modifications verified the conclusions of the initial study. The main features are:

- (1) The room was located to minimize the added counterweight and rotating mass.
- (2) The reflector back-up structure was modified to maintain its original deflection characteristics with the added weight of the room and its equipment.
- (3) The room was designed as a rigid structural unit, shop-fabricated and to be erected as a unit.
- (4) The added antenna loads caused by the room weight and new balancing counterweight necessitated replacement of the elevation bearings with higher capacity bearings.
- (5) The locations of the added antenna loads caused the center of gravity location of the original counterweight to move more than 8 ft. This, coupled with the need for the removal of existing counterweight members tying to the back-up structure, led to the design of a new, rigid counterweight structure, with a stiffness 8 times that of the one that was removed.

b. Premodification support work. Prior to implementation of these contracted modifications, the following preparations were necessary:

- (1) Field measurements taken previously of the antenna surface (as discussed in SPS 37-47, Vol. II, pp. 115-120) indicated that a large amount of hysteresis exists in the back-up structure. Therefore, the reflector and back-up structure were rebolted.

- (2) Measure, label, remove and store the reflector surface panels.
- (3) Remove the existing counterweight plates; counterweight structure; transmitter coolant lines, pumps and filters; maser coolant lines, and relocate the cryogenic pump.
- (4) Install access hatch to alidade and kingpost area.
- (5) Remove the datex and limit switches from both axes (including the connecting "magic tee" which transmits azimuth rotation from the elevation bearings to the azimuth readout at the bottom of the pedestal) and the feed cone and cone ring.
- (6) Alter the ladder and platforms to clear the new counterweight structure.
- (7) Remove (a) all the cables above the elevation axis and (b) the old environmental control system.

Most of the above work was completed during the period of November 1, 1967 through December 15, 1967. The amount of hardware removed is apparent by comparing Figs. 9 and 10.

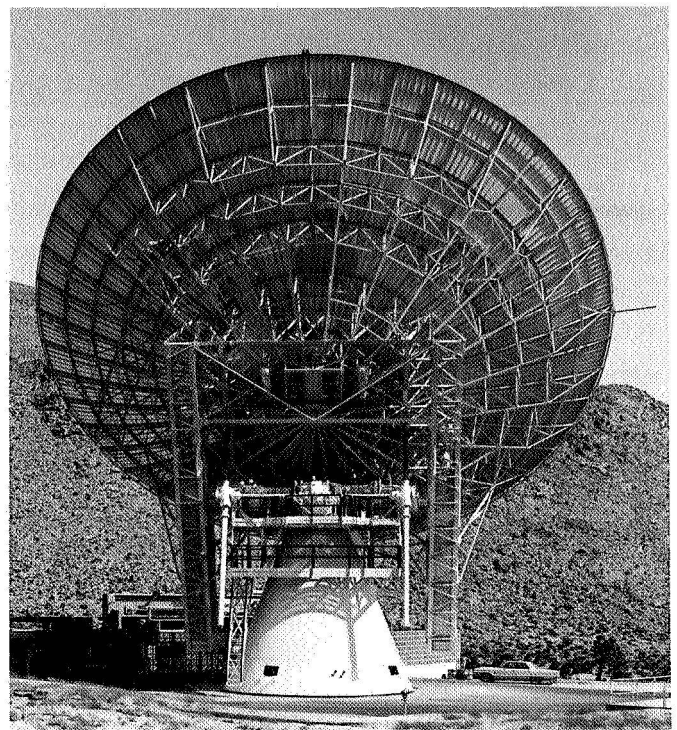


Fig. 9. DSS 11 85-ft antenna before modification

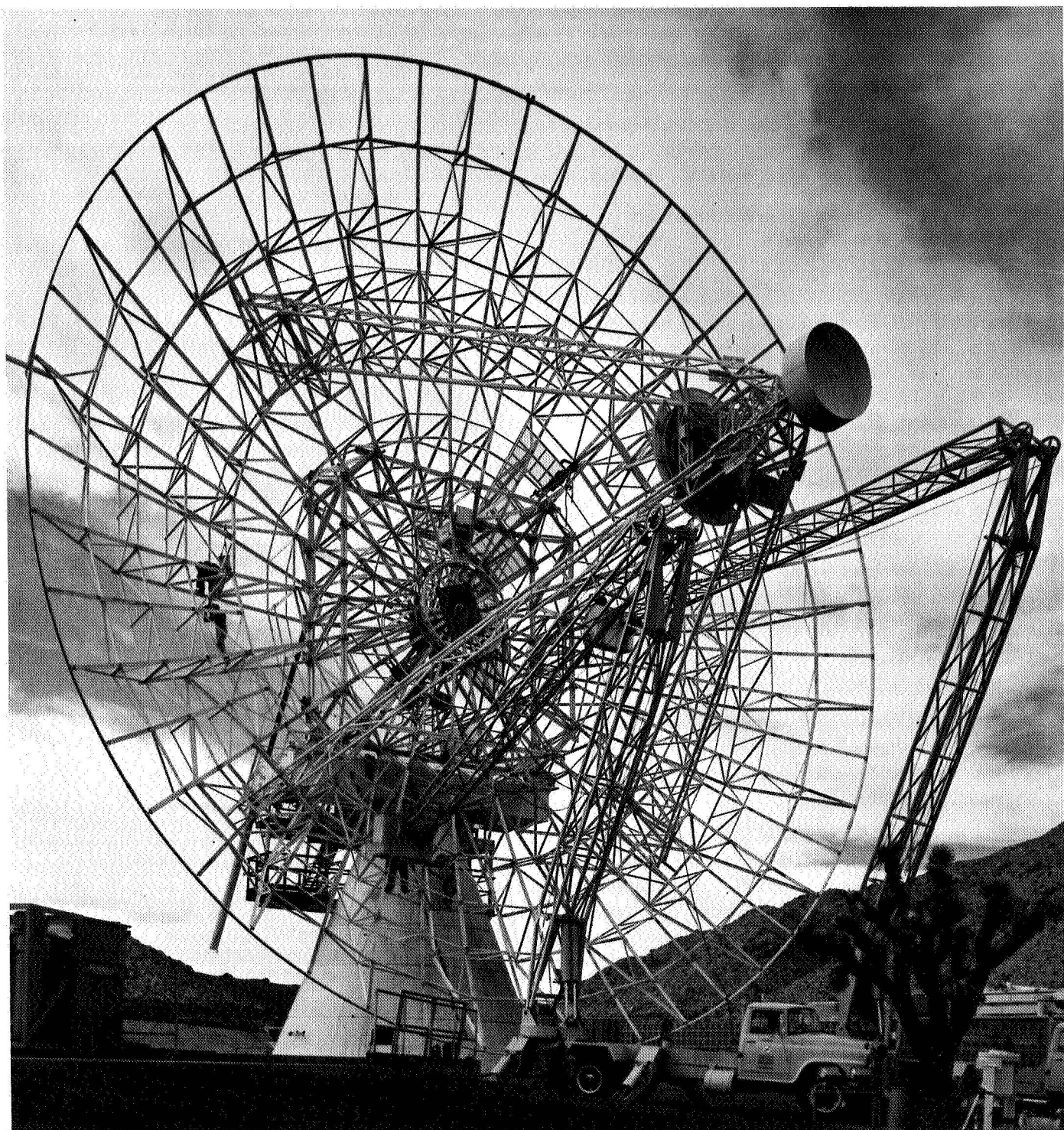


Fig. 10. DDS 11 85-ft antenna after preparatory work for modification

2. Orthogonality Adjustment of the Master Equatorial Axes, H. D. McGinness

An unusual feature of the DSS 14 antenna master equatorial system is the method employed for obtaining almost perfect orthogonality between its declination and polar axes. If the axis orthogonality error is to be of the same order of magnitude as other errors in the master equatorial system, it must not exceed 0.50 arc seconds. Since the declination axis bearings are spaced 26 in. apart, the relative offset error corresponding to 0.50 arc seconds is $65 \mu\text{in.}$ Because it would have been virtually impossible to machine the master equatorial yoke structure to this degree of accuracy, it was necessary to incorporate a position adjustment for one of the bearings.

The essential features of the design¹ and arrangement of the position adjustable bearing is shown schematically in Fig. 11. From Fig. 11 it may be seen that one of the declination-axis angular contact ball bearings is mounted within an auxiliary bearing capsule containing a pair of preloaded angular contact ball bearings, which is mounted eccentrically with respect to the bore of the

¹The detail design is shown on JPL drawings 9435629 and 9435582.

declination axis bearing. The position adjustment is executed by moving the tangent arm attached to the innermost ring of the auxiliary bearing capsule. The tangent arm is moved by turning two opposing set screws which hold the tangent arm. The amount of the auxiliary bearing eccentricity is 0.025 in., and the angular range of the arm is ± 10 deg from its neutral position, thus producing a ± 0.0045 -in. adjustment range in the direction of the z axis. As the two declination-axis bearings are spaced 26 in. apart, the angular adjustment range is ± 34 arc seconds. One turn of the tangent arm set screw changes the declination axis angle by 2.10 arc seconds. Adjustment in the z direction is accompanied by a displacement in the x direction, but this latter displacement does not affect the orthogonality of the axes.

The most significant feature of this design is that the orthogonality adjustment can be made without relieving or changing the preload on the declination-axis main bearings or on any other part of the structure. While observing an alignment autocollimator, the set screws holding the tangent arm can be turned slightly, thus obtaining an orthogonality accuracy equal to the resolution of the autocollimator. Considering the accuracy of the

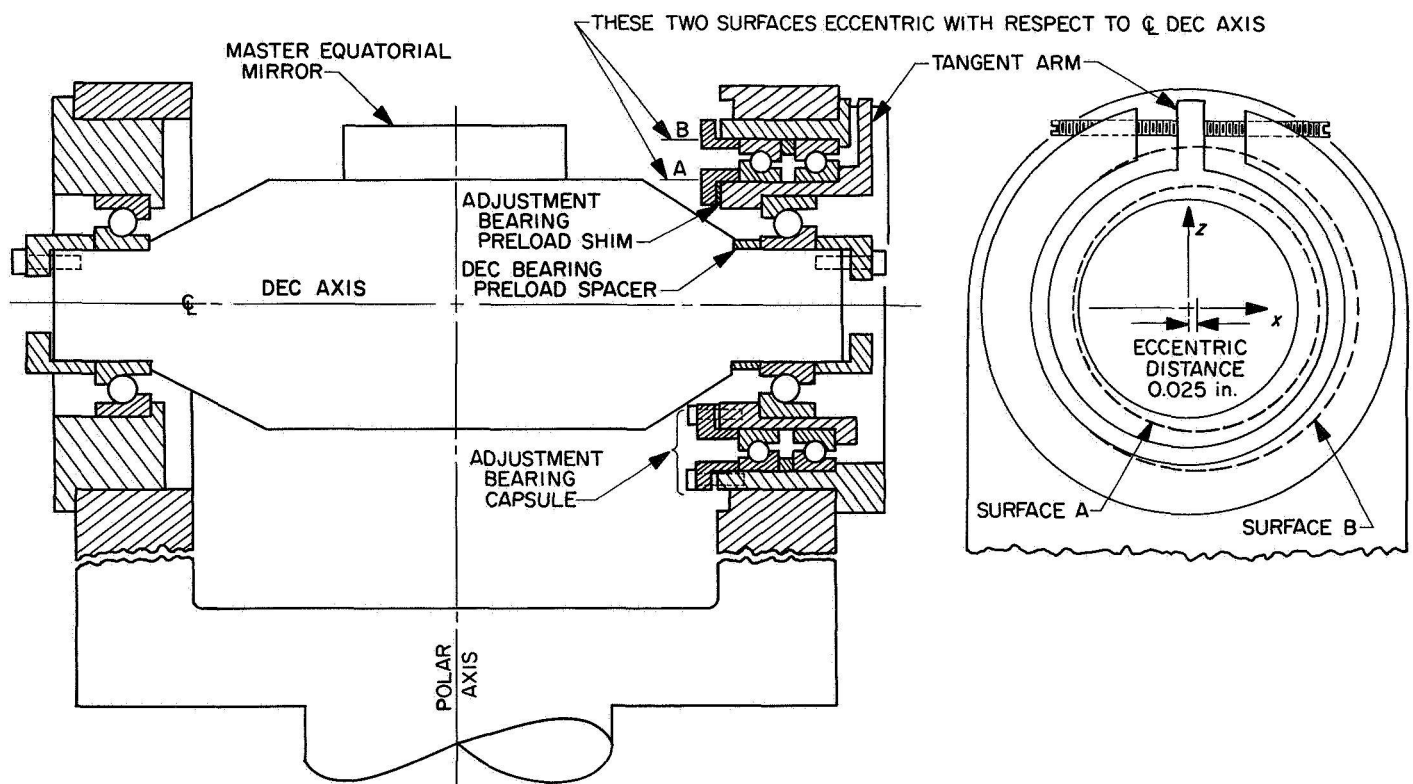


Fig. 11. Orthogonality adjustment of master equatorial axes

particular autocollimator used for aligning the master equatorial, it is believed that the axis orthogonality error does not exceed 0.15 arc seconds.

The alignment bearing capsule was fabricated by assembling the two auxiliary ball bearings between the inner and outer rings of the capsule and preloading the bearings to 5000 lb by adjusting the preload shim thickness until a prescribed drag torque was reached. The tangent arm was locked tightly in its neutral position and the open ends of the capsule temporarily sealed. Then the inner and outer cylindrical surfaces of the capsule assembly were precision-ground to fit the declination bearing and its housing.

3. Remote Indicating Level Assembly, D. L. Lambdin and C. Lundy

During each pretrack calibration and each monthly maintenance check the antenna level vials, located at the center of the primary reflector vertex plate, beneath the cassegrain cone, must be checked in order to verify the Datex indication for antenna zenith position. This requires one person to climb the antenna, remove a floor plate from the cassegrain cone, and read the levels back to the servo-operator. The servo-operator, in turn, commands the antenna in declination or hour angle at the direction of the person reading the level vials until the antenna is

bracketed to level. Then the Datex readouts are checked and corrected, if necessary.

The need for a more practical method of making this check was evident, and a new system was recommended which uses electronic levels with remote readouts located at the servo-console. Several off-the-shelf devices were considered, but only one which incorporates a self-damping feature met the requirements, due to antenna vibration. This Talyvel² unit is a viscous damped pendulum type using magnetic pickup transducers (Fig. 12). However, several questions had to be answered, and a study was conducted.

The first concern was repeatability. A motor-driven gimbal test table was constructed which cycled the level sensor through 75-deg pitch, roll, and yaw motion once every 12 s (Fig. 13). It was allowed to run for approximately 500 h and periodically retested on a surface table, with another Talyvel unit and a precision master spirit

²Manufactured by Rank Organization, Taylor Hobbs Div., England.



Fig. 12. Talyvel unit

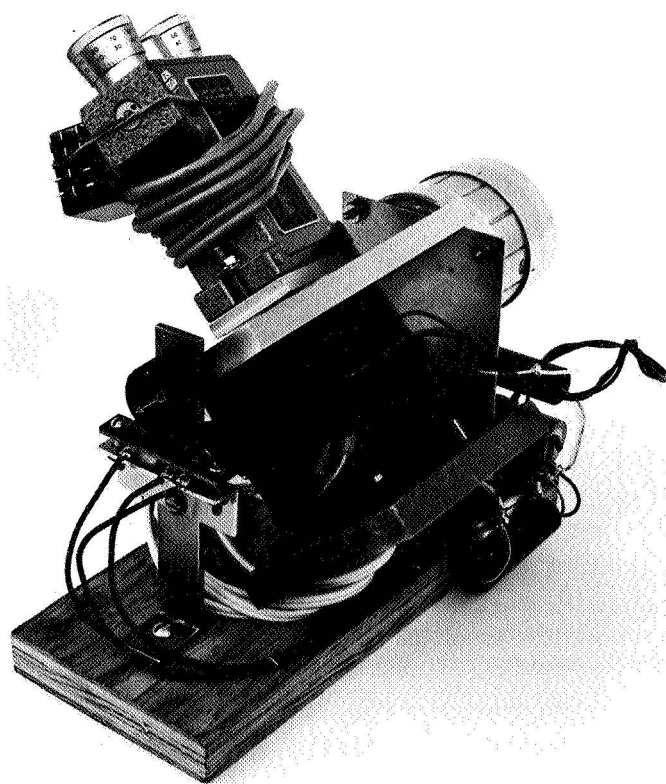


Fig. 13. Motor-driven gimbal test table

level as a reference. This severe test had no apparent effect on the repeatability of the instrument.

The second concern was accuracy. The sensor assembly was then mounted on an angle plate which, in turn, was mounted to a Leitz precision dividing head and a front surface $\frac{1}{4}$ -wave mirror was mounted to the angle plate perpendicular to the sensing axis of the Talyvel sensor. This dividing head was then rotated until the Talyvel read-

out indicated no level error. Then a Hilger-Watts theodolite was set up, precisely leveled, and autocollimated to the mirror. This provided a two-way check of the Talyvel readout: (1) the dividing head vertical circle was used to set in known offsets from level and compared to the Talyvel readout, and (2) the Hilger-Watts theodolite was used to monitor the dividing head and the Talyvel readouts via angular offsets of the autocollimated image. This test uncovered up to a 3-s error, which apparently was due

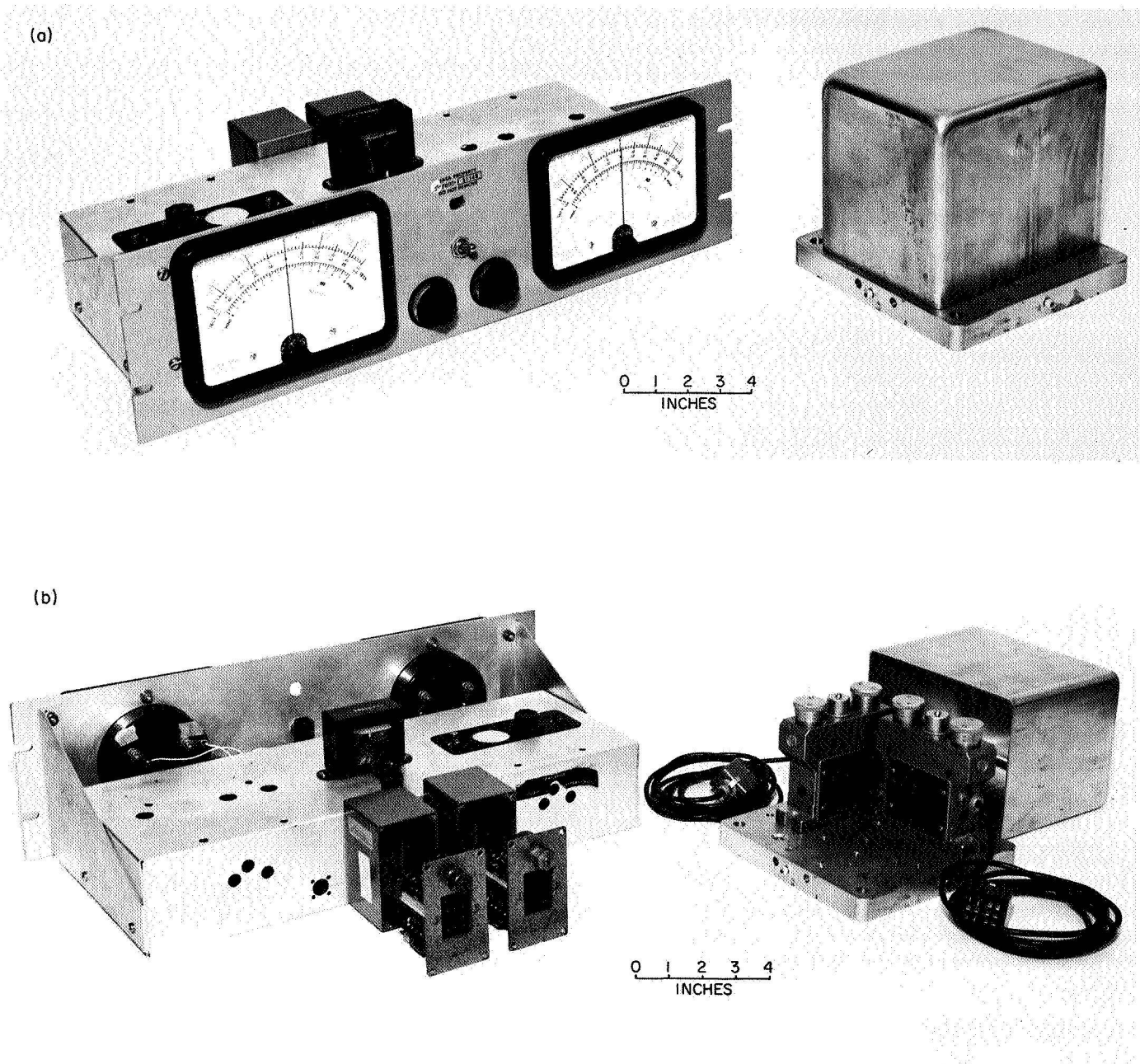


Fig. 14. Prototype model of remote indicating level assembly

to stiction in the meter movement of the Talyvel readout. The error was considered negligible.

The third concern was for stability due to temperature variation. The sensor was cycled through a temperature range of from -10 to $+97^{\circ}\text{F}$ several times and continuously monitored. Again no apparent adverse effect was encountered.

Completion of the testing³ on the readout package prototype showed the following: (1) the battery power supply (which has since been replaced by a full-wave power supply) proved to be the only weak link in the level system; and (2) it can be used to measure accurately to

³Lundy, C., interoffice memo to F. Stoller, September 21, 1964, (JPL internal document).

gravity with a resolution of one second of arc, or better, and an accuracy of three seconds of arc, or better.

The remote indicating level assembly has been modified to facilitate repackaging. Figure 14 shows the prototype model of the final configuration.

4. Installation of 4-ft HA-dec Time-Synchronization Antenna at DSS 42, M. Kron

During June 1967 a time-synchronization system antenna was installed at DSS 42 to establish the first overseas link of the time-synchronization program. A foundation frame was installed and optically aligned atop the control-room building. It was operational at DSS 42 approximately two weeks after installation of the antenna and electronics. Figure 15 shows the final installation.

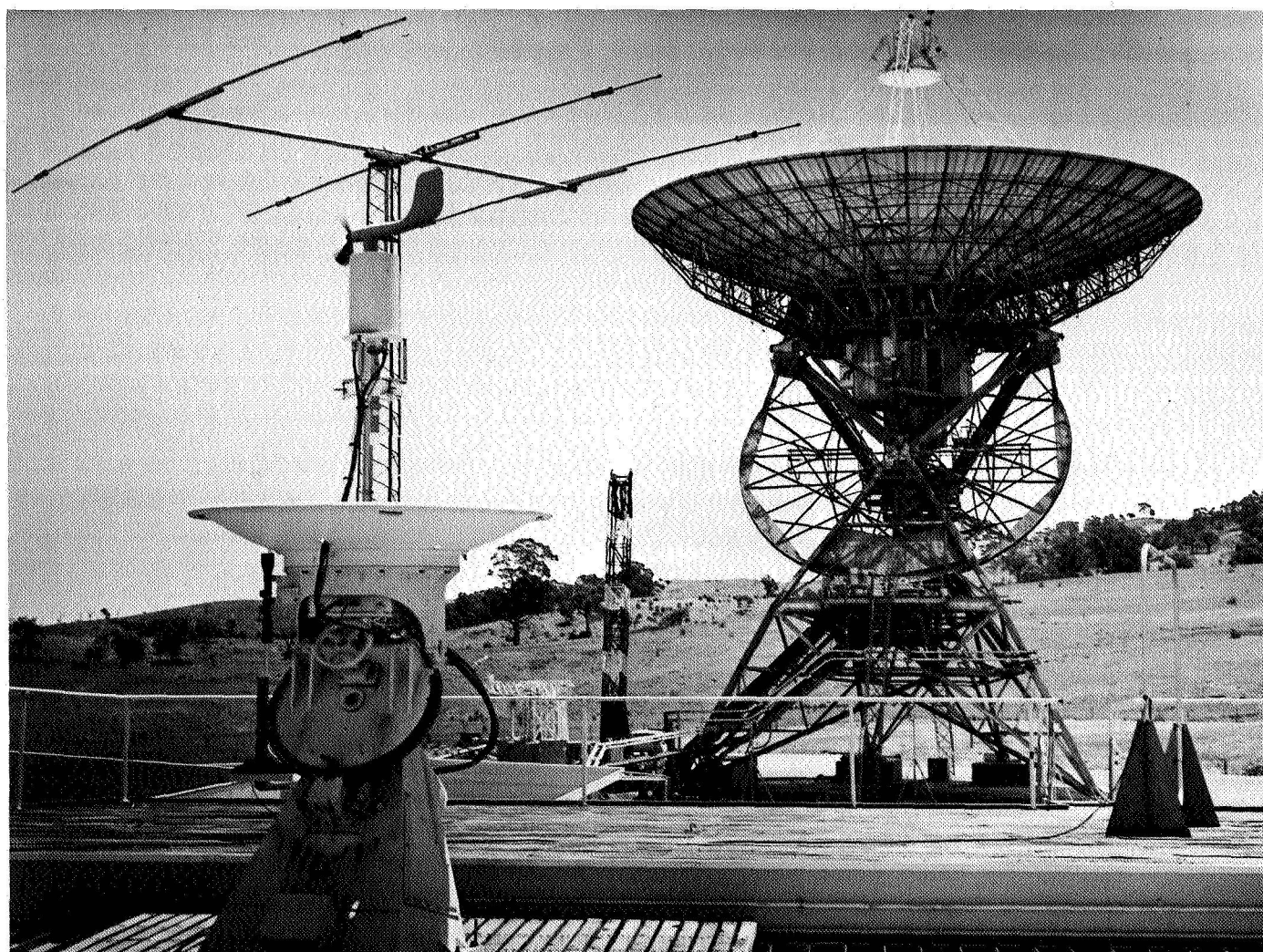


Fig. 15. Time-synchronization antenna at DSS 42

5. Cone Repair of 210-ft AAS Cassegrain Antenna,

A. Nicula

The cassegrain cone assembly at DSS 14 was damaged during the process of removal from the 210-ft diam antenna. The standard lifting fixture for cassegrain cones developed for the handling of cones at 85-ft diam antenna sites could not be used for the 210-ft diam installation or removal of cones because the elevation angle of the 210-ft antenna established for personnel safety during removal of the cone is quite different from that used in cone removal at 85-ft antenna sites; therefore, a smaller spread bar, chokers, and tag lines were used. In addition, a dynamometer was not used during the removal attempt, therefore, there was no indication of the magnitude of load exerted on the cone structure. All 24 bolts were engaged at the time of application of load in the attempt to remove slack in the lifting cables.

a. Inspection of damaged cone. Inspection of the cone while resting on its mobile trailer disclosed:

- (1) One of the top east-west lifting lugs had started to fail in bearing.
- (2) Similar elongation was noticed on the southeast lifting lug.
- (3) Between the top and center sections of the assembly, a gap of $\frac{1}{16}$ to $\frac{1}{4}$ in. has appeared where it has been stretched. This occurred directly under the top lifting lug that had shown bearing failure. On the top sections four interconnecting section bolts had stretched over the yield point and broken, and the same sections were found to be out of round.
- (4) In the bottom section, 90 deg clockwise from the elongated lifting lug, four rivets had failed.
- (5) The bottom mounting ring was warped and showed approximately a $\frac{1}{4}$ -in. gap between the trailer and ring, for a length of approximately 3 ft.

b. Corrective procedures. The following changes have been made:

- (1) All lifting lugs have been redesigned to take greater loads, increase the safety factor, and eliminate the observed failure in bearing.
- (2) The installation and removal procedures for the cassegrain cones were revised for use on the 210-ft AAS.
- (3) Instruction plates with lifting diagrams, stating load, and maximum angle of lifting cables at the attach point at each lifting lug have been provided for the 210-ft AAS cones.

6. Bolt and Joint Integrity Project, V. B. Lobb and D. L. Lambdin

a. Introduction. Tower bolts, and more recently, high-strength bolts, have been the principal structural fasteners used in the DSS antennas and related structures. These bolts are usually placed in holes that are nominally $\frac{1}{16}$ in. larger than the bolt diameter. Thus, when these fasteners have been subjected to vibrations and dynamic loads during antenna operation, joint slippage and fastener loosening have occurred. This has necessitated a continuing program of bolt maintenance and antenna realignment.

The use of a corrosion-protecting material on the antennas was required. Hot-dip galvanize and a zinc-rich primer with a reflective white acrylic paint are the two current methods being used. These coatings and the ones used on the fasteners have caused problems with initial installation torque, joint slippage, quality checks, replacement and retightening methods, and the painting of fasteners.

b. Objectives. The project will provide data for:

- (1) Generating specifications for purchase and installation procedures for bolts and nuts used in fabrication and maintenance of DSS antenna and related structures.
- (2) Preparing design criteria for the designing of slip-free structural bolted joints for dynamic applications on DSS antennas and related structures.

It comprises the following phases:

Phase 1. A test of a group of representative high-strength bolts to determine the optimum combination of plating, lubrication and tightening procedures to achieve a reliably tensioned fastener. The test procedure was described in SPS 37-47, Vol. II, pp. 135-138.

Phase 2. Test of a selected group of typical antenna structural joints, with and without various platings and bolt types, for slippage and joint relaxation.

Phase 3. Gathering and evaluation of articles and reports pertinent to this project from various external research sources and relation of this data with JPL-developed data.

Phase 4. Implementation of any of the tests that are resolved necessary by phase 3.

Phase 5. An engineering report with recommendations for field application.

c. Implementation. The phase 1 tests are currently being carried out utilizing the instrumentation for bolt

testing. The test fixture is currently being used to determine the needed bolt and nut characteristics for different coatings and lubricants.

The first series of tests will require 200 test samples. Each different finish and different lubricant will be tested. Each test will consist of 5-bolt specimens. Results for each specimen will be computer-processed and printed in final format. In addition, at the end of the 5-bolt test series a summary will be computer-processed and printed.

d. Progress to date. All required instrumentation has been designed, fabricated and checked out.

The phase 1 bolt tests are about 50% complete.

Phase 2 testing, which is being done by an external contractor is about 80% complete, with final testing to be completed early in 1968. That is, the long-term joint creep tests, with and without transverse vibrations, are complete with data reduced and the final report now in process, and the joint cyclic load reversal tests are in process.

From the current phase 1 and 2 test data and field experiences, an interim bolting procedure has been developed which will be used for future fastener installations in JPL antennas and related structures. The final version is to be modified as required by the results of this project.

7. Work Platforms for Cassegrain Cones, A. Nicula

A modified cone trailer was needed to provide work area for several of the existing and planned antenna cassegrain cones. This work platform would provide a 4-ft-high working space under the cone itself and allow storage for the equipment used in the cone construction.

A quick stress analysis on the existing utility trailer now in use throughout DSN and rated for a maximum safe load of 6500 lb capacity proved it to be quite inadequate for this requirement, even with drastic design modification. Therefore, a new heavy-duty mobile trailer and work platform was designed capable of supporting the extra weight and height requirements under wind load conditions up to 100 mph.

The basic trailer is approximately 15 ft long, 10 ft wide, with 6-in. I-beam welded construction, provided with four sets of pneumatic dual-wheel casters, each capable of supporting 4,600 lb. Four leveling jacks, each with 10,000 lb lift capacity, stowable type, with a 16-in.-square pad were selected. A Greenlee tool box, size 2 ft \times 4 ft

can be easily installed at the front end of the trailer. The 4-ft adaptor section, which provides ample space and work area under the cone assembly, is bolted directly to the mobile unit. Four I-bolts located inside the adaptor section will provide an easy way for slinging, loading, and unloading of the section to and from the trailer.

A less costly but immobile approach was also investigated. This work platform consists of the same welded assembly adaptor section (4 ft high \times 110 in. diam), air conditioner, transition duct, and hoses as the mobile unit but mounted on a concrete base.

8. Field Staging Area at DSS 12, R. McKee and J. Carlucci

Due to the vast amount of antenna work carried on throughout the DSN, ranging from new antenna installations, repair of joint damage and rebolting through new cable wrapups, new surface panels and retrofit upgrade modifications and the need to fit these operations into shifting flight schedules, it was necessary to design and fabricate hardware in advance and then store it in readiness for installation when gaps in the tracking schedules permitted.

As a result of the above requirements a staging and implementation area was developed at DSS 12 which provides: a storage area; a trailer containing work bench, dark room, and shelves; a concrete slab for testing and assembly; and fenced-off areas for steel storage, receiving, and staging.

9. Study of Environmental Wind Conditions at DSS 14, M. S. Katow, W. W. Van Keuren, and M. G. Newsted

a. Introduction. The operational limits of large radio antennas with respect to the environmental wind conditions are a function of:

- (1) The long-term average of the magnitude and direction of the wind velocity.
- (2) The ratio of the peak wind velocity to the average velocity.
- (3) The magnitude of the change in direction of the wind with respect to the average velocity.
- (4) The frequency spectrum of the magnitude and the direction of the wind.

In a limited effort to obtain experimental data with respect to the first three items of wind characteristics

described above, a 300-ft tower was instrumented at three levels to measure the wind velocity and direction. A 5-min period was used for all three items. Data was collected from September 1966 through August 1967 and reduced.

b. Instrumentation. At three levels of the 300-ft tower, located 564 yd from the 210-ft antenna in the southwest direction, propeller-type anemometers, direction vanes and a potentiometer connected to the center body were mounted. The levels were at 50 ft, 152 ft, and 286 ft above the ground level at the tower. For the purposes of the discussion, the levels will be referred to as 50, 150 and 300 ft.

The described sensing and recording system was limited in response frequency by the recorder characteristic. Its time period was $\frac{1}{2}$ s, with the recording mechanism critically damped. However, for the 5-min period used to compute the three characteristics of the wind as previously described, this time response was adequate.

c. Recorded data. For each sensor, three strip charts advancing at a rate of 6 in./h recorded the wind velocity, the wind direction measured in the horizontal plane, and the wind direction measured in the vertical plane.

d. Results. IBM cards with the punched tabulated data were produced by contract with Meteorology Research, Inc. The cards were then input to the 7094 computer with a special data-processing program to produce the tabulated charts. The data was reduced to reflect the percentage frequency of occurrence of each item of the wind characteristics.

e. Summary. Environmental wind data for a period of one year starting at September 1, 1966 and ending at August 31, 1967 was recorded and reduced in the form of probability charts. The data will be available in a complete report at a later date with descriptions of the methods used to reduce the data with general comments of the environmental wind conditions by Meteorology Research, Inc.

Abbreviations

AAS	advanced antenna system	LCP	left-handed circular polarization
A/D	analog to digital	LE	lunar ephemeris
A/DC	analog-to-digital converter	LO	local oscillator
ADS	advanced data system	LP	linear polarization
AGC	automatic gain control	MDE	mission-dependent equipment
AIL	Airborne Instrument Laboratories	MGC	manual gain control
APS	antenna pointing subsystem	MIE	mission-independent equipment
BCD	binary-coded decimal	MMTS	multiple-mission telemetry system
CAE	computer-assisted entry	moc	minimum operating condition
CEP	continuous estimation program	MSFN	Manned Space Flight Network
CW	continuous wave	NASCOM	NASA Communications Network
DIS	digital instrumentation subsystem	NBS	National Bureau of Standards
DPODP	double-precision orbit determination program	OD	orbit determination
DSCC	deep space communication complex	ODP	orbit determination program
DSIF	Deep Space Instrumentation Facility	PLL	phase-locked loop
DSN	Deep Space Network	PN	pseudo-noise
DSS	deep space station	RCP	right-handed circular polarization
ET	Ephemeris Time	SAF	Spacecraft Assembly Facility (JPL)
ETL	Environmental Test Laboratory (JPL)	SDA	subcarrier demodulator assembly
FTS	frequency and timing subsystem	SDODP	single-precision orbit determination program
GCF	Ground Communication Facility	SFOF	Space Flight Operations Facility (JPL)
GSDS	Goldstone duplicate standard	SMC	station monitor and control
HP	Hewlett-Packard	STADAN	Space Tracking and Data Acquisition Network
HRT	high-rate telemetry	TCP	telemetry and command processor
HRTS	high-rate telemetry system	TTY	teletype
HSDL	high-speed data line	TWM	traveling-wave maser
IAPS	interim antenna pointing subsystem	USNO	United States Naval Observatory
I/O	input/output	VCO	voltage-controlled oscillator
IPMS	International Polar Motion Service	VSWR	voltage standing-wave ratio